Synthesis and Analysis of Bimetallic Nanoparticles

Dissertation

Carolin Rademacher
University of Bielefeld
Faculty of Physics
April 2014

Hiermit erkläre ich, dass mir die geltende Promotionsordnung der Fakultät für Physik der Universität Bielefeld vom 10. Januar 2012 bekannt ist.

Die vorliegende Arbeit habe ich alleine und nur mit den angegebenen Hilfsmitteln verfasst. Alle wörtlich oder inhaltlich übernommenen Stellen habe ich als solche gekennzeichnet.

Dritte haben weder unmittelbar noch mittelbar geldwerte Leistungen von mir für Vermittlungstätigkeiten oder für Arbeiten erhalten, die im Zusammenhang mit dem Zustandekommen oder dem Inhalt der Dissertation stehen.

Ich habe die Dissertation oder wesentliche Teile davon nicht als Prüfungsarbeit für eine staatliche oder andere wissenschaftliche Prüfung eingereicht. Ich habe keine gleiche, in wesentlichen Teilen ähnliche oder eine andere Abhandlung an einer anderen Hochschule als Dissertation eingereicht.

Bielefeld, 14. April 2014

(Carolin Rademacher)

Gutachter

1. Prof. Dr. Andreas Hütten
2. Prof. Dr. Thomas Huser

Contents

1. Introduction

Nanomaterials are expected to be the key-motivation for new technologies emerging at the dawn of the 21st century, where the prefix nano classifies sizes of a billionth meter. The properties of thin films or wires with small diameters, as well as miniaturized particles vary compared to bulk-materials, because the surface to volume ratio O/V is greatly increased. This case is depicted for the example of a sphere in Fig. 1.1. The extremely high surface to volume ratio causes surface effects, which have a minor influence in bulk materials, to determine the behavior of the material. Thus the mechanical, optical, electronic and magnetic characteristics of the material are altered [1, 2].

Particles with diameters of less than 100 nm are referred to as nanoparticles. They have already be used unknowingly since the middle ages. Nanoparticles of gold or silver are the source of the metallic glaze on lusterware dating back to the 9th and 10th century in Mesopotamia [3]. In 1676 Andreas Cassius invented a heat-stable pigment, which was used to color glass [4]. Its red color is caused by gold nanoparticles suspended in the glass matrix.[1] The existence of nanoparticles remained unknown for a long time, because there were no adequate visualization methods. This changed when the electron microscope was invented in 1935 by Ruska and Knoll [6]. Subsequent improvements made the display of structures below the resolution limit of a light-microscope possible. The invention of scanning probe microscopy methods by Binning and Rohrer in the 1980s [7, 8] provided an additional method with similar resolution.

Nanoparticles can be manufactured from a variety of materials, including metals [9], their alloys [10] and oxides [11] and it is possible to form nanoparticles of several different shapes and sizes [12] depending on material and synthesis process [13], for example, titan-oxide nanoparticles are an inherent part of wallpaint, toothpaste (as pigments) or sunscreen [2, 14]. Nanoparticles made of a ferromagnetic material [15] are of special interest. Embedded in a conducting matrix they can show a giant magnetoresistance effect, where

---

[1] The size of the gold particle determines which part of the electromagnetic spectrum is absorbed. Particles with a diameter below 20 nm lead to a deep red coloring, which changes to blue with increasing particle size [5].
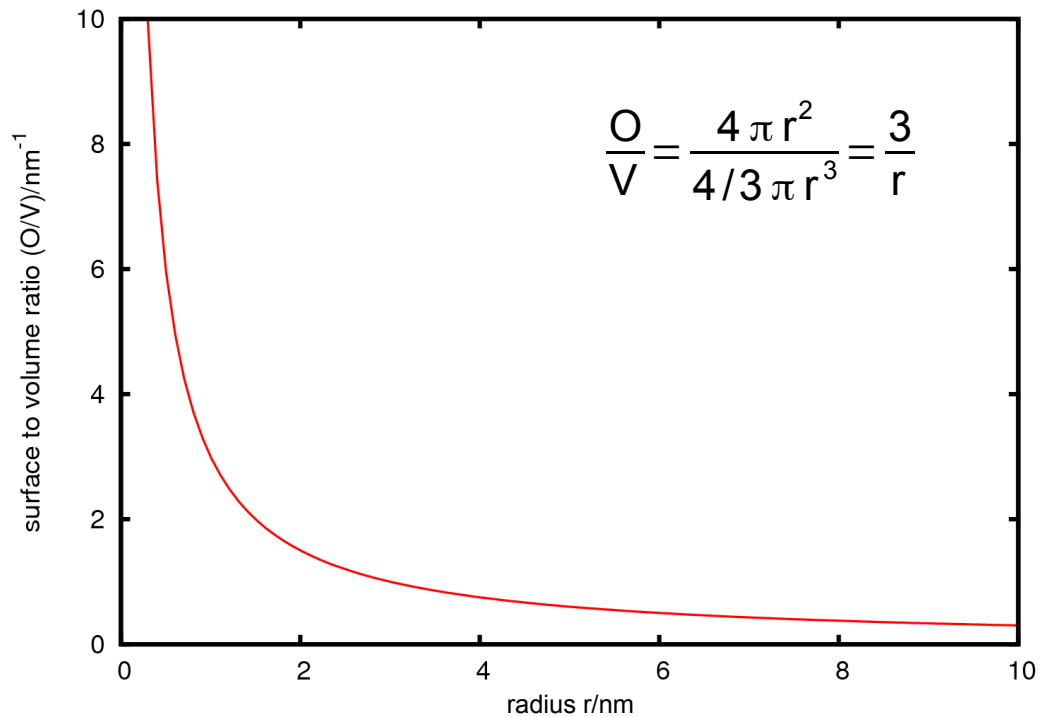
Fig. 1.1: Surface O to volume V ratio of a sphere. The surface to volume ratio O/V increases with decreasing volume V and therefore radius r. The increase in surface area causes surface effects to dominate over volume effects.

the conductivity of the sample is changed by applying an external magnetic field [16, 17]. Further promising applications can be found in cancer-treatment. Cancer cells can directly be treated by magnetic nanoparticles. In magnetic hyperthermia nanoparticles are injected into a tumor. An alternating magnetic field, which changes the magnetization of the particles at rates up to $100\,\mathrm{kHz}$, is applied and the surrounding tissue is heated up [18]. This weakens the cancer cells and makes them more susceptible for chemo- or radiation-therapy or destroys them completely[2]. Usually nanoparticles of iron oxide are used for this application, because they are biocompatible and possess stable magnetic properties. However, it is possible to increase the effectiveness of the therapy by choosing a material with a higher saturation magnetization. The saturation magnetization values of iron oxide particles are around $M_S = 400\,\frac{\mathrm{emu}}{\mathrm{cm}^3}$. This is small compared to the value of pure cobalt $1400\,\frac{\mathrm{emu}}{\mathrm{cm}^3}$ or $Fe_{50}Co_{50}$ $1900\,\frac{\mathrm{emu}}{\mathrm{cm}^3}$ [16].

---

[2]This method received approval in the European Union for treatment of glioblastoma multiforme [19].

Oxidation represents a major problem in nanoparticle systems, since it alters the properties of the particles. While cobalt is ferromagnetic, cobalt oxide behaves anti-ferromagnetic [20]. The oxidation properties of cobalt nanoparticles have been investigated in detail by Vogel [21]. Cobalt is cytotoxic, which further complicates the application on biological samples. A solution to avoid these problems was found in synthesizing a precious metal shell around the functional magnetic core, for which a patent has been issued by Cheon and Park [22] in 2004 followed by a synthesis route by Lee et al. [23], who reported a synthesis route for gold coated cobalt particles. The gold surface stabilizes the core against oxidation, renders the cobalt particle biocompatible and makes it possible to attach a large number of different molecules via thiol-groups to its surface [24]. Other groups also published syntheses for so-called core-shell particles with a variety of different material combinations [25–30]. However, core-shell type particles are not yet commercially available, fourteen years after the synthesis routes were first published, indicating that there are problems producing such nanoparticles or yielding acceptable amounts of core-shell type particles. There has not been a study on why the synthesis of core-shell type particles can fail, yet.

This thesis revises two syntheses reported by Bao et al. [31] in 2005 and Bao et al. [32] in 2007. The aim is to clarify, if core-shell type particles can be generated by these syntheses and if not, what particles are generated and what exactly prevents a successful synthesis. Chapter 2 of this thesis gives a summary on the classical nucleation theory by LaMer and Dinegar [33] and covers the particulars of magnetism in nanoscale materials. The devices used to characterize the micro-structural, magnetic and elemental properties of the nanoparticles are listed and explained in chapter 3. The chosen syntheses and the authors' characterization results are introduced in chapter 4. Chapter 5 is dedicated to simulations of diffraction data for different modifications of cobalt [34] to identify the correct crystal structure of the polymorphic material. The results of the synthesis reproduction of Bao et al. [31] 2005 are listed in chapter 6, while the results of the synthesis by Bao et al. [32] 2007 are listed in chapter 7. The knowledge gained by the investigation of both syntheses is summarized in chapter 8 and an outlook on possible future projects is given in chapter 9.

2. Theory

This chapter covers the basic nucleation and growth theory for bottom-up nanoparticle synthesis and an introduction to magnetism in bulk and nanosized materials.

2.1. Nanoparticle synthesis

Nanoparticles can be obtained either by "top-down methods" like grinding or milling a bulk-size material until the fragments are small enough or by "bottom-up methods", where the particles are built up from their smallest subunits, called monomers, which can be molecules or atoms. Although huge amounts of the particles can easily be produced via a top-down method, they are often arbitrary shaped and show a wide size-distribution. This presents itself as a problem, because of size-dependent properties [35]. It is possible to obtain ensembles of nanoparticles, which are uniform in size and shape, from bottom-up methods. Unfortunately, these syntheses cannot always be up-scaled; only milliliter amounts of nanoparticle suspensions or a few grams are often yielded from a single approach. This thesis is limited to wet chemical synthesis approaches and neglects alternative processes from e.g. gaseous phases. Wet chemical methods include the reduction of metallic precursors, inverse micelle processes or the rapid ultrasonic or thermal decomposition of metallic carbonyls [15, 36]. The latter is used in this thesis and details on the reaction can be found in chapter 4. The next section gives a comprehensive summary on nucleation and growth of nanoparticles from wet chemical processes. The terms **homogeneous** and **heterogeneous** in context with nucleation events are defined. In this thesis the term **homogeneous nucleation** refers to a nucleation taking place in an environment, which does not contain any preformed crystals or other deliberately added nucleation centers. In the case that the reaction solution contains crystals, which serve as nucleation centers, the nucleation is considered to be a **heterogeneous nucleation**. It is almost impossible to have an environment free of impurities like dust or cavities in the reaction vessels, which serve as nucleation centers. A nucleation event can

be triggered by the presence of these impurities [37], however this effect is not considered in this work.

2.1.1. Homogeneous nucleation described by the LaMer-model

The LaMer-model was originally used to describe the formation of hydrosols [33], but can be applied to the nucleation of nanoparticles in a liquid solution, too [38]. The course of the nucleation is depicted in Fig. 2.1 and qualitatively described. In phase I the injected precursors are thermally decomposed and release monomers into the reaction environment and their concentration increases beyond the saturation limit (S=1) of the system, without the formation of any particles. The monomers are released from the injected precursor, which is thermally decomposed in the reaction solution. At the beginning of phase II the solution's oversaturation reaches a critical limit S_C. Beyond this limit the oversaturation is high enough that stable nuclei, which can grow into particles, are formed in the solution. Nuclei are always formed and as fast dissolved in the solution, due to local variations of the Gibbs free energy ΔG. Only above the critical nucleation limit the nuclei are faster formed than dissolved and accumulate in the solution. A nucleus developed at the beginning of phase II has more time to grow than one formed at the end of phase II. The time the system remains in phase II defines the size-distribution of later obtained nanoparticles. A stable nucleus formed at the beginning of phase II starts to grow, while other nuclei are still formed. The longer the system forms nuclei, the more the resulting nanoparticles differ in diameter. Ideally all nuclei are formed at the same time, which can be achieved by a fast injection of the precursor. After the nucleation event is triggered the free monomer concentration decreases rapidly, because the monomers are consumed by the nucleation process and particle growth. The oversaturation drops below the critical limit and the nucleation is disrupted. The monomer concentration continues to drop in phase III. Now the monomers are consumed through growth of the nuclei into solid particles.

The previously qualitatively explained LaMer-model can be quantified through thermodynamic considerations [37, 38]. The Gibbs free energy ΔG for the formation of a spherical crystal with radius r from the monomers in solution is given by the sum of the surface excess free energy ΔG_S, which is the difference between the excess free energy of a monomer at the surface and in the bulk of a particle and the volume free excess energy ΔG_V, which gives the difference
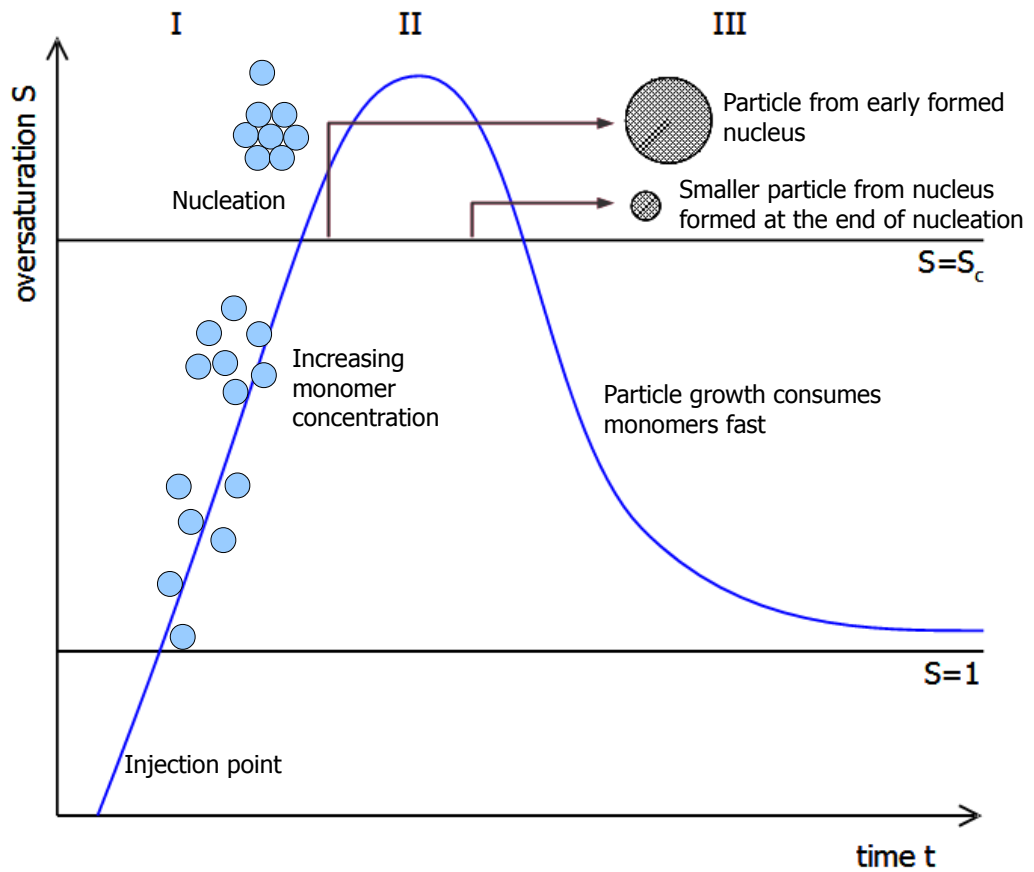
Fig. 2.1: The LaMer diagram. In phase I the monomer concentration increases until the critical oversaturation S_C is exceeded and the nucleation event is triggered. In phase II nuclei are formed, which grow into particles, if they exceed a critical radius r_c. A stable nucleus formed at the beginning of the nucleation event immediately starts to grow and will reach a larger diameter than a particle grown from a nucleus formed at the end of the nucleation event. Nucleation and particle growth decrease the oversaturation S and below S_C no new nuclei are formed. During phase III the monomer concentration decreases further, because particle growth processes use remaining free monomers. [33, 38]

between the free excess energy of a very large particle and the solute in solution

$$\Delta G = \Delta G_S + \Delta G_V = 4\pi r^2 \gamma + \frac{4}{3}\pi r^3 \Delta g_v \quad . \qquad \text{(eq. 2.1)}$$

ΔG_S is the product between the surface area of a sphere $4\pi r^2$ and the constant interfacial tension γ between the crystal and the surrounding solution. ΔG_V is the product between the volume of a sphere $\frac{4}{3}\pi r^3$ and the parameter $\Delta g_v = -\frac{RT \ln S}{V_m}$, with gas constant R, temperature T, degree of oversaturation S and the molar volume of the bulk crystal V_m. The contribution ΔG_V, although ΔG is written as a sum, has a negative sign caused by the parameter Δg_v. It gives the energy difference per unit volume between a solvated monomer and a monomer in a bulk crystal. ΔG, ΔG_S and ΔG_V are plotted against the radius in Fig. 2.2. The maximum value of the Gibbs free energy ΔG_C and the critical radius for a stable nucleus r_c can be calculated from $\frac{\mathrm{d}\Delta G}{\mathrm{d}r} = 0$.

$$r_c = \frac{2\gamma V_m}{RT \ln S} \qquad \text{(eq. 2.2)}$$

The maximum is located at the critical radius r_c. This is the smallest radius a stable nuclei can have. The corresponding critical free energy is given by [38]

$$\Delta G_c = \frac{16\pi\gamma^3}{3\left(\Delta G_V\right)^2} = \frac{16\pi\gamma^3 V_m^2}{3\left(RT \ln S\right)^2} = \frac{4}{3}\pi\gamma r_c^2 \quad . \qquad \text{(eq. 2.3)}$$

During nucleation the increasing number N of stable nuclei per time t can be noted as an Arrhenius equation

$$\frac{\mathrm{d}N}{\mathrm{d}t} = A\exp\left[-\frac{\Delta G_c}{kT}\right] = A\exp\left[\frac{16\pi\gamma^3 V_m^2}{3k^3 T^3 N_A^2 \left(\ln S\right)^2}\right] \quad . \qquad \text{(eq. 2.4)}$$

This equation can be rewritten to deliver a value for S

$$\ln S = \sqrt{\frac{16\pi\gamma^3 V_m^2}{3k^3 T^3 \ln\left[A/\frac{\mathrm{d}N}{\mathrm{d}t}\right]}} \quad , \qquad \text{(eq. 2.5)}$$

which defines the point of oversaturation at which the number of nuclei increases, even if smaller unstable nuclei are dissolved [38].
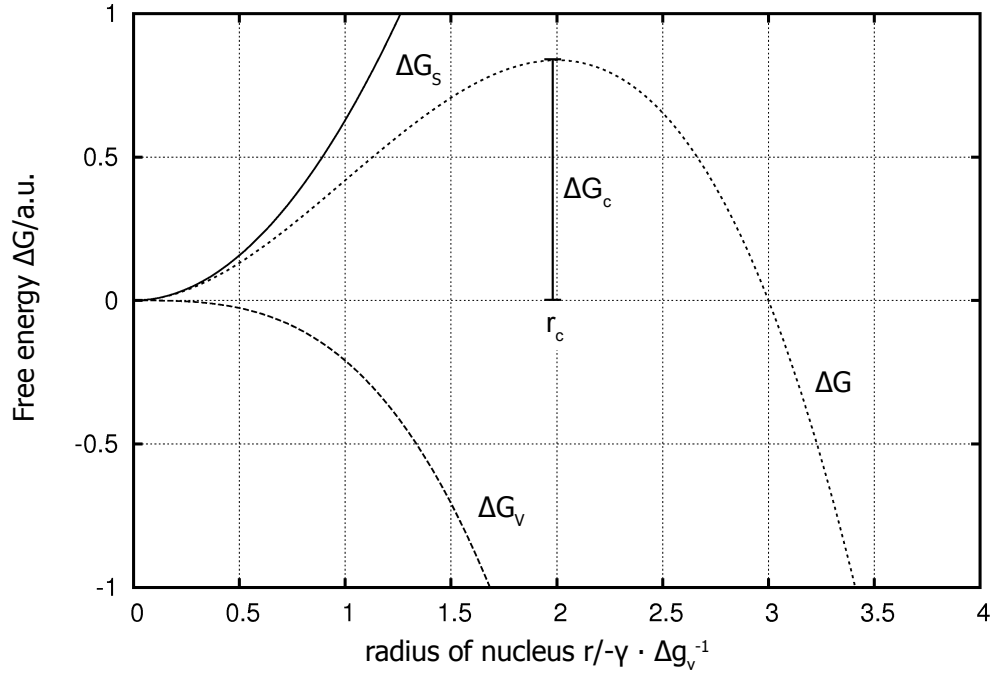
Fig. 2.2: Dependence of the surface ΔG_S and volume ΔG_V free excess energy ΔG for the formation of a spherical crystal. ΔG_S minimizes with decreasing radius, while ΔG_V minimizes with increasing radius. This leads to a maximum of ΔG located at a critical radius r_c. The corresponding critical energy ΔG_C needs to be overcome to form a stable nucleus with $r > r_c$, which will continue to grow, while smaller nuclei are dissolved. [37, 38]

2.1.2. Heterogeneous nucleation and shell formation

The heterogeneous nucleation can be qualitatively described within the LaMer model, as depicted in Fig. 2.3. Spherical seed particles, e.g. produced through homogeneous nucleation, act as nuclei in the second step. Added monomers are consumed by deposition on the seeds. Subsequent monomer additions grow shells of decreasing thickness around a seed particle considering a purely heterogeneous nucleation. Ideally, the monomer addition does not trigger a second homogeneous nucleation event. This would produce competing nuclei, which deplete the monomers and prevent their deposition on the seed particles.

The critical energy needed for a nucleation on an already formed spherical seed is lower, than the energy needed for a homogeneous nucleation [37, 40, 41]

$$\Delta G'_c = \phi \cdot \Delta G_c \ . \tag{eq. 2.6}$$
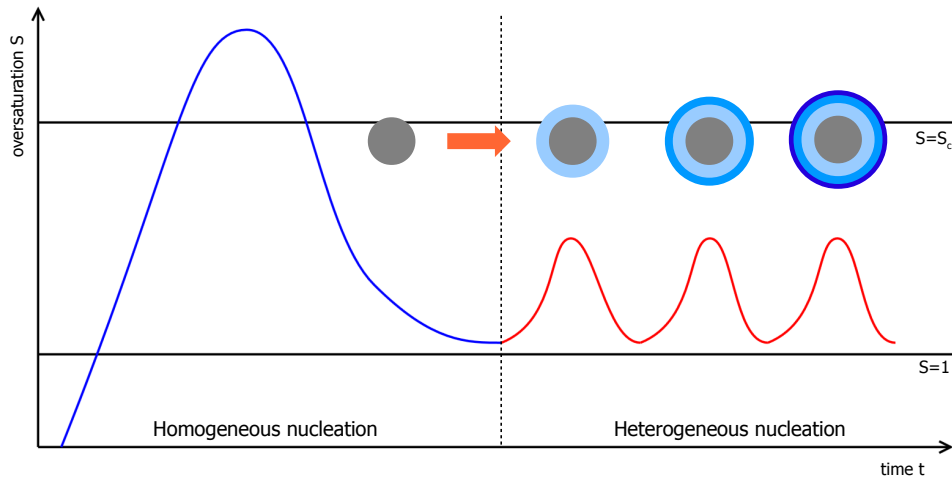
Fig. 2.3: A homogeneously nucleated spherical particle is used as nucleation center during a heterogeneous nucleation. Small amounts of monomers are added, without triggering a homogeneous nucleation event. The monomers are deposited on the present seed particles, which decreases their concentration. On this way it is possible to increase the size of a particle, if monomers of the same material are added. Monomers from a second material grow a distinguishable shell around the seed particle. The thickness of these shell(s) decreases with every monomer addition, if the same amount of monomers is added. [39]

The parameter ϕ lies between 0 and 1 and is given by [37, 40]

$$\phi = \frac{(2 + \cos\Theta)\,(1 - \cos\Theta)^2}{4} \quad .$$ (**eq.** 2.7)

It determines by how much the energy barrier is lowered in comparison to a homogeneous nucleation event. The parameter Θ is the contact-angle between the two material phases, as depicted in Fig. 2.4. Three different interfacial tensions occur at the contact area[1]: one between the two different crystalline materials $\gamma_{1,2}$ and two between the materials and the surrounding liquid[2], $\gamma_{\ell,1}$ and $\gamma_{2,\ell}$. The contact angle Θ is

$$\cos\Theta = \frac{\gamma_{\ell,1} - \gamma_{2,1}}{\gamma_{2,\ell}} \quad .$$ (**eq.** 2.8)

Three different cases can occur depending on the contact-angle Θ, which is dependent on the interfacial energies of the materials [37, 40].

---

[1]This ansatz is not valid for $\Theta = 180°$, because the two crystalline phases are not in contact.
[2]The liquid is the solvent-surfactant mixture, in which the synthesis is executed and it is noted with the index ℓ. A more familiar example for such an interfacial energy diagram is a droplet wetting a solid surface under its own vapor.
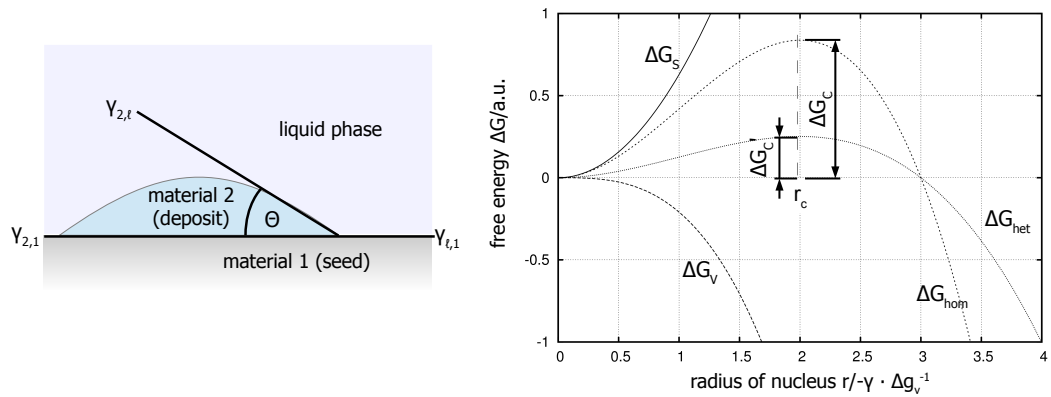
Fig. 2.4: Left: Interfacial energies and the contact angle between two crystalline phases and one liquid phase [37, 40]. The schematic is inspired by a droplet wetting a flat surface under its own vapor. Right: The energy barrier $\Delta G'_c$, that a heterogeneous system needs to overcome is much smaller compared to the energy barrier of a homogeneous nucleation (this figure is an expansion of Fig. 2.2).

No contact   The second material is not wetting the seed-particle. The contact angle is $\Theta = 180°$ and $\phi = 1$. Forming an interface between the deposit and seed is energetically more unfavorable than to form an interface between the liquid and the two solid phases. Because the second material and the seed are not in contact, the system needs to overcome the same energy-barrier as in case of a spontaneous nucleation
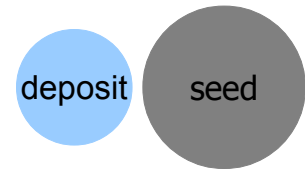
Fig. 2.5: Contact angle $\Theta = 180°$

$$\Delta G'_c = \Delta G_c \ .$$

(**eq.** 2.9)

Partial affinity   The contact-angle Θ is between 0° and 180°, which results in $\phi < 1$. The seed particles provide suitable nucleation sites, but are not entirely covered by the second material. Therefore, at one point during the synthesis it is unfavorable to increase the interface between the two crystals and the seed particle is only partial covered. The critical energy is in this case less than needed for a homogeneous nucleation
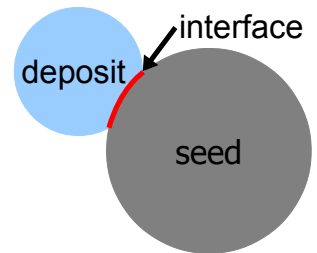
Fig. 2.6: Contact angle $0° < \Theta < 180°$

$$\Delta G'_c < \Delta G_c \ .$$

(**eq.** 2.10)

Complete coverage The second material is completely covering the seed. Forming an interface with the seed and the surrounding liquid is energetically more favorable, than maintaining the interface between the seed and the surrounding liquid. The contact angle is $\Theta = 0°$ and $\phi = 0$. The material deposited on the seed particles increases the diameter of each particle and the free energy of nucleation therefore is
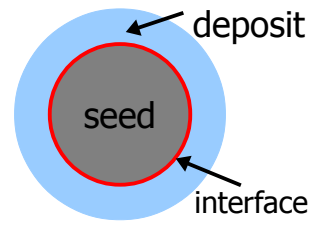
Fig. 2.7: Contact angle $\Theta = 0°$

$$\Delta G'_c = 0 \quad .$$

(**eq.** 2.11)

In case of complete coverage, the whole seed particle is seen as nucleus for the heterogeneous nucleation of the second material and it is expected, that a homogeneous shell of the second material is formed around the seed particle. The successive addition of monomers from the same material the seeds are composed of has been reported to form a homogeneous shell and leads to nanoparticles with increased diameter [39]. If monomers of a different material are added and a heterogeneous nucleation takes place a shell of the second material can be grown around the seed particle obtaining a core-shell particle. This is also referred to in literature as "heterogeneous seeded growth" [42]. In case of partial affinity, only small parts of the surface area of the seed become covered with the second material. The area, where the deposit attaches to the surface is called a nucleation site. It is possible, that one seed particle has several nucleation sites.

2.1.3. Particle growth

The growth of the nuclei into solid particles with uniform size can be described by a model first proposed by Reiss [43] and summarized by Park et al. [38]. The increase of the particle radius r is described by the monomer flow J through a spherical shell $4\pi r^2$ around the nucleus

$$J = \frac{4\pi r^2}{V_m} \frac{\mathrm{d}r}{\mathrm{d}t} \quad ,$$

(**eq.** 2.12)

with V_m, the molar volume and r the radius of the crystal and $\frac{\mathrm{d}r}{\mathrm{d}t}$ the particle growth per time. An isolated particle is surrounded by a spatial concentration

11
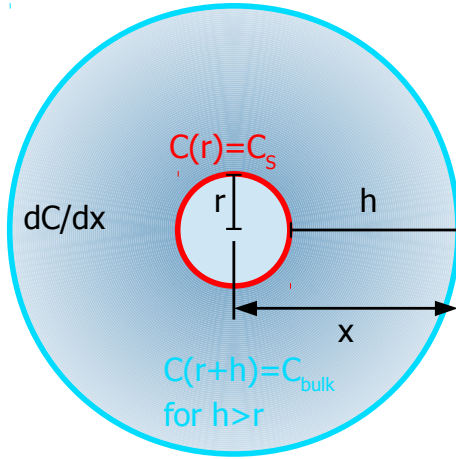
Fig. 2.8: A growing particle with radius r is surrounded by a spatial monomer concentration gradient dC/dx. The concentration at the particle's surface equals $C(r) = C_S$, while the concentration at $r + h$ away from the particle center is $C(r + h) = C_{\text{bulk}}$, which equals the bulk monomer concentration of the solution.

gradient $\frac{dC}{dx}$. The flow of monomers towards the particle can be described by Fick's law and the equation is expanded to

$$J = -4\pi x^2 D \frac{dC}{dx} \quad , \tag{eq. 2.13}$$

whereas D is the diffusion coefficient of the monomers and x the distance to the center of the particle. Integration over x from the particle surface at r, with the corresponding concentration $C(r) = C_S$ to a position away from the particle center at $r + h$, where the monomer concentration is $C(r + h)$ changes (**eq.** 2.13) to

$$J = 4\pi D \frac{r(r+h)}{h} \left[C(r+h) - C(r) \right] \quad . \tag{eq. 2.14}$$

If the distance from the particle surface h is large compared to the particle radius r, the corresponding monomer concentration at h matches the bulk-concentration C_{bulk} of the surrounding solution. This is depicted in Fig. 2.8. The equation can be further simplified to

$$J = 4\pi r D \left(C_{\text{bulk}} - C_s \right) \quad . \tag{eq. 2.15}$$

The rate of growth $\frac{dr}{dt}$ therefore is reciprocally dependent on the particle radius r, if (**eq.** 2.12) and (**eq.** 2.15) are combined

$$\frac{dr}{dt} = \frac{V_m D}{r} \left(C_{\text{bulk}} - C_s \right) \quad . \tag{eq. 2.16}$$

This means that the speed of growth decreases with increasing particle diameter. The particle stops to grow, when all monomers are consumed. Afterwards it is possible that ripening processes alter the size of the particles.

2.1.4. Ostwald ripening and form of the size-distribution

After the growth process the particles are described by a particle size-distribution. The shorter the time the system stayed above the nucleation limit, the narrower is the size-distribution of the resulting particles [33, 38]. A particle batch with a standard deviation of less than 10% is considered mono-disperse, while distributions with a standard deviation of 20% are called "narrow" [44, 45]. After the particle growth stops the diameter distribution can be fit with a Gaussian function, which is illustrated by

$$F\left(d\right)_{\text{Gauss}} = y_0 + A \cdot \exp\left[-\left(\frac{d - \langle d \rangle}{\sqrt{2}\sigma}\right)^2\right] \quad . \tag{eq. 2.17}$$

A is the amplitude of the curve at its maximum. The maximums position equals the mean diameter[3] $\langle d \rangle$ and describes the calculated number of particles having this diameter. y_0 gives the y-axis offset[4] and σ is the standard deviation of diameters around the mean diameter, containing 68.3% of all measured values [46, 47]. The full width at half maximum (FWHM) can be calculated for a Gaussian distribution from the standard deviation via $\text{FWHM} = 2,3548 \cdot \sigma$. An example is depicted in Fig. 2.9, left side.

It is possible, that the size distribution of a particle batch changes after the growth process is completed. Smaller particles are dissolved, because they have a high surface energy. The particle system minimizes its surface energy by dissolving smaller particles and adding the crystal monomers to larger particles [48]. This process is called Ostwald ripening [49, 50] and continues until the surface energy reaches a minimum [51]. The number of smaller particles decreases during Ostwald ripening and the resulting size-distribution is asymmetric. The mean particle diameter shifts to larger values, the number of particles present in the solution decreases and the distribution develops a "tail" towards larger diameters. The size distribution's form is that of a log-normal distribution and this and the "tailing effect" is an indication for Ostwald ripening processes occurring during the particle synthesis [52]. A log-normal

---

[3]The mean, mode and median are located at the same position in a Gauss distribution, which is symmetric.

[4]y_0 does not have a physical meaning in this case.

distribution plotted against the logarithm of the diameter $\ln(d)$ again gives a Gaussian function. The fit function used for a log-normal distribution is described by

$$F(x)_{\text{log-normal}} = y_0 + A \cdot \exp\left[-\left(\frac{\ln(d) - \ln(d_0)}{\sqrt{2}\ln(\sigma')}\right)^2\right] \quad , \qquad \textbf{(eq. 2.18)}$$

with A the maximum amplitude at the position of the mode d_0 and σ' the (multiplicative) standard deviation [46]. The median, separating the distribution into two equal halves[5], is calculated by $\bar{d} = d_0 \exp[\sigma'^2]$ [53, 54]. The mean diameter is also calculated from the mode by $\langle d \rangle = d_0 \exp\left[\frac{3}{2}\sigma'^2\right]$. The standard deviation of a log-normal distribution cannot be added simply to the mean or median[6], respectively. The first confidence interval is calculated using the multiplicative standard deviation $d \pm \sigma = \bar{d} \cdot \exp\pm[\sigma']$. Again this leads to dissimilar x-axis intercepts left and right of the median, corresponding to the first confidence interval. Both cases are depicted in Fig. 2.9.
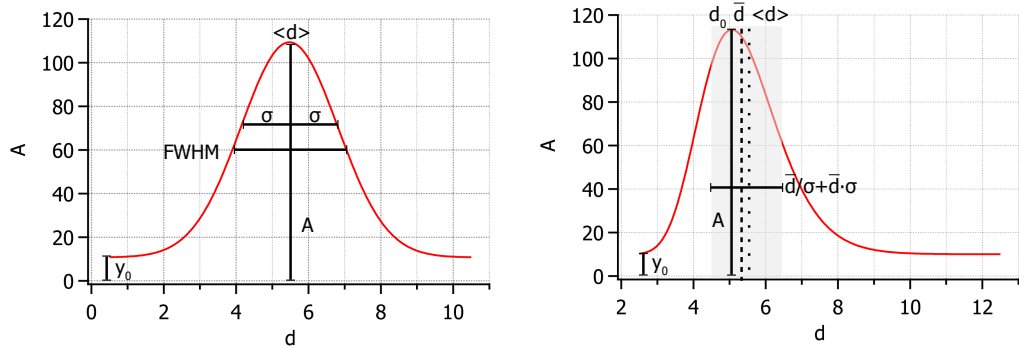
Fig. 2.9: Left: Example of a size-distribution in gaussian form, with y_0 the y-offset of the curve, the amplitude A of the most frequently occurring diameter d, the mean diameter $\langle d \rangle$, the standard deviation σ and the full width at half maximum *FWHM*. Right: Example of a log-normal size distribution, with the mode d_0, median $\bar{d}$ and mean $\langle d \rangle$ located at separate positions due to the asymmetric shape of the distribution. The first confidence interval of the multiplicative standard deviation $d \pm \sigma = \bar{d} \cdot \exp\pm[\sigma']$ is located at the median and also asymmetrically shaped. A log-normal distribution is an indication for Ostwald ripening during particle synthesis.

---

[5]The number of distributed elements with values below the median equals the number of elements above the median.

[6]The mean, median and mode of a Gaussian distribution have the same value, because the distribution is symmetrical. In case of a log-normal distribution the value of the median exceeds the value of the mode and the mean exceeds both values.

2.1.5. Stabilization
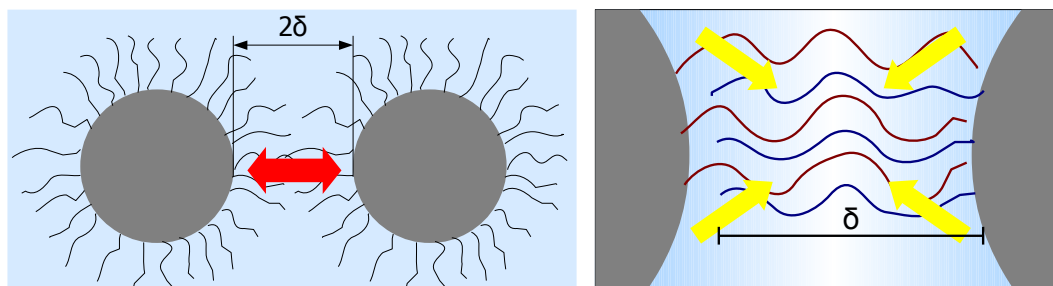
Fig. 2.10: Steric stabilization is achieved by surfactants covering the particle surface. For example, non-polar alkyl-chains are connected to the surface via polar head groups. The surfactants of two particles (depicted in red and blue) interlace when the distance of the two particles is below the double surfactant layer thickness 2δ. The interlaced surfactants are less mobile, which increases the free energy of the system and they push aside solvent molecules in the interlaced areas (depicted through the color gradient of the background). The resulting osmotic pressure pushes the solvent molecules in between the particles (yellow arrows) and separates the nanoparticles again. The repulsing force is depicted through red arrows.

The particles need to be stabilized against agglomeration[7]. This can be done by either forming an electrical double layer around the particles or coating them with surfactants [44]. In an aqueous environment adsorbed ions at the particle surface will attract their corresponding counter ions and an electrical double layer will be formed, separating the particles. This is not an option, if the synthesis is carried out in a water- and air-free environment. Here the steric stabilization through surfactants or a polymer is used, which is depicted in Fig. 2.10. Amphiphilic molecules like oleic acid, bind with their hydrophilic heads to the surface of the particle, while their hydrophobic tails point outwards into the surrounding non-polar solvent [44]. If two surfactant-covered particles move towards each other and are separated by a distance less than twice the thickness of their surfactant layer the steric interactions between their surfactants cause a repulsive force. Two effects are responsible for this repulsive force. First the interlaced surfactants are less mobile, which decreases the entropy of the system. Second the solvent is pressed from the areas of interlaced surfactants. The resulting osmotic pressure causes a solvent-flow to the areas of previously low solvent concentration. This forces the particles apart and prevents the agglomeration [21, 55].

---

[7]Van-der-Waals and magnetic dipole forces attract single nanoparticles, which form three dimensional clusters. These cluster do not show the large surface to volume ratios of nanosized materials and do not benefit from their changed properties [44].
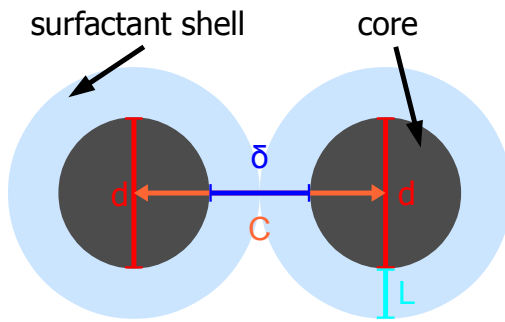
Fig. 2.11: Distances in a TEM-image of nanoparticles. The diameter of the individual particles is denoted as d. The center-to-center distance C is not measured, but the inter-particle distance δ is used to determine the thickness $L = \frac{\delta}{2}$ of the surfactant layer around the particles.

Spherical nanoparticles are able to form monolayers with a hexagonal order on e.g. carbon coated TEM-grids [44]. The distance between two adjacent particles is determined by the thickness of the surfactant layer L. This is displayed in Fig. 2.11. Sterical repulsion balancing attractive forces lead to minimal distance between the nanoparticles. The interparticle distance δ can be used to some extend to estimate the thickness of the surfactant shell and therefore the length of the surfactants [21]

$$L = \frac{\delta}{2} \quad .$$
(**eq.** 2.19)

Besides the stabilization against agglomeration surfactant molecules also influence the shape and size of a particle. Ostwald ripening process can be prevented by surfactants covering the surface of a particle [56]. Furthermore the selective attachment of surfactants to certain crystal faces alters the form of the resulting nanoparticles [12]. The size of particles can be influenced by the choice of surfactants and their concentration, too. The higher the binding affinity of the surfactant, the smaller the resulting particles become [55]. However this has not been investigated in detail yet and is a topic of ongoing discourse.

2.2. Magnetism

Magnetism is a widely used effect in everyday life, for example in data-storage on hard-drives and electric motors. The microscopic cause of a material's magnetic behavior are its atom's electrons and nucleus. The contribution of the nucleus to the overall magnetic moment of the atom can be neglected compared

to the contribution of the electrons. Every electron's magnetic moment arises from its orbital angular moment $\vec{L}$ and its spin angular moment $\vec{S}$,

$$\vec{m}_L = -\frac{1}{\hbar}\mu_B\vec{L} \qquad \text{and} \qquad \vec{m}_S = -g_s\frac{1}{\hbar}\mu_B\vec{S} \ , \tag{eq. 2.20}$$

with $\hbar = \frac{h}{2\pi}$ with the Planck constant h, $\mu_B = \frac{e\hbar}{2m_e} = 9.27 \cdot 10^{-24} \frac{\text{J}}{\text{T}}$ as the Bohr-magneton and $g_s = 2.00232$ as the Landé-factor[8][57–59].

The sum of both contributions is the magnetic moment $\vec{m}$ of the atom

$$\vec{m} = \sum \vec{m}_L + \vec{m}_S \ . \tag{eq. 2.21}$$

The magnetization $\vec{M}$ of a material with volume V is the sum over all its magnetic moments $\vec{m}$

$$\vec{M} = \frac{\sum\limits_{i=1}^{N} \vec{m}_i}{\sum\limits_{i=1}^{N} V_i} \ . \tag{eq. 2.22}$$

An external magnetic field $\vec{H}$ causes the magnetic induction $\vec{B}$ in the material and is described by

$$\vec{B} = \mu_0 \left(\vec{H} + \vec{M} \right) \ , \tag{eq. 2.23}$$

with the magnetic vacuum permeability $\mu_0 = 4\pi \cdot 10^{-7} \frac{\text{N}}{\text{A}^2}$. The magnetization $\vec{M}$ in a material and the external field are connected through the relation

$$\vec{M} = \chi \cdot \vec{H} \tag{eq. 2.24}$$

where the susceptibility χ measures the influence of $\vec{H}$ on the material. It is connected to the relative permeability μ_r and the permeability of a specific medium μ through

$$\mu_r = 1 + \chi = \frac{\mu}{\mu_0} \ . \tag{eq. 2.25}$$

---

[8]This factor gives the difference between the classical anticipated magnetic moment, which only takes the orbital angular momentum into account, and neglects the spin. In case of $\vec{m}_L$ the Landé-factor equals 1.

2.2.1. Forms of magnetism in bulk materials

In bulk materials different forms of magnetism occur and magnetization curves of dia-, para- and ferromagnetism[9] are depicted in Fig. 2.12. The magnetic spin moments $\vec{m}_S$ align parallel and the orbital moments $\vec{m}_L$ anti-parallel to an applied the external field. If the spin moments are the dominating part of a material's magnetic moments, their parallel alignment to the external field increases the magnetization $\vec{M}$ within the material, which is then called paramagnetic [59]. Paramagnetic materials have permanent magnetic dipole moments, which can be aligned to a certain degree by an external magnetic field. Without an external field they are randomly orientated due to thermal motion, which opposes the alignment of the dipoles even under the influence of an external field [58, 59].

If the orbital moments $\vec{m}_L$, anti-parallel aligned to the external field, are dominating the magnetic moments of material, than the magnetization in the material is decreased in an external field and the material is called diamagnetic [59]. It does not have any permanent magnetic moments, but will form induced dipole moments, when placed in an external field $\vec{H}$. Those dipole moments align anti-parallel to the external field according to Lenz's law and decrease the magnetic induction $\vec{B}$ in the material. The effect exists in all materials, however effects like para- or ferromagnetism superimpose it, because induced magnetic dipole moments are a lot smaller and weaker than permanent magnetic moments [58].

A ferromagnetic material has permanent magnetic moments, that align spontaneously in microscopic, limited areas without the presence of an external field. These areas are called domains and their orientation towards each other always tends to keep the magnetic flux within the material [61]. Hence the material does not show any net-magnetization. The domains aligned parallel to an external field start to grow, when the field is increased, at expense of those, which are more unfavorably aligned. The magnetization $\vec{M}$ in the material increases strongly, even if only weak external fields are applied. If only one domain with magnetic moments parallel aligned to the external field remains in the material [62, 63], it reaches its saturation magnetization value M_S. Further increasing the applied magnetic field does not increase the material's magnetization value. If the external field is turned off the magnetization of the saturated material

---

[9]Other forms of collective magnetism, anti-ferromagnetism and ferrimagnetism are not considered here. An anti-ferromagnetic sample does not show a net-magnetization in an external field, while ferrimagnetism is a weaker form of ferromagnetism. Details on both cases can be found in Nolting and Ramakanth [59].
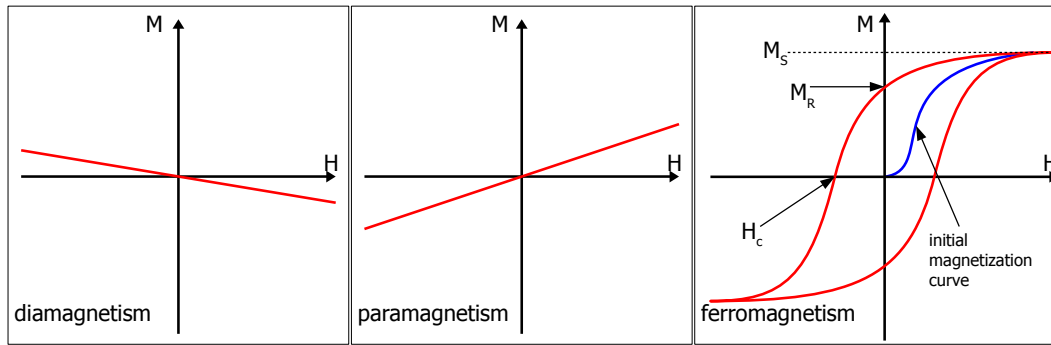
Fig. 2.12: Dependences between external magnetic field $\vec{H}$ and the magnetization $\vec{M}$ for dia- and para- and ferromagnetic materials. The magnetization shows a linear dependence on the external field for dia- and paramagnetic materials. Ferromagnetic materials show increasing magnetization even for small external fields and the magnetization increases until the material reachs saturation at M_S. After the external field is turn off the material keeps a net-magnetization of M_R. An external field in the opposite direction needs to be applied to de-magnetize the sample again at H_C. This more complex behavior causes the hysteresis form of the magnetization curve [58, 60].

does not drop to zero; usually a net-magnetization remains; this value is called the remanence $\vec{M}_R$. A state of zero magnetization can only be achieved by applying an external field in the opposite direction. At a certain external field value, the coercivity H_C, the material's magnetization equals zero again. If the external field is increased the material will reach its saturation magnetization again, but with all magnetic moments aligned in the opposite direction. This behavior leads to a hysteresis curve for the magnetization plotted against the external magnetic field (see Fig. 2.12).

2.2.2. Magnetism in nanoscale materials

If the structure size of a ferromagnetic material decreases, some of its characterizing parameters change. The saturation magnetization is not affected by the size changes, but remanence M_R and coercivity H_C are. The development of the coercivity with decreasing particle size is depicted in Fig. 2.13. H_C increases and reaches its maximum value at the critical particle diameter d_{SD}, where only a single magnetic domain remains in the particle. It is energetically more unfavorable to form a domain wall to reduce the stray field of the particle, than to accept the stray field itself. If the particle size is further reduced the coercivity's value vanishes completely. This happens when the particle's diameter reaches the superparamagnetic limit d_{SP} [64].
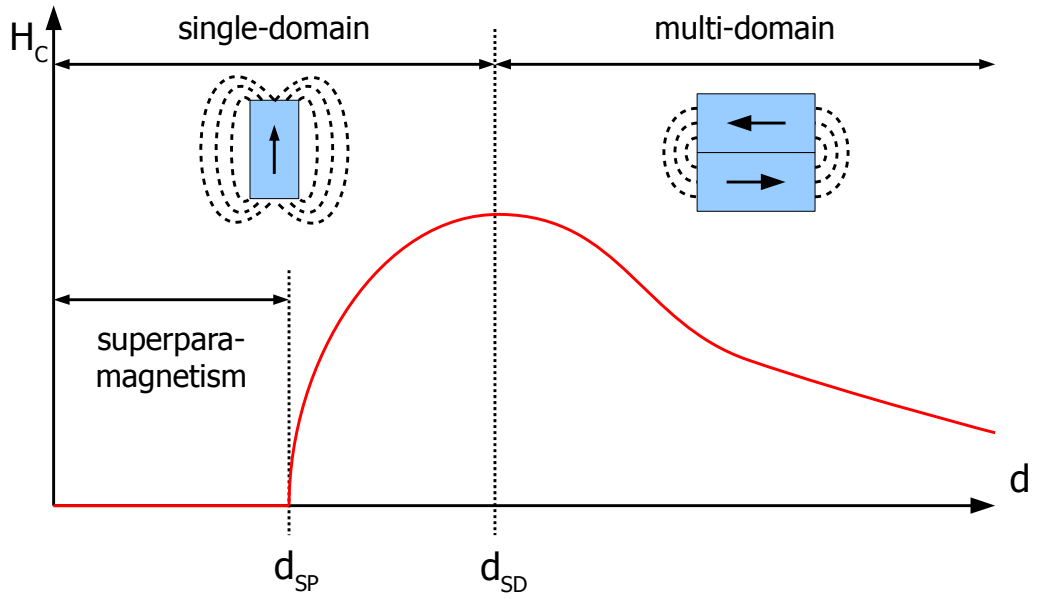
Fig. 2.13: Behavior of the coercivity if the specimen's structure size is reduced. Below a critical diameter d_{SD} the specimen consists of a single domain and H_C reaches its maximum value. Afterwards H_C drops until no coercivity is present in the specimen. At this point the diameter reaches another critical value d_{SP}, the superparamagnetic limit. [64]

Ferromagnetic materials keep a remanent magnetization and therefore the orientation of their magnetic moments, without the influence of an external magnetic field. In contrast to that the orientation of the magnetic moment of a superparamagnetic particle is easily altered through thermal energy. The necessary amount of energy $k_B T$ for that can easily be provided by temperatures above the blocking temperature T_B for small particles [65]. The energy necessary to change the direction of its magnetic moment is dependent on the volume of the particle V and the effective magnetic anisotropy constant K_{eff}, which gives the anisotropy energy per volume unit. Its main contribution is the crystal anisotropy, which is intrinsic to the material. Shape, surface, magnetoelastic and induced anisotropy can further contribute to its value [66].

$$\Delta E \sim K_{\mathrm{eff}} \cdot V \leq k_B T \ , \qquad\qquad (\textbf{eq. } 2.26)$$

Without the influence of an external magnetic field the magnetic moment of a single domain particle is disarranged faster by thermal fluctuations than remanence or coercivity can be measured. This causes a hysteresis free magnetization curve, as depicted in Fig. 2.14 [64]. Its form can be best described for
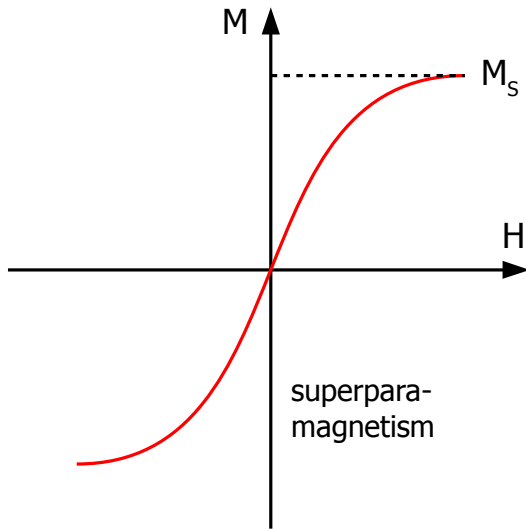
Fig. 2.14: Hysteresis free magnetization curve of a superparamagnetic material in an external field.

non-interacting particles by (**eq.** 2.27) using a Langevin function and taking into account the particles' size distributions [16], if they are not equally sized.

$$\frac{M(H_{\text{ext}})}{M_S} = \int\limits_{0}^{\infty} \frac{1}{\sqrt{2\pi\sigma}} \exp\left[-\frac{(d - \langle d \rangle)^2}{2\sigma^2}\right] \cdot \tag{eq. 2.27}$$

$$\left(\coth\left[\frac{4/3\pi \left(\frac{d}{2}\right)^3 M_S H_{\text{ext}}}{k_B T}\right] - \frac{k_B T}{4/3\pi \left(\frac{d}{2}\right)^3 M_S H_{\text{ext}}}\right) \mathrm{d}D \quad .$$

The function describes the magnetization process with the normalized magnetic moment $\frac{M(H_{\text{ext}})}{M_S}$, the size distribution with mean diameter $\langle d \rangle$ and its standard deviation σ and the thermal energy $k_B T$ provided by room temperature. The size distribution of the nanoparticles' over all diameters leads to an integration over different Langevin functions. The base for the calculations in this case is the particles' mean diameter and a size distribution taking a 5σ interval on both sides of the mean diameter into account. The superparamagnetic limit d_{SP} is a material constant, which is also dependent on the material's crystal-structure. It is possible to asses this critical diameter with the Neel-Arrhenius equation [21, 64]

$$\ln\left(\tau \cdot f_0\right) = \frac{K_{\text{eff}} V}{k_B T} \approx 25 \quad . \tag{eq. 2.28}$$

It gives a relation for the time τ the magnetic moment of the domain is stable after an external field is turned off, the particle's volume, effective anisotropy constant of the material and its temperature T. τ needs to exceed or equal the time a complete measurement takes to record ferromagnetic behavior. The measurement time is usually given with $t_{\text{mess}} = 100\,\text{s} \leq \tau$ [16, 21]. The value $f_0 = 10^9\,\frac{1}{\text{s}}$ is field-independent and called the frequency factor [64]. In case of a spherical particle (**eq.** 2.28) can be written as

$$r_{\text{SP}} = \frac{d_{\text{SP}}}{2} = \sqrt[3]{\frac{25 \cdot k_B T}{K_{\text{eff}} \cdot \frac{4}{3}\pi}} \quad . \tag{eq. 2.29}$$

The temperature T is another critical factor for the value of the superparamagnetic limit. The lowest temperature, for which superparamagnetic behavior is expected, is the blocking-temperature T_B. It marks the critical value, at which the behavior of a samples changes from ferromagnetic to superparamagnetic. The sample will show ferromagnetic behavior for temperatures below, because the thermal fluctuations are too weak to change the alignment of magnetic moments before the measurement is completed. The anisotropy constant used to calculate the limit is often the bulk anisotropy constant, although its value may differ greatly for nanosized structures of the same material. A list of anisotropy constants for different cobalt configurations and their calculated critical diameters is given in Tab. 2.1.

Tab. 2.1: List of effective anisotropy constants K_{eff} of different configurations of cobalt [67, 68] and the corresponding superparamagnetic limits d_{SP} for spherical particles calculated from (**eq.** 2.29) at the temperature T.

configuration	T/K	$K_{\text{eff}}/\frac{\text{J}}{\text{m}^3}$	d_{SP}/nm
fcc-Co-bulk	RT	$2.7 \cdot 10^5$	8.9
fcc-Co-nano	92	$2.1 \cdot 10^3$	15.4
hcp-Co-bulk	RT	$4.1 \cdot 10^5$	7.8
ϵ-Co-nano	RT	$1.5 \cdot 10^5$	10.9
ϵ-Co-nano	47	$8.0 \cdot 10^4$	7.3

3. Characterization methods

The synthesized nanoparticles are investigated with a variety of methods. Different electron microscopy techniques (TEM/STEM/HRTEM) are used to record images of the nanoparticles and analyze their micro- and crystal structure, which is also examined by X-Ray Diffractometery (XRD). The elemental composition is determined by Energy-dispersive X-ray Spectroscopy (EDX). Finally the magnetic properties of the samples are investigated with an Alternating Gradient Magnetometer (AGM). This chapter explains the working principles of all used methods and describes the sample preparation techniques for the corresponding analyses.

3.1. Transmission Electron Microscopy (TEM)

The first transmission electron microscope (TEM) exceeding the resolution of conventional light-microscopy was constructed by Erik Ruska in 1933 [6]. It made the observation of particles and structures in the nanoscale possible, which were not observable before. A schematic overview of a TEM, similar to the used *Philips CM100 Transmission Electron Microscope*, is displayed in Fig. 3.1. At the top electrons are generated by thermionic emission from a small tungsten wire-filament. Electrons overcome the work-function of tungsten, when the filament is heated to $2000\,^{\circ}\mathrm{C}$. Afterwards they are focused into a convergent beam by the Wehnelt cylinder and accelerated due to a potential difference U between the negatively charged cylinder and a grounded anode (see Fig. 3.2). An acceleration voltage of $U = 80\,\mathrm{kV}$ is used to record the images in this work.

The electron's masses need relativistic corrections after acceleration through U and their relativistic impulse is given by [69]

$$p = \sqrt{\frac{E^2 - E_0^2}{c^2}} = \sqrt{\frac{(eU)^2 + 2eUm_0c^2}{c^2}} \ , \qquad\qquad (\textbf{eq. } 3.1)$$

Electron gun

Acceleration tube

1st condensor lens
2st condensor lens
Condenser aperture
assembly

Goniometer

Objective aperture

Specimen holder

Objective lens

Selected field aperture

Intermediate lens

Projector lens

Binocular

Viewing port

Small fluorescent
screen

Large fluorescent
screen

Camera chamber
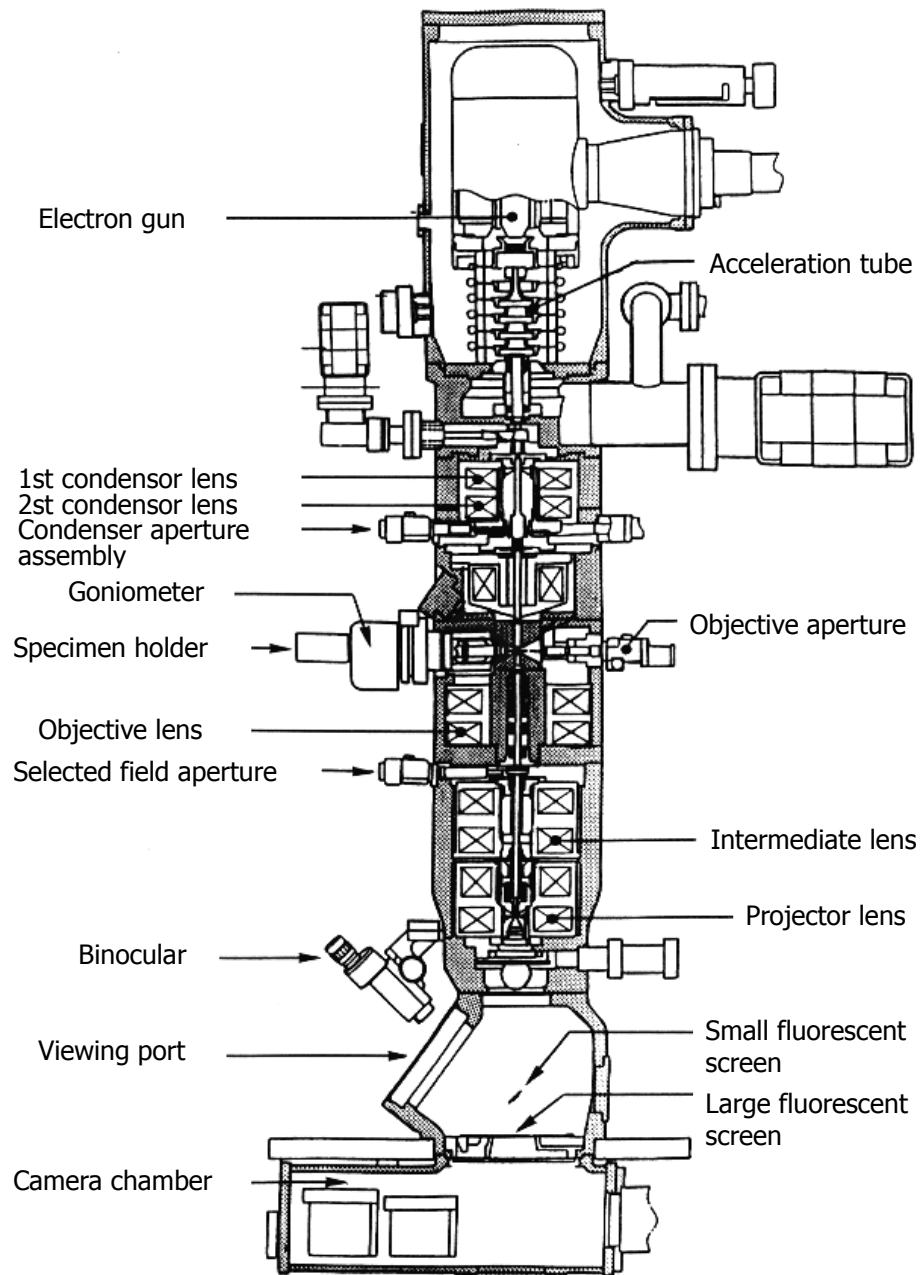
Fig. 3.1: Cross-section view of a transmission-electron-microscope, similar to the used Phillips CM-100 (reprinted from B. Fultz, J. Howe, Transmission Electron Microscopy and Diffractometry of Materials, Graduate Texts in Physics, ©Springer-Verlag Berlin Heidelberg 2013, p. 59, TEM-Querschnitt, with kind permission of Springer Science+Business Media).

with E the electron's total energy, c the speed of light, e elementary charge and m_0 the electron's rest mass and E_0 its rest energy. This leads to **eq.** 3.2 for the electron's de-Broglie wavelength, whereas h is planck's constant

$$\lambda_e = \frac{h}{p} = \frac{hc}{\sqrt{(eU)^2 + 2eUm_0c^2}} \quad .$$ (**eq.** 3.2)

The matter-wavelength limits the theoretical possible resolution of the TEM, but the resolution is further limited by lens aberrations. Those aberrations occur at all lenses in the TEM and a list of possibly occurring aberrations is given by Reimer [70], Reimer and Pfefferkorn [71]. After acceleration the electrons pass a set of condensor lenses, which focus the electrons on parallel tracks and onto the specimen. The electron-beam interacts with the sample and the incident electrons are scattered. Next they pass the objective lens, which forms a diffraction pattern in the back focal plane. For a bright-field (BF) image only the primary electron beam is selected by the objective aperture and used to generate the primary image. Other modes, like dark-field (DF) imaging [72, 73] are not used in this work. The intermediate and projector lens further magnify the primary image generated in the image plane and it is focused on the viewing screen or camera chip. This is depicted in Fig. 3.3.
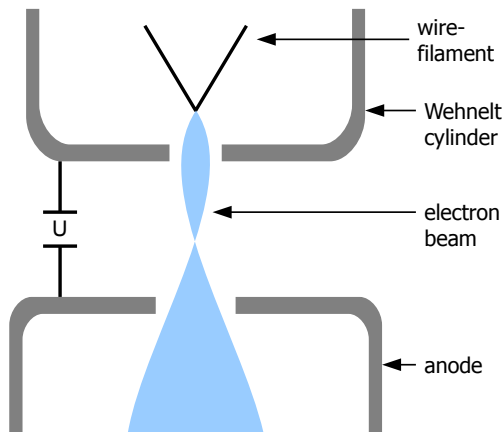
Fig. 3.2: Schematic view of the Wehnelt cylinder. The cup-like structure encloses the wire-filament. Through an aperture at the bottom of the cylinder thermionic emitted electrons leave the negatively charged cylinder. The electrons are focused crossover and accelerated towards a grounded anode. The potential difference U between the cylinder and the anode determines the electrons matter-wavelength [73].
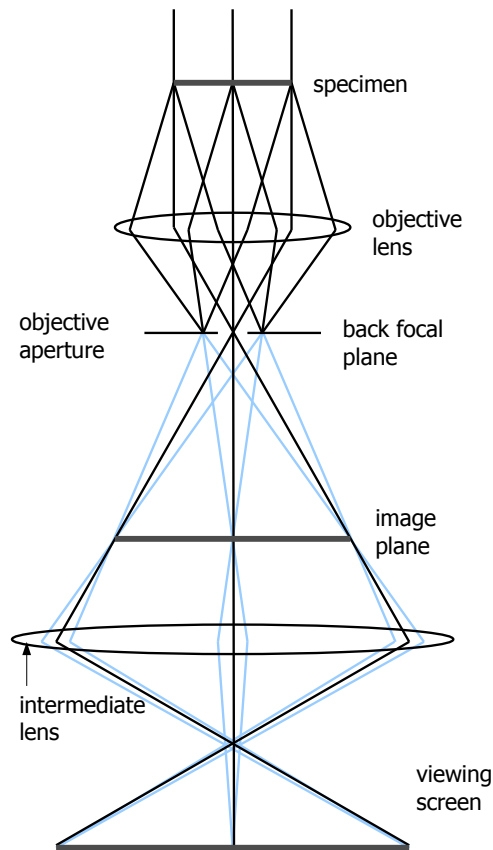
Fig. 3.3: Path of electron beams for bright-field imaging. Behind the aperture a diffraction pattern is formed in the back focal plane. The primary beam forms the image in the image plane, which is afterwards enlarged and focused on the screen. Rays blocked by the aperture are continued in light gray. They can be used for alternative imaging modes [73].

3.2. High-Resolution Transmission Electron Microscopy (HRTEM)

The crystal structure of materials can be displayed using high-resolution transmission electron microscopy (HRTEM). The electrons are accelerated by a higher voltage, which results in a smaller matter-wavelength, which thereby increases the maximum resolution. It is possible to directly image atomic lattice planes this way. The general setup of a HRTEM is similar to a conventional TEM. Electrons passing the sample are scattered by it. Those, which are scattered elasticaly are used to form final image. Its contrast is thereby a phase contrast, formed through interference of diffracted beams with the transmitted one. The relation between sample thickness, defocussing conditions and crystal orientation is non-trivial and affects the quality of the image. Detailed descriptions are given by Reimer [70], Reimer and Pfefferkorn [71], Fultz and Howe [73], Smith [74]. A *Phillips CM-200* HRTEM, equipped with a LaB_6

cathode, is used for all the high resolution microscopy. The acceleration voltage is $U = 200\,\text{kV}$. The more complex power up and alignment procedure for this device is done by Dr. Wiebke Hachmann, who supervises the Transmission Electron Microscopes.

3.2.1. Indexing of electron diffraction patterns from single crystallites

It is possible to determine the crystal structure of a sample by indexing its diffraction pattern. Electrons form a diffraction pattern in the back focal plane of a HRTEM after interacting with the sample. The intermediate and projector lenses of a TEM form a real image from the diffraction pattern. The diffraction data can later be extracted from the HRTEM-image by taking fast-fourier-transformation (FFT) of selected areas in the HRTEM-image. These areas are single crystalline regions, which generate a clear diffraction pattern. Different crystal grains in the selected area produce a superimposed diffraction pattern, which cannot be correctly indexed. In this thesis the FFT's are taken of HRTEM-images by using the software "Digital Micrograph" from *Gatan, Inc.* It includes a feature called "live-FFT". A rectangular region of interest can be moved over the HRTEM-image and the FFT of the selected area is immediately calculated. Areas promising for indexing are easily selected on this way. The diffraction patterns need to be indexed to identify the crystal structure. This can be done manually[1] or the diffraction pattern can be compared to electron diffraction patterns simulated with software packages like *CrystalMaker*™. It is possible, that patterns appear, which do not fit any of the possible structures. In this case the electron beam does not hit the crystal along one of its zone axis and the pattern cannot be used for identification of the crystal lattice structure.

3.3. Scanning Transmission Electron Microscopy (STEM)

In scanning transmission electron microscopy (STEM) an electron beam is scanned line-by-line over the sample, instead of illuminating it at once. At every scan-point only transmitted electrons reach the detector, which is located below

---

[1]A step-by-step instruction is given by Brent Fultz, James Howe [75].
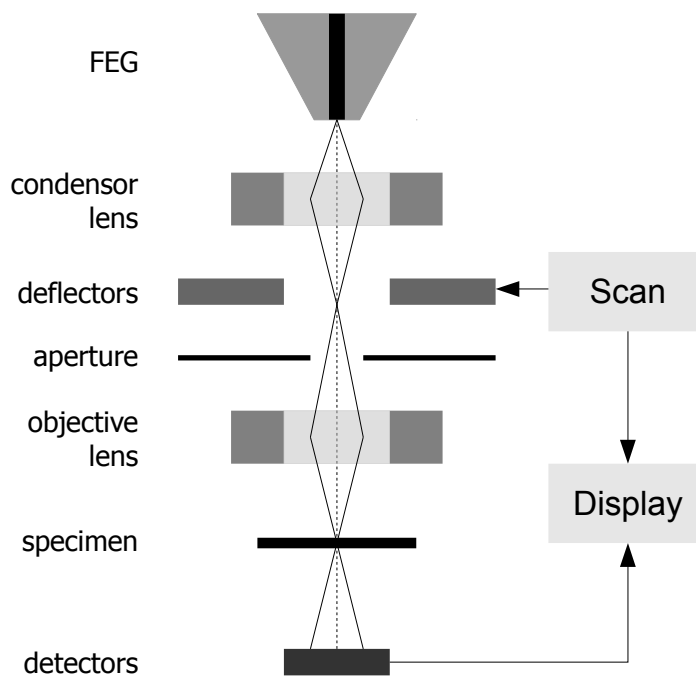
Fig. 3.4: STEM Setup. The electrons are focused by the condensor and objective lenses into the incident electron beam, which is scanned line by line over the sample by a pair of deflector coils. After the beam passes the specimen different detectors can record different image. [76, 77].

the sample. A schematic overview over the STEM is depicted in Fig. 3.4. The specimen needs to be thin (less than 100 nm [78]) to be observable. Otherwise all electrons are absorbed by the sample and do not reach the detector. The electron source is usually a field emission gun (FEG), providing an electron beam with a small diameter. The beam is focused by a system of electrostatic and electromagnetic lenses. It passes a set of coils, which are used to deflect the beam and therefore move it over the sample line-by-line. The detector collects the transmitted electrons at every point and forms a picture. This can be done in different modes. Every imaging mode, bright-field (BF), annular dark-field (ADF) or high angle annular dark field (HAADF) uses its own detector. It is possible to record images in different modes by selecting one of three detectors without any realignment procedures. The scattering angle between the optical axis and the incident electron beam determines which detector collects the electrons [76, 77], as is depicted in Fig. 3.5.

Bright-field imaging (STEM-BF) The detector collects transmitted electrons, which are scattered less than 10 mrad from the optical axis. Features on the sample, which scatter or block incident electrons appear dark in the image [76, 77].
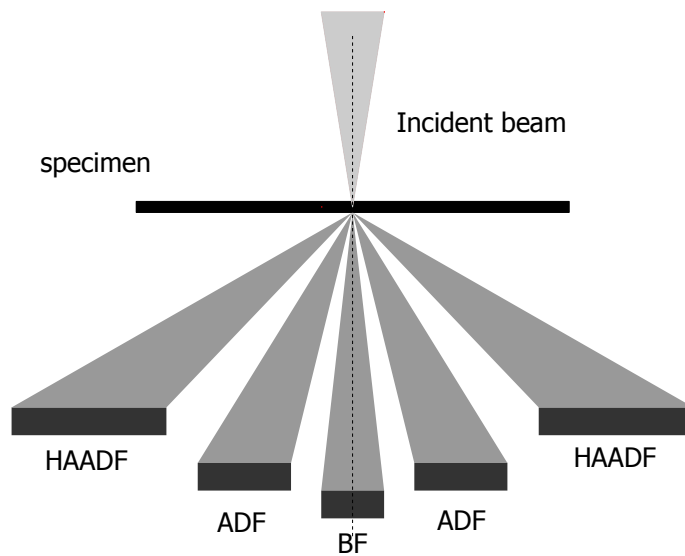
Fig. 3.5: STEM detectors and their location around the incident beam [76, 77, 79].

Annular dark-field imaging (STEM-ADF)   The detector for this imaging mode is located around the bright-field detector. It detects electrons, which are scattered 10 mrad to 50 mrad away from the optical axis. The scattering is due to elastic interaction between the incident electrons and the electron cloud of atoms located in the sample. The image formed from this electrons is the inverse image to the BF-image [76, 77].

High angle annular dark-field imaging (STEM-HAADF)   In this mode electrons scattered farther (more than 50 mrad) from the optical axis are recorded. The scattering from incident electrons to such high angles is caused by incoherent scattering of incident electrons at the nulceii of the specimen atoms (Rutherford scattering). The chance that an electron is scattered to such a high angle increases with the atomic number of the investigated material. The contrast is directly proportional to the square of the atomic number ($\sim Z^2$) [78, 80]. Because of this dependence, the imaging-mode is also called Z-contrast imaging. Thicker areas of the specimen still show an enhanced contrast, which is linear dependent on the sample thickness [81]. Since the Z-contrast is dominant thin features made of a heavy element are expected to appear with more contrast than thicker samples of lighter materials in the final image. This method enables the determination between high Z and low Z areas, which can afterwards be investigated by element sensitive methods [76, 77].
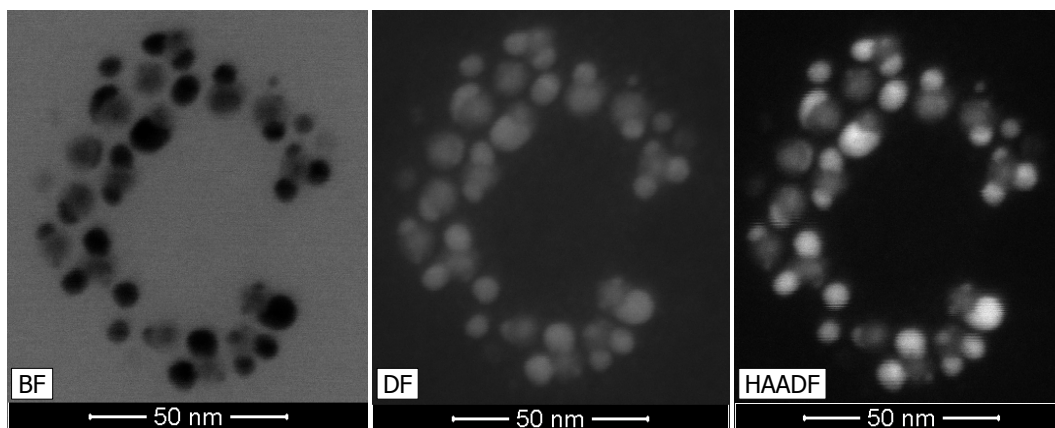
Fig. 3.6: Contrast differences due to detector choice. The same area is recorded using the different STEM-imaging modes. The relatively poor material contrast in the bright and dark field images is exceeded by the contrast rich image taken with the HAADF-detector. The sample is synthesized following the instructions of *Bao2005dir*.

Electrons scattered by other mechanisms do not reach the detector [76–78]. The contrast differences of all three imaging modes are illustrated in Fig. 3.6 using a sample, which contains two elements of different atomic numbers[2]. Structures appearing homogeneously bright in the dark-field image, light up if the HAADF-detector is used. This makes the determination between different elements in the sample possible. All STEM-images were recorded with a *Helios Nanolab 600* (FEI) dual[3] beam device. Only the SEM/STEM mode of the device is used to investigate the particles. An acceleration voltage of 20 kV and a beam current of 86 pA are used, if nothing else is noted. The device is operated by Annalena Wolff, if nothing else is noted.

3.4. Energy-dispersive X-ray spectroscopy (EDX)

Incident electrons hitting the specimen are not only diffracted or transmitted, but can interact with the specimen's atoms. The incident electrons can eject an electron from the atom, which was bound near the nucleus. This ionizes the atom and the vacancy is subsequently filled by an electron from a higher state

---

[2]The element distribution within the sample (*Bao2005dir*) is investigated in more detail later on. This only serves as an example for the different imaging-modes.

[3]The device combines a Scanning Electron Microscope with a Focused Ion Beam system.
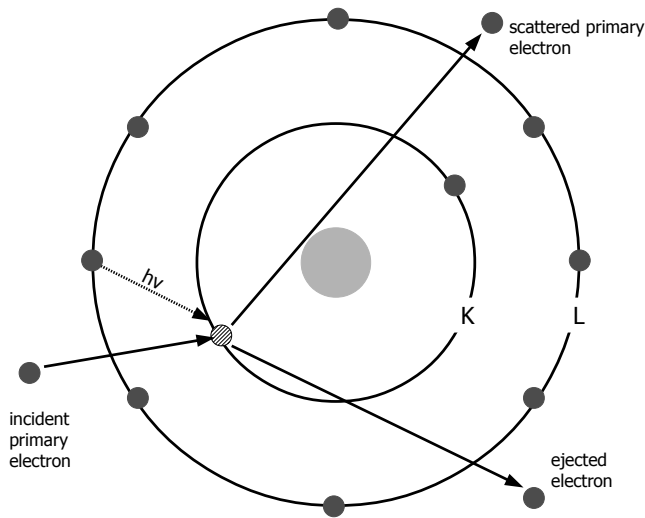
Fig. 3.7: Left: Schematic of electron ejection from the K-shell and the subsequent filling of the vacancy from the L-shell [81].

of potential energy. The excess potential energy is emitted as a photon[4]. This process is depicted in Fig. 3.7.

The energy differences between two specific states in an atom are unique for every element, making it possible to identify a material by detecting photons with an energy corresponding to potential energy differences between the states. The two innermost electrons occupying the lowest state in an atom are located in the $1s$-orbital, which is the K-shell. The next states are part of the L-shell. This includes the $2s$, $2p^{1/2}$ and $2p^{3/2}$ orbitals, which are noted as L_1, L_2 and L_3 [58]. It is possible for an electron from the L_2- or L_3-state to fill a vacancy in the K-shell, but not for the electrons in the L_1-state. The latter transition is forbidden quantum mechanically and the selection rules determine, whether or not a transition is allowed [83]. A known obstacle in EDX-analysis is peak overlapping. Some transitions in different elements occur at similar energies, which makes peak identification difficult. This often occurs between the K_α- and K_β-peaks in transition metals [81]. The three ferromagnetic metals iron, cobalt and nickel (Z=26,27,28) are a good example. The K_β from iron interferes with the K_α-peak from cobalt, whose K_β-peak, on the other hand, interferes with the K_α-peak from nickel.

The acceleration voltage, which determines the kinetic energy of the incident electrons also limits which transitions can be observed. The ionization energy of an electron bound near the nucleus can easily exceed the kinetic energy of

---

[4]There are also alternative ways the energy difference can be ejected, e.g. Auger electrons (see [81, 82] for details).

the electron beam. For example, the ionization energy of an electron from the K-state in gold estimates approximately 80 keV [84] and any incident electron needs more kinetic energy to eject this electron. At lower acceleration voltages gold is only detected by transitions occurring in between higher states. An example is gold's K_α-peak, which is caused by the transition of electrons from the M_4- or M_5-state to the L_3-state. It is located at an energy of 9.712 keV [81].

3.4.1. Measurements

The composition of a sample can be determined by recording an element map. First an overview spectrum of the selected area is recorded and present elements are identified using literature [81, 85] or inbuilt software features. The elemental mapping is done by recording a spectrum at every point of the area of interest. If an selected element is detected in the spectrum its presence is noted in the map by taking the relative peak intensities for different materials into account. An electron microscopy image of the same area can be overlaid with the pattern formed in the map and the elemental composition can be allocated to features in the image. In case of cobalt-gold core-shell particles a cobalt signal in the center and gold-signal in the shell area of a particle is expected. The schematic of the expected elemental map is shown in Fig. 3.8. The intensity of the shell material is expected to be weaker than the intensity caused by the core material, due to the compact core and the comparably thin shell. This is displayed schematically in Fig. 3.8. The first image shows a STEM-HAADF-image of core-shell type particles, as well as single-phase particles consisting of only the shell- or the core-material. The next picture shows the elemental map of the shell-material. The solid particle causes a stronger signal than the thin shells, because more material is present at the points, where the EDX-spectra are recorded. The third picture, showing the elemental map of the core material, is picture next. The intensity of the signal is equal for all cores and the equally sized single phase particle. If both elemental maps are overlain with the STEM-image the elemental composition of the sample can be attributed to certain features in the image.

Recording an elemental map can fail, if the detectable volume is very small. Background noise can prevent the correct detection of weak peaks in the spectrum. A counter measure is increasing the measurement time at every point of the region of interest. This dramatically increases the time necessary to record the elemental map. The increased measurement time ($>$15 h) leads to

STEM-HAADF   EDX: shell-material (1)   EDX: core-material (2)
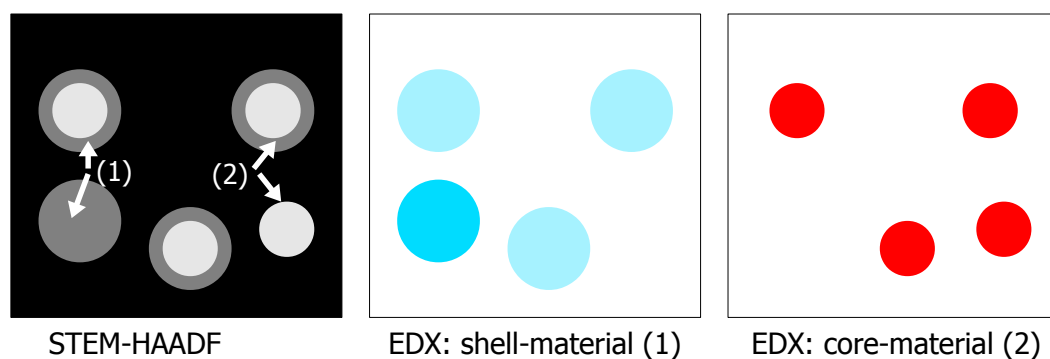
Fig. 3.8: Expected patterns for an element mapping of core-shell and single-phase particles. Areas consisting of materials with different atomic numbers are identified in the STEM-HAADF image. Next, single elemental maps for the shell- (1) and core-materials (2) are recorded. The intensity of the signal creating the elemental maps is dependent on the amount of material detectable in every point of the measurement. The shell material causes weaker signals, than an equally sizes single-phase particle or the compact cores.

particle melting or the destruction of the TEM-grid rendering the measurement useless. An alternative method, which can overcome the issues that arise from an increased measurement time is the selection of features in the SEM mode of the dual beam device. Different compositions can be identified by Z-contrast imaging and are selected by the SEM area selection tool. It is possible to control the position of the scanned area visually and actively counteracted drifting effects[5]. Two EDX systems are used in this work to evaluate the composition. The *Oxford ISIS 300*, which is part of the *ZEISS Leo1530* SEM, is used to estimate the elemental composition of samples prior to XRD-measurements. The *EDAX Apollo 10/300mm* system, which is part of the *Helios Nanolab 600* dual beam device, is used for more detailed analyses of single particles. It is operated with the *Genesis 6.02 software*.

Sample preparation   The same samples were used for TEM-, STEM-imaging and for EDX-analysis. In general copper TEM-grids coated with carbon [Plano, Nr. S160-4] or silicon oxide [Plano, Nr. S165] are used. Carbon grids are used for conventional TEM- and HRTEM-imaging. Silicon oxide coated grids were primarily used for STEM-images and EDX-analysis. The carbon coating of TEM-grids contaminated the samples during STEM-imaging and EDX-analysis and affected the image-quality. The particle suspensions were all drop-casted onto the grid's shiny side. A volume of $V = 1\,\mu L$ was used. The excess

---

[5]Drifting can move the investigated features out of the scanned area during the measurement.

suspension was drained from the surface with filter paper. This ensures that only a single layer of particles remains on the grid. Multi-layers of particles block all electrons and images cannot be recorded. Moreover the grid can be damaged if to much material is deposited onto it. The dried samples were stored in individual boxes and kept under argon-atmosphere to keep them from oxidizing.

3.5. Alternating Gradient Magnetometer (AGM)

An alternating gradient magnetometer is used to measure the magnetic properties of the samples. The device consists of two pairs of coils, a hall-probe, a piezo-electrical transducer probe and an amplifier set, as is shown in Fig. 3.9. The field coils generate a static magnetic field that magnetizes the sample and aligns its magnetic moments to form a dipole. The gradient coils generate an alternating sinusodial field, causing an inhomogeneous time-dependent gradient-force, which deflects the sample [86]. A change in the external homogeneous field will change the magnetization of the sample and will therefore alter the force-influence of the gradient field. This changes the deflection-amplitude, which is detected by a piezo electric element generating a voltage if deformed. The bending of the piezo and therefore the generated voltage, are monitored and plotted against the homogeneous field [21, 87]. The device used is a commercially available *Model 2900™MicroMag Alternating Gradient Magnetometer* (AGM) from *Princeton Measurements Corporation*[6].

There are two different types of transducer-probes for in-plane and perpendicular measurements. The in-plane case is shown in Fig. 3.9 and the perpendicular holder is rotated at an angle of 90°. All measurements were executed with the in-plane sample holder, because for spherical nanoparticles the orientation of the sample holder should not lead to different results [87].

Sample preparation and measurement   The sample is a small piece (maximum edge-length 4 mm) of a silicon-wafer [Crystek, 100 nm native oxide layer], onto which 2 µL of the particle suspension is drop-casted and dried. The samples are all handled with non-magnetic titan-tweezers to prevent ferromagnetic contamination of the sample by a normal stainless-steel tweezer.

---

[6]Princeton Measurements Corporation was acquired by LakeShore in 2013.
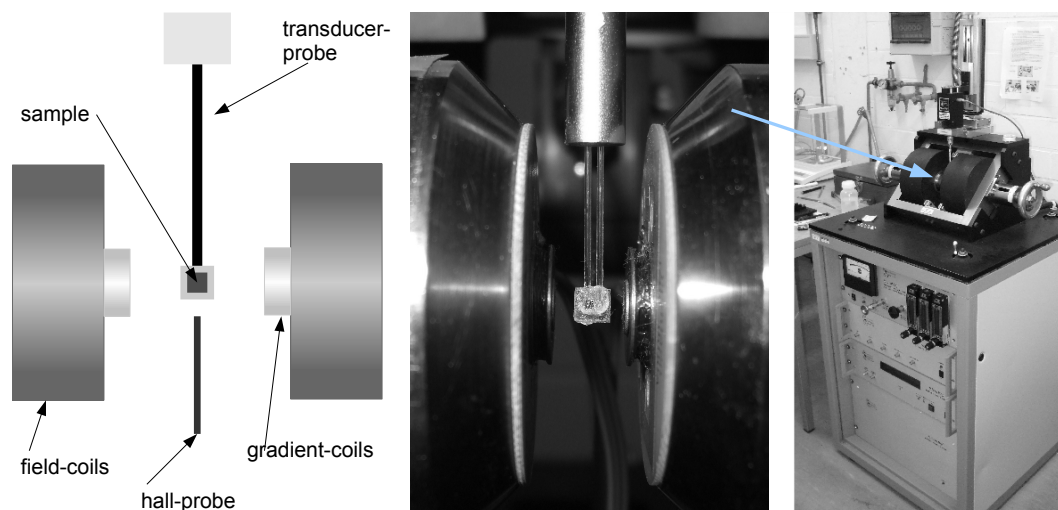
Fig. 3.9: Left and middle: Schematic [86] and photograph of the coil array of the AGM. Right: Complete setup, the arrow locates the sample and surrounding coils.

In general the magnetization of a sample is noted in relation to the sample's magnetic volume or its mass

$$M_\mathrm{vol/mass} = \frac{M_\mathrm{S}}{V_\mathrm{sample} \text{ or } m_\mathrm{sample}} \quad . \qquad \textbf{(eq. 3.3)}$$

These values cannot be determined for particle samples, because the magnetically active sample volume is not known. Both the number of applied particles and the amount of oxidized material within them is unknown. Moreover a very small volume of particles is applied, whose mass can hardly be measured correctly. Therefore, in this work only the magnetic moment m of a sample is measured. The applied field maximum during the measurement is 14 kOe and the measurement starts, when the sample is saturated. The bidirectional measurement is carried out in steps of $\mathrm{d}H = 112\,\mathrm{Oe}$ and at every measuring-point the signal is average for 100 ms.

3.6. X-Ray Diffraction (XRD)

X-ray diffractometry is used to gain access to the microscopic composition and structure of a material. If the material is crystalline, a monochromatic X-ray-beam of wavelength λ focused on the material is diffracted at the lattice
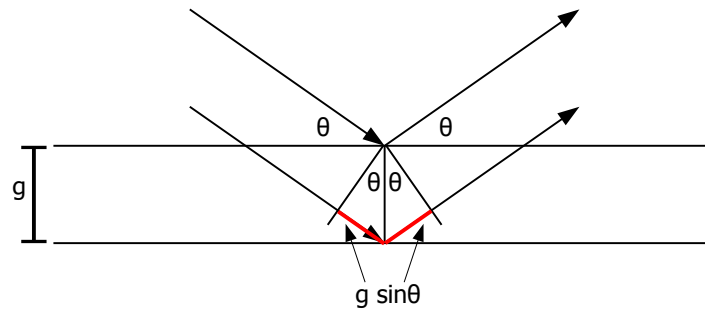
Fig. 3.10: Geometry of Bragg's law [73]. Lattice planes with the distance g reflect X-rays with wavelength λ, which hit the material at the angle θ.

planes with distance g[7]. Two beams diffracted under the same angle θ at two different lattice planes interfere positively if Bragg's law is fulfilled

$$n\lambda = 2g \sin\theta \quad , \tag{eq. 3.4}$$

whereas the integer n gives the diffraction order.

The sample is mounted on a rotating disk and illuminated by the X-ray-source under different angles θ. The detector also moves around the sample, but with twice the speed as the sample rotates, so that the diffracted beam always meets the detector. This measurement geometry is called Bragg-Brentano-geometry [88]. It is possible to record spectra with good resolutions and intensities in this configuration. The recorded spectrum is usually displayed logarithmically against the rotation-angle of the detector 2θ and compared to literature data [89, 90] or simulated patterns generated with the software-package "Crystal Maker™", to identify the existing crystal configurations in the material. Prior to XRD-measurements the samples are investigated by EDX-analysis to exclude the presence of foreign materials. Since a doped single-crystal silicon-wafer is used as the substrate, it is recommended to turn the sample out of position of about 3°. This is called ω-offset and is achieved by tilting the x-ray source and the detector against the sample. This will suppress the otherwise prominent silicon-[400] reflection at $2\theta = 69.2°$ and also forbidden reflections caused by the doping of the silicon-substrate will be prevented [91].

---

[7]Conventionally this parameter is called d, but this letter is used for the particle diameter in this thesis.
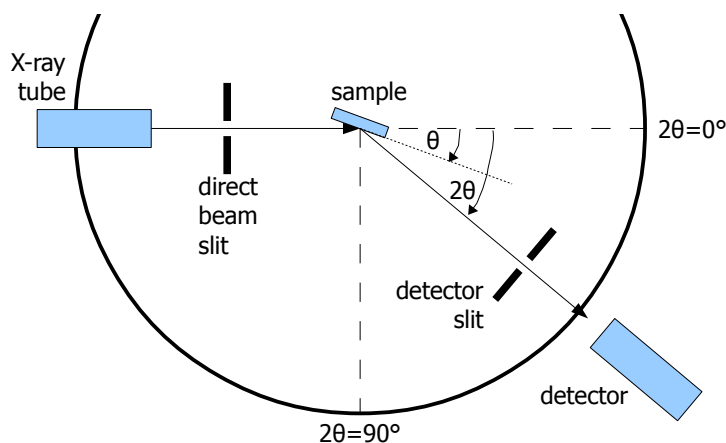
Fig. 3.11: Bragg-Brentano-geometry [73]. If an ω-offset is used during the measurement the angle θ between the sample and X-ray source is increased by the offset. The incoming X-rays hit the sample under a different angle now, but still reach the also tilted detector.

It is possible to estimate the diameter for particles smaller than 1 µm from the peak-broadening in a XRD-spectrum. The particle diameter can be quantified by Scherrer's equation

$$D' = \frac{C_{\text{form}} \cdot \lambda \cdot 57.29}{\text{FWHM} \cdot \cos\theta} \quad , \qquad\qquad (\textbf{eq. } 3.5)$$

whereas D' is the measured diameter of a grain perpendicular to the diffracting lattice plane, C_{form} is a form-constant, which takes values between 0.89 and 1.39, λ is the wavelength of the X-rays, FWHM gives the peak's full width at its half height and the factor $57.29 = \frac{2\pi}{360°}$ is used to convert the FWHM-parameter to radian measure. It can be left out, if FWHM is given in radian. Small corrections of $\Delta\text{FWHM} = 0.01°$ are subtracted from the FWHM-value. This removes peak-broadening due to effects caused by the device itself [10]. The used XRD device is a *Philips Analytical X´Pert Pro MPD Diffractometer* and is operated by Christian Sterwerf. A copper cathode is used to generate the X-rays, using its K_α-radiation with a wavelength of $\lambda = 154\,\text{pm}$. The scans were executed from 20° to 140°, taking a measurement every 0.04° and integrating the signal for 20 s. Measurements with this values delivered good results before [10, 16].

Sample preparation   Silicon wafer substrates [Crystek, 100 nm native oxide layer] with an edge-length 1 cm are covered with 100 µL of the particle suspension and the solvent is evaporated under vacuum. This is repeated five times until the substrate is thickly covered by the particles.

4. Syntheses

This chapter presents the syntheses published by Bao et al. in 2005 [31] and 2007 [32], which are revised in this thesis. The analyses by Bao et al. of the particles and their results are reported as well.

Both syntheses are based on the hot-injection method. A metallic precursor, in this case dicobalt octacarbonyl, is injected into a boiling mixture of solvent and surfactants. The carbonyl is decomposed in the boiling solvent and releases cobalt atoms into the reaction-mixture. This causes a nucleation event and the subsequent growth of nuclei into particle. In a second reaction step the gold-precursor and a surfactant are injected into a boiling solution containing the preformed cobalt seed particle. This forms a shell around the cobalt seed particles via heterogeneous nucleation. A schematic of the reaction is depicted in Fig. 4.1.
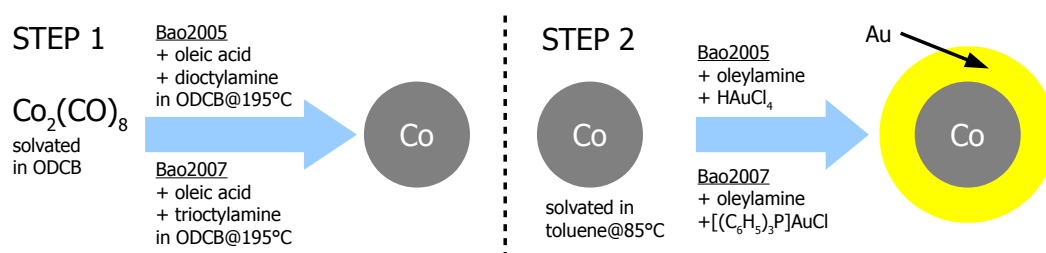
Fig. 4.1: Schematic of the two-step reactions. Both recipes, *Bao2005* and *Bao2007* follow the same reaction, but use different surfactants and gold sources.

Both syntheses were conducted under argon atmosphere to prevent oxidation. Chemicals, used in the syntheses, were obtained from commercial sources and used without further purification, according to Bao et al. [31].

4.1. Synthesis by Bao et al. 2005
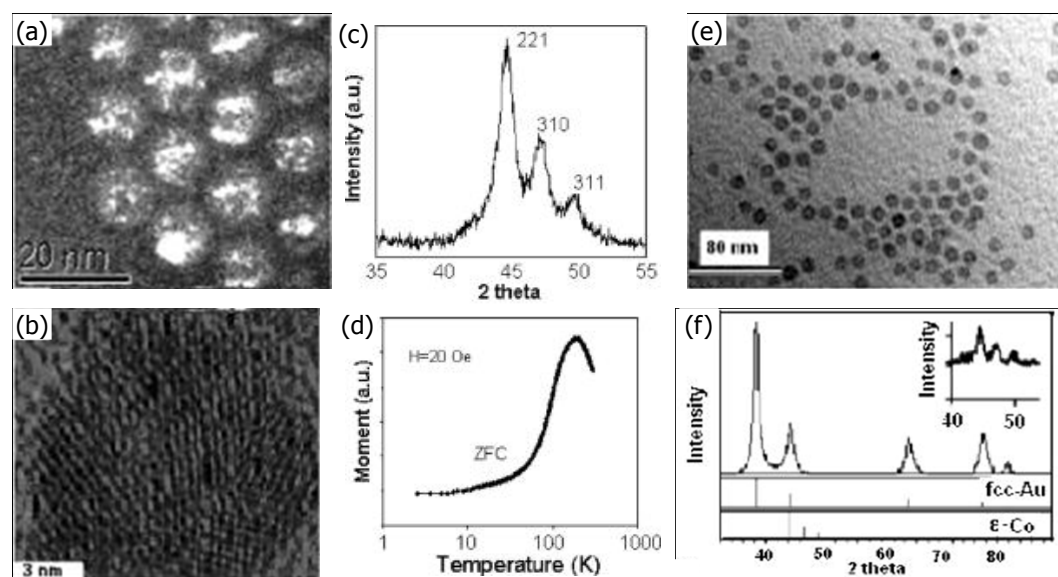
Fig. 4.2: Results of particle analysis conducted by Bao et al. (a) TEM-DF-image of $10\,\text{nm}$ cobalt seed-particles. (b) HRTEM-image of a single cobalt particle. (c) XRD-measurement showing peaks attributed to ϵ-cobalt. (d) Blocking peak at $220\,\text{K}$ of a ZFC-measurement. (e) TEM-image of cobalt-gold particle after the second reaction step. (f) XRD-measurement of the cobalt-gold particles showed only peaks corresponding to fcc-gold; peaks from ϵ-cobalt, as shown in the inset or in (c) have not been detected. Reprinted at original resolution with kind permission from [31], Copyright ©2005, American Institute of Physics.

In the first reaction step $0.54\,\text{g}$ dicobalt octacarbonyl are solvated in $3\,\text{mL}$ ortho-dichlorbenzene (ODCB). They are injected into an unknown volume of boiling ($182\,°\text{C}$) ODCB containing $0.34\,\text{mL}$ dioctylamine (DOA) and $0.2\,\text{mL}$ oleic acid as surfactants and the mixture is kept in reflux for $15\,\text{min}$. Spherical, multi grained, cobalt-particles with a diameter of $d = 10\,\text{nm}$ were obtained. A TEM-image (Fig. 4.2, (a)) depicts the particles and in a corresponding HRTEM-image (Fig. 4.2, (b)) the multi-grain structure of a single particle is visible. The publication does not show a size-distribution, but the authors claim it is narrow. XRD-analysis, based on peak position and relative peak height, shows that the particles are composed of ϵ-cobalt (Fig. 4.2, (c)). A zero-field-cooling measurement[1] of the cobalt particles shows a narrow blocking peak at $220\,\text{K}$ (Fig. 4.2, (d)). All particles are superparamagnetic at room temperature. The temperature at which a particle shows superparamagnetic

---

[1]Details on this method can be found in appendix A.3.1.

characteristics is dependent on its diameter. The width of the peak is therefore dependent on the sample's size-distribution. A narrow blocking peak suggests a narrow size distribution.

In the second reaction step 0.5 mL of the particle suspension are mixed with 5 mL toluene and heated to 85 °C. The gold precursor solution of 0.01 g gold(III) chloride hydrate (HAuCl$_4$) and 0.25 mL oleylamine solvated in 3 mL toluene is injected and the mixture is kept at 85 °C for one hour.The particles are obtained with 6 nm core-diameter and a shell-thickness of 1.5 nm. The sizes were measured from a BF-TEM-image shown in Fig. 4.2, (e). The XRD-measurement of these particles shows only peaks corresponding to fcc-gold (seeFig. 4.2, (f)). The absence of cobalt peaks in the spectrum is attributed to peak broadening and the difficulty to distinguish cobalt from gold. A ZFC-measurements shows a narrow blocking peak at 55 K, which is used to indicate a cobalt core size of 5 nm to 6 nm. This corresponds well with sizes measured in the TEM-images.

4.2. Synthesis by Bao et al. 2007

The second synthesis route was also published by Bao et al. [32] in 2007, the same group, and is quite similar to the first one. In contrast to the first synthesis a different surfactant and a different gold source is used in the shell synthesis step. This synthesis also uses 0.54 g dicobalt octa carbonyl solvated in 3 mL ortho-dichlorbenzene (ODCB) as cobalt precursor solution. It is injected into an unknown volume of boiling (180 °C) ODCB containing 0.34 mL trioctylamine (TOA) and 0.2 mL oleic acid as surfactants. The reaction mixture is refluxed for 15 min. The resulting cobalt particle are spherical single crystals with a diameter of $d = 5$ nm to 6 nm, as depicted in Fig. 4.3, (a). Their crystal structure corresponds to ϵ-cobalt, because the three distinct peaks attributed to ϵ-cobalt are found in the XRD-spectrum.

For the second reaction step 2 mg of precipitated cobalt seed particles are redispersed in toluene and the solution is heated to 95 °C. The injected gold precursor solution consists of 0.01 g chloro(triphenylphosphine)gold(I) ([(C$_6$H$_5$)$_3$P][AuCl]) and 0.5 mL oleylamine solvated in 3 mL toluene. The mixture is stirred and kept at the temperature of 95 °C for one hour after the gold precursor solution is injected.

The cobalt-gold particles are investigated with TEM-, HRTEM- and Z-contrast imaging (see Fig. 4.3). The diameter of the spherical particles is given with 9 nm,
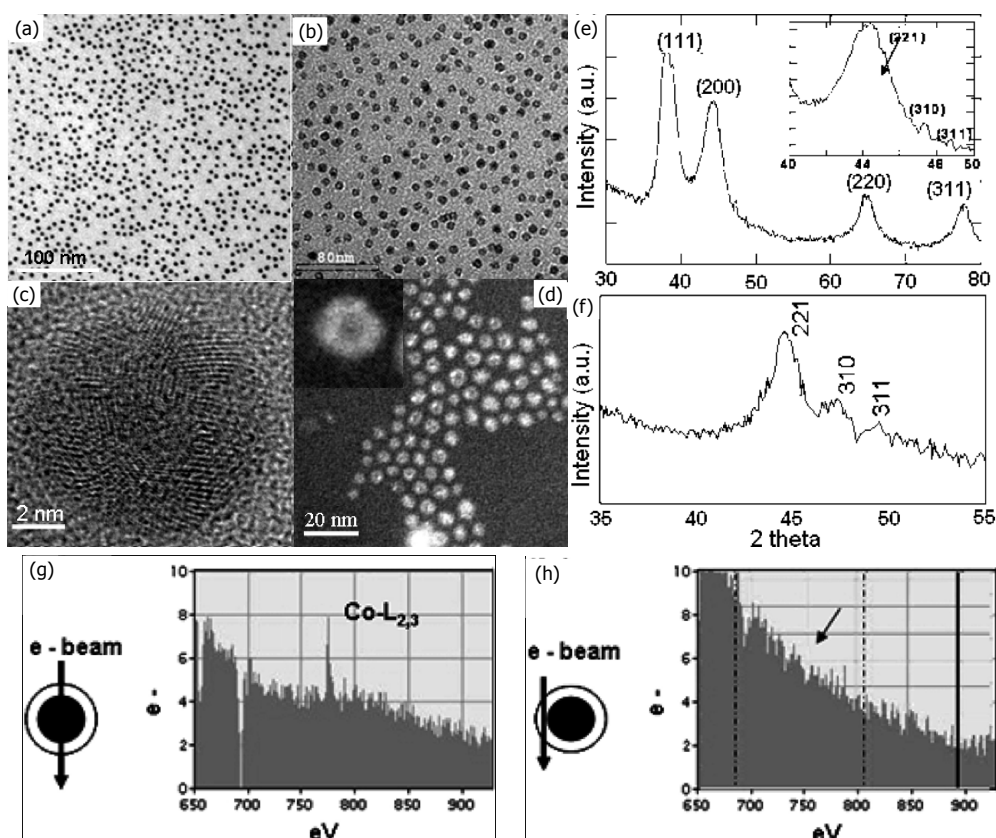
Fig. 4.3: (a) TEM-BF-image from the $5\,\text{nm}$ to $6\,\text{nm}$ cobalt seed-particles. (b) TEM-BF-, (c) HRTEM- and (d) Z-contrast-image of the cobalt-gold core-shell nanoparticle with a total diameter of $9\,\text{nm}$. (e) XRD-measurement of the core-shell particle. The inset shows a more detailed scan between $2\Theta = 40°$ and $2\Theta = 50°$. (f) shows a diffractogram of the pure cobalt seeds. (g) EELS measurements through core and shell and (h) through the shell only. Reprinted with permission from [32], Copyright ©2007, American Chemical Society.

while the core is of $5\,\text{nm}$ to $6\,\text{nm}$ diameter, which results in a shell thickness of $1.5\,\text{nm}$ to $2\,\text{nm}$. The core-shell structure is shown in the BF-TEM-image in Fig. 4.3, (b). The HRTEM-image (Fig. 4.3, (c)) shows the multi-grain structure of the shell in more detail. The Z-contrast image (Fig. 4.3, (d)) shows particles with varying contrast and the more detailed image of a single particle in the inset shows a contrast-rich shell surrounding a core with less contrast. Bao et al. [32] attributed this to the higher contrast caused by gold (Z=79) and the comparably lower Z-contrast of cobalt (Z=27).

XRD-analysis (Fig. 4.3, (f)) of the cobalt seed particles shows three distinct peaks at $2\Theta = 45°$, $2\Theta = 47°$ and $2\Theta = 49°$, which are the three peaks of
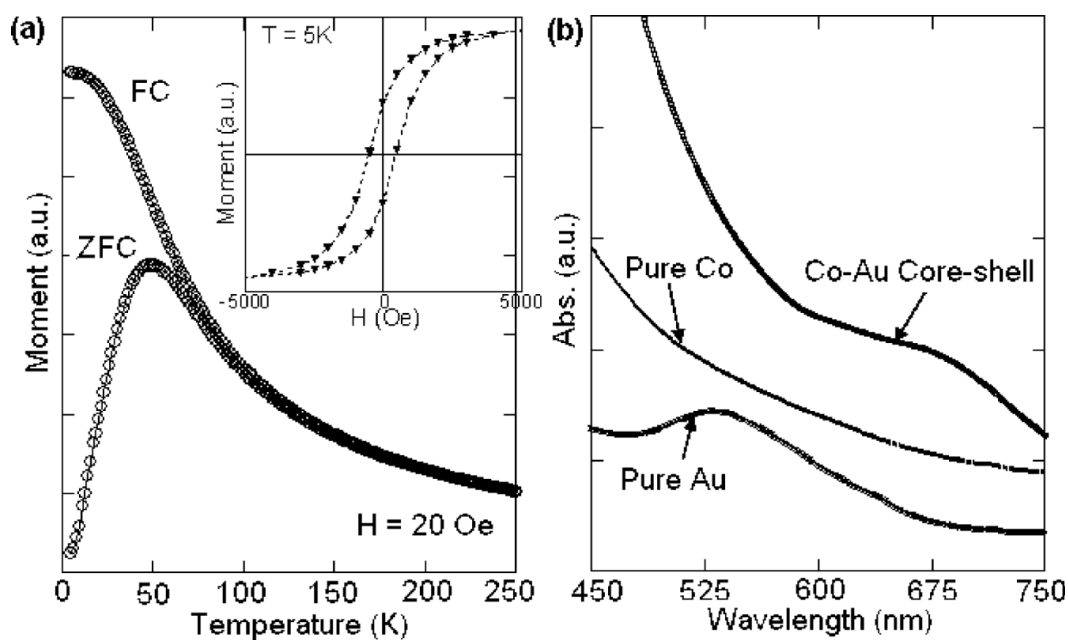
Fig. 4.4: SQUID-measurements of assumed core-shell type particles after Bao et al. [32]. UV-VIS-spectroscopy of pure cobalt seeds, equally large gold particles and the assumed cobalt-gold core-shell type ones. Reprinted with permission from [32], Copyright ©2007, American Chemical Society.

ϵ-cobalt with highest intensity. Fig. 4.3, (e) shows the diffractogram of the bimetallic particles and at first only peaks attributed to gold can be seen at approximately $2\Theta = 39°$, $2\Theta = 44°$, $2\Theta = 65°$ and $2\Theta = 78°$. A more detailed scan between $2\Theta = 40°$ to $50°$ reveals the gold (200)-peak at $2\Theta = 44°$ to have a shoulder and two smaller peaks in its right slope. Those peaks have the same position as the three main peaks of ϵ-cobalt and they are assumed to be overlapping with the broadened gold (200)-peak.

EELS spectra are taken from the middle of a particle and its edge. EELS is an element sensitive method, that detects the loss of kinetic energy electrons undergo after passing the sample. Details on this method are summarized by Egerton [92]. The spectrum recorded at the particle center (Fig. 4.3, (g)) includes a peak caused by cobalt, while this feature is missing in the spectrum taken at the particle's edge. This is taken as proof, that cobalt is only located in the core.

The particles show a narrow blocking peak at $55\,\mathrm{K}$ in a ZFC-measurement (see Fig. 4.4, (a)). Details on this technique are given in appendix A.3.1. The blocking temperature is used to estimates the magnetic volume of the core and

therefore the mean core diameter via the Neel-Arrhenius equation (**eq.** 2.28). The value of the used effective anisotropy constant is not mentioned, but the mean diameter is calculated to $d = 6\,\text{nm}$ with a measurement time of $100\,\text{s}$.

One additional measurement was carried out to further characterize the formed gold-shell. UV/VIS-spectra of pure cobalt-particles, pure gold-particles and the cobalt-gold particles were recorded (Fig. 4.4, (b)). The curve from pure gold-particles shows an absorption peak around $525\,\text{nm}$ due to plasmon resonance, the pure cobalt particles show an decreasing absorption towards longer wavelength. The cobalt-gold particle produced a flat absorption peak around $680\,\text{nm}$. The red-shift of the absorption-peak in case of the core-shell particle is said to be attributed to the enhanced absorption of the gold-shell. This behavior was reported for a gold-coated dielectric core and is highly dependent on the diameter-ratio between the core and the shell [93]. Details on UV-VIS spectroscopy and the shift of the resonance peak are given in the appendix A.3.2.

5. Diffraction data simulations with *CrystalMaker*™

This chapter presents the results of crystal diffraction data generated by the program *CrystalMaker*™ and its accompanying programs *SingleCrystal*™ and *CrystalDiffract*™. The main program is used to generate a crystal structure file, which is used for the simulation of X-ray diffraction spectra and electron diffraction patterns. X-ray powder diffraction spectra are simulated and indexed for comparison with XRD-measurements via *CrystalDiffract*™. Single crystal electron diffraction patterns are generated and also indexed with *SingleCrystal*™ for comparison with electron diffraction patterns generated through FFT of selected areas in a HRTEM-image. The results of all simulations are summarized in this chapter. They serve as reference for the crystal structure evaluation of all investigated particles.

5.1. Powder spectra of cobalt

Cobalt shows two different crystal-phases in bulk-material, a hexagonal-closed packed (hcp) and a face-centered cubic (fcc) structure. The lattice parameters of the hexagonal structure are $a = b = 2.5071$ Å, while the distance between two atomic layers is $c = 4.069$ Å. The fcc structure has an edge length of $a = 3.548$ Å. Both forms are also found in nanoparticles. A third structure, ϵ-cobalt, was found only in nanosized cobalt particles, which are prepared by a thermal decomposition process, similar to the one used in this work [94]. This new modification of cobalt has a cubic unit cell with edge length $a = 6.097$ Å. The unit cell contains 20 cobalt atoms and is arranged similar to a high-temperature phase of manganese [95]. It shows a threefold symmetry along its [111]-axis (see Fig. 5.1, bottom).

Fig. 5.1: Simulated powder diffraction pattern for all possible cobalt modifications indexed with the corresponding Miller indexes. The visualizations of the unit cells from fcc- and hcp-cobalt are arbitrarily oriented to allow a better three dimensional view of the unit cell. The unit cell of ϵ-cobalt is viewed along its [111]-axis to show its threefold symmetry.

45

The fractional atomic coordinates used for the fcc- and hcp-structure of cobalt are taken from [96] provided by the "American Mineralogist Crystal Structure Database" (AMCSD) [89]. The visualizer software of the program *FindIt*[1] is used to produce a structure file, which is imported into *CrystalMaker*™. The fractional atomic coordinates of ϵ-cobalt are taken from [94] and manually entered into the visualizer of *FindIt* to obtain a structure-file. X-ray powder patterns for an x-ray wavelength of 154.18 pm and a particle size of 10 nm are simulated using the program *CrystalDiffract*™ with the structure files created in *CrystalMaker*™.

Fcc-cobalt displays two peaks with high intensities at $2\theta = 44.21°$ and $2\theta = 51.52°$, while hcp-cobalt displays a high intensity peak at $2\theta = 47.46°$ preceded by two peaks with less intensity at $2\theta = 41.59°$ and $2\theta = 44.54°$. ϵ-cobalt displays many small peaks throughout the whole spectrum. A specific region is found between $2\theta = 40°$ and $2\theta = 50°$. Three consecutive peaks with comparably high intensity, which is decreasing every peak, can be found at $2\theta = 44.54°$, $2\theta = 47.1°$ and $2\theta = 49.54°$. The number of peaks and the different peak-intensities help with the identification of the crystal phase.
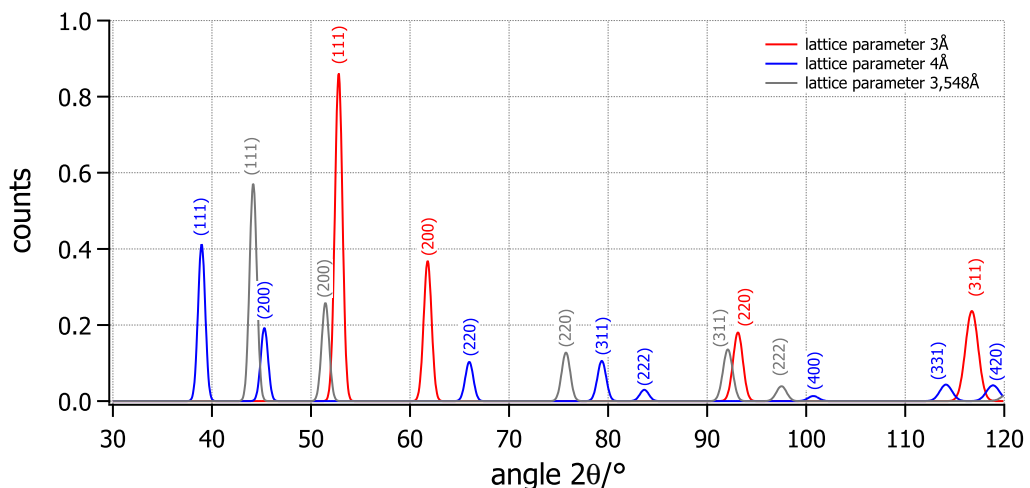
Fig. 5.2: Simulated X-ray powder diffraction spectra for regular fcc-cobalt (g=3.548 Å, gray) and fcc-cobalt with a compressed (g=3 Å, red) and an expanded unit cell (g=4 Å, blue). If the unit cell is compressed all XRD-peaks are shifted to bigger angles 2θ and moved farther apart, while their intensity is enhanced compared to the regular fcc unit cell. If the unit cell is compressed all peaks are shifted two smaller angles and move closer together, while their intensity is reduced. This can be observed especially well in case of the fcc(111) peak.

---

[1]Program, which uses the "Inorganic Crystal Structure Database" (ICSD)[90].

The regular lattice of a crystal can be disturbed by defects, which can alter the unit cell of the material. This also effects the powder spectrum obtained in XRD-measurements. A uniform unit cell expansion, which increases the lattice constant, usually lowers the intensity of all peaks in a XRD-spectrum, shifts them to smaller angles and moves them closer together. A compression of the unit cell, decreasing the lattice constant, increases the intensity of all peaks, shifts them to higher angles and moves them farther apart. These cases are depicted in Fig. 5.2 for fcc-cobalt (grey) and for cases with smaller (3 Å, red) or larger (4 Å, blue) lattice parameters, respectively.

If the unit cell is distorted as well and additional peaks appear through peak-splitting[2], it is very difficult to identify the crystal structure from X-ray diffraction measurements alone.

5.2. Electron diffraction patterns

Simulated single crystal diffraction patterns for all three cobalt modifications and several viewing directions have been generated with *SingleCrystal*™ . The calculated reflexes are dependent on the matter-wavelength of the incident electrons and the thickness of the crystal. These three parameters are set to $\lambda_h = 2.51$ pm for electrons at an acceleration voltage of 200 kV and 10 nm, which corresponds to the diameter of the cobalt seed particle.

The electron diffraction patterns observation along low order zone axes for all three possible modifications are given on the next pages and they can be distinguished by their reflex patterns and the special aspect ratios between the reflexes. The distinct aspect ratios of fcc-cobalt are measured and depicted in Fig. 5.3. ϵ-cobalt shows many diffraction spots of low intensity dominated by major spots forming an octagonal pattern, in contrast to the patterns caused by hcp and fcc cobalt. The octagonal patterns are caused by lattice planes of the {310}-family for the [001]-direction. All lattices can generate an array of reflexes, which form ideal hexagons ([111]epsilon, [001]hcp, [100]hcp, [110]hcp and [111]fcc). Diamond shaped patterns can be generated by all different lattice modifications, too ([211]epsilon, [131]hcp, [210]hcp, [211]hcp, [212]hcp, and [211]fcc). It is hard to determine which crystal structure causes the diffraction pattern, if only two reflexions besides the transmitted beam are shown, as is the case for e.g. [310]hcp and [221]fcc. Non-ideal hexagonal patterns from hcp and fcc structures can be distinguished by different aspect ratios. The

---

[2]Different lattice planes from the same family {hkl} produce individual peaks.

diffraction spots of the fcc crystal structure form an oblated hexagon, if the incident electrons hit along the [110]fcc axis. It has a distinct aspect-ratio of 2:1 between the dissections a and b and the distance a is always longer than c, as depicted in Fig. 5.3. The hcp crystal generates hexagonal patterns, that look vertically stretched compared to the [110]fcc diffraction-pattern. The distance a is always shorter than c. Fcc-cobalt also forms a unique squared diffraction pattern, if the incident electrons enter the crystal along the [100]-axis.
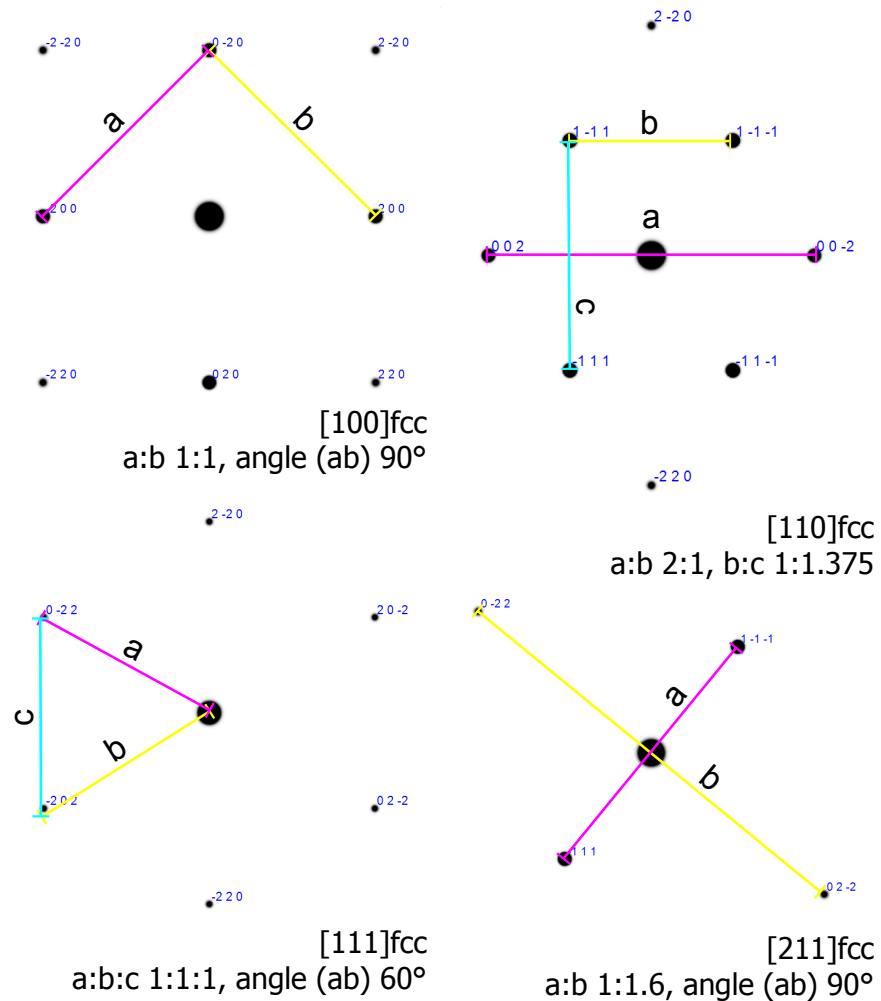
Fig. 5.3: Electron diffraction patterns generated from a fcc-crystal by *Crystal-Maker*™ *SingleCrystal*™. Ratios and angles used to identify the fcc crystal structure are sketched into the patterns.
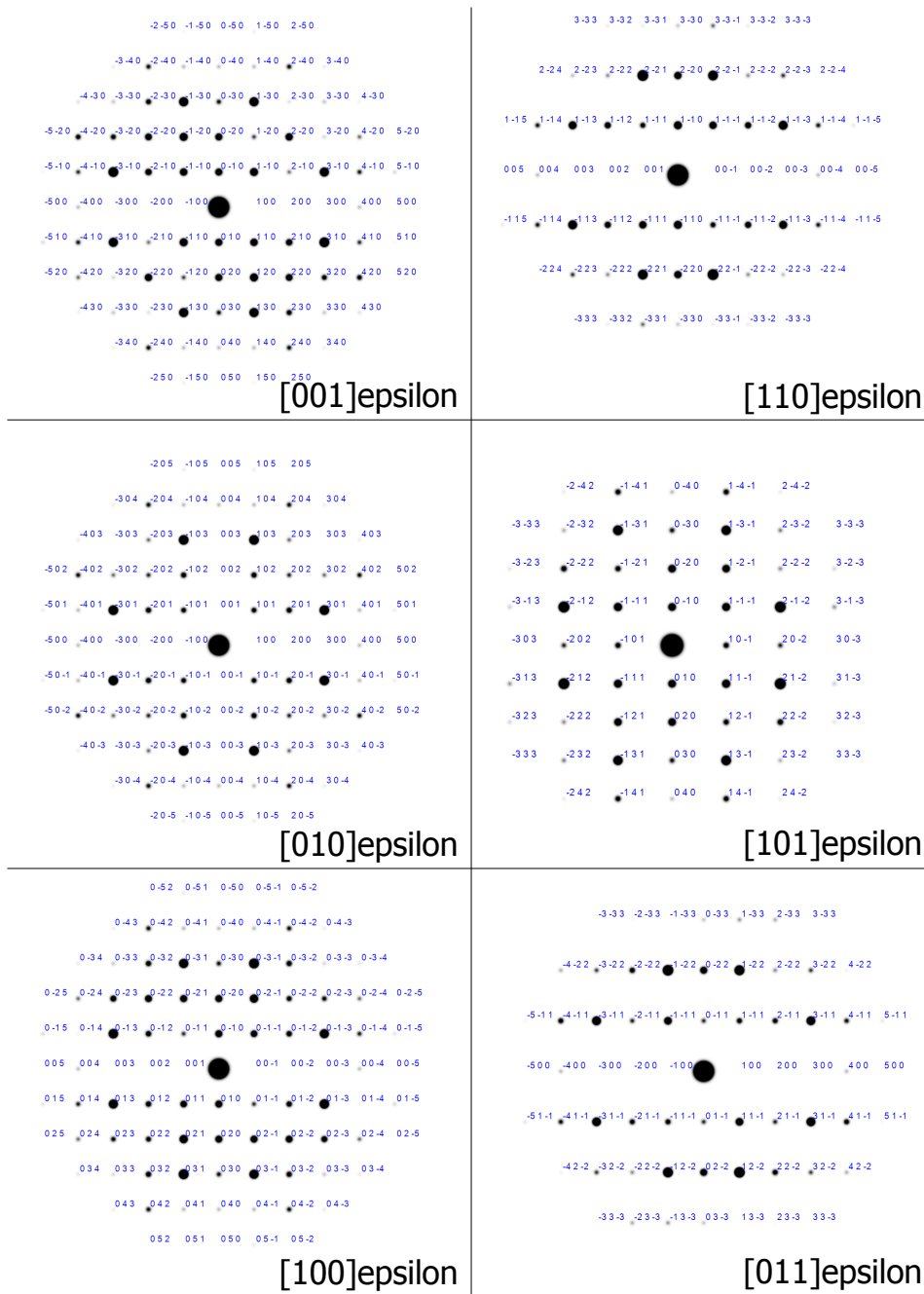
Fig. 5.4: Electron diffraction patterns for the [001], [110], [010], [101], [100] and [011] direction of ϵ-cobalt.
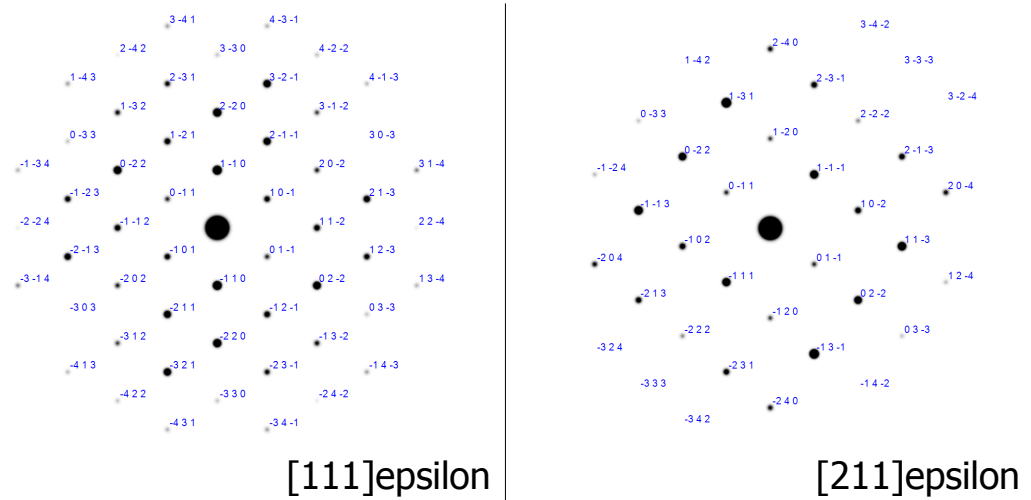
Fig. 5.5: Electron diffraction patterns for the [111] and [211] direction of ϵ-cobalt.
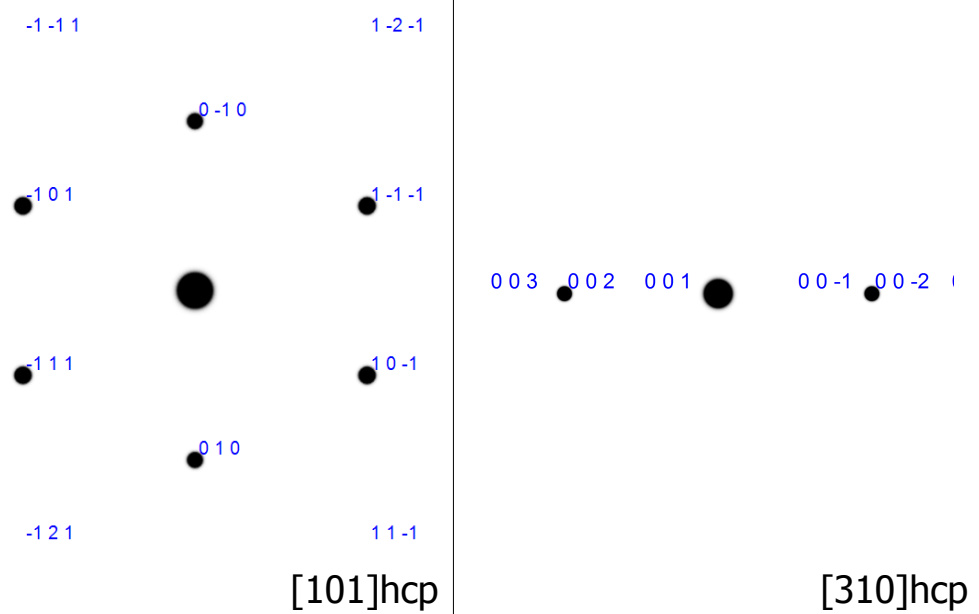
Fig. 5.6: Electron diffraction patterns for the [101] and [310] direction of hcp-cobalt.
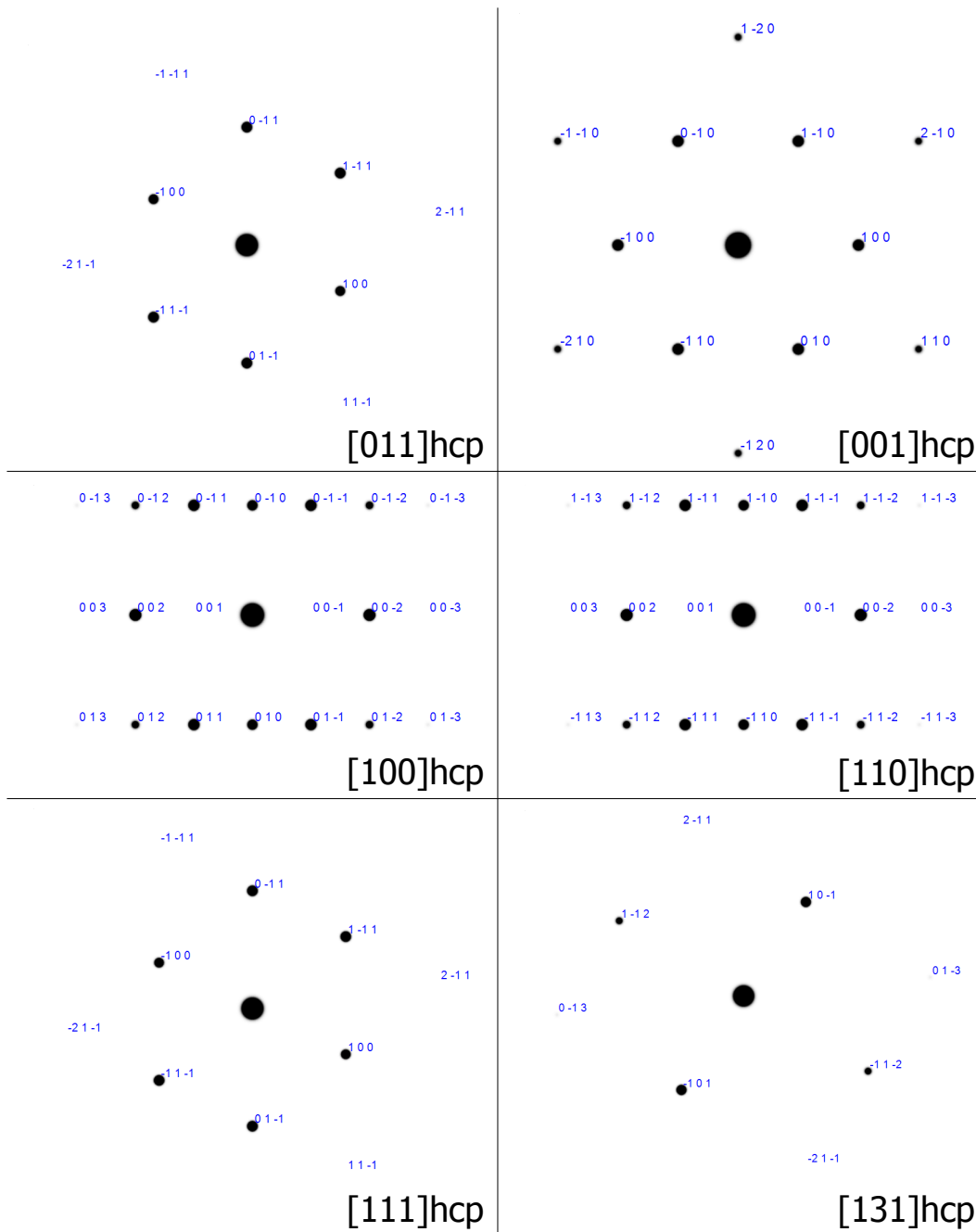
Fig. 5.7: Electron diffraction patterns for the [011], [001], [100], [110], [111] and [131] direction of hcp-cobalt.
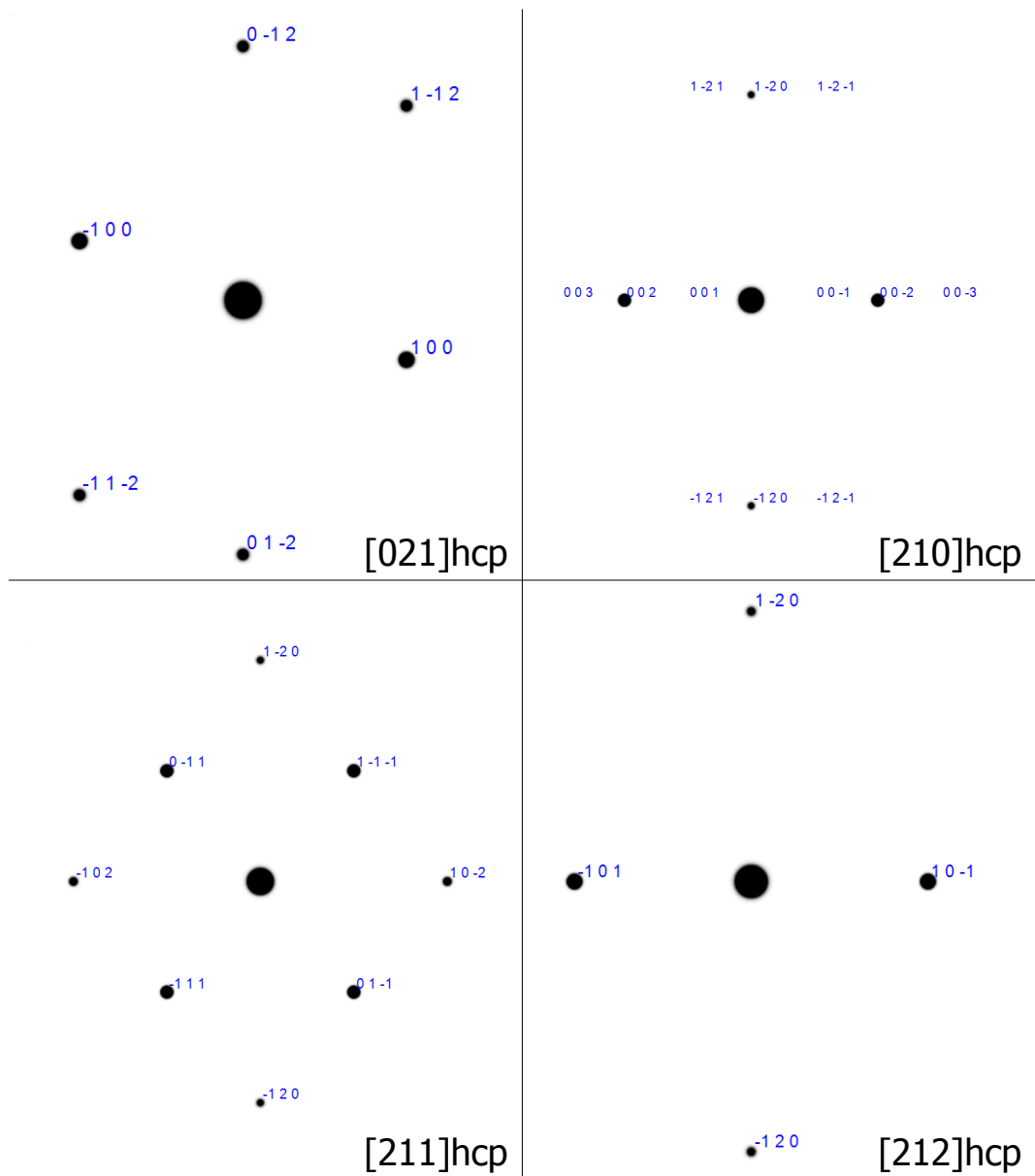
Fig. 5.8: Electron diffraction patterns for the [021], [210], [211] and [212] direction of hcp-cobalt.
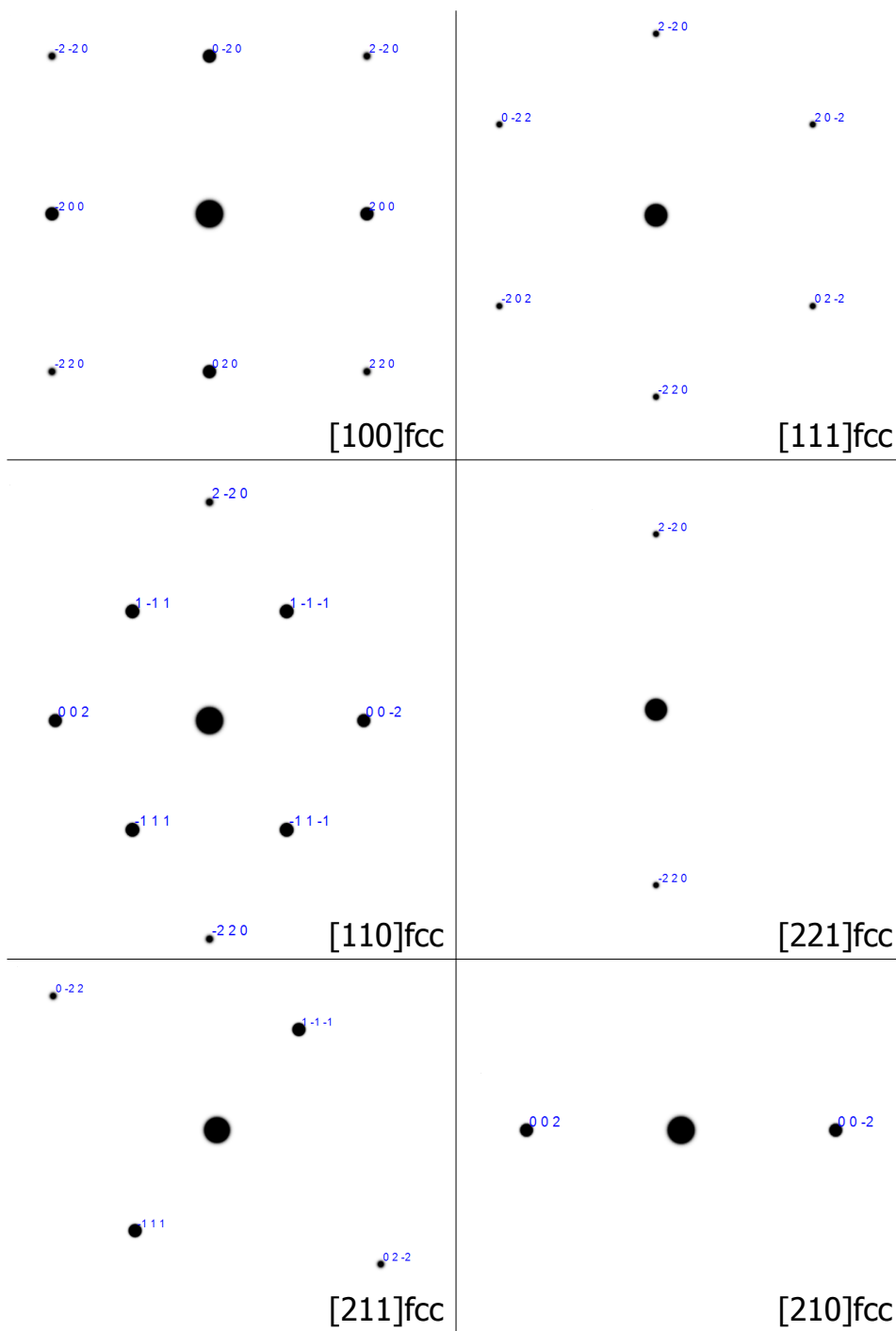
Fig. 5.9: Electron diffraction patterns for the [100], [111], [110], [221], [211] and [210] direction of fcc-cobalt.

6. Results and discussion of the nanoparticle synthesis following instructions of Bao et al. 2005

This chapter discusses the results of the adapted synthesis route, which has been originally published by Bao et al. in 2005. Details on the publication and the authors' results are given in section 4.1. The adaption of the synthesis can be separated into two parts; first the synthesis of the seed particles, which are used during the second reaction step as heterogeneous nucleation centers for the shell synthesis. The cobalt seed particles synthesized by the first reaction step are studied using transmission electron microscopy (TEM) from which particles' size and inter-particle distance distributions are determined. The crystal structure of the particles is determined by XRD-measurements as well as HRTEM-imaging and finally, the magnetic properties are investigated by AGM-measurements. A control experiment, to investigate, if the shell synthesis step is able to homogeneously nucleate gold nanoparticles is executed as well. The shell synthesis step is investigated, to determine if it is able to homogeneous nucleate nanoparticles. The results of the second synthesis step are discussed afterwards including size and growth determinations by TEM. The elemental composition of the particles is investigated by Z-contrast imaging and EDX-analysis. Finally, all results are discussed.

6.1. Adaption of the synthesis

The synthesis published by Bao et al. [31] in 2005 (see section 4.1) does not list all necessary volumes to exactly reproduce the synthesis. The volume of the boiling solvent containing the surfactants to which the precursor solution is added to synthesize the cobalt seed particle is not given. This parameter is crucial, because it determines the total volume of the synthesis mixture and therefore defines the particle concentration in the suspension. Since a

certain volume of the seed particle suspension is used for the second reaction step, the amount of seed particles present in the second synthesis step depends on the particle concentration. The surfactant concentration is also defined by the initial solvent volume. Although, no reports are found on how the surfactant concentration influences the synthesis of cobalt particles through thermal decomposition of a metallic carbonyl, a different concentration may have an influence on the stabilization of particles and their growth. For example, the binding affinity of the surfactant seems to influence the size of resulting nanoparticles (see Fig. 2.10).

At first, the synthesis is executed with an initial solvent volume of 5 mL. This value is chosen, because the resulting total reaction volume (8 mL, after injecting 3 mL cobalt precursor solution, see section 4.1) is easy to handle with the laboratory equipment. This adaption of the synthesis is referred to as *Bao2005red*.

The synthesis route published by Puntes et al. [97], which is referenced by the article, is a standard method to obtain cobalt nanoparticles through thermal decomposition of a metal carbonyl. The synthesis is carried out by injecting the precursor solution into 12 mL of boiling solvent containing surfactants. Hence the seed particle synthesis is conducted with an initial solvent volume of 12 mL and seen as a direct reproduction of the original synthesis. The synthesis is later on referred to as *Bao2005dir*. The amount of particles used for the second reaction step is given with 0.5 mL in case of *Bao2005dir*. This volume is extracted from the seed particle suspension and added to the second reaction mixture. In case of the synthesis with reduced solvent volume *Bao2005red* half of the synthesized particles are precipitated and added to the second reaction mixture without solvent.
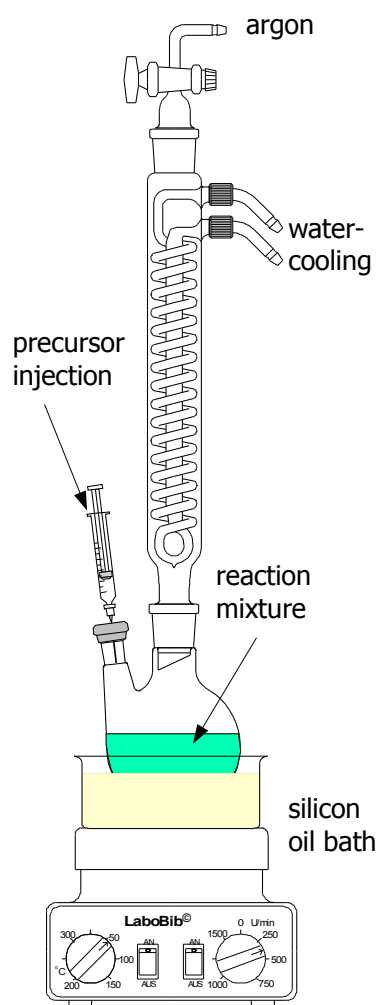
Fig. 6.1: Schematic of a synthesis setup.

All chemicals are purchased commercially (Sigma Aldrich, Chemielager Universität Bielefeld) and used without further purification. The syntheses are conducted in reflux under argon-atmosphere in baked-out glass vessels (see appendix A.1.1 for more details). Weighting of all solids is done under argon atmosphere in a glove-box. The used liquids are all distilled to ensure that they are free from residual water. These measures are taken to prevent the oxidation of any reactants prior and during the nanoparticle synthesis. The reaction setup consists of a two-neck vessel containing the solvent-surfactant mixture. The metallic precursor solution is added through a septum sealing one neck using a syringe. The other neck contains the reflux condenser with water-cooling. The argon inlet is connected at the top of the condenser. The reaction solution is heated by a heating mantle or a silicon oil bath on a hotplate. The setup is depicted in Fig. 6.1. The nanoparticle suspensions are cleaned after the syntheses by precipitation; the method is described in appendix A.1.2. All nanoparticle suspensions are stored under argon atmosphere at 4 °C in eppendorf tubes sealed with parafilm. All syntheses discussed in this thesis are executed by Nadine Mill.

These instructions are used for both syntheses *Bao2005red* and *Bao2005dir*:

- 0.34 mL dioctylamine (DOA) and 0.2 mL oleic acid are added to 5 mL (*Bao2005red*) or 12 mL (*Bao2005dir*) ODCB. The mixture is heated to 190 °C[1].

- The cobalt precursor solution consisting of 0.54 g dicobalt octa carbonyl is solvated in 3 mL ODCB and quickly injected into the boiling solvent-surfactant mixture.

- The reaction solution is kept at reflux temperature for 15 min and given 30 min time to cool down to room-temperature. Afterwards the particle suspensions are cleaned by precipitation.

- In case of *Bao2005dir* 0.5 mL seed particles in ODCB are added to 5 mL of toluene for the second reaction step. In case of *Bao2005red* particles precipitated from 4 ml seed particle suspension are used and redispersed in 5 mL toluene.

- The toluene suspension containing the cobalt seed particle is heated to 85 °C[2] by a silicon oil bath and stirred at 750 rpm.

---

[1]The boiling point of ODCB is 179 °C. The temperature is measured between the reaction vessel and the heating mantle. The reaction is started, when the targeted temperature is reached.

[2]The temperature is measured in the silicon oil bath.

- The gold precursor solution containing $0.01\,g$ gold(III) chloride hydrate ($HAuCl_4$) and $0.25\,mL$ oleylamine solvated in $3\,mL$ toluene is injected at once and the mixture is kept at $85\,°C$ for one hour and subsequently given time to cool down.

- Samples ($100\,µL$) are collected from the reaction mixture after $5\,min$, $20\,min$, $45\,min$ and $60\,min$ to monitor the shell's development.

The second reaction step is investigated further to determine, whether the reaction mixture is able to homogeneously nucleate gold particles. The second step of the above described synthesis is repeated, but without any seed particles present in the boiling toluene. All following steps are executed according to the synthesis instructions. This synthesis is referred to as *Bao2005-gold* and its results are discussed in section 6.3.

6.2. Cobalt seed particles

TEM-BF-imaging is used to visualize the synthesized cobalt seed particle. Size-distributions, giving a mean diameter for the particle batches are obtained by manual measuring the seed particles' diameters. Additionally, the interparticle distance is measured, which can be used to identify the surfactant covering the particle's surface for surfactants with different sizes. XRD and HRTEM-images are used to investigate the crystal structure of the cobalt seed particles, since the different modifications of cobalt have a great effect on the magnetic properties of a nanosized particle. AGM-measurements are used to determine the behavior of the nanoparticles in an external magnetic field including the coercivity, remanence and the saturation moment.

6.2.1. TEM-analysis

TEM-images and size distributions of the particle batches *Bao2005red* and *Bao2005dir* are given in Fig. 6.2 and Fig. 6.3, respectively. The mean diameter $\langle d \rangle$ is determined statistically from the TEM-images for both particle batches. Diameters of several hundred particles are measured with *ImageJ* and displayed as a histogram with a bin-width of $1\,nm$. The histograms are fitted with the internal fit-routines of *IGOR Pro 6, WaveMetrics*, depending on their shape[3],

---

[3]A symmetric size-distribution is fitted with gauss distribution, while a distribution with tailing and a maximum shifted to higher values is fitted with a log-normal distribution (see section 2.1.4).
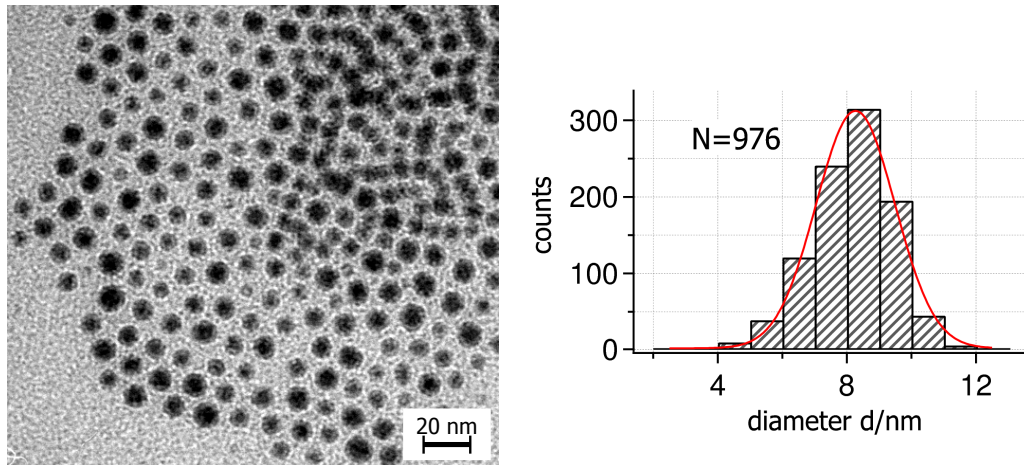
Fig. 6.2: TEM-image and size-distribution of the cobalt seed-particles obtained by the synthesis *Bao2005red*. The particle's mean diameter and standard deviation is $\langle d \rangle = 8.3\,\text{nm} \pm 1.2\,\text{nm}$ for a total number of $N = 976$ measured particles.

to obtain the mean diameter and its standard deviation. The particles of both syntheses are present in clusters of $200\,\text{nm}$ to $500\,\text{nm}$ length. In the areas near the edges of the clusters the particles form a monolayer, while the particles are arrange in multilayers in the cluster center. The particles measured for the size- and distance-distribution are from the monolayered edge areas, since the outlines of different particles in the multi-layered areas cannot be distinguished. Additionally, areas, which are only covered by a single particle layer are also evaluated for size distributions. The synthesis *Bao2005red* yields spherical nanoparticles with a mean diameter of $\langle d \rangle = 8.3\,\text{nm} \pm 1.2\,\text{nm}$ and has a narrow size-distribution with a standard deviation of $15\,\%$. The size-distribution of the particles is of gaussian form and therefore fitted with (**eq.** 2.17).

The synthesis *Bao2005dir* yields spherical nanoparticles, as shown in Fig. 6.3. Their mean diameter is $\langle d \rangle = 9.8\,\text{nm} \pm 1\,\text{nm}$ and the batch is almost monodisperse with $\sigma = 10\,\%$. The diameter distribution is of gaussian form. The mean diameter is in good correspondence with the value given in the publication (see section 4.1). It is not possible to decide, if both particle batches, *Bao2005red* and *Bao2005dir*, are multi-grain or single crystals. The TEM-image of *Bao2005dir* (Fig. 6.3) shows particles with homogeneous contrast. This has been seen as an indication for the single crystal nature of the particles [16]. The particles *Bao2005red* show an thin oxide shell around an unoxidized core, which looks like a lighter shell surrounding a darker core (see Fig. 6.2). This is caused by insufficient protection from oxygen for this particular TEM-sample.
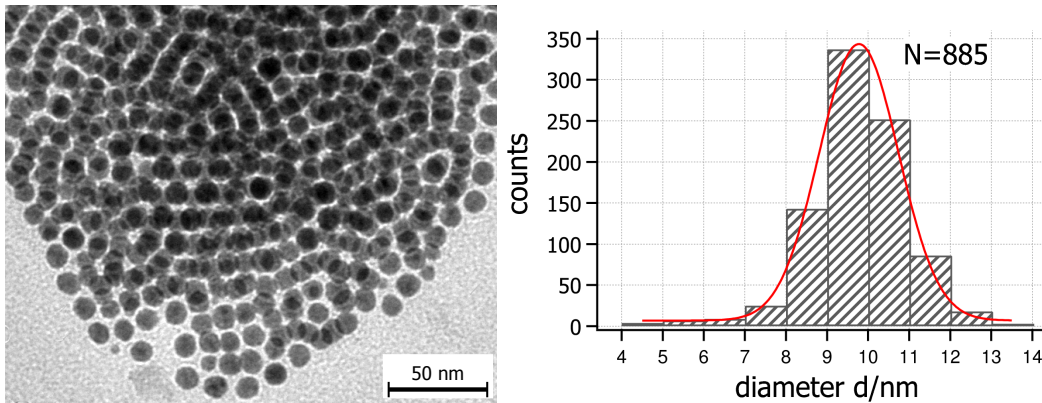
Fig. 6.3: TEM-image and size-distribution of the cobalt seed-particles obtained by the synthesis *Bao2005dir*. The particle's mean diameter and standard deviation is $\langle d \rangle = 9.8\,\mathrm{nm} \pm 1\,\mathrm{nm}$ for a total number of $N = 885$ measured particles.

The particles produced through the instruction *Bao2005red* have a 1.5 nm smaller mean diameter, than those of the reproduction *Bao2005dir*, but both size distributions have a considerable overlap. The mean diameter's divergence from the synthesis *Bao2005red* is outside the first confidence interval, but not very far, since the standard deviation equates to $\sigma_{\mathrm{Bao2005red}} = 1.2\,\mathrm{nm}$. How the amount of solvent changes the reaction conditions resulting in different size distributions cannot be determined entirely. A larger amount of solvent results in a lower surfactant concentration, as well as the decreased cobalt carbonyl concentration after the precursor injection. However, the ratio between metallic precursor and surfactants has been preserved. The results are in agreement with the few reports found in literature. Farrell et al. [98] report, that the surfactant to precursor ratio mostly influence the final size of their homogeneously nucleated iron-nanoparticles. [97] reported, that the diameter of cobalt nanoparticles increases if a bigger amount of metallic precursor used, while the same volume of solvent and surfactants are used. However, the influence of the concentration of surfactants and metal source has not been investigated in detail and is still a topic of discussion at present.

The mean inter-particle distance $\langle \delta \rangle$ is also determined by manually measuring the distances between particles in the TEM-images and afterwards fitting the results. Both interparticle distributions are display in section 6.2.1. The interparticle distance for the sample *Bao2005red* corresponds to $\langle \delta \rangle = 4.6\,\mathrm{nm} \pm 1\,\mathrm{nm}$ and for *Bao2005dir* a mean interparticle distance of $\langle \delta \rangle = 4.2\,\mathrm{nm} \pm 1\,\mathrm{nm}$ has been found. The thickness of the particles' surfactant shell corresponds to $L = \frac{\delta}{2}$, according to (**eq.** 2.19). L is around 2 nm to 2.3 nm for both synthesis
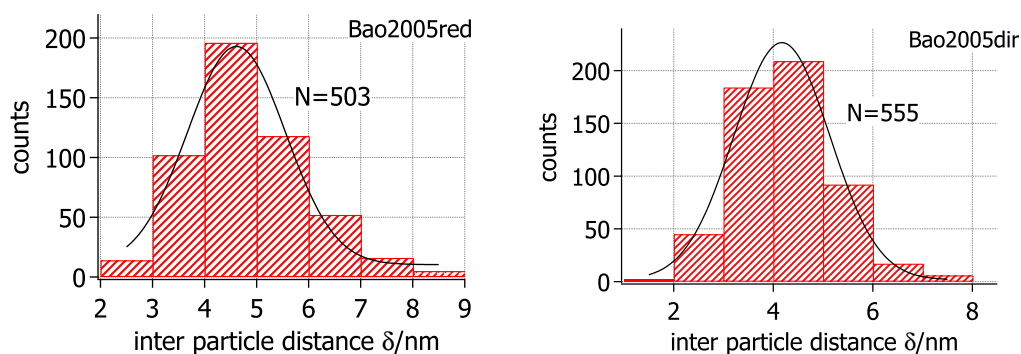
Fig. 6.4: Inter particle distance distributions for the syntheses *Bao2005red* (left) and *Bao2005dir* (right). The mean inter-particle distance for *Bao2005red* is $\langle \delta \rangle = 4.6\,\text{nm} \pm 1\,\text{nm}$ and for *Bao2005dir* it amounts to $\langle \delta \rangle = 4.2\,\text{nm} \pm 1\,\text{nm}$.

batches, which can be compared to know values for oleic acid, dioctylamine and tri-octylamine [21]. Two different surfactants, depicted in Fig. 6.5 (including oleylamine, which is used in the second reaction step), are used during the synthesis and it is possible, that both functionalized the particles' surface. The surfactant shell thickness L corresponds to the calculated length of oleic acid (OA) $L_{\text{OA}} = 2.4\,\text{nm}$ [21]. Oleic acid has a chain-length of 18 carbon atoms and is therefore longer than dioctylamine. DOA attaches itself via its amine-group[4] to the particle surface. The length of the amine is determined by its two alkyl-chains, which consist of 8 carbon atoms. Its length is expected to be around 1 nm [21]. If DOA is the only surfactant present on the particles' surface, it would lead to a significantly smaller mean interparticle distance. The measured values indicate that oleic acid is present on the particle surface and defines the interparticle distance. The amine group is believed to bind weaker to the nanoparticles' surface, than a carboxyl-group [21, 55], therefore DOA must be superseded by oleic acid on the particle surface. The role DOA plays in the syntheses and how it interacts with the other reactants is not known. Bao et al. [99] proposed, that DOA causes the formation of many nuclei that grow into small particles, which afterwards aggregate to the final particles. This results are compared to a trioctylphosphine oxide (TOPO) related synthesis, that produces single crystal particles of the same diameter. However, the role surfactants play during nanoparticle synthesis is a topic of ongoing discussion.

---

[4]The amine-group is more polar than the alkyl-chains and therefore it is energetically favorable to turn the head-group towards the nanoparticle.
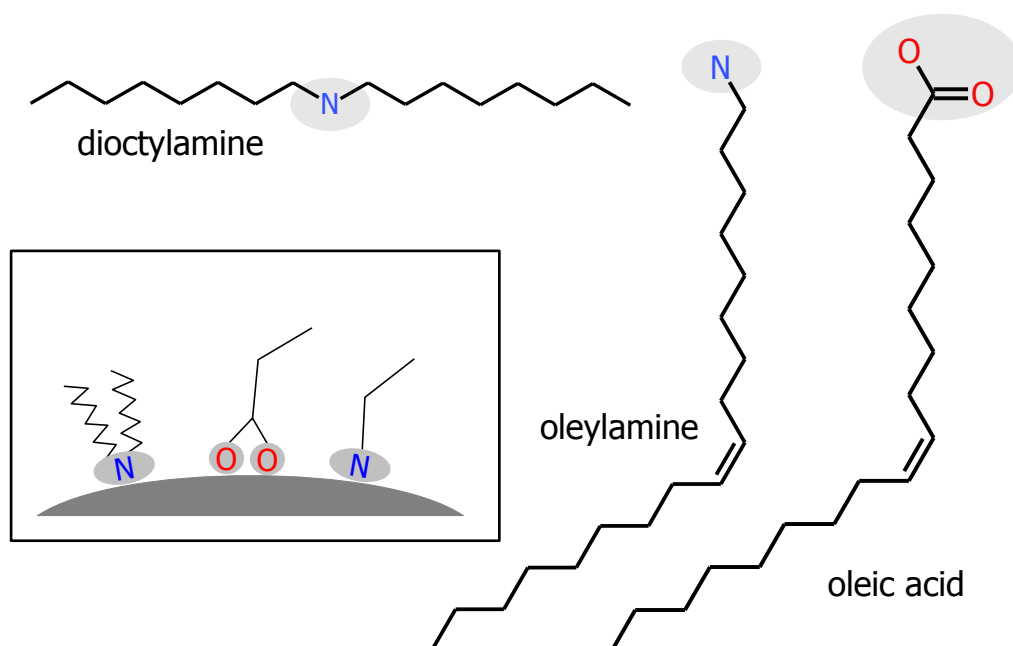
Fig. 6.5: Skeletal formulas generated with *Accelrys Draw 4.0* (Symyx Solutions Inc.) of all surfactants, dioctylamine, oleic acid and oleylamine, used in the syntheses *Bao2005red* and *Bao2005dir*. The polar head groups binding with the nanoparticles' surface are highlighted by gray ovals. The inset schematically shows the behavior of the unploar tails, if the head group is in contact with a nanoparticle.

6.2.2. Crystal structure

The crystal structure has a great influence on the magnetic properties of the cobalt nanoparticles. Two methods are applied to determine the crystal structure of the cobalt seed particles. First the results of XRD-analysis are discussed and later compared to powder spectra simulated for all modifications of cobalt (see section 5.1). The crystallite sizes are determined via Scherrer's equation from peak broadening due to the particle sizes determined before. The results are compared to the grain sizes visible in the HRTEM-images. The results obtained through indexing of the FFTs generated from HRTEM-images and simulated single crystal electron diffraction pattern for different cobalt structures are compared. Both methods should indicate the crystal structure of the cobalt seed particle.

Chemical impurities represent a problem during for the crystal structure analysis, which can cause crystal defects altering the final X-ray powder spectrum. EDX-analyses are preformed on the same samples to ensure, that pure cobalt
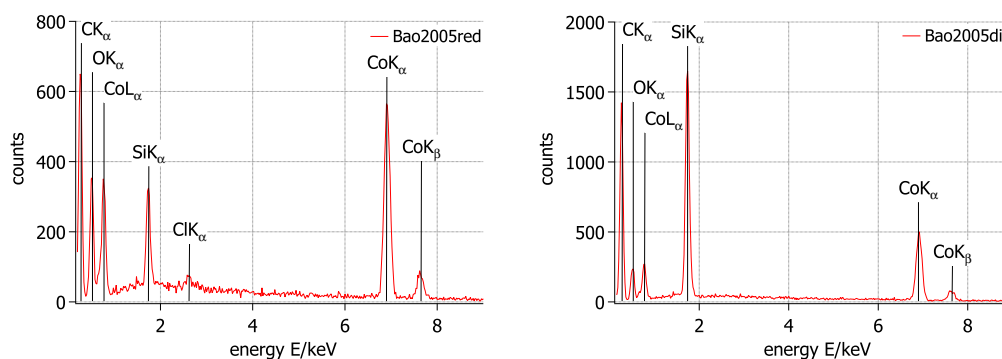
Fig. 6.6: EDX-analyses of the seed particles from syntheses *Bao2005red* (left) and *Bao2005dir* (right). All elements found in the samples are either from residual air or the surfactant coating of the particles (carbon and oxygen), the silicon substrate or the pure cobalt particles. The sample *Bao2005red* shows an small peak at $2.8\,\text{keV}$ attributed to chlorine, which is caused by residues of the solvent ODCB. The measurement shows, that pure cobalt seed particles are obtained by the syntheses.

particles have been produced. The measurements are displayed in Fig. 6.6. The spectra only show peaks corresponding to cobalt and silicon, besides oxygen and carbon. The latter can be caused by residual air or surfactants on the particles, while silicon is used as substrate. The small chlorine peak is caused by residues of the solvent ODCB. The measurements verify, that pure cobalt seed particles are obtained by both syntheses.

The XRD-measurements of both particle batches are conducted with an omega offset of 3° in the range of $\theta = 20°$ to 120° and the resulting XRD-spectra are displayed in Fig. 6.7 and 6.8 for *Bao2005red* and *Bao2005dir*, respecitvely. The spectra of both samples show peaks at $\theta = 44.4°$, $\theta = 92°$ and $\theta = 98°$, which correspond very well with the (111)-, (311)- and (222)-peaks of the simulated powder pattern of fcc-cobalt. In both cases the (200)- and (220)-peak is not clearly resolved and overlapped by the broadened cobalt fcc (111)-peak and the silicon (400)-peak, respectively. The sample *Bao2005dir* shows additional peaks at $\theta = 33°$ and $\theta = 61°$. The position of the former coincides with the (210)-peak of ϵ-cobalt, but since this peak is of weak intensity and stronger ϵ-cobalt peaks are missing in the spectrum it is most likely not caused by ϵ-cobalt. The peak at $\theta = 61°$ cannot be attributed to any possible modification of cobalt. However, the measurements show, that the seed particles are composed of fcc-cobalt in case of both syntheses *Bao2005red* and *Bao2005dir*.
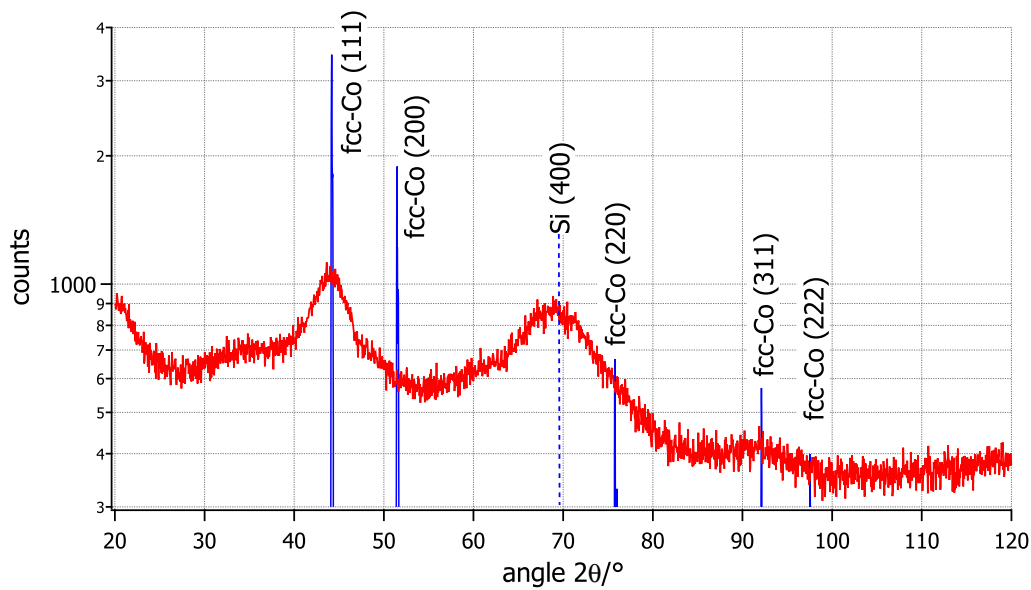
Fig. 6.7: X-ray powder diffraction spectrum of *Bao2005red*. The peaks at $\theta = 44°$, $\theta = 92°$ and $\theta = 97°$ correspond to the (111)-, (311)- and (222)-peaks of fcc-cobalt. The (200)- and (220)-peaks are not clearly resolved in the spectrum and superimposed by the broadened fcc-cobalt (111)- and the silicon (400)-peak, respectively. The peaks indicate an fcc-structure.
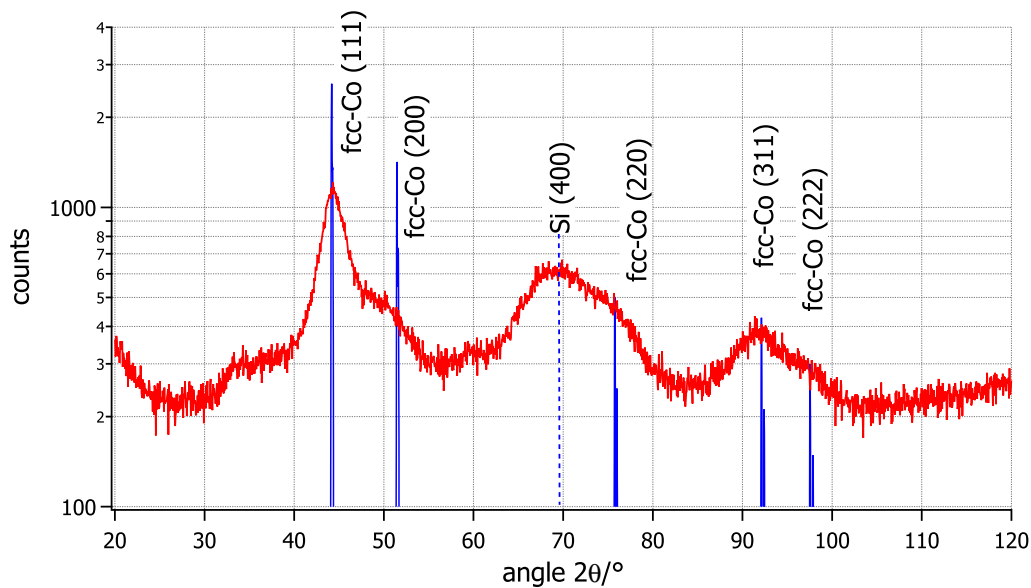
Fig. 6.8: X-ray powder diffraction spectrum of *Bao2005dir*. The peaks at $\theta = 44°$, $\theta = 92°$ and $\theta = 97°$ correspond to the (111)-, (311)- and (222)-peaks of fcc-cobalt. The (200)- and (220)-peaks are not clearly resolved in the spectrum and superimposed by the broadened fcc-cobalt (111)- and the silicon (400)-peak, respectively. The peaks also indicate an fcc-structure.

63
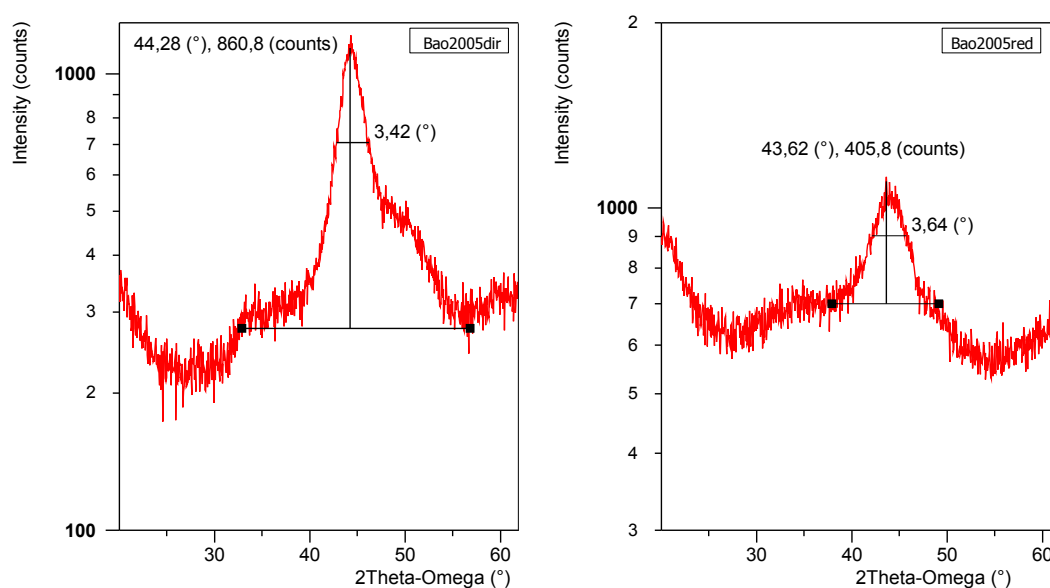
Fig. 6.9: Determination of peak FWHM values for grain size determinations from XRD-measurements. Left: The width of the fcc-cobalt (111)-peak of *Bao2005dir* at $2\theta = 44.28°$ is determined to a broadening corrected FWHM value of $3.41°$. Right: The fcc-cobalt (111)-peak of sample *Bao2005red* is located at $2\theta = 43.62°$ and its width is determined to a corrected FWHM value of $3.63°$.

The Scherrer equation (**eq.** 3.5) is used to determine the grain size of crystallites within the particles, which are oriented perpendicular to the incident X-rays. The form-factor C_{form} is set to a value of 0.9, which is empirically recommended for cubic crystals [10, 100]. The (111)-peak of the spectra from samples *Bao2005red* and *Bao2005dir* is used, because of its high intensity. The FWHM-value of the peaks are measured with the "X'Pert data viewer" and displayed in Fig. 6.9. The values are corrected to remove peak broadening caused by the diffractometer. This leads to an FWHM-value of 3.41° for *Bao2005red* and 3.63° for *Bao2005dir*. The resulting crystallite sizes D' therefore are 2.5 nm for *Bao2005red* and 2.4 nm for *Bao2005dir*. The crystallite sizes are smaller than the mean particle diameter of 9.8 nm for *Bao2005dir* and 8.3 nm for *Bao2005red*. Hence, the particles produced by both syntheses have a multi-grain composition, because the grain size is expected to equate to the particle diameter for a single-crystal nanoparticle and smaller values for multi grain particles. The multi grain nature for cobalt nanoparticles produced in presence of oleic acid and DOA has also been reported in the previously referenced article of Bao et al. [99]. The article compared two syntheses; one uses a surfactant mixture of TOPO

and oleic acid, while the other uses oleic acid and DOA[5]. The TOPO-related synthesis produced 10 nm single crystals, while multi grain particles of the same diameter are produced by the DOA-related synthesis. This result is explained by Bao et. al. with the shape of the surfactants TOPO and DOA. TOPO, which is assumed to be a strong surfactant, limits the reactivity of all available monomers, resulting in the production of few nuclei and a high excess monomer concentration, which leaves the solution with a high chemical potential. This would favor, according to Bao et. al., the growth of single crystals. In contrast, DOA is a compact surfactant, which leads to a high monomer reactivity and the formation of many nuclei growing into small particles leaving the amount of excess monomers small. The final 10 nm particles are agglomerations of these small particles. However, the assumption that TOPO is a strong surfactant compared to DOA was disproven by Vogel [21]. DOA supersedes TOPO on a cobalt nanoparticle, hence DOA has a higher binding affinity. Therefore the basis of the proposed formation mechanism is not valid and leaves doubt about the model's correctness.

Further investigations of the cobalt particles' crystal structure are done by HRTEM-imaging. The higher resolution of a HRTEM compared to the conventional TEM allows further analysis of the crystal lattice. It is helpful to investigate the reciprocal lattice of the crystallites to identify the modification of the material. Therefore, FFTs of selected areas of the HRTEM-images are generated, which yield the same information as electron diffraction images of the crystals. FFTs, inverted and contrast enhanced for better visibility, and the corresponding HRTEM-images of the samples *Bao2005red* and *Bao2005dir* are given in Fig. 6.10 and 6.11. The crystallites visible in the HRTEM-images have sizes of 2 nm to 3 nm, which correspond to the crystallite sizes calculated via Scherrer's equation. The crystallites have a continuous lattice structure and are separated by grain boundaries. The FFTs are compared to simulated electron diffraction patterns, present in section 5.2 to determine the crystal structure via a process of elimination. All FFTs show the reflexion patterns of an oblated hexagon with the distinct aspect ratio of 2:1 between the dissections *a* and *b* and *a* is always longer than *c*. This pattern is unique for an fcc-crystal structure and is generated by electrons diffracted along the [110]fcc axis. The aspect ratios of different reflexion patterns generated by an fcc-crystal are given in Fig. 5.3. A hcp-cobalt crystal can also cause hexagonal reflexion patterns, but they have a different aspect ration, than the oblated hexagon of an fcc-crystal (see section 5.2). The ϵ-cobalt structure generates a multitude of reflexions

---

[5]The synthesis corresponds to the seed particle synthesis of *Bao2005dir* and uses the same reactants and reaction parameters.

dominated by octagonal arrangements of intensive reflexes for directions with low Miller indices, which are not found in the FFTs, either. Investigation of the reciprocal lattice confirms together with the XRD-measurements, that the cobalt seed particles are composed of fcc-cobalt. The results deviate from the original publication by Bao et al. [31], which reported an ϵ-cobalt structure for the cobalt seed particles.
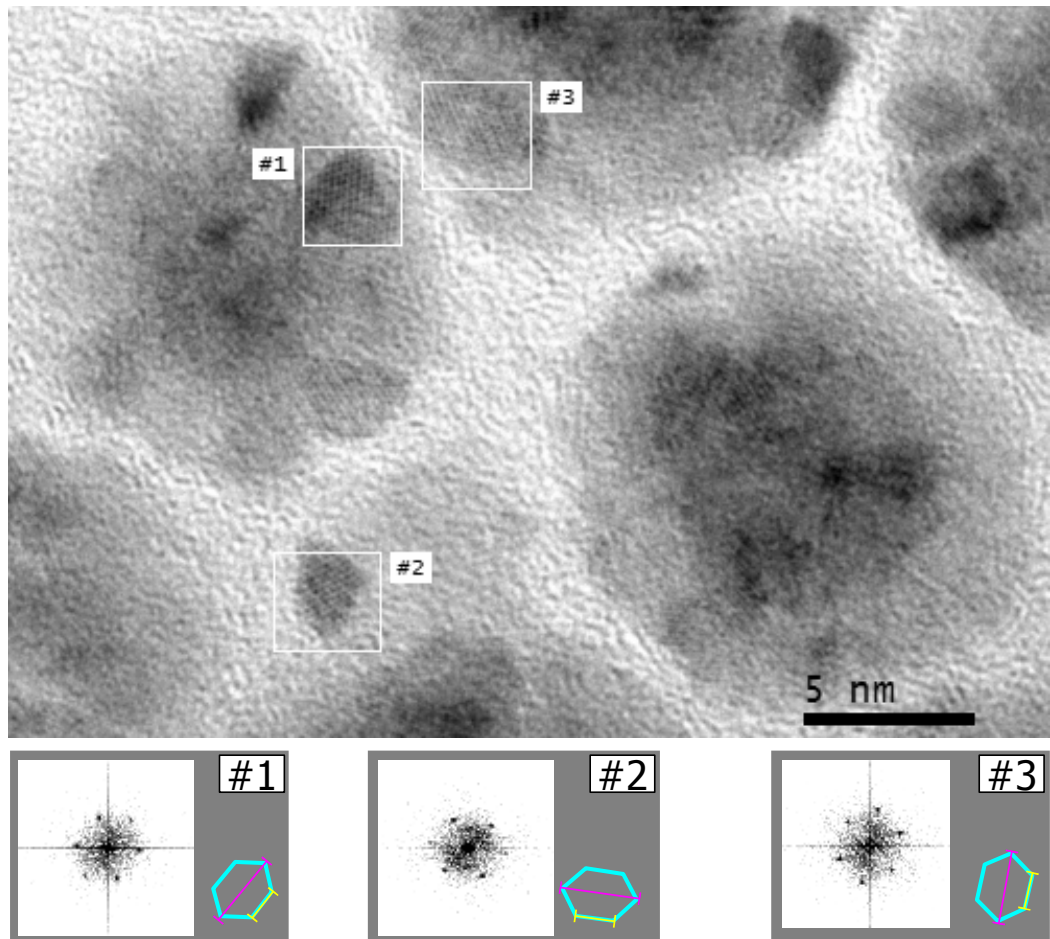
Fig. 6.10: HRTEM-image from *Bao2005red*. Areas investigated for the reciprocal lattice by FFTs are outline in the image and the FFTs are displayed inverted and with enhanced contrast for better visibility.. The FFTs correspond to electron diffraction patterns indicating an fcc-structure, because only oblated hexagons with a distance ration of 2:1 between the magenta and yellow section are found.
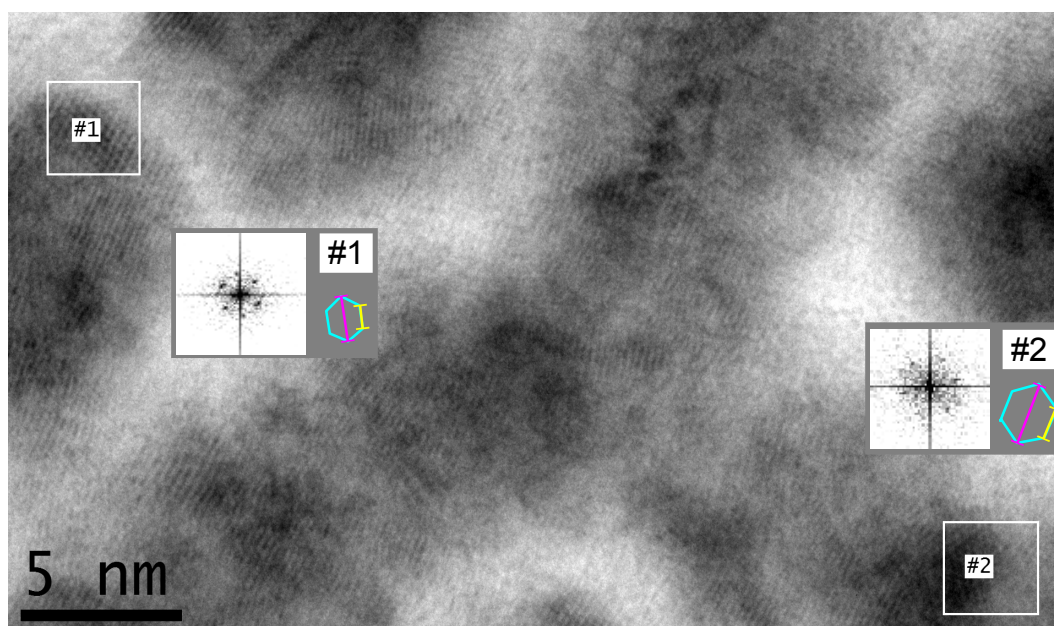
Fig. 6.11: HRTEM-image from *Bao2005dir*. Areas investigated for the reciprocal lattice by FFTs are outline in the image and the FFTs are displayed inverted and with enhanced contrast for better visibility. The FFTs correspond to electron diffraction patterns indicating an fcc-structure, because only oblated hexagons with a distance ration of 2:1 between the magenta and yellow section are found.

The parameters, which define the cobalt modification during a synthesis have not yet been determined. Early publications on the ϵ-cobalt structure associated the concentration of the surfactant TOPO with the formation of the specific structure [94, 101]. Later studies concerning the formation of ϵ-cobalt reported the synthesis of ϵ-cobalt nanoparticles using different surfactants [102]. The synthesis *Bao2005dir* reproduces the synthesis of Bao et al. [31] as accurately as possible, but the obtained particles still have a different crystal modification. This shows, that the reactants do not necessarily produce a certain crystal structure. It is likely, that environmental factors like reaction temperature, duration of precursor injection or the presence of magnetic fields through e.g. magnetic stir bars in the reaction solution influence the crystal structure of the cobalt nanoparticles, instead.

6.2.3. Magnetic properties
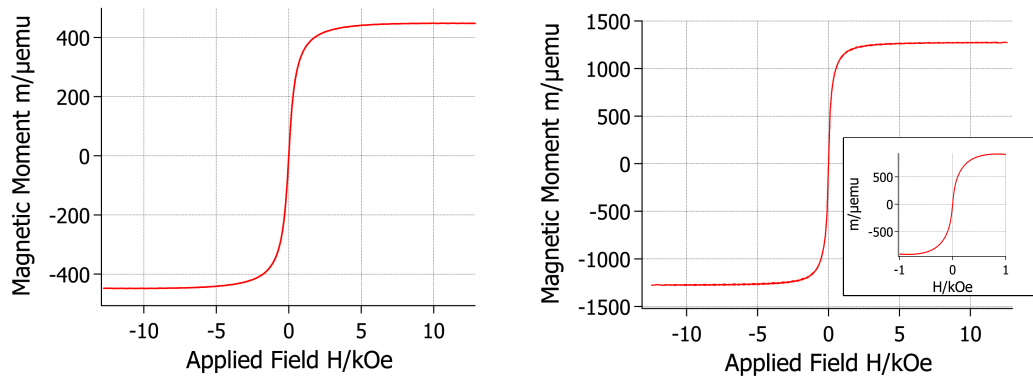
Fig. 6.12: Magnetization curves of *Bao2005red* (left) and *Bao2005dir* (right), which display the superparamagnetic behavior of the samples. The inset in the right diagram shows a more detailed measurement between $-1\,\mathrm{kOe}$ to $1\,\mathrm{kOe}$, in which no coercivity is visible, either. Both samples reach saturation before an external field of $5\,\mathrm{kOe}$ is applied.

Both syntheses yielded cobalt-particles with an fcc crystal structure. All diameters measured for the size-distributions are below the calculated superparamagnetic limit of $d_{\mathrm{SP}} = 15.4\,\mathrm{nm}$, therefore superparamagnetic behavior is expected. Hysteresis loops of *Bao2005red* and *Bao2005dir* are recorded with a field maximum of $14\,\mathrm{kOe}$ and the resulting magnetization curves are displayed in Fig. 6.12 with an inset in the top diagram showing a more detailed measurement around the origin of sample *Bao2005dir*. The samples display superparamagnetic behavior during the measurement. Values for the parameters m_{S}, m_{R} and H_{C} are summarized in Tab. 6.1. Both samples are saturated before an external field of $5\,\mathrm{kOe}$ is applied. It is not possible to determine the volume or mass magnetization from the saturation moments, because of the unknown amount of particles in the sample volumes. Furthermore, oxidation can decrease the magnetically active volume of the particles.

Magnetization curves with the samples' respective size distributions are calculated using (**eq.** 2.27). The mean diameters and standard deviations are also listed in Tab. 6.1. The calculations are done only for maximum external field values of $H_{\mathrm{ext}} = \pm 5\,\mathrm{kOe}$, due to the limited data storage within the *MathCAD* program. The diagrams are displayed in Fig. 6.13 and show three different curves for each sample. The circles depict the progression of the measured AGM-curve, while the solid and dotted lines depict calculated curves for the noted mean diameters and standard deviations. The dotted lines are calculated based on the mean diameters determined through the size distribution, but

they do not reproduce the progression of the measured curves entirely. The solid lines are a better match and they are calculated for particle batches with a decreased mean diameter and the same standard deviation. The mean diameter of *Bao2005red* is determined to 8.3 nm, but the magnetization curve calculated for a mean diameter of 6.8 nm corresponds better to the measured magnetization curve. The same can be observed in case of sample *Bao2005dir*. The determined mean diameter is 9.8 nm, but the curve calculated for a mean diameter of 8.3 nm better fits the measured results. This can be explained by simple oxidation of the cobalt nanoparticles. The preparation and the measurement of an AGM-sample usually takes a few minutes and the otherwise protected particles are exposed to oxygen during this time. The high surface area of the particles can lead to surface oxidation, as is visible in the TEM-image of sample *Bao2005red* (Fig. 6.2). This oxidation process decreases the magnetically active volume of a particle sample, because cobalt oxide is anti-ferromagnetic and does not contribute to the overall magnetization of the sample. The oxidized sample acts like an unoxidized sample consisting of smaller nanoparticles. The formation of an oxide shell is assumed for both samples and it is approximately 0.75 nm thick in both cases. The standard deviations are not changed by the surface oxidation, if a constant oxide shell thickness is assumed for all nanoparticles. To conclude, the shape of the measured AGM-curves of samples *Bao2005red* and *Bao2005dir* can be attributed to the samples' size distributions with regard to their decreased magnetic volume.
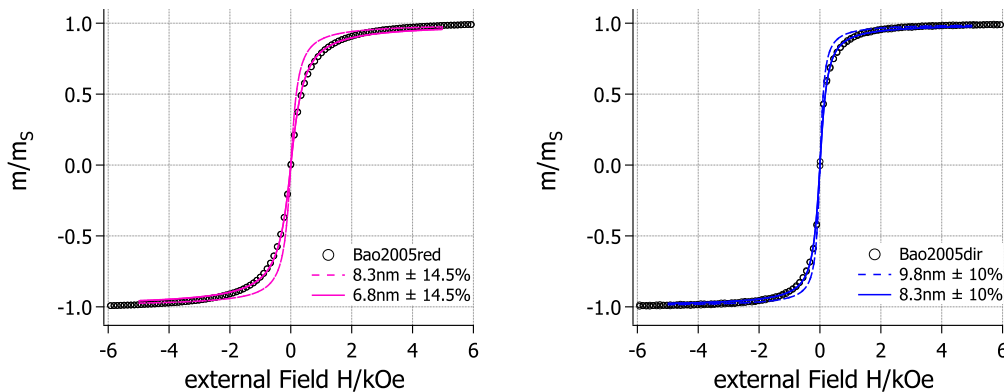
Fig. 6.13: Left: The size distribution of *Bao2005red* is used to calculate the dashed curve, which does not follow the progression of the measured curve (circles). The solid curve calculated with $\langle d \rangle = 6.8\,\text{nm} \pm 14.5\,\%$ fits the AGM-results better. Right: The same applies to sample *Bao2005dir*. The dashed line calculated does not follow the progression of the measured curve, while the solid curve calculated for a decreased diameter of $\langle d \rangle = 8.3\,\text{nm} \pm 10\,\%$ is a better match.

Tab. 6.1: Magnetic saturation moment m_S, remanence m_R and coercivity H_C of the samples *Bao2005red* and *Bao2005dir*. The respective mean diameters $\langle d \rangle$ and standard deviations σ are determined as explained in section 6.2.1.

sample	m_S/μemu	m_R/μemu	$H_\mathrm{C}/$Oe	$\langle d \rangle /$nm	σ /nm
Bao2005red	448.0	1.2	1.5	8.3	$1.2 \mathrel{\hat{=}} 10\,\%$
Bao2005dir	1273.4	8.1	0.8	9.8	$1.0 \mathrel{\hat{=}} 14.5\,\%$

6.3. Control experiment *Bao2005-gold*
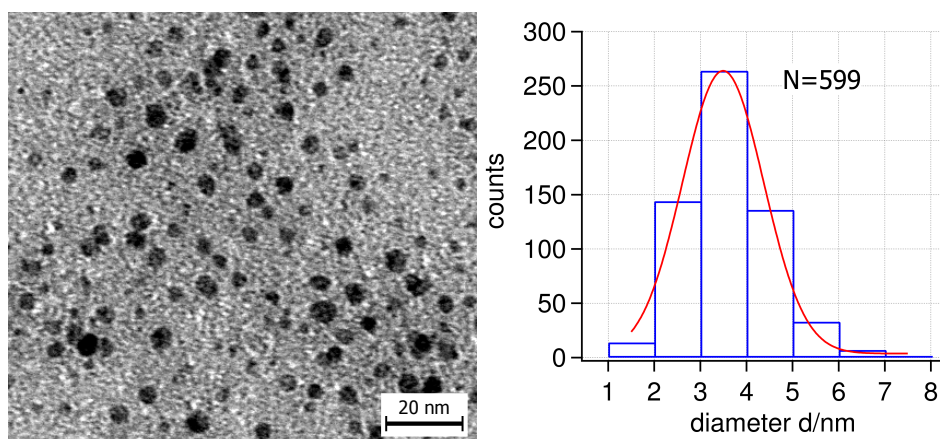
Fig. 6.14: TEM-image and size-distribution of gold particles yielded by a homogeneously nucleation process of the reaction mixture *Bao2005-gold*. The nanoparticles have a mean diameter of $\langle d \rangle = 3.5\,\mathrm{nm} \pm 0.9\,\mathrm{nm}$.

The control experiment *Bao2005-gold* is executed to evaluated, if the shell synthesis step can homogeneously nucleate gold nanoparticles. If gold nanoparticles are formed during the control experiment, it is possible, that this happens during the shell synthesis, when cobalt seeds are present. In this case the gold nuclei would serve as competing nucleation centers to the seeds, which affects the actual intended synthesis. $HAuCl_4$ is used as gold source in this control experiment and only the gold precursor and surfactant are injected into boiling toluene and the mixture is refluxed for one hour. Fig. 6.14 displays round, but arbitrary shaped gold particles. Their mean diameter is about $\langle d \rangle = 3.5\,\mathrm{nm} \pm 0.9\,\mathrm{nm}$ with a standard deviation of $\sigma = 25\,\%$. The nanoparticles can not be precipitated from the toluene suspension, therefore an alternative purification method is used, in which the uncleaned particle

suspension is drop-casted onto a TEM-grid, as described in section 3.4.1. After the excess suspension is drained and the grid is dried, a drop of ODCB is applied and also removed. This is repeated three times. The residues covering the particles are removed on this way, which makes TEM-imaging possible. The experiment shows, that the system nucleates homogeneously, without any cobalt-seeds present.

6.4. Bimetallic cobalt-gold particles *Bao2005*

The previously characterized superparamagnetic cobalt seed particles are used as nucleation centers for the gold shell in the second reaction step. A gold-precursor solution containing another surfactant oleylamine, which should stabilize the gold-shell and reduce the gold source, are added to a boiling suspension containing the cobalt-seeds. Samples are collected after 5 min, 20 min, 45 min and 60 min to monitor the shell growth. First TEM-imaging is used to visualize the particles and to determine their size distribution. Furthermore, Z-contrast imaging and EDX-analyses are used to determine the elemental composition in the particles. First the results of the synthesis *Bao2005red* are listed and discussed followed by the same analyses by *Bao2005dir*.

6.4.1. TEM-imaging

The TEM-images of all samples collected during the synthesis *Bao2005red* are displayed in Fig. 6.15 to 6.18. All TEM-images show two different types of nanoparticles, the cobalt seed particles, appearing light gray in the images and a new kind of nanoparticles with higher contrast, appearing black. Example are highlighted in Fig. 6.18. Separate size-distributions for both particle types are shown together with the TEM-images. The gray hatched histograms represent the size distributions of the low contrast seed particles, while the blue framed histograms represents the size distributions for the high-contrast particles. The change in diameter for both particle types of the synthesis *Bao2005red* is displayed in Fig. 6.19. The mean diameter of the cobalt seed particles has been determined to 8.3 nm during analysis of the seed particles and the mean diameter remains constant within the standard deviation during the synthesis with values between 8.3 nm and 9 nm. The mean diameter of the higher contrast particles stays constant within the standard deviation as well. It deviates between 3.8 nm and 4.4 nm. The results show, that second synthesis step is not influencing the size and shape of the seed particles.
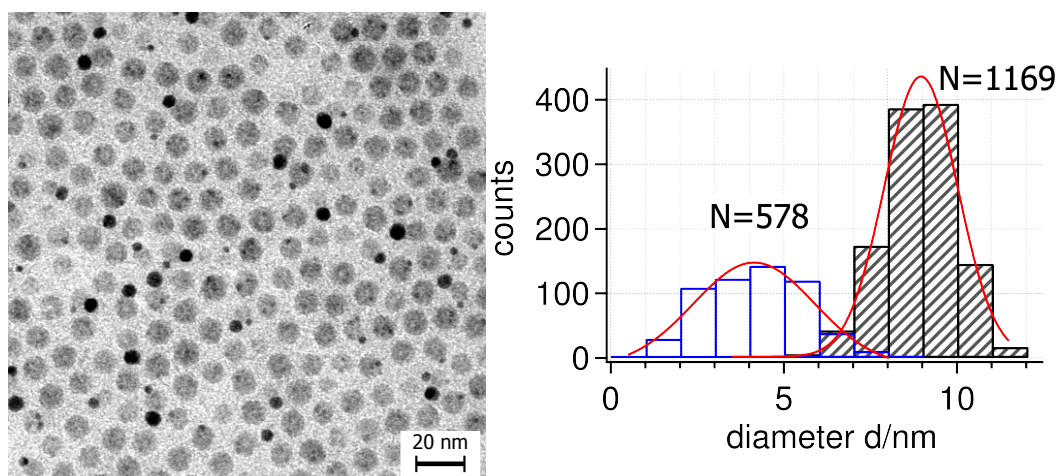
Fig. 6.15: TEM-image and size-distribution the particle batch *Bao2005red*. The sample is taken $5\,\mathrm{min}$ after the gold-precursor is injected. Two types of nanoparticles are visible, the low contrast seed particles and a second type of particles with higher contrast, which are interconnected with the seed particles. The mean diameter of the seed particles is determined to $\langle d \rangle = 9\,\mathrm{nm} \pm 1\,\mathrm{nm}$, while the mean diameter of the high-contrast particles is determined to $\langle d \rangle = 4.1\,\mathrm{nm} \pm 1.8\,\mathrm{nm}$.
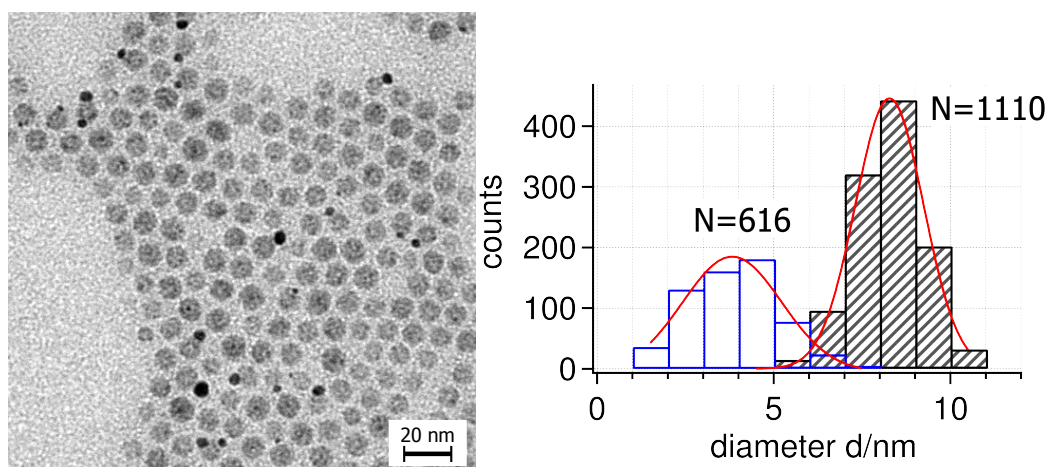
Fig. 6.16: TEM-image and size-distribution the particle batch *Bao2005red*. The sample is taken $20\,\mathrm{min}$ after the gold-precursor is injected and two particle types are visible as before. The mean diameter of the seed particles is $\langle d \rangle = 8.3\,\mathrm{nm} \pm 1\,\mathrm{nm}$ and the high-contrast particles have a mean diameter of $\langle d \rangle = 3.8\,\mathrm{nm} \pm 1.4\,\mathrm{nm}$.
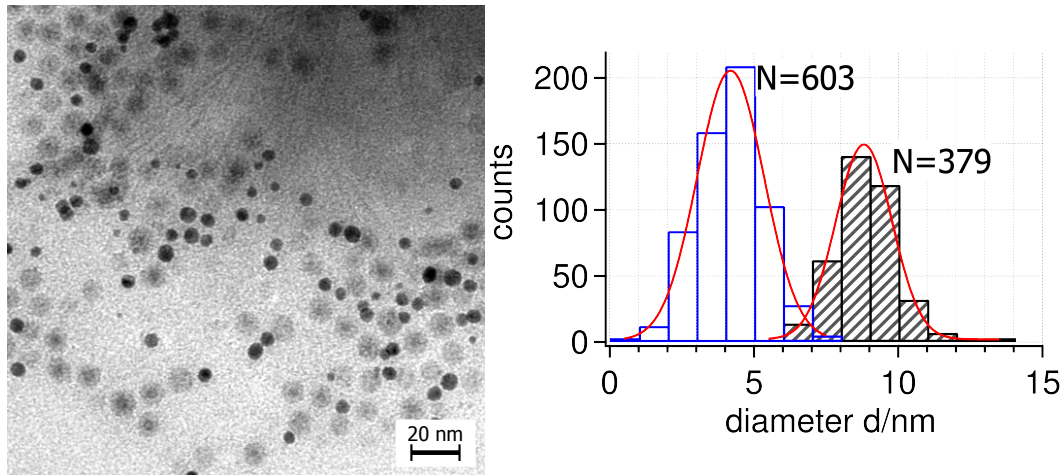
Fig. 6.17: TEM-image and size-distribution the particle batch *Bao2005red*. The sample is taken 45 min after the gold-precursor is injected. The mean diameter of the seed particles is $\langle d \rangle = 8.8\,\text{nm} \pm 1\,\text{nm}$ and the high-contrast particles have a mean diameter of $\langle d \rangle = 4.2\,\text{nm} \pm 1.2\,\text{nm}$.
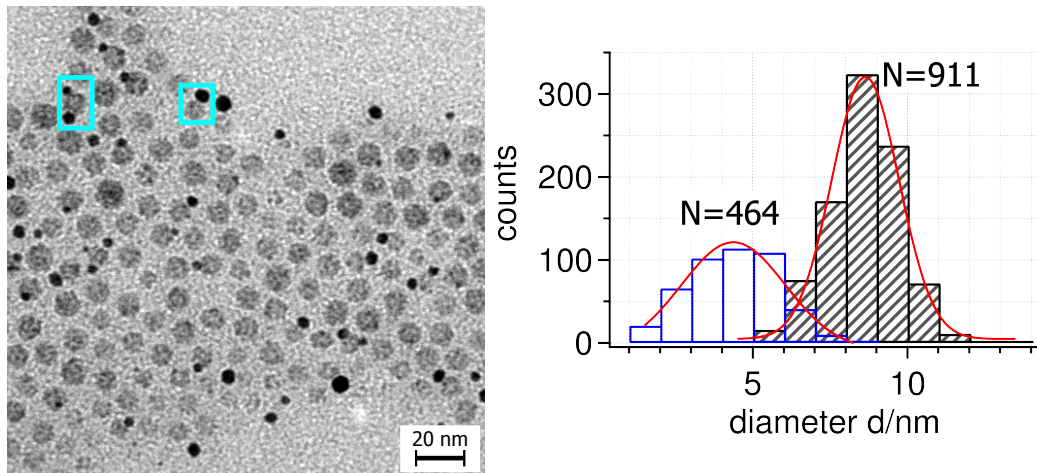
Fig. 6.18: TEM-image and size-distribution the particle batch *Bao2005red*. The sample is taken 60 min after the gold-precursor is injected. The mean diameter of the seed particles is $\langle d \rangle = 8.6\,\text{nm} \pm 1.1\,\text{nm}$ and the high-contrast particles have a mean diameter of $\langle d \rangle = 4.4\,\text{nm} \pm 1.7\,\text{nm}$. Structures of interconnected seed and high-contrast particles are highlighted in this image (turquoise frames).
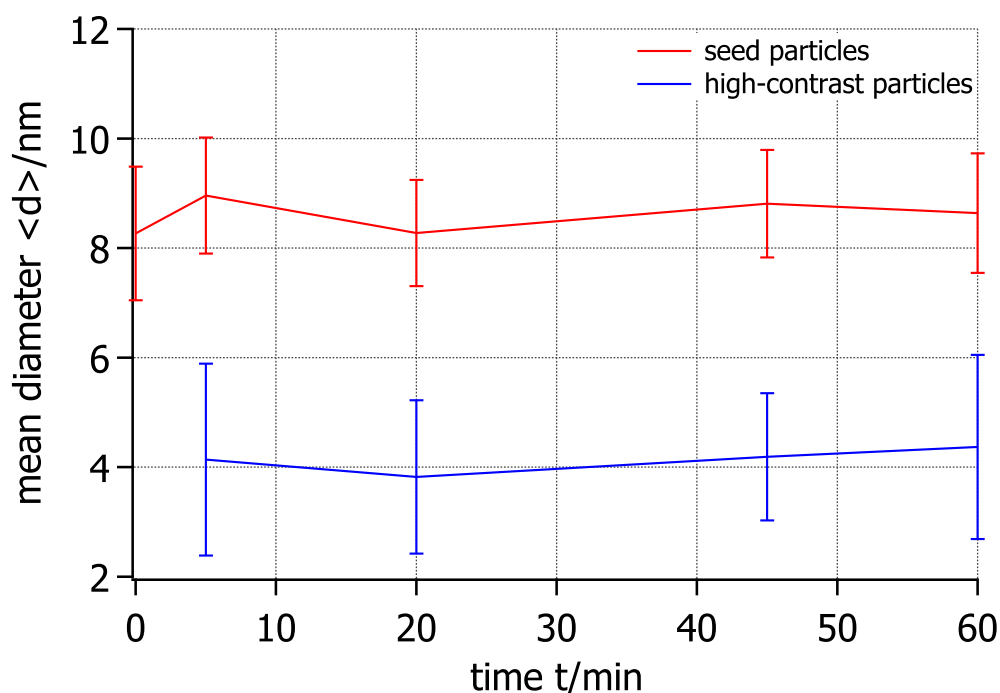
Fig. 6.19: Change in mean diameter of both high-contrast (blue curve) and seed particles (red curve) during the synthesis of *Bao2005red*. The error bars corresponds to the standard deviation and the line connecting the points only serves as a guide to the eye.

The formation process of the high-contrast particles appears to be already completed, when the first sample is collected 5 min after the precursor injection, because their mean diameter does not change significantly afterwards. The high-contrast particles are always in contact with a seed particle, as can be seen in all TEM-images. This is first evidence, that a heterogeneous nucleation took place, since a complete shell has not been formed, but single spherical particles emanated from the nucleation site on the seed particles.

TEM-images and size distributions of the synthesis approach *Bao2005dir* are displayed in Fig. 6.20 to 6.23. The seed particles are heavily covered with high-contrast particles and some seeds are deformed. Examples of tripod or cap-like structures can be found in all TEM-images of the sample *Bao2005dir*, highlighted by turquoise arrows. Additionally, high-contrast particles, which are not in contact with a seed particle, are found in the TEM-images highlighted by yellow arrows. The change in mean diameters for both particle types at different times during the synthesis is displayed in Fig. 6.24. The mean diameters of the cobalt seeds remained constant after dropping to values around 7 nm.
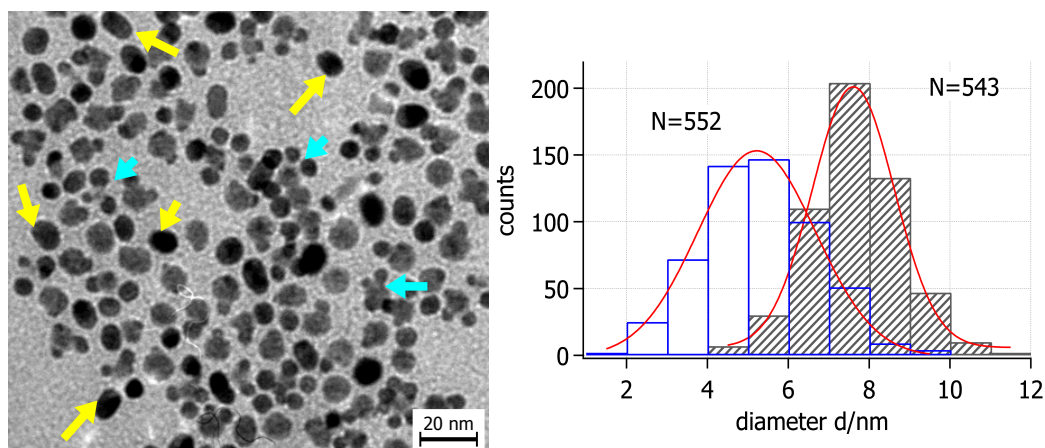
Fig. 6.20: TEM-image and size-distribution of the particle batch *Bao2005dir* containing two types of particles. The sample is taken $5\,\mathrm{min}$ after the gold-precursor is injected. The cobalt seed particles (gray particles) have a mean diameter of $\langle d \rangle = 7.6\,\mathrm{nm} \pm 1\,\mathrm{nm}$ and the high-contrast particles have a mean diameter of $\langle d \rangle = 5.2\,\mathrm{nm} \pm 1.5\,\mathrm{nm}$. Turquoise arrows point to interconnected seed and high-contrast particles forming e.g. tripod structures and the yellow arrows point out high-contrast particles, which are not in contact with any seeds.
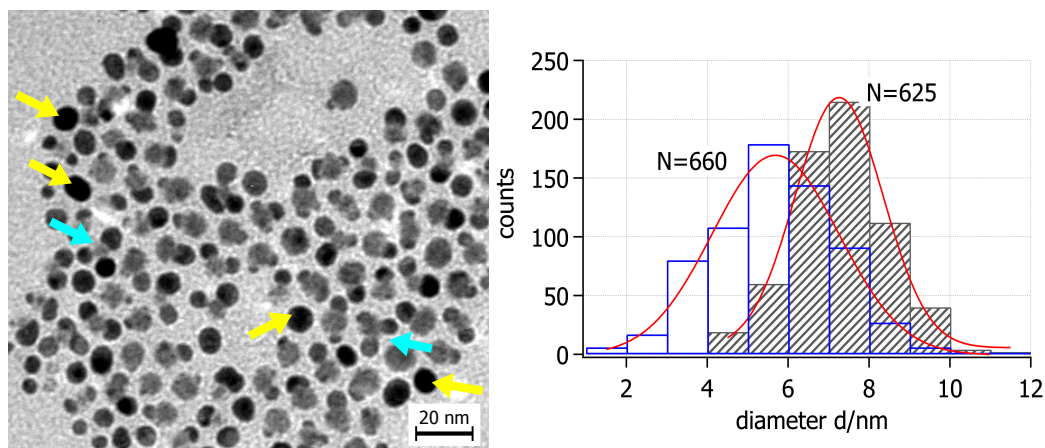
Fig. 6.21: TEM-image and size-distribution the particle batch *Bao2005dir*. The sample is taken $20\,\mathrm{min}$ after the gold-precursor is injected. The seed particles' mean diameter is determined to $\langle d \rangle = 7.3\,\mathrm{nm} \pm 1.1\,\mathrm{nm}$ from $N = 625$ measured particles and the mean diameter of the high-contrast particles is determined to $\langle d \rangle = 5.7\,\mathrm{nm} \pm 1.6\,\mathrm{nm}$ from $N = 660$ measured particles. The turquoise arrows point to tripod structures, while the yellow arrows point out high-contrast particles, which are not in contact with a seed particle.
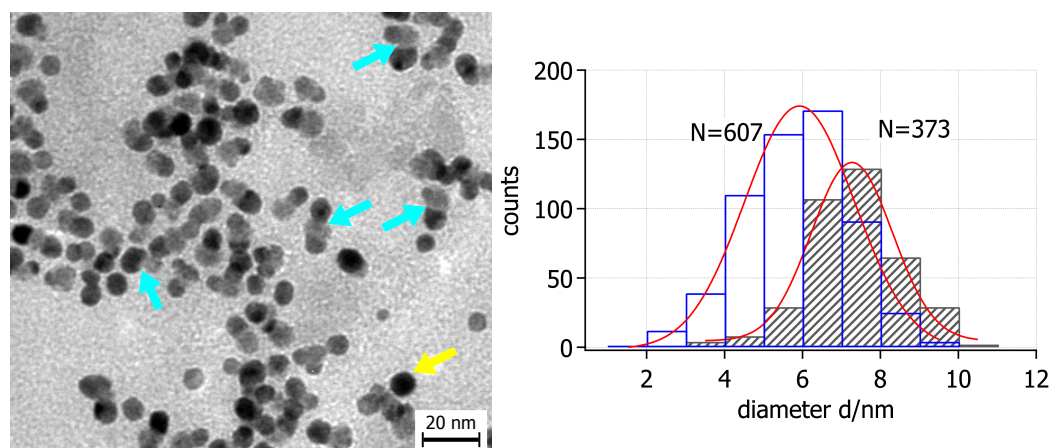
Fig. 6.22: TEM-image and size-distribution the particle batch *Bao2005dir*. The sample is taken $45\,\mathrm{min}$ after the gold-precursor is injected. Cobalt particles have a mean diameter and standard deviation of $\langle d \rangle = 7.3\,\mathrm{nm} \pm 1\,\mathrm{nm}$ measured from $N = 373$ particles and the high-contrast particles have a mean diameter of $\langle d \rangle = 5.9\,\mathrm{nm} \pm 1.4\,\mathrm{nm}$ measured from $N = 607$ particles. Turquoise arrows point out interconnected high-contrast and seed particles, while the yellow arrow points out a high-contrast particle not in contact with a seed.
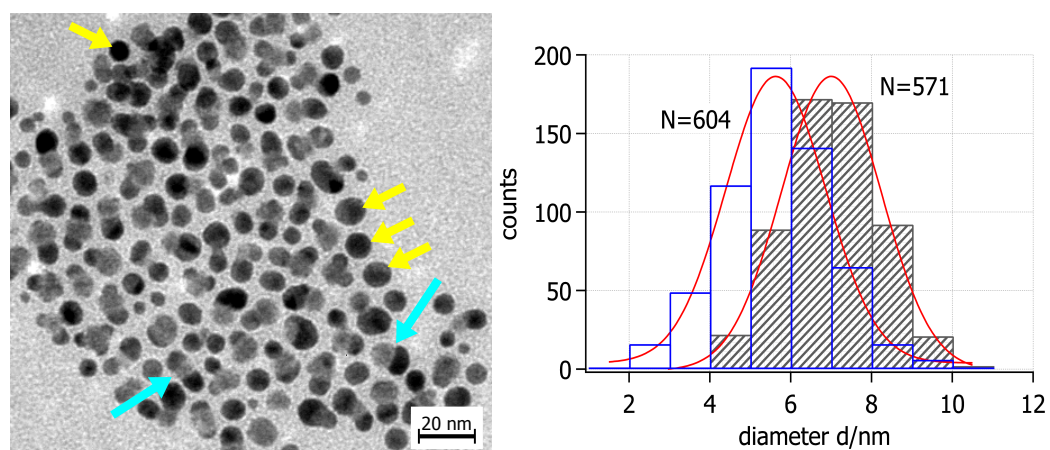
Fig. 6.23: TEM-image and size-distribution the particle batch *Bao2005dir*. The sample is taken $60\,\mathrm{min}$ after the gold-precursor is injected. $N = 571$ cobalt seed particles are evaluated for the mean diameter of $\langle d \rangle = 7.0\,\mathrm{nm} \pm 1.2\,\mathrm{nm}$, while $N = 604$ high-contrast particles are evaluated for the mean diameter $\langle d \rangle = 5.6\,\mathrm{nm} \pm 1.2\,\mathrm{nm}$. The turquoise arrows point to examples of a cap-like structures and an elongated seed particle with two high-contrast particles located at opposite ends. The yellow arrows point out high-contrast particle, which are not in contact with a seed particle.

This significant decrease in the mean diameter can be explained by the deformation of seed particles through attached high-contrast particles. Three high-contrast particles located on a single seed stretched it into a tripod (see Fig. 6.21) or two high-contrast particles located at opposite ends of a seed (see Fig. 6.23) elongate it until it loses its spherical form. The smallest diameter of these deformed particles is measured for the size distributions, which explains the drop in the mean diameter. The mean diameter of the high-contrast particles remains constant within the standard deviation and changes between 5.2 nm and 5.9 nm. Therefore the growth of the high-contrast particles seems to be completed at least 5 min after the gold precursor is injected, which corresponds to *Bao2005red*.
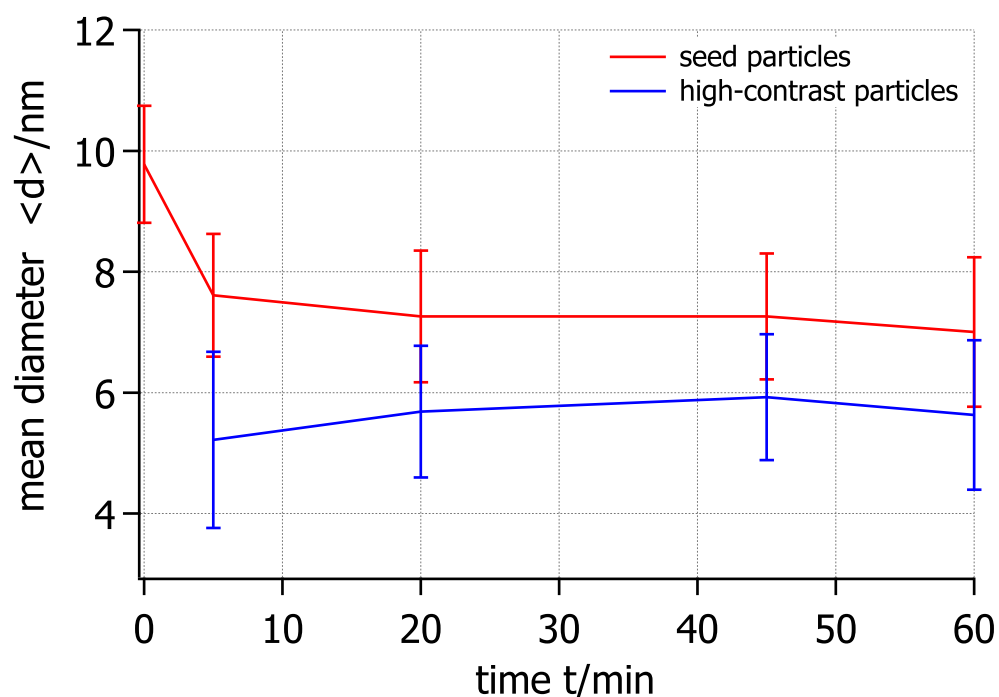
Fig. 6.24: Change in mean particle diameter for both the high-contrast (blue curve) and seed particles (red curve) through the shell synthesis step of *Bao2005dir*. The error bars represent the standard deviation of the mean diameter and the line connecting the points only serves as a guide to the eye.
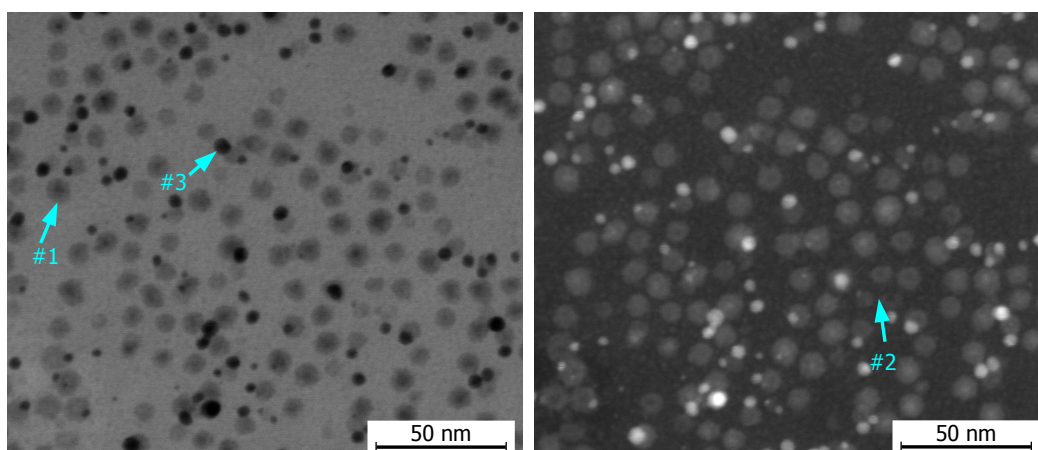
Fig. 6.25: STEM-BF- (left) and -HAADF-image (right) of the sample *Bao2005red*, taken at the end of the synthesis. Both image show the cobalt seed particle in more detail. An oxide shell formed around the cobalt core, which has an even weaker contrast than the core (arrow #1). Furthermore, seed particles, which seem to be a hollow shell can be seen (arrow #2). This is indicated by the negligible contrast of the center area of some particles. The high-contrast particles show a stronger contrast than the seed particles, although they are smaller (arrow #3). The intensified contrast for elements with high atomic numbers is very well shown in the HAADF-image.

6.4.2. STEM-imaging and EDX-analysis

The contrast in the TEM-images of the different particles provides a first insight into the element distribution within the particles. The low contrast particles are the seed-particles appearing gray in both the BF- and HAADF-image and they show a lighter oxide shell around the cobalt core (compare to Fig. 6.3). Additionally, seed particles, which appear to be a hollow shell, indicated by the vanishing contrast in the center of the particles can be seen in the STEM-images shown in Fig. 6.25. This is caused by improper protection from oxygen, first leading to an oxide shell around the cobalt core and afterwards to entirely oxidized hollow shells, which can be directly synthesized by processes reported in [103, 104]. A second kind of particle with higher contrast is formed in the suspension during the shell synthesis step. These particles appear black in the BF- and bright in the HAADF-images. The HAADF-image in Fig. 6.25 shows a high difference in contrast between the two particle types. The particles have a higher contrast in the images than the seeds, although they are of a smaller diameter. Since the contrast in the HAADF-image is element sensitive, where materials with a higher atomic number have a higher contrast it can be assumed that the newly formed particles are have a higher atomic number. The

hypothesis, that the high-contrast particles are of gold and the low-contrast seed-particles are unaffected by the synthesis and hence of cobalt needs to be further confirmed.

EDX-analysis is used to determine the composition of both particle types. An elemental mapping, as introduced in section 3.4, did not yield any usable results. The background noise prevented a successful allocation between particles and the elements present in the sample. Because the sample contains two different types of particles they are analyzed individually. Individual or small groups of particles are selected via the "reduced area selection tool" and a spectrum of the selected area is recorded. The scanned areas are shown in Fig. 6.26 and insets show the sample after the measurement. The focused electron beam melted the seed particles. The high-contrast particle is only deformed under the influence of the electron beam, while surrounding cobalt particles are melted as well.
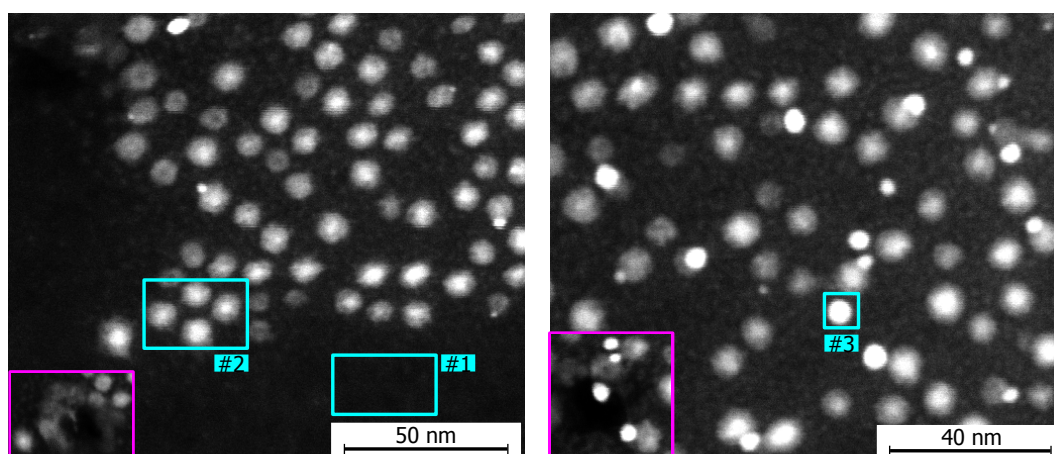
Fig. 6.26: Areas selected for EDX-analysis of the background without particles (#1), assumed pure cobalt seed particles (#2) and an isolated high-contrast particle (#3). The magenta-marked insets in both images show the areas after the EDX-scan. The low-contrast particles (left image) melt away during the scan, while the contrast-rich particle (right image) stayed intact and other near by low-contrast particles partially melt. The background-measurement taken from a particle-free area does not alter the appearance of that area.

At position #1 an EDX-spectrum of the background is recorded and displayed in Fig. 6.27. Only elements caused by the environment, like carbon and oxygen from residual air or the particles' surfactant coating, copper and silicon from the TEM-grid and aluminum from the sample chamber are found, hence the analysis of both particle types is not interfered by reaction residues, as should be the case after purifying the particle batches. The appearance of the investigated area does not visibly change after the measurement, because no particles,

which can undergo melting or deformation are present. The EDX-spectrum recorded at position #2 is shown in Fig. 6.28. It shows all peaks caused by the background and small cobalt peaks. Peaks corresponding to gold are not found in the spectrum, hence the cobalt seed particles did not incorporate gold atoms and do not form a composite. The investigated area #3 is limited to a single high-contrast particle, as shown in Fig. 6.26, with several cobalt seed particles present in the local environment. The measurement deforms the analyzed particle and partially melts the surrounding seed particles, as can be seen in the inset of Fig. 6.26, right image. The EDX-spectrum shows, besides all environmental elements, strong peaks corresponding to gold and some weaker peaks from cobalt. The electron beam affected the surrounding seed particle, which explains the detection of cobalt in the spectrum. The seed particle are not altered by the shell synthesis step, e.g. their diameter stays constant. Accordingly, it is unlikely that cobalt is incorporated into the newly formed gold-particles. The Z-contrast images show particles with homogeneous contrast and literature on alloyed cobalt-gold particles show that they appear with contrast differences in TEM- and STEM-images due to locally different compositions, see Girgis et al. [105].
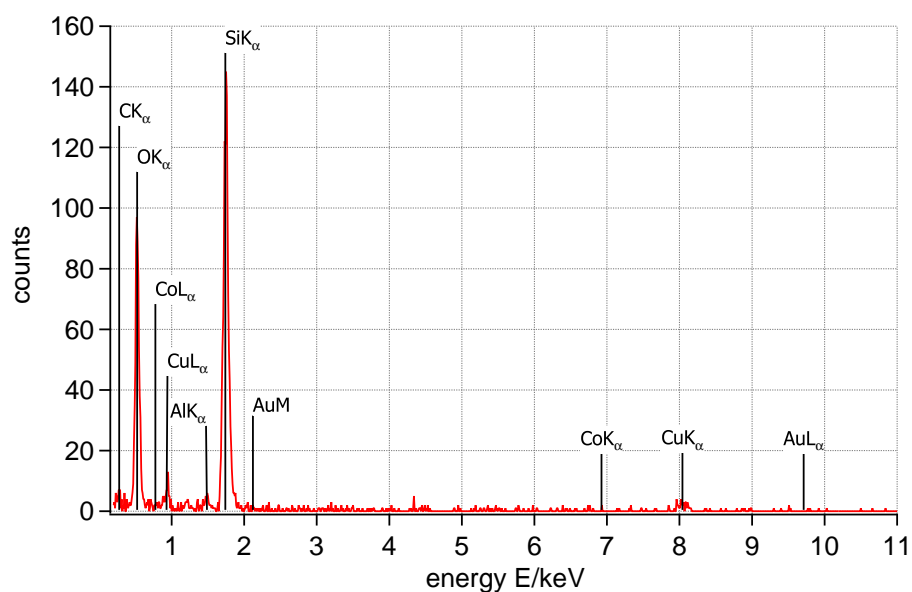
Fig. 6.27: EDX-spectrum of the position #1 marked in Fig. 6.26 from the particle batch *Bao2005red*. Only peaks from carbon and oxygen from residual air or the surfactant-coating of the particles, aluminum, from which the sample chamber and all holders are composed and copper and silicon from the TEM-grid used as substrate are found.
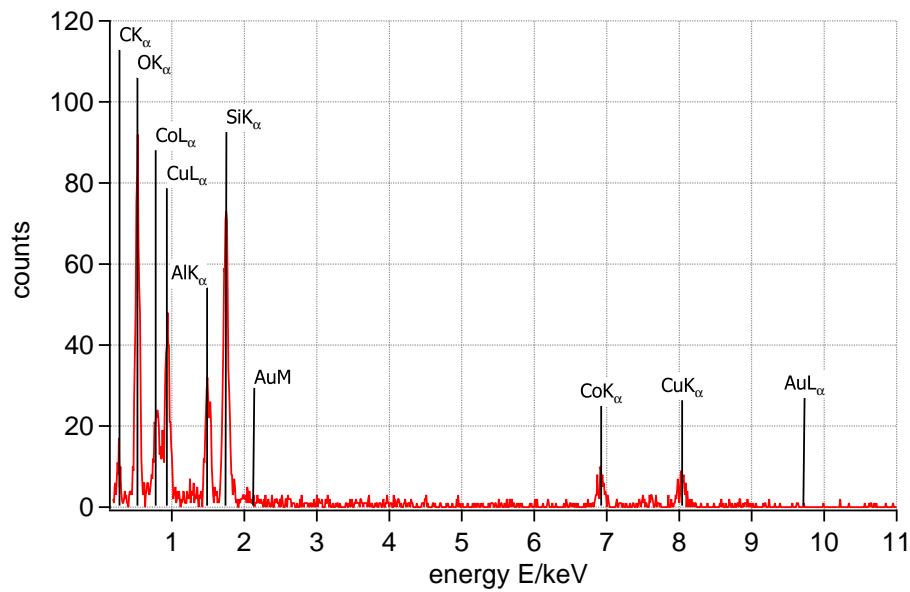
Fig. 6.28: EDX-spectrum of the position #2 marked in Fig. 6.26 from the particle batch *Bao2005red*. Only small peaks corresponding to cobalt are found besides elements present in the environment.
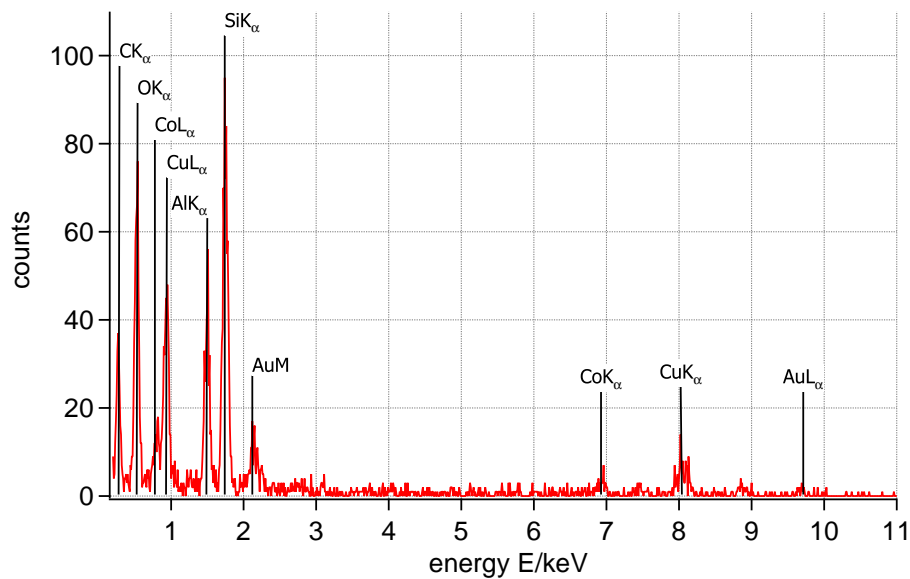
Fig. 6.29: EDX-spectrum of the position #3 marked in Fig. 6.26 of the particle batch *Bao2005red*. Besides environmental peaks strong peaks corresponding to gold are found. Also, weak peaks attributed to cobalt are found. They are caused by the surrounding and partially melted seed particles.
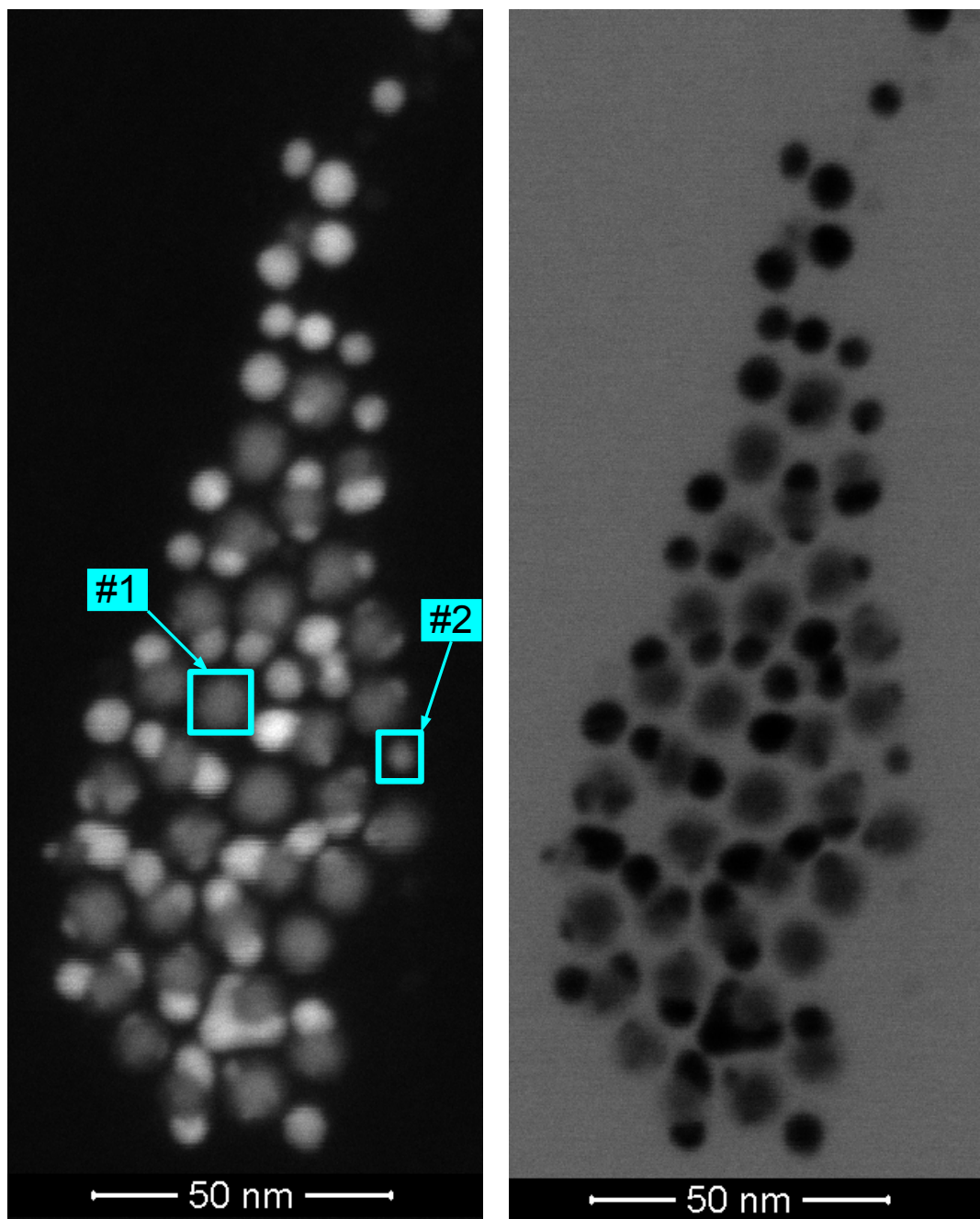
Fig. 6.30: Z-contrast image of *Bao2005dir*. High- and low-contrast particles in contact are visible as is the case for *Bao2005red*. A low-contrast particle, most likely a pure cobalt seed (#1) and a smaller particle of equal contrast (#2) are selected for EDX-analysis. The results are displayed in Fig. 6.31 and 6.32.

The second synthesis *Bao2005dir* is also investigated by EDX-analysis. The STEM-images presented in Fig. 6.30 show the same mixture of low- and high-contrast particles as seen in the images of sample *Bao2005red* before. The concentration of high-contrast particles is higher compared to the other synthesis, as is already addressed during TEM-image analysis. One low-contrast particle is selected for EDX-analysis #1 and a smaller particle with identical contrast but smaller diameter is chosen for the second analysis #2. The EDX-spectrum of the first particle shows the presence of gold and cobalt in the selected area, but only cobalt is expected for the seed particle. The additional gold signal can be attributed to neighboring gold particles, which are arranged around the seed in a circular manner. The second analyzed particle shows a high gold signal, but cobalt is also detected in the spectrum. Cobalt seeds are arranged around the particle, which explains the cobalt peaks. The assumptions for pure particles of gold or cobalt are made on the experience gained during the analysis of the particle batch *Bao2005red*. Z-contrast images on both samples appear equivalent and no composites are found.
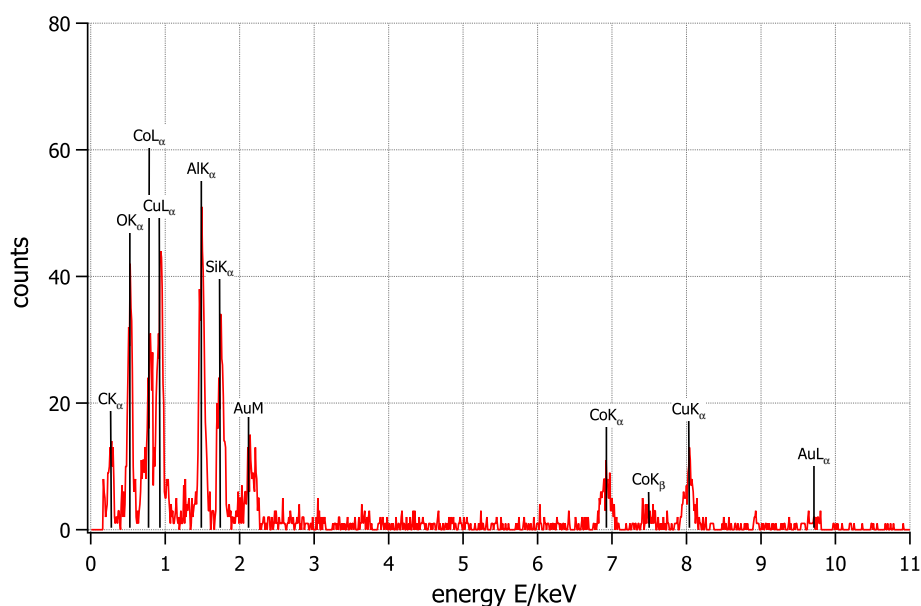
Fig. 6.31: EDX-spectrum of position #1 marked in Fig. 6.30 of the particle batch *Bao2005dir*. Cobalt and gold are both detected, the former from the seed particle and the latter through neighboring gold deposits.
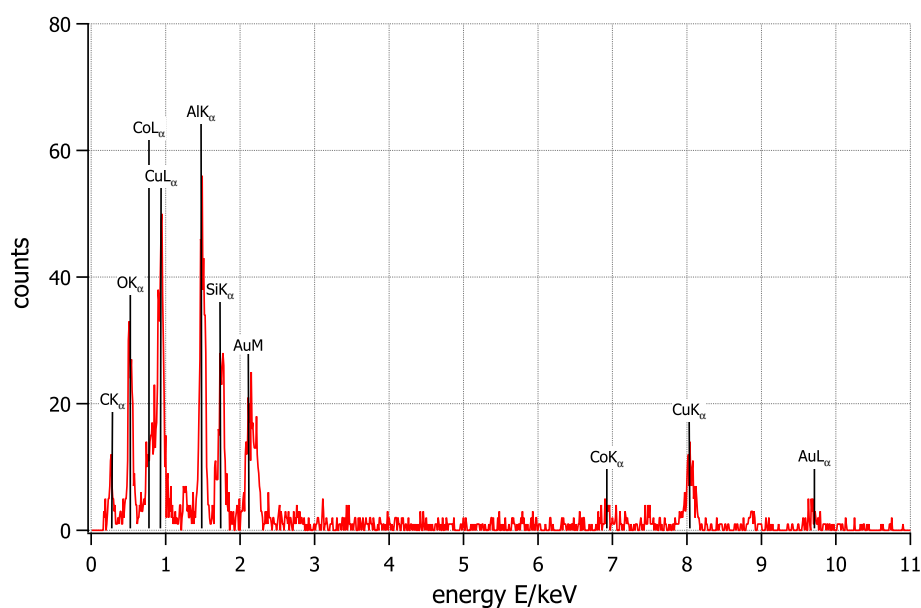
Fig. 6.32: EDX-spectrum of position #2 marked in Fig. 6.30 of the particle batch *Bao2005dir* shows a strong gold-signal, but also traces of cobalt, which can be explained by cobalt seed particles around the isolated gold particle.

The formation of individual interconnected nanoparticles of pristine materials can be reported. The elemental composition has been investigated and the high-contrast particles consist of gold, while the low contrast cobalt seed particles have not change their initial composition of pure cobalt. The results show, that the cobalt seeds of both syntheses *Bao2005red* and *Bao2005dir* provide nucleation sites for heterogeneous nucleated gold particles. The seed particles of the synthesis *Bao2005dir* are more densely covered with gold deposits, than the seed particles of the synthesis *Bao2005red*. This is due to the different amount of seed particles used in the syntheses and how this takes an influence on the resulting bimetallic particles is discussed in the next section, which primarily addresses the question why the shell synthesis is unsuccessful.

6.5. Heterogeneous nucleation on seed particles

The TEM- and STEM-images of both syntheses presented earlier clearly show, that the cobalt seed particles serve as nucleation centers, but they are not entirely surrounded by a gold shell. Furthermore, a single seed particle can serve as nucleation center for several gold particles. Partial encasing of the

cobalt seeds by one or more gold particles has been observed, as well as the deformation of seed particles by attached gold particles (see Fig. 6.20 to 6.23, highlighted by turquoise arrows). In case of the synthesis *Bao2005red* all gold particles are in contact with a cobalt seed, with a small interface area. The gold particles grow from the cobalt surface and form spheres, hence the contact area is minimized. The gold particles cover more of the seeds in case of the synthesis *Bao2005dir*, but the cobalt seed particles are not entirely covered either. The gold particles form mostly spheres, but caps covering one third of a seed are also found. The different coverage rates between the syntheses *Bao2005red* and *Bao2005dir* can be explained by the different amounts of seed particles used during the respective shell synthesis step. Half of the seed particle suspension (seeds from 4 mL seed particle suspension) produced through the first reaction step is used in case of *Bao2005red*, thus many particles providing nucleation sites are present during the reaction. The synthesis *Bao2005dir* only uses cobalt particles from 0.5 mL of the seed particle suspension using an initial total solvent volume of 15 mL and therefore fewer seed particles are used. The reduced number of seed particles also reduces the amount of possible heterogeneous nucleation sites. The same amount of gold precursor is used in both syntheses, but is distributed between fewer nucleation sites in case of *Bao2005dir* than it is in case of *Bao2005red*. This explains the denser coverage with gold particles in case of *Bao2005dir*, because of the reduced number of possible nucleation sites. In addition the gold particles of *Bao2005dir* are larger in comparison to the gold particles of *Bao2005red*, as observed in the TEM-images and size distributions. The gold particles of the synthesis *Bao2005red* have a mean diameter around 4 nm and are therefore smaller than the gold particles of *Bao2005dir*, with a mean diameter around 6 nm. An increase in the amount of gold monomers per seed particle into the suspension should, according to the theory, lead to completely covered seed particles. However, a different behavior can be observed in the TEM-images of sample *Bao2005dir*. Several gold particles exist, which have not nucleated at the surface of a seed particle. These gold particles with diameters around 10 nm are highlighted in Fig. 6.20 to 6.23 with yellow arrows. It is unlikely, that these particles nucleated heterogeneously on the seed particles and afterwards detached from the cobalt surface. The heterogeneous nucleation decreases the energy necessary to form the gold particles in comparison to homogeneous nucleation. Relinquishing the interface between the materials afterwards is energetically unfavorable, because this increases the surface area of both particles and would lead to the formation of new interfaces between the solid gold and cobalt and the surrounding liquid medium. This leaves only the possibility of a homogeneous nucleation event happening at the same time

as the heterogeneous nucleation. When the gold precursor is added to the reaction mixture, heterogeneous nucleation instantaneously begins to decrease the oversaturation S. An additional homogeneous nucleation process occurs, if the oversaturation remains above the homogeneous nucleation limit $S > S_C$ after all heterogeneous nucleation sites are saturated (compare to section 2.1.1). This processes are illustrated in Fig. 6.33. The fact, that the shell synthesis step allow the homogeneous nucleation of gold particles is shown in the control experiment *Bao2005-gold* (see section 6.3). Heterogeneous nucleation does not consume as many monomers as does homogeneous nucleation at the beginning, because the heterogeneous nuclei are already present and do not need to be formed by consuming monomers. The results suggest that, increasing the amount of gold precursor will lead to the formation of more isolated gold particles instead of a complete coverage of the seed particles. The TEM-images showing the interconnected particles (see Fig. 6.15 to 6.18 and 6.20 to 6.23) show, that the gold particles only attach at some areas on the seed particle, raising the question why single areas of a seed particle get in contact with the gold and allow a heterogeneous nucleation, while other areas are not suited for the deposition of gold? A possible explanation of this observed effect concerns the interfacial energies between cobalt and gold and is discussed in the next section.
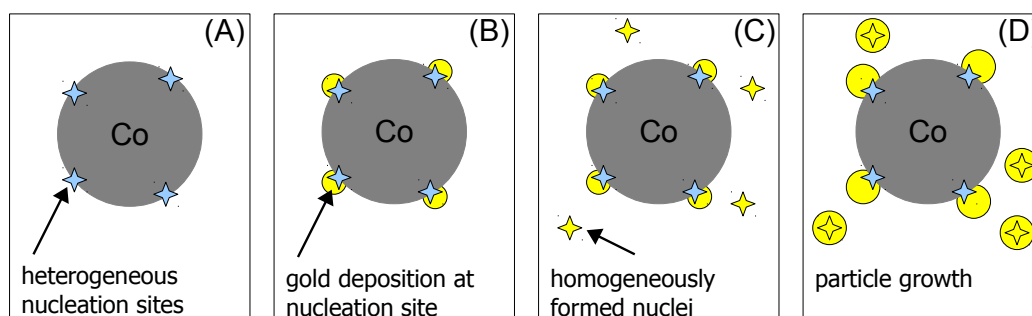
Fig. 6.33: Schematic of a dual nucleation event for gold monomers in presence of cobalt seed particles. (A) The cobalt seed particles in the reaction mixture provide suitable nucleation sites for a heterogeneous nucleation. (B) If gold monomers are added, they are deposited at the nucleation sites and grow into particles connected with the seeds. (C) If the concentration of gold monomers in the solution still exceeds the homogeneous nucleation limit $S > S_C$ after the gold deposits on the seed particles start to grow, then new homogeneous gold nuclei are produced. (D) Gold nanoparticles grow interconnected with the seed particles or isolated in solution depending on the nucleus.

Considerations based on interfacial energies

All images of the bimetallic particles from particle batches *Bao2005red* and *Bao2005dir* show gold particles, which are deposited on the cobalt seed particles. The gold particles are in contact with the seeds, but do not cover them completely, which indicates a partial affinity of the gold to the cobalt surface (compare to Fig. 2.6). The gold particles always have a contact angle between 0° and 180°. In the further course of this thesis the term **interfacial energy** is used for the free surface energy of two different crystals in contact, while the term **surface energy** refers to a bare surface. The surface and interfacial energies are the predominate influenced in a nanoparticular system and regarding the investigated nanoparticle syntheses of *Bao2005red* and *Bao2005dir* the total energy of both systems is best minimized by the formation of heterodimeric particles, instead of the intended core-shell type. The formation of a core-shell particle needs a contact angle equal to $\Theta = 0°$ between the core material and deposit forming the shell, which simplifies (**eq.** 2.8) to

$$\gamma_{\ell,1} = \gamma_{2,1} + \gamma_{2,\ell} \ . \qquad \qquad \textbf{(eq. 6.1)}$$

The result of (**eq.** 6.1) shows, that the interface between two crystalline phases with the interfacial energy $\gamma_{2,1}$ and the interface energy $\gamma_{2,\ell}$ between the deposited phase and the surrounding liquid need to be completed with the initial interfacial energy $\gamma_{\ell,1}$ between the seed particle and the surrounding liquid medium[6]. This requirement must be met for the formation of a core-shell type particle. To determine promising material combinations for core-shell type particles, the interfacial energies γ between all participating phases must be known. There are reports in literature on measured and calculated surface energies for different materials in their own liquid environment or vacuum (see Vitos et al. [106], W.R. Tyson and W.A. Miller [107], Vinet et al. [108]). However values for interfacial energies between two solid crystallite phases have not yet been reported.

In addition to the lack of literature reports for the interfacial energies, the proposed model does not consider curved nucleation sites. The crystal phase providing the nucleation sites for the deposited material is assumed to be planar in the model (compare Fig. 2.4), however nanoparticles serving as nucleation sites posses heavily curved surfaces. Their surface energy is dependent on the

---

[6]In this special case $\gamma_{2,1}$ describes the interfacial energy between the cobalt seeds and the gold particles, $\gamma_{\ell,1}$ between the cobalt seeds and the surrounding reaction solution and $\gamma_{2,\ell}$ between the gold particles and the reaction solution.

curvature and therefore the particle diameter, which also affects the interfacial energy. The diameter dependence of the surface energies is studied in [109–114] and it can be assumed that a diameter dependence of the interfacial energies also exists. Hence, it is not possible to derive a quantitative explanation on why the syntheses for cobalt-gold core-shell type particles failed. Qualitatively, the interfacial energy $\gamma_{\ell,1}$ between the core material and the surrounding liquid must accommodate the interfacial energies between the core and shell material $\gamma_{2,1}$ and between the shell and the surrounding liquid $\gamma_{2,\ell}$ to allow the formation of a core-shell particle. Therefore the core-liquid interface must have a rather high interfacial energy, while the interfaces occurring in the core-shell particles need low interfacial energies to accommodate the formation of a core-shell structure. Otherwise the system's energy is not minimized by forming core-shell particles.

Considerations on interface appearances

A better understanding of why core-shell type particles are not formed can be obtained by looking at the interface between seed particle and deposit. Porter et al. [40] gives a comprehensive summary on possible occurring interfaces between two different crystal phases, where the atom lattices of both materials meet.

The interface with lowest interfacial energy is a coherent one as depicted in Fig. 6.35. The interplanar atomic spacings of adjacent lattice planes on both sides of the interface match and the atomic configurations of both faces is identical. An example for the atomic configuration for the most dense planes occurring in fcc-lattices gives Fig. 6.34. The atomic configuration of the fcc
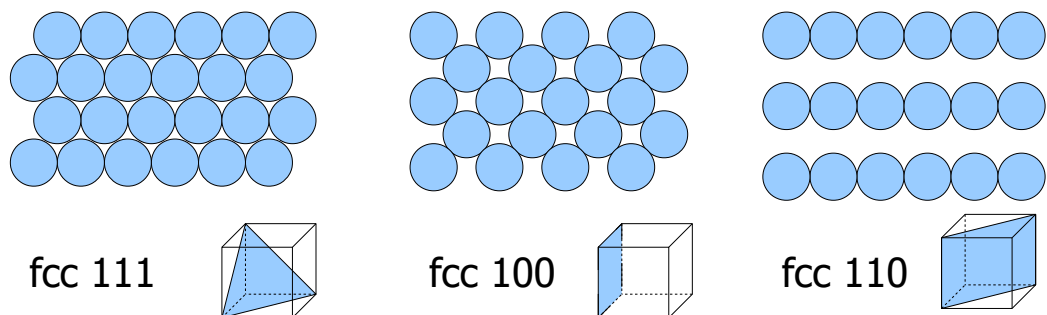
Fig. 6.34: Atomic configurations of the most dense lattice planes and their orientation of an fcc unit cell. The fcc {111} plane shows a hexagonal, the fcc {100} plane the expected face centered cubic and the fcc {110} plane a linear arrangement of the atoms [40].
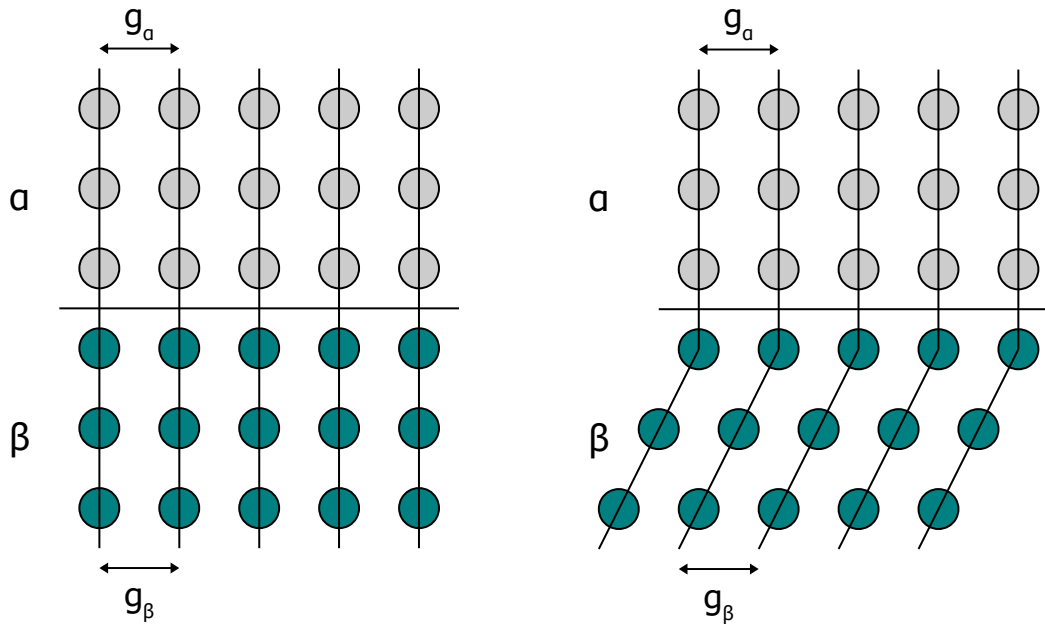
Fig. 6.35: Coherent interfaces. If the atomic configuration of a certain plane and the interatomical distances $g_{\alpha/\beta}$ of two different crystal phases α and β are identical a fully coherent interface is established between the phases. If the atomic distances do not fully correspond a coherent interface can still be maintained by straining the crystal lattice of one or both phases. The formed coherency strains add to the interfacial energy [40].

{111} planes is of hexagonal order, while the {100} shows the expected face centered cubic arrangement and the {110} shows a linear order. The only contribution to the interfacial energy arises for a fully coherent interface through the different chemical species α and β on both sides of the interface

$$\gamma\,(\text{coherent}) = \gamma_{\text{chemical}} = 1\,\frac{\text{mJ}}{\text{m}^2}\ \text{to}\ 200\,\frac{\text{mJ}}{\text{m}^2}\quad . \qquad (\textbf{eq. 6.2})$$

A coherent interface can still be maintained, if the interplanar spacings of the two phases differ a little. Coherency strains on one or both sides of the interface are formed and the lattice is distorted. This adds to the interfacial energy.

If the interface area or the misfit η between both phases exceeds a certain value it is energetically more favorable to form a semi-coherent interface with periodical dislocations along the interface instead of coherency strains. This case is depicted on Fig. 6.36. The misfit η between the lattice planes of equal atomic configuration at the interface can be calculated by

$$\eta = \frac{g_\beta - g_\alpha}{g_\alpha}\quad , \qquad (\textbf{eq. 6.3})$$
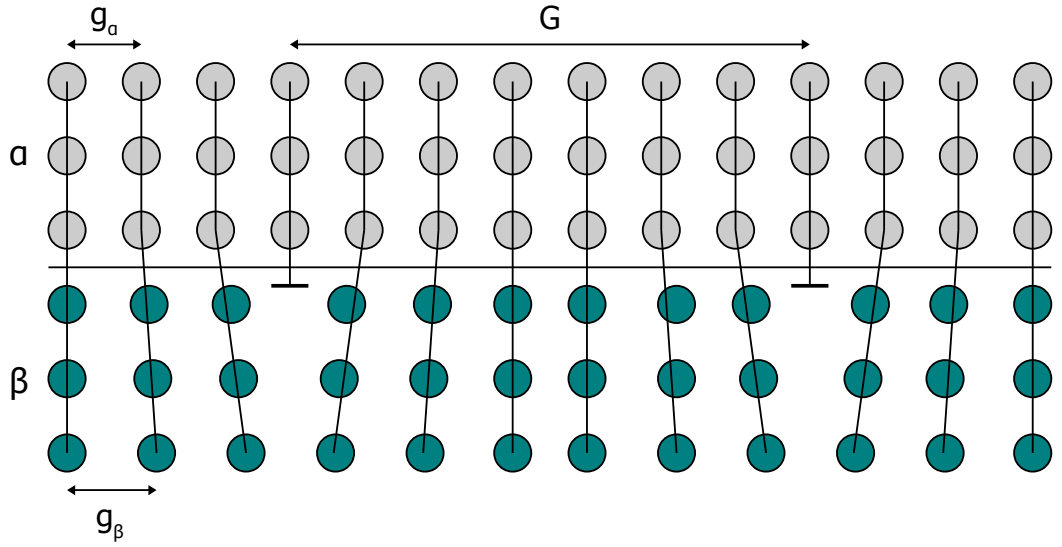
Fig. 6.36: Semi-coherent interface between the different phases α and β with different interatomical distances g_α and g_β. Periodical dislocations with distance G relieve coherency strains along the interface. Except for the dislocations, where one or both lattices are heavily disordered an almost coherent interface can be formed [40].

for $g_{\alpha,\beta}$ the respective unstressed interplanar lattice spacings. The dislocations limited to one of the phases for a one dimensional lattice misfit are separated by the distance $G = \frac{g_\beta}{\eta}$. The interfacial energy is in this case increased by a contribution from the misfit dislocations, which is dependent on the mismatch η, if it is small enough

$$\gamma\,(\text{semi-coherent}) = \gamma_{\text{chemical}} + \gamma_{\text{missfit}} = 200\,\frac{\text{mJ}}{\text{m}^2}\ \text{to}\ 500\,\frac{\text{mJ}}{\text{m}^2}\ .\quad (\textbf{eq. }6.4)$$

If the atomic configurations of two adjacent phases do not match or their misfit exceeds $\eta > 0.25$[7] an incoherent interface results, which has a higher interfacial energy

$$\gamma\,(\text{incoherent}) = 500\,\frac{\text{mJ}}{\text{m}^2}\ \text{to}\ 1000\,\frac{\text{mJ}}{\text{m}^2}\ ,\quad\quad\quad (\textbf{eq. }6.5)$$

that is not dependent on the orientation of the two joined crystal planes. The atomic appearance of an incoherent interface is hardly known, but is believe to lack the long range order of (semi-)coherent interfaces [40].

---

[7]The planes next to the dislocation shown in Fig. 6.36 are distorted. A misfit equal to $\eta > 0.25$ means a dislocation every four interplanar spacings, which leads to overlapping regions of poor fit around the dislocations.

Both crystal phases in the bimetallic heterodimeric particles are of an fcc configuration. The lattice parameters of gold and fcc-cobalt are $g_{Au} = 407.8$ pm and $g_{fcc\text{-}Co} = 354.4$ pm and have a misfit of

$$\eta_{fcc\text{-}Au,fcc\text{-}Co} = \frac{407.8 \,\text{pm} - 354.4 \,\text{pm}}{354.4 \,\text{pm}} = 0.15 \qquad (\textbf{eq. 6.6})$$

therefore semi-coherent interfaces can be formed between fcc-cobalt and fcc-gold. The atomic configurations between corresponding lattice planes are identical, but the different lattice parameters lead to different atomic spacings and hence interfaces of the lowest energy cannot be formed. Accommodating the interfacial energy of semi-coherent interface can make the formation of large interface areas energetically unfavorable and so the interface is limited to small parts of the seed particles, as has been observed for both syntheses *Bao2005red* and *Bao2005dir*. The contact-angle between the cobalt surface and the gold deposits is therefore $\theta > 0°$. This decreases, according to (**eq. 2.8**) the interfacial energy $\gamma_{2,\ell}$ between the deposit and the reaction solution and therefore makes the interface formation between the gold deposits and the cobalt seeds possible. The formation of core-shell type particles between fcc-cobalt and fcc-gold is therefore not expected and not found.

The original synthesis by Bao et al. [31] 2005 has been reported to produce ϵ-cobalt seed particles, instead of fcc-cobalt. Whether the ϵ-cobalt structure can be linked to the successful formation of core-shell type particles, as observed in the synthesis of Bao et al. [31], can be determined by the interfacial energies and is discussed in the next paragraph.

ϵ-cobalt has a more complex unit cell than an fcc-crystal with a larger lattice parameter $g_{\epsilon\text{-}Co} = 609.7$ pm. The misfit between ϵ-cobalt and fcc-gold for unstrained lattices is determined to

$$\eta_{\epsilon\text{-}Co,fcc\text{-}Au} = \frac{609.7 \,\text{pm} - 407.8 \,\text{pm}}{407.8 \,\text{pm}} = 0.5 \quad, \qquad (\textbf{eq. 6.7})$$

which only allows the formation of incoherent interfaces. Furthermore, the atoms in the unit cell are arranged less symmetrical than in an fcc unit cell, as shown in Fig. 5.1. The atoms' positions lead to unsymmetrical atomic configurations for all lattice planes in the ϵ-cobalt crystal. Fig. 6.37 shows the ϵ-cobalt unit cell sliced along the (200), (220) and (111) planes to show the atomic configurations of the respective plane. The atoms' arrangement for the planes in case of ϵ-cobalt lack the symmetry and order of the atomic configurations of fcc-cobalt. These facts contradict, that interfaces with lower interfacial energy are formed between ϵ-cobalt and fcc-gold than are formed

between fcc-cobalt and fcc-gold. Therefore, the formation of core-shell type particles with an ϵ-cobalt core is as unlikely as it is for an fcc-cobalt core. The ϵ-cobalt structure cannot be linked to the successful formation of cobalt-gold core-shell type particles.

An example for the successful synthesis of core-shell type particles is given by Yang et al. [29]. They showed the formation of silver-gold core-shell nanoparticles in TEM-images and supported their findings with elemental sensitive analyses. The successful formation of a core-shell structure between silver ($g_{Ag} = 408.53 \, \text{pm}$) and gold ($g_{Au} = 407.82 \, \text{pm}$) is not unexpected, since the lattice parameters of both materials are almost the same and they both crystallize in an fcc-lattice. Hence, the formation of large interfaces with low interfacial energy is possible, which would also allows the formation of core-shell structures.
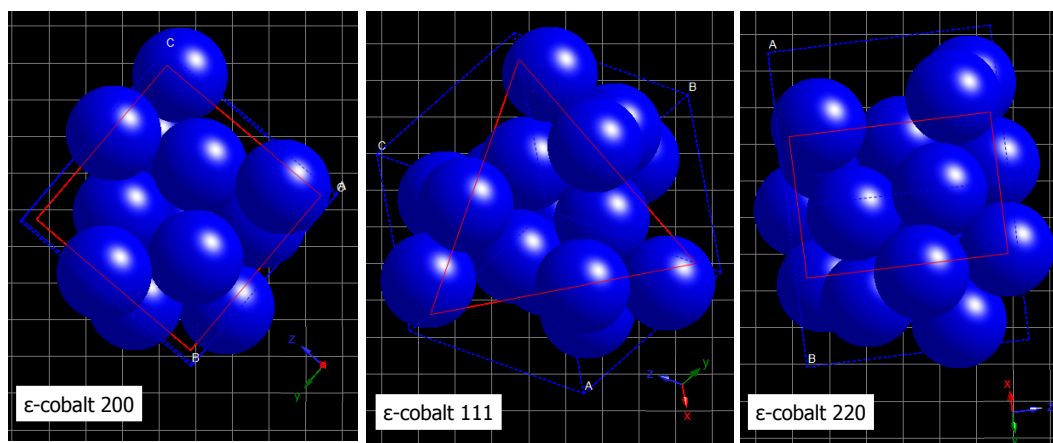
Fig. 6.37: Ball-and-stick model of the ϵ-cobalt unit cell generated by *CrystalMaker*™. The model is sliced along the (200)-, (111)- and (220)-plane to allow a view on the atomic configuration of the respective plane.

6.6. Conclusion

The bimetallic nanoparticles, which are synthesized through a reproduced synthesis approach reported by Bao et al. [31] 2005, are not core-shell type particles. Instead, heterodimeric particles consisting of interconnected cobalt and gold particles have been obtained. Two syntheses, *Bao2005red* and *Bao2005dir* are executed with different amounts of solvent. The first synthesis step produces seed particles, which have a mean diameter of 8.3 nm in case of *Bao2005red* and 9.8 nm in case of *Bao2005dir*. The interparticle distance is dominated by

oleic acid present on the seed particles surface in case of both syntheses. DOA is most likely not present on the seed particles surface, because of its weaker binding affinity. However, its role during the synthesis is not yet determined. The cobalt seed particles behave superparamagnetically at room temperature. The nanoparticles' crystal structure is determined to fcc for both syntheses *Bao2005red* and *Bao2005dir*. The publication both syntheses are based on, however reports the formation of ϵ-cobalt particles. The reactants are therefore not determining the crystal structure of the cobalt nanoparticles. The cobalt seed particles serve as heterogeneous nucleation centers during the shell synthesis step. The seeds are covered with gold particles emanating from the cobalt surface, but the gold does not form a closed shell. These results are found for both syntheses *Bao2005red* and *Bao2005dir*. Both syntheses differ in the amount of seed particles used during the shell synthesis step. In case of *Bao2005red* cobalt particles precipitated from 4 mL of the seed particle suspension are used, while the synthesis *Bao2005dir* with a larger initial solvent volume only uses seeds from 0.5 mL. The seed particles of *Bao2005red* are only in contact with single gold particles, whereas the seed particles of *Bao2005dir* are covered with more gold nanoparticles, partly deforming the seeds. Furthermore, isolated gold particles, which are not in contact with a cobalt seed are found in the synthesis *Bao2005dir*. This indicates, that the available nucleation sites on the seed particles are saturated with monomers and the remaining oversaturation of gold monomers causes a homogeneous nucleation event, forming the independent gold particles. The reaction mixture of the shell synthesis step is able to homogeneously nucleate gold nanoparticles, as has been shown in the control experiment *Bao2005-gold*. Therefore, increasing the amount of gold monomers in the reaction solution does not complete the coverage of the seed particles, but only forms additional gold nanoparticles. A closer look at the TEM-images provided in the original report by Bao et al. [31], depicted in Fig. 4.2 indicates that, there are only single bimetallic particles found, which look like core-shell particles. In addition, heterodimeric particles, as have been observed during the syntheses *Bao2005red* and *Bao2005dir* and seed particles, which are not in contact with any gold particles are also visible. This leaves doubt about the correct interpretation of the analysis results. The cobalt gold interface is investigated to find an explanation, why core-shell type particles do not form. Fcc-cobalt and gold are able to form semi-coherent interfaces, which is not a low energy interface. The heterogeneous nucleation needs to overcome a smaller energy barrier than homogeneous nucleation, because heterogeneous nucleation sites provided by the cobalt seed particles are used as nuclei. However, the formation of interfaces between gold and cobalt increases the energy of the system. This limits the interface areas to small parts of a seed particle and

results in gold deposits, which have a contact angle $\theta > 0°$ against the seed particles surface. The requirement stated by (**eq.** 6.1) cannot be fulfilled, because the interfacial energy $\gamma_{2,\ell}$ between the deposits and seed particles needs to be reduced to make the interface formation possible. All these consideration completely neglect how the used surfactants and solvents affect the syntheses. It is mostly unknown, how they influence the results of the syntheses.

Literature is checked for a successful reproduction of the synthesis by Bao et al. [31], 2005, because no core-shell type particles have been yielded. The report Bao et al. [31] is cited 41-times[8] and while most of these publications [32, 50, 115–131] quoted Bao et al. [31] as an example for the synthesis of cobalt nanoparticles and their magnetic properties and the possibility and advantages of core-shell type particles structure, only two of all reports are concerned with the synthesis of cobalt-gold core-shell type particles, Johnson et al. [132], 2010 and Mandal and Krishnan [133], 2007. Both articles only report a modified synthesis process. Johnson et al. [132] conducted the core-particle synthesis in pure trioctylamine (TOA) in the presence of oleic acid instead of using ODCB containing both surfactants. The final particle analysis does not include element sensitive analyses. TEM-images are presented, which show particles with a barely perceptible core of lower contrast. The magnification of the image is too low, to see any details. HRTEM-image are given to show moire patterns caused by the superimposition of the gold and cobalt crystal lattice, however which are not visible in the images. Mandal and Krishnan [133] use a different surfactant (TOPO) and another gold source, but conducted the synthesis otherwise similar to Bao et al. [31]. During the shell synthesis step a replacement reaction between cobalt surface atoms of the seeds and gold atoms from solution is assumed. TEM-images of the nanoparticles show a core-shell structure, but the particles have a low-contrast shell surrounding a core with slightly more contrast. According to basic TEM-image formation theory and as has been shown during TEM- and STEM-imaging gold causes high-contrast features in a TEM-images compared to cobalt. The contrast differences indicate, that the shell consists of a lighter material than the core. A more likely explanation for the contrast differences is surface oxidation of the cobalt particles, as has been also seen in Fig. 6.2. Element sensitive analyses able to determine the composition of the particles correctly are not conducted. In both cases the analyses of the assumed bimetallic particles does not prove, that core-shell type particles are formed.

---

[8]Google Scholar, November 2013

Hence, considering the above mentioned publications, there are no literature reports on a successful reproduction of the synthesis by Bao et al. [31] 2005. A definite production of cobalt gold core-shell type particles can neither be found in literature nor in the reproduced syntheses. The considerations on interfacial energies and the interface appearance contradict the successful formation of core-shell type particles. The TEM-images given in the original publication do not show the core-shell structure of the particles, either.

7. Results and discussion of the nanoparticle synthesis following instructions of Bao et al. 2007

The results of a second synthesis approach to produce cobalt-gold core-shell nanoparticles reported by Bao et al. [32] 2007 are presented. The nanoparticle synthesis is similar to previously investigated synthesis. Thermal decomposition is used to synthesized cobalt seed particles, which are employed as heterogeneous nucleation sites in the second reaction step to synthesize the gold shell. Details on the author's methods and particle analyses are given in section 4.2. The recipe of the reproduced synthesis is explained in the next section. A detailed analysis of the cobalt seed particles produced through the first reaction step is discussed afterwards. A control experiment showing if the reaction mixture of the shell synthesis step is able to homogeneously nucleate gold particles is described. The final bimetallic particles synthesized afterwards by the shell synthesis step are analyzed and all results are discussed in the last part of this chapter.

7.1. Adaption of the synthesis

The synthesis published by Bao et al. [32] in 2007 lacks the same specifications as the previously investigated synthesis Bao et al. [31], 2005. All volumes are noted, but the amount of boiling solvent, to which the cobalt precursor solution is added during synthesis of the seed particles is not given. Again, two different syntheses are carried out, one with a solvent volume of $5\,\mathrm{mL}$ called *Bao2007red* and the other synthesis with a solvent volume of $12\,\mathrm{mL}$ called *Bao2007dir*. They are performed on the basis of Puntes et al. [97] approach (*Bao2007dir*) and an approach with handable solvent volumes (*Bao2007red*). During the synthesis of the cobalt seed particles tri-octylamine (TOA) is used as the second surfactant besides oleic acid. It substitutes the same amount of DOA, which is

used during the syntheses adapted from Bao et al. [31] in 2005. In the shell synthesis step the double amount, 0.5 mL of oleylamine are used, compared to the amount use during the syntheses *Bao2005red* and *Bao2005dir*.

The amount of seed particles used for the shell-synthesis step is given with 2 mg [1]. The shell synthesis step of *Bao2007red* is done with seed particles precipitated from 4 mL of the seed particle suspension. After purification the cobalt seeds are redispersed in 5 mL toluene and afterwards heated up to reflux temperature for the shell synthesis. Less seed particle are used during the synthesis *Bao2007dir*. 0.5 mL of the seed particle suspension are dried after purification in an eppendorf tube, which yields approximately 10 mg of dried cobalt seeds. They are redispersed in 5 mL toluene and used for the shell synthesis step.

The general annotations on the experimental details made in section 6.1 apply to these syntheses, as well including temperature measurements and the preparation of chemicals and laboratory equipment. The final recipes for *Bao2007red* and *Bao2007dir* are given in the following paragraph.

- 0.34 mL tri-octylamine (TOA) and 0.2 mL oleic acid are added to 5 mL (*Bao2007red*) or 12 mL (*Bao2007dir*) of ODCB. The mixture is heated to 190 °C.

- The cobalt precursor solution consisting of 0.54 g dicobalt octacarbonyl ($Co_2(CO)_8$) is solvated in 3 mL ODCB and is quickly injected into the boiling solvent-surfactant mixture.

- The reaction solution is kept at reflux temperature for 15 min and given subsequently 30 min time to cool down to room-temperature. Afterwards the particle suspensions are cleaned by precipitation.

- In case of *Bao2007dir* 0.5 mL of seed particles suspension in ODCB is precipitated, yielding approximately 10 mg cobalt seeds. They are redispersed in 5 mL of toluene for the second reaction step. In case of *Bao2007red* particles precipitated from 4 ml of the seed particle suspension are used and redispersed in 5 mL toluene.

- The toluene solution containing the cobalt seed particles is heated to 85 °C by a silicon oil bath and stirred at 750 rpm with a magnetic stirrer.

- The gold precursor solution containing 0.01 g chloro (triphenylphosphine) gold(I) ($[(C_6H_5)_3P][AuCl]$) and 0.5 mL oleylamine solvated in

---

[1]A small error for the extracted mass is expected, because the dryed seed nanoparticles form a thick oily residue, making an exact extraction difficult.

3 mL toluene is injected at once and the mixture is kept at 85 °C for one
hour and subsequently given time to cool down.

- Samples of 100 µL are collected from the reaction mixture after 5 min,
  20 min, 45 min and 60 min to monitor the shell development.

The shell synthesis step is again further investigated individually to determine,
if the reaction mixture is able to homogeneously nucleate gold particles. This
synthesis is referred to as *Bao2007-gold* and is carried out equivalently to
Bao2005-gold.

7.2. Cobalt seed particles

The cobalt seed particles of both syntheses *Bao2007red* and *Bao2007dir* are
analyzed by TEM-imaging and the mean diameter and mean interparticle
distance are determined statistically. Subsequent, the crystal structure of the
seed particles is investigated by XRD-measurements and HRTEM-imaging.
Finally, their magnetic properties are determined via AGM-measurements and
the characteristics of the curves compared to calculated magnetization curves.

7.2.1. TEM-imaging
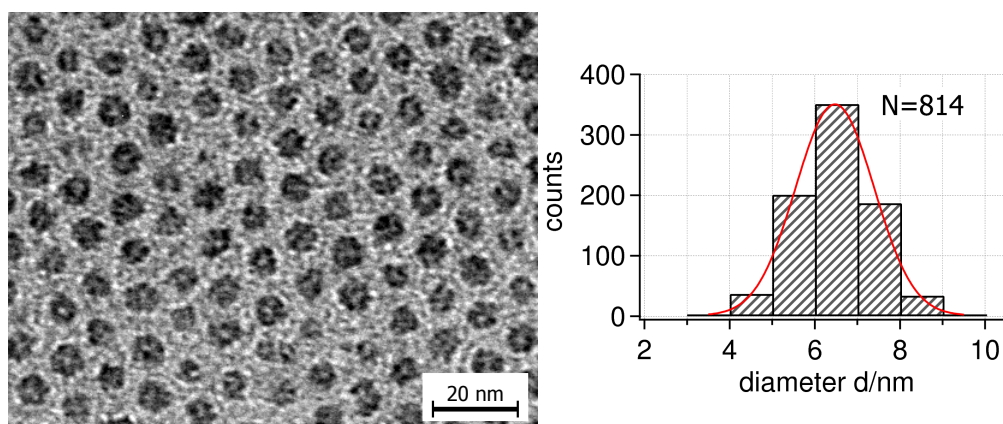
Fig. 7.1: TEM-image and size-distribution of the cobalt seed-particles obtained by the synthesis
Bao2007red. The particles' mean diameter is $\langle d \rangle = 6.5\,\text{nm} \pm 0.9\,\text{nm}$. A total number of $N = 814$
particles are measured. The red curve represents the gaussian fit of the histogram.
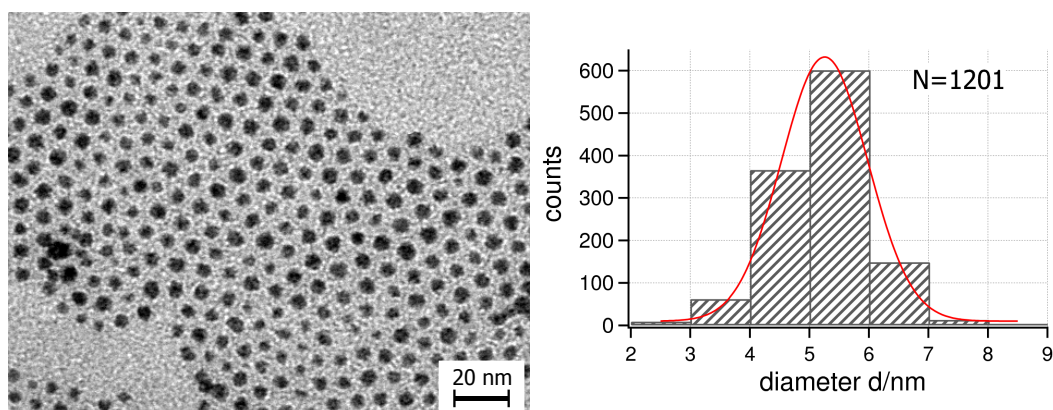
Fig. 7.2: TEM-image and size-distribution of the cobalt seed-particles obtained by the synthesis *Bao2007dir*. The particle's mean diameter is $\langle d \rangle = 5.3\,\text{nm} \pm 0.75\,\text{nm}$. A total number of $N = 1201$ particles are measured. The red curve represents the gaussian fit of the histogram.

The synthesis *Bao2007red* yields spherical nanoparticles with a mean diameter of $\langle d \rangle = 6.5\,\text{nm} \pm 0.9\,\text{nm}$, which corresponds to a standard deviation of $14\,\%$. A TEM-image and the size-distribution are shown in Fig. 7.1. The particles align in a monolayer with hexagonal order and cover areas of several µm^2. The formation of undisturbed, large-area monolayers with a distinct hexagonal order is only possible if all particles are of similar sizes [44] as is the case for a narrow size distribution. The synthesis *Bao2007dir* yields smaller particles with a mean diameter of $\langle d \rangle = 5.3\,\text{nm} \pm 0.75\,\text{nm}$, depicted in Fig. 7.2. The batch has a narrow size-distribution, too, with $\sigma = 14\,\%$ and forms a hexagonal ordered monolayer.

The order is not as perfect as in the case of *Bao2007red*, but is disturbed by particles with smaller or bigger diameters. The areas of highly ordered particle monolayers are smaller (only a few hundred nanometer squared), than in case of the adapted synthesis *Bao2007red*. Both mean diameters correspond well with the diameter of 6 nm given by Bao et al. [32], 2007. The values deviate less than the first confidence interval from the reported mean diameter and both size-distributions are overlapping. The different amounts of solvent used for the syntheses *Bao2007red* and *Bao2007dir* have an influence on the synthesis and alter the reaction conditions, but the ratio between metallic precursor and surfactants remains unchanged. This ratio is already identified to have a great influence on the final size of nanoparticles in a few literature reports [97, 98, 102]. it can therefore be assumed that the change in reaction conditions has only a minor influence of the mean particle diameter.
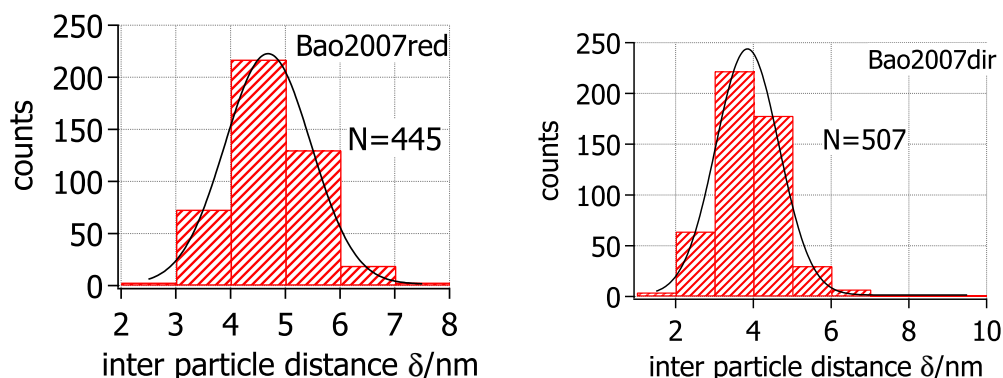
Fig. 7.3: Inter particle distance distributions. The mean inter-particle distance for *Bao2007red* is $\langle\delta\rangle = 4.7\,\mathrm{nm} \pm 0.8\,\mathrm{nm}$ and the distances between $N = 445$ particles are measured, while the distances between $N = 507$ cobalt nanoparticles are measured to determine the interparticle distance of $\langle\delta\rangle = 3.8\,\mathrm{nm} \pm 0.8\,\mathrm{nm}$ for *Bao2007dir*.

The mean interparticle distances measured in the TEM-images is determined to $\langle\delta\rangle = 4.7\,\mathrm{nm}\pm0.8\,\mathrm{nm}$ for *Bao2007red* and $\langle\delta\rangle = 3.8\,\mathrm{nm}\pm0.8\,\mathrm{nm}$ for *Bao2007dir*. This equates to a surfactant shell thickness of $L = 2.35\,\mathrm{nm}$ and $L = 1.9\,\mathrm{nm}$, respectively. Both values again correspond well with the calculated length of oleic acid [21]. Following the same considerations as in case of *Bao2005red* and *Bao2005dir* oleic acid is present on the particle surface, as it governs the interparticle distance. The length of tri-octylamine is calculated to $1\,\mathrm{nm}$ [21] as well, because it also attaches the particles' surface via its amine group, similar to DOA. If TOA governs the interparticle distance, it results in a smaller interparticle distance, than is measured. It is still possible, however unlikely, that the amine is present on the cobalt surface besides oleic acid. Since the amine group has a weaker affinity to the nanoparticle surface than the carboxyl group of oleic acid [55], the amine is superseded on the cobalt surface. The syntheses *Bao2005red* and *Bao2005dir* differ only at one point from the syntheses *Bao2007red* and *Bao2007dir*. The second surfactant DOA is exchanged for TOA. This influences the size of the cobalt seed particles greatly. Compared to the cobalt seed particles produced through the syntheses *Bao2005red* and *Bao2005dir*, the seed particle from *Bao2007red* and *Bao2007dir* have approximately only half the diameter.

All surfactants used during the syntheses *Bao2007red* and *Bao2007dir* are depicted in Fig. 7.4 and the inset shows how the molecules attach to the surface of a nanoparticle. The affinity of a surfactant to the surface of a nanoparticle can influence its final size, e.g. oleic acid is believed to inhibit growth and
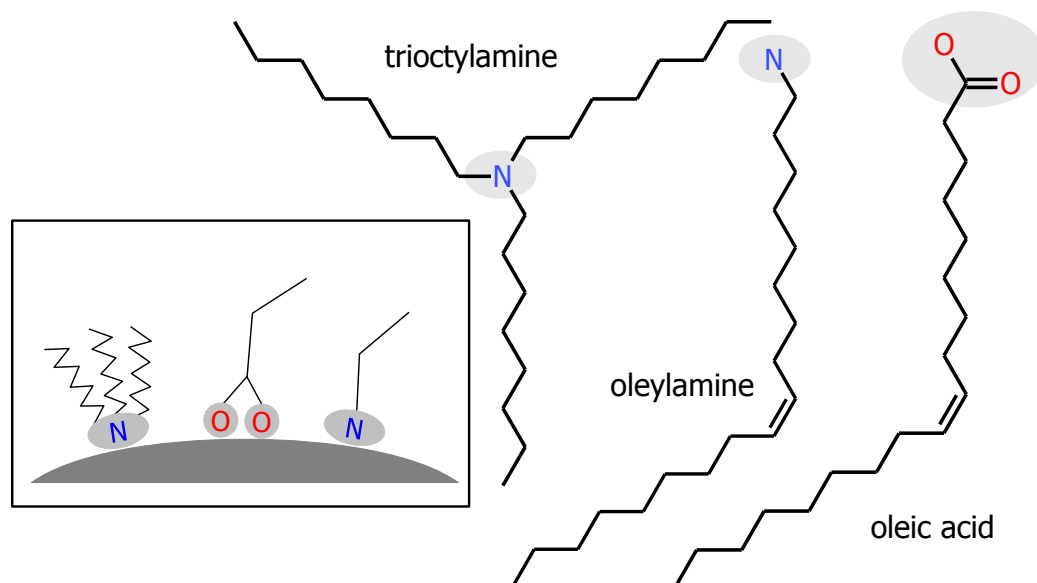
Fig. 7.4: Skeletal formulas generated with *Accelrys Draw 4.0* (Symyx Solutions Inc.) of all surfactants, dioctylamine, oleic acid and oleylamine, used in the syntheses *Bao2007red* and *Bao2007dir*. The polar head groups binding with the nanoparticles' surface are highlighted by gray ovals. The inset schematically shows the behavior of the non-polar tails, if the head group is in contact with a nanoparticle.

ripening processes [55, 99, 101]. The two different amines are most likely not present on the surface of the cobalt nanoparticles at the end of the syntheses. The difference between the amines is, that TOA with its third alkyl chain is much bulkier than DOA, which only has two non-polar tails. It may be possible that TOA limits the monomer mobility in the solution, which would favor the formation of smaller nanoparticles, because many stationary nuclei are formed, which final diameters are limited by the maximum amount of cobalt in the reaction solution. The exact mechanism cannot be fully determined from the data. Further measurements need to be conducted to fully evaluate the influence of the amine.

7.2.2. Crystal structure

EDX-spectra of both samples *Bao2007red* and *Bao2007dir* are recorded to determine the seed particles composition prior to the crystal structure analysis. The spectra are depicted in Fig. 7.5 and show peaks corresponding to carbon, oxygen, silicon, chlorine and cobalt. The peak attributed to chlorine is caused
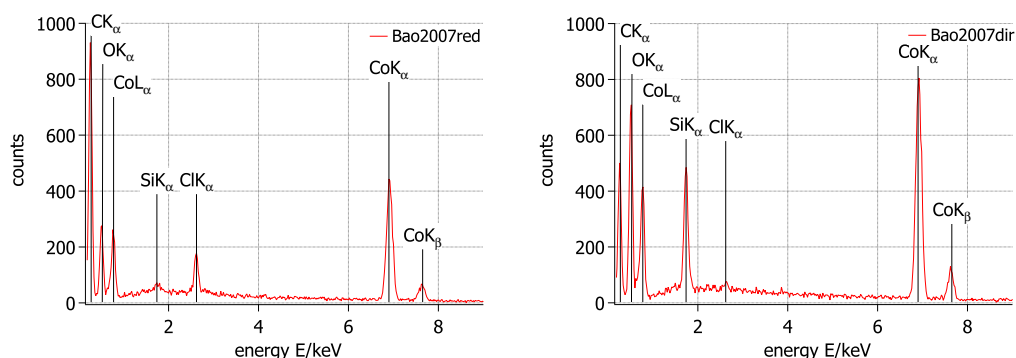
Fig. 7.5: EDX-analyses of the seed particles from syntheses *Bao2007red* (left) and *Bao2007dir* (right). All elements found in the samples are either from residual air or the surfactant coating of the particles (carbon and oxygen), the silicon substrate or the pure cobalt particles. Both samples show an additional peak attributed to chlorine, which is caused by residues of the solvent ODCB.

by residues of the solvent ODCB. The origin of all other peaks is given in detail in section 6.2.2. The cobalt peaks caused by the nanoparticles can clearly be seen in the EDX-spectra. The XRD-measurements of the samples *Bao2007red* and *Bao2007dir* are executed for angles $2\theta = 20°$ to $120°$ with an ω-offset of $3°$ suppressing peaks caused by the silicon substrate. Fig. 7.7 and Fig. 7.6 show the recorded spectra for *Bao2007dir* and *Bao2007red*, respectively, and the peak positions for all three cobalt modifications are noted as stick-spectra[2] in the images. The spectra of both samples unfortunately cannot be attributed to any modification of cobalt. Both spectra show a distinct peak around $2\theta = 60°$, which is not present in any of the simulated diffraction spectra of cobalt (see section 5.1 or compare to stick spectra). Another distinct peak visible in both measured XRD-spectra is positioned at $\theta = 33°$. Its position corresponds to the position of the ϵ-cobalt (210)-peak. However, the (210)-peak of ϵ-cobalt is of weak intensity and therefore it is unlikely, that the peak is caused by ϵ-cobalt. Furthermore, there are no other peaks corresponding to peaks of ϵ-cobalt found in the spectra (compare to Fig. 5.1). The two mayor peaks in the XRD-spectrum of *Bao2007dir* shown in Fig. 7.7 have an interesting feature. Their left slopes are comparably steep, resulting in two asymmetrical peaks. This peak form is a sign of lattice straining, which is not unexpected in case of nanoparticles [91]. Thus, it is not possible to determine the crystal structure of these two samples by X-ray diffraction. Neither the observed peak broadening nor possible peak overlaps can explain these spectra.

---

[2]The stick spectrum of ϵ-cobalt only shows peaks with an intensity of at least 10% from the (221)-peak with highest intensity. This is done to keep the overview over the otherwise overcrowded spectrum clear and concise.
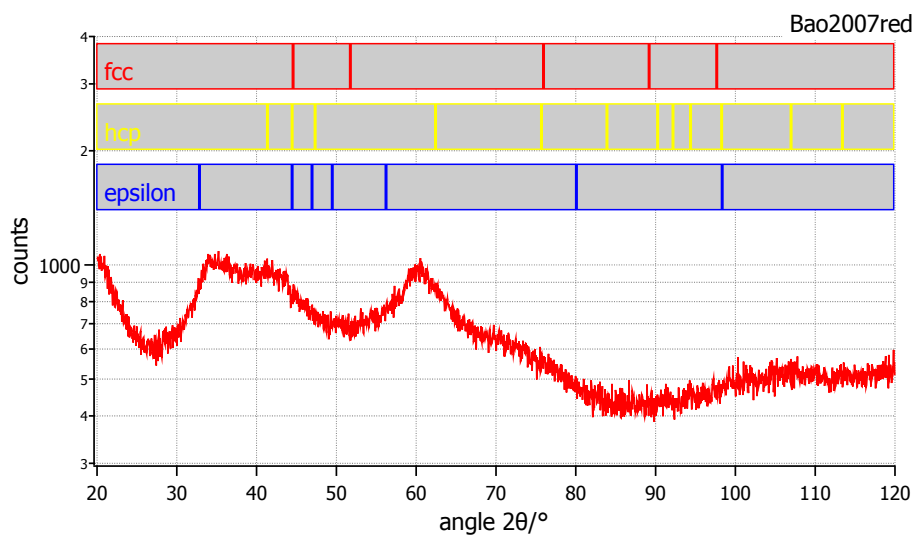
Fig. 7.6: X-ray powder diffraction spectrum of *Bao2007red*. The peak spectrum cannot be matched to one of the three possible cobalt modifications. For example, the major peak at $2\theta = 60°$ is not present in any of the stick spectra displayed above the XRD-spectrum. The stick spectrum does not show different peak intensities, but only gives possible locations for peaks. The complete powder spectra shown in Fig. 5.1 need to be consulted to identify a peak correctly.
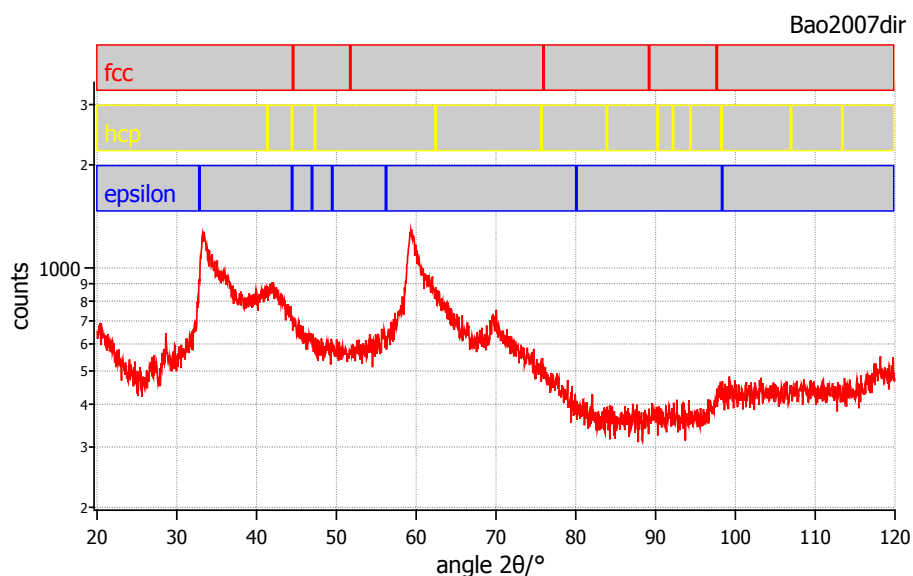
Fig. 7.7: X-ray powder diffraction spectrum of *Bao2007dir*. The peak spectrum cannot be matched to one of the three possible cobalt modifications. For example, the major peak at $2\theta = 60°$ is not present in any of the stick spectra displayed above the XRD-spectrum. The stick spectrum does not show different peak intensities, but only gives possible locations for peaks. The complete powder spectra shown in Fig. 5.1 need to be consulted to identify a peak correctly.

HRTEM imaging is further applied to determine the crystal structure of the cobalt nanoparticles (see section 6.2.2). FFTs of selected areas of HRTEM-images and the HRTEM-images are shown in Fig. 7.8 for the particle batch *Bao2007red* and in Fig. 7.9 for the particle batch *Bao2007dir*. The FFTs showing the reciprocal lattice of the investigated crystallites are shown inverted and with enhanced contrast for better visibility of the patterns. The FFTs in Fig. 7.8 show the unique squared and oblated hexagonal patterns of fcc-cobalt. This indicates an fcc-crystal structure for the investigated crystallites. The HRTEM-images and enhanced FFTs of the *Bao2007dir* seed particles are displayed in Fig. 7.9. The found squared and oblated hexagonal patterns are generated by an fcc-crystal lattice (Fig. 5.3). Both other possible modifications, hcp and ϵ-cobalt are ruled out as before, since neither can generate patterns with aspect ratios unique to the fcc-lattice. The results do not correspond to the ϵ-cobalt crystal structure reported in Bao et al. [32] 2007. However, the fcc-crystal structure for the cobalt seed particles has also been found for the nanoparticles of the syntheses *Bao2005red* and *Bao2005dir*. The results of these syntheses show, that the reactants do not determine the crystal structure, which is in good agreement with the syntheses *Bao2005red* and *Bao2005dir*. Again, environmental influences may play a decisive role in the determination of the crystal modification. What factors determine the crystal structure of a nanoparticle in the end is still under discourse (see section 6.2.2).
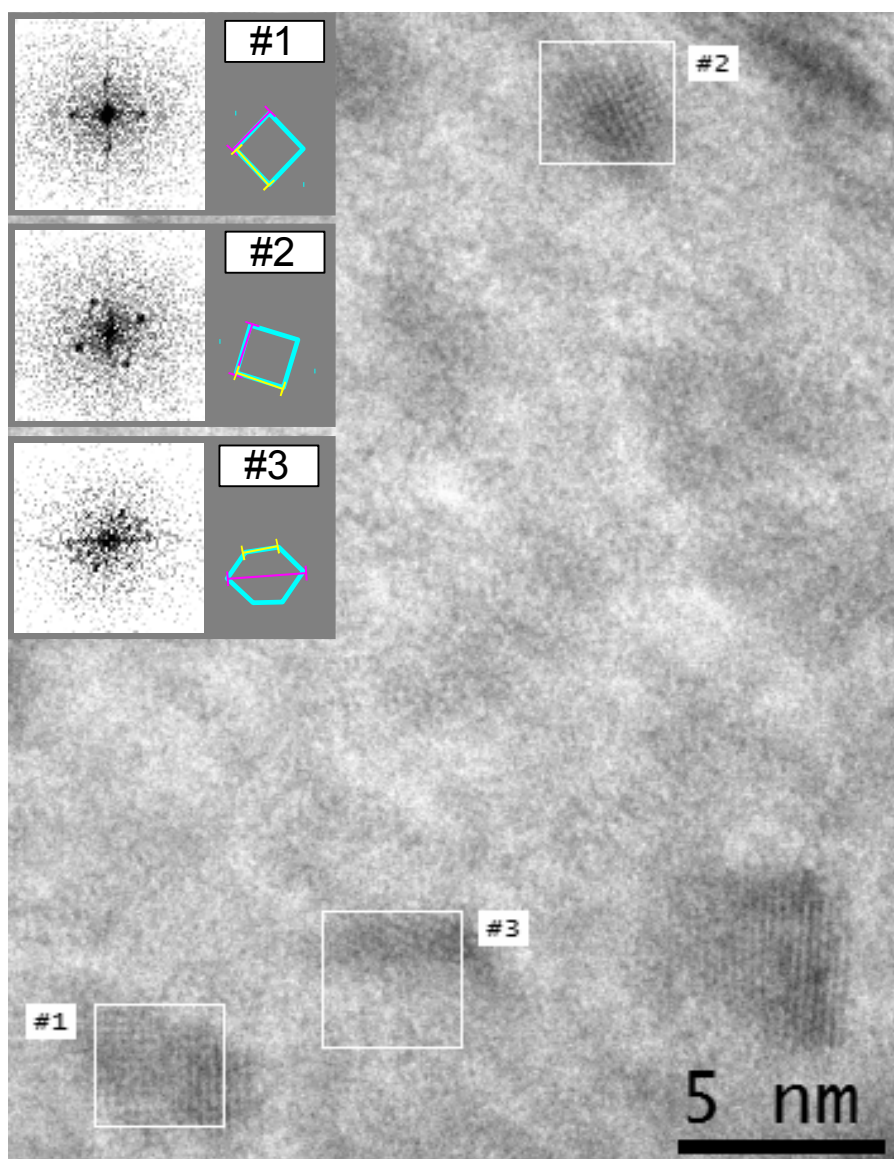
Fig. 7.8: FFTs of selected areas from *Bao2007red* indicating an fcc-structure. The oblated hexagons show a distance ration of 2:1 between the magenta and yellow section and the squared pattern only occurs during electron diffraction of a fcc-crystal. The diffraction patterns are displayed inverted with enhanced contrast for better visibility.
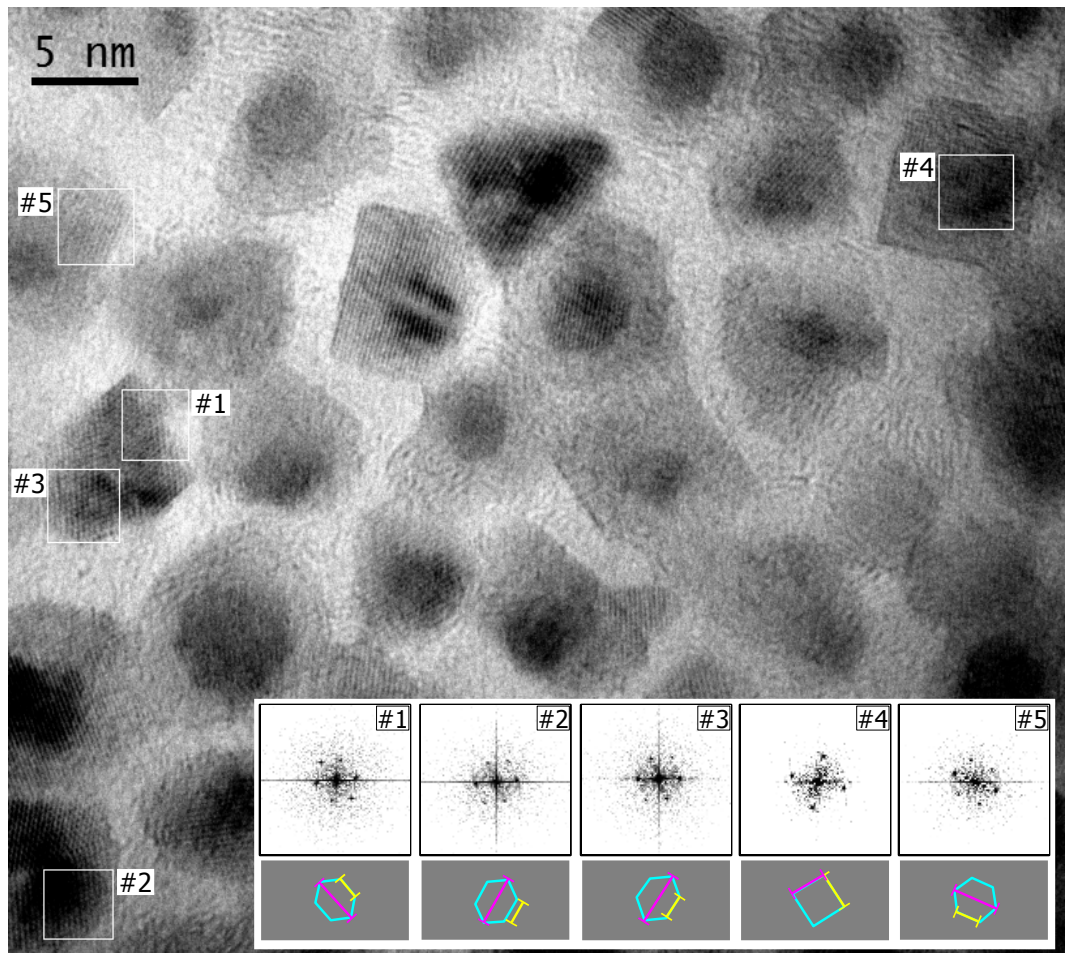
Fig. 7.9: FFTs of selected areas from *Bao2007dir* displayed inverted and contrast enhanced for better visibility. Both hexagons show the right 2:1 ratio for the magenta and yellow cross-section of [110]fcc and the squared pattern of [100]fcc.

7.2.3. Magnetic properties
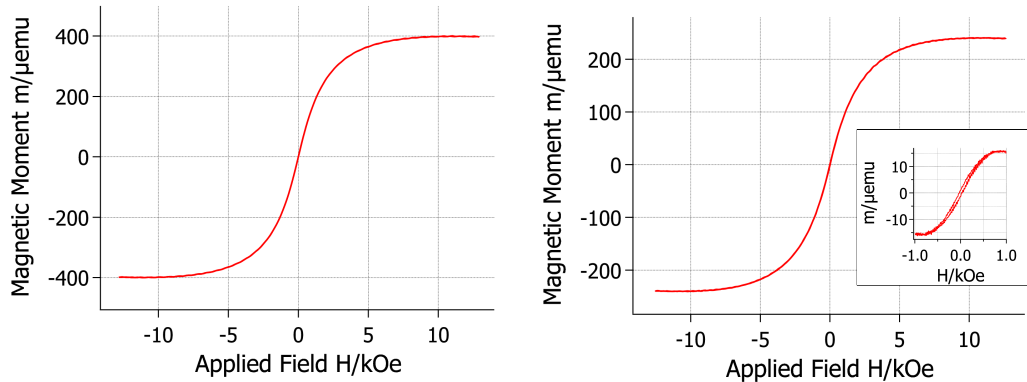
Fig. 7.10: The left diagram shows the magnetization curves of *Bao2007red* and the right diagram belongs to the batch, synthesized using *Bao2007dir*. Both samples show superparamagentic behavior. The inset in the right diagram shows a more detailed measurement between $-1\,\mathrm{kOe}$ to $1\,\mathrm{kOe}$ with a small hysteresis, displaying a coercivity of approximately $27\,\mathrm{Oe}$. Both samples reach saturation, when an external field of $10\,\mathrm{kOe}$ is applied.

Superparamagnetic behavior is expected for both samples, *Bao2007red* and *Bao2007dir*. The crystal structure analysis shows, that both particle batches consist of fcc-cobalt, for which a superparamagnetic limit of $15.4\,\mathrm{nm}$ for the particle diameter has been calculated by (**eq.** 2.29). The size distributions given in Fig. 7.1 and Fig. 7.2, respectively, do not include particles exceeding the superparamagnetic limit and therefore ferromagnetic effects are not expected.

The hysteresis curves are recorded with an applied field maximum of $14\,\mathrm{kOe}$ and displayed in Fig. 7.10. The parameters m_S, m_R and H_C are listed in Tab. 7.1, together with samples' the mean diameters and standard deviations. Both samples *Bao2007red* and *Bao2007dir* reach saturation around $10\,\mathrm{kOe}$ in contrast to the samples *Bao2005red* and *Bao2005dir*, which reach their saturation moment after an external field of $5\,\mathrm{kOe}$ is applied. The particles of *Bao2007red* and *Bao2007dir* need a stronger external field to saturate.

The magnetization curves of *Bao2007red* and *Bao2007dir* do not display coercivity. Only a more detailed measurement around the origin of sample *Bao2007dir* shows a small hysteresis with $H_C = 27.6\,\mathrm{Oe}$ and $m_R = 1.39\,\mathrm{\mu emu}$. Although the hysteresis is visible in the measurement, the absolute value is still comparably small.

Both measured AGM-curves are compared to calculated curves derived from (**eq.** 2.27) for external field values of $H_{\mathrm{ext}} = \pm 5\,\mathrm{kOe}$ with *MathCAD*. The

Tab. 7.1: Magnetic saturation moment m_S, remanence m_R and coercivity H_C of all investigated samples. The mean diameters $\langle d \rangle$ and their standard deviations σ are determined in section 7.2.1.

sample	m_S/μemu	m_R/μemu	$H_C/$Oe	$\langle d \rangle/$nm	$\sigma/$nm
Bao2007red	398.3	0.54	2.76	6.5	$0.9 \cong 13.8\,\%$
Bao2007dir	239.5	1.39	27.6	5.3	$0.75 \cong 14.2\,\%$

calculated curves and the AGM-measurements are displayed together for the both samples in Fig. 7.11. The dotted lines represent the calculation based on the mean diameters and standard deviations determined in section 7.2.1. The curves, calculated for $\langle d \rangle = 6.5\,\text{nm} \pm 13.8\,\%$ and $\langle d \rangle = 5.3\,\text{nm} \pm 14.2\,\%$ are similarly shaped, but do not follow the progression of the measured curves. Curves calculated from decreased mean diameters of 4.5 nm and 4.2 nm follow the progression better, but not as well as in case of the samples *Bao2005red* and *Bao2005dir* (see section 6.2.3). Inevitable oxidation during sample preparation and measurements decreases the magnetic volume of the cobalt particles, explaining the better fit of the calculated curves from smaller diameters. The oxidation does not influence the standard deviation of the mean diameter, if a constant oxide shell thickness is assumed.
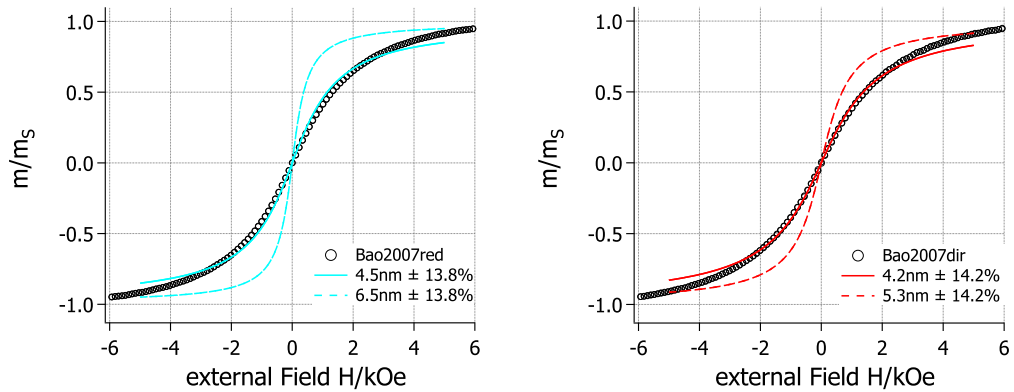
Fig. 7.11: Left: The size distribution of *Bao2007red* is used to calculate the dashed curve, which does not follow the progression of the measured curve (circles). The solid curve calculated with $\langle d \rangle = 4.5\,\text{nm} \pm 13.8\,\%$ fits the AGM-results better. Right: The same applies to sample *Bao2007dir*. The dashed line calculated does not follow the progression of the measured curve, while the solid curve calculated for a decreased diameter of $\langle d \rangle = 4.2\,\text{nm} \pm 14.2\,\%$ is a better match.

7.3. Control experiment *Bao2007-gold*
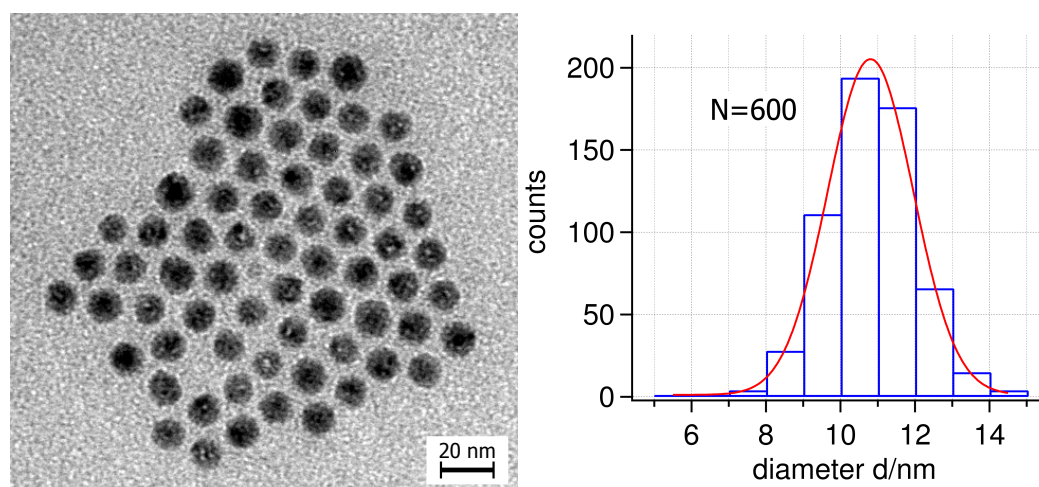
Fig. 7.12: TEM-image and size distribution of the sample *Bao2007-gold*. The image shows spherical gold nanoparticles with a mean diameter of $\langle d \rangle = 10.7 \, \text{nm} \pm 1.15 \, \text{nm}$. The red curve represents the gaussian fit of the size distribution.

This control experiment, referred to as *Bao2007-gold*, is performed to study, if the gold shell synthesis step is able to produce homogeneously nucleated gold nanoparticles, which can act as competing nucleation centers to the seed particles, as has been determined for *Bao2005-gold*. The shell synthesis step of the syntheses *Bao2007red* and *Bao2007dir* is similar to the shell synthesis step of *Bao2007red* and *Bao2007dir*. However, $[(\text{C}_6\text{H}_5)_3\text{P}]\text{AuCl}$ is used as gold source and a different amount of oleylamine as reported by the original article from Bao et al. [32] 2007. Almost monodisperse, spherical nanoparticles with a mean diameter of $\langle d \rangle = 10.7 \, \text{nm} \pm 1.15 \, \text{nm}$ and a standard deviation of $\sigma = 10.7 \, \%$ are produced. This system also nucleates homogeneously and is able to produce competing nucleation centers.

7.4. Bimetallic cobalt-gold particles *Bao2007*

The cobalt seed particles are employed as heterogeneous nucleation centers in the shell synthesis step. The resulting particles are investigated by TEM- and STEM-imaging, as well as EDX-analysis to determine the elemental distribution within the particles.

7.4.1. TEM-imaging
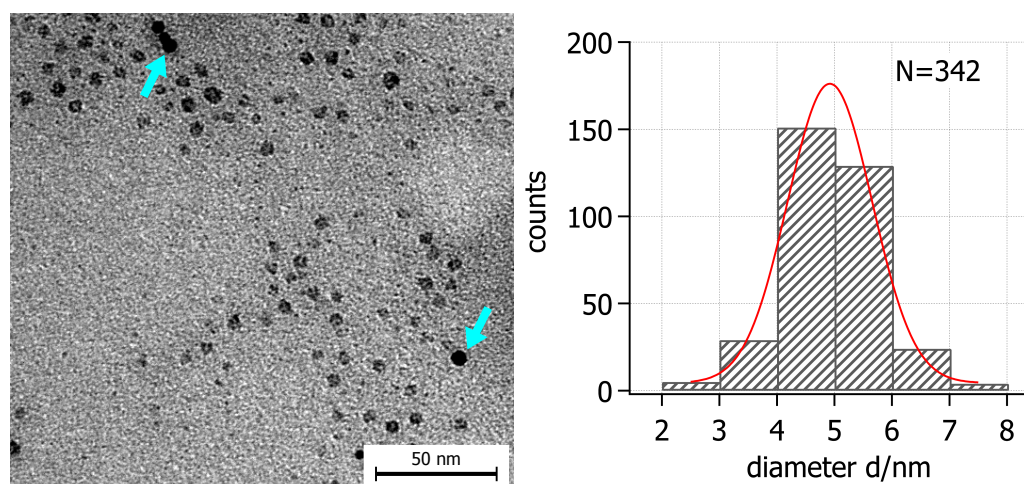
Fig. 7.13: TEM-image and size distribution of *Bao2007red* $5\,\mathrm{min}$ after the gold precursor is injected. The arrows point out high-contrast particles among the seed particles. The red curve is the gaussian fit of the seed particles' size distribution and their mean diameter is determined to $\langle d \rangle = 4.9\,\mathrm{nm} \pm 0.7\,\mathrm{nm}$. The mean diameter of the high-contrast particles is determined by an arithmetic mean to $\langle d \rangle = 5.1\,\mathrm{nm} \pm 1\,\mathrm{nm}$.

Representative TEM-images and size-distributions of all samples taken from *Bao2007red* are displayed in Fig. 7.13 to 7.16. Instead of a core-shell type particle only high- and low-contrast seed particles are found. The high-contrast particles are not in contact with any seed particles, as is expected for a heterogeneous nucleation event and has been observed in the syntheses *Bao2005red* and *Bao2005dir*. The gray hatched histograms represent the size-distribution of the seed particles, while the blue framed represent the high-contrast particles. The number of high-contrast particles in the images of the first three samples is remarkably low and there are too few ($N \leq 100$) particles to obtain a decent size-distribution. A simple arithmetic mean and the standard deviation for a discrete random variable are used for the evaluation instead.

No high-contrast particles are found in images of the sample taken after $45\,\mathrm{min}$, therefore it is not considered for the evaluation of diameter changes during the synthesis. The sample taken after $60\,\mathrm{min}$ however, shows many high-contrast particles and a size distribution is acquired, but the low-contrast particles are hardly recognizable against the background and their mean diameter cannot be determined. The gray hatched histograms represent the size distributions of the low contrast seed particles, while the blue framed histogram represents the size distributions for the high-contrast particles.
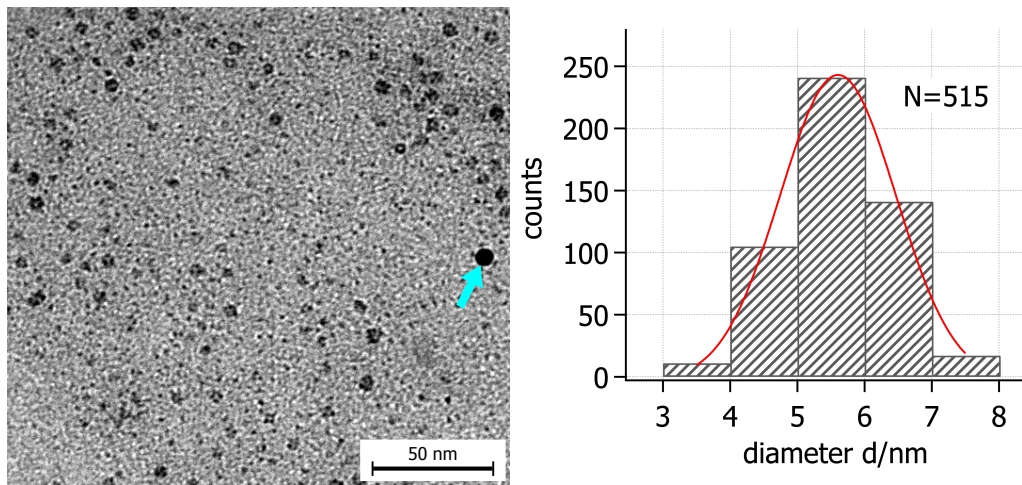
Fig. 7.14: TEM-image and size distribution of *Bao2007red* 20 min after the gold precursor is injected. The arrows point out high-contrast particles among the seed particles. The red curve is the gaussian fit of the seed particles' size distribution and their mean diameter is determined to $\langle d \rangle = 5.6\,\text{nm} \pm 0.9\,\text{nm}$. The mean diameter of the high-contrast particles is determined by an arithmetic mean to $\langle d \rangle = 5.1\,\text{nm} \pm 1\,\text{nm}$.
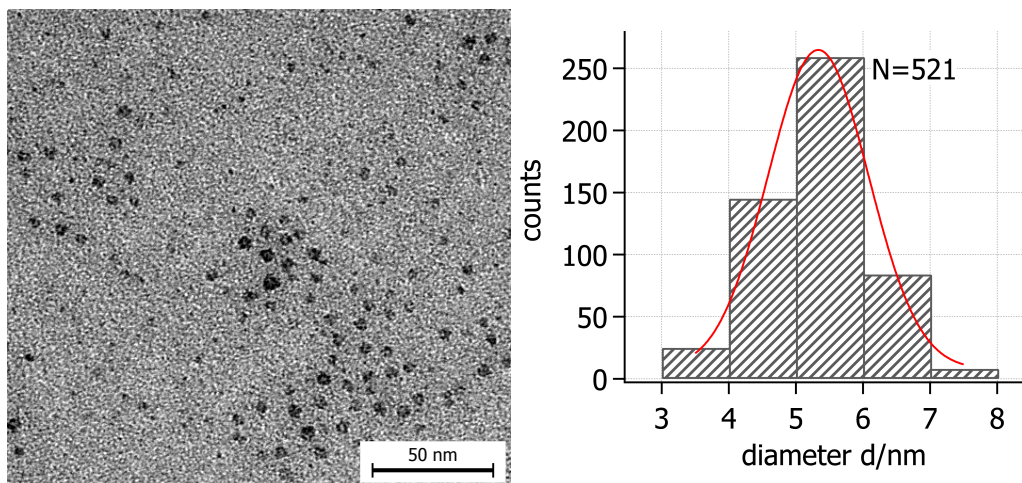
Fig. 7.15: TEM-image and size distribution of *Bao2007red* 45 min after the gold precursor is injected. There are no high-contrast particles found in the sample. The red curve is the gaussian fit of the seed particles' size distribution and their mean diameter is determined to $\langle d \rangle = 5.3\,\text{nm} \pm 0.75\,\text{nm}$.

111
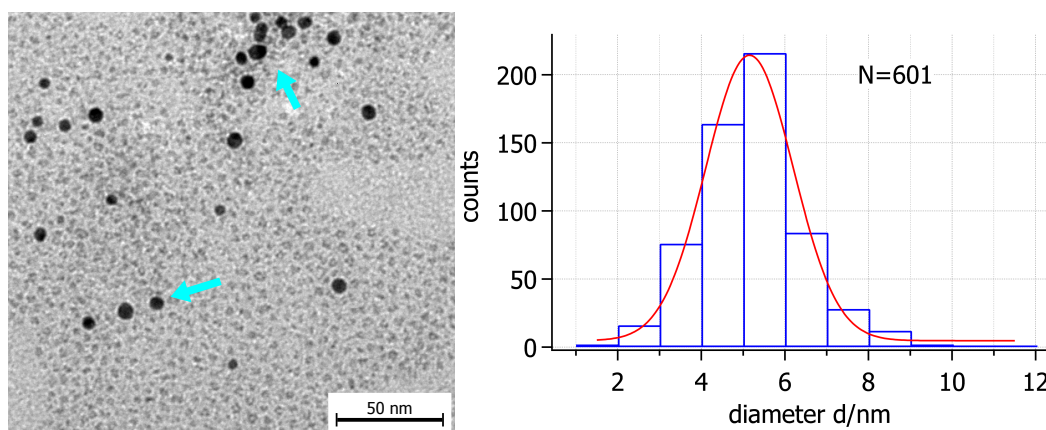
Fig. 7.16: TEM-image and size distribution of *Bao2007red* 60 min after the gold precursor is injected. The arrows point out high-contrast particles among the seed particles. The mean diameter of the high-contrast particles is determined to $\langle d \rangle = 5.2\,\text{nm} \pm 1\,\text{nm}$. The red curve represents the gaussian fits of the histograms. The outlines of the seed particles cannot be distinguished against the background.
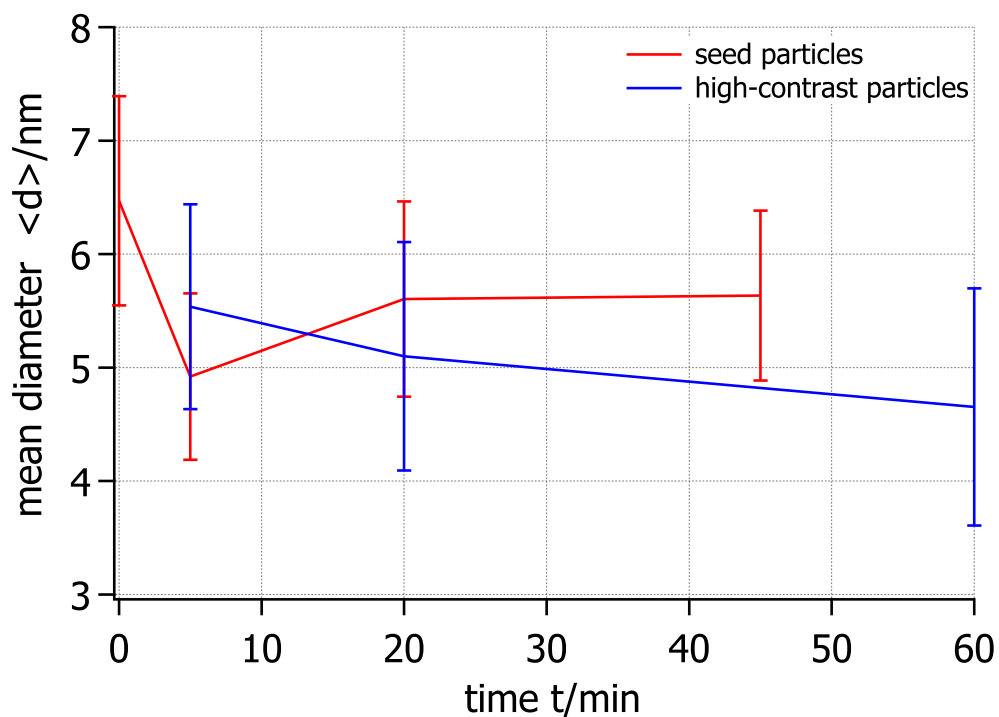
Fig. 7.17: Development of the mean diameter during the shell synthesis step of *Bao2007red* for the low-contrast seed particles (red curve) and high-contrast particles (blue curve). The error bars represent the standard deviation of the mean diameter and the line connecting the points only serves as a guide to the eye.

The mean diameter of the seed particles stays constant at approximately 5.5 nm during the synthesis as long as it is monitored after an initial drop from 6.5 nm. The same behavior can be observed for the high-contrast particle, which mean diameter slightly varies around 5 nm. The development of the mean diameter for both kinds of particles is depicted in Fig. 7.17.

TEM-images of all samples taken from *Bao2007dir* and size-distributions are given in Fig. 7.18 to 7.21. High- and low contrast particle are observed in all TEM-images. The high-contrast particles are not in contact with any seed particles. The mean diameter of the high-contrast particles, which are pointed out in the TEM-images by arrows, is determined by a simple arithmetic average, because of the small number of countable particles. The seed particles start out with a mean diameter of 5.3 nm, which varies between 5.1 nm and 5.5 nm during the shell synthesis. The mean diameter of the high-contrast particles varies between 5.8 nm and 6.7 nm. The number of sampled diameters is very small ($N < 50$), explaining the large standard deviations. The development of the mean diameters during the synthesis is shown in Fig. 7.22 with the standard deviations noted in the error bars. The synthesis does not yield core-shell type particles, either. The mean diameter of both high- and low-contrast particles stays constant during the synthesis and varies only within the limits of the standard deviation. The particles undergo no visible changes after the first 5 min, it is therefore possible to reduce the duration of the syntheses. Both syntheses are similar in results, but differ in the amount of seed particles used during the shell synthesis step. The amount of seed particles used during the shell synthesis step is higher in case of *Bao2007red*, which uses seeds precipitated from 4 mL particle suspension. In case of *Bao2007dir* cobalt seed particles from 0.5 mL are precipitated and used for the shell synthesis step. The particle suspension volume yields approximately 10 mg seed particles. The concentration of cobalt seeds in the particle suspension is lower, because the synthesis *Bao2007dir* is conducted with a larger initial solvent volume than the synthesis *Bao2007red*. However, an influence of the seed particle concentration on the syntheses can not be concluded from the data. The 1 nm difference in diameter of the high-contrast particles between the syntheses *Bao2007red* and *Bao2007dir* falls within the standard deviation. The syntheses are intended to deposit gold at the surface of a preformed cobalt seed particle. The core-shell structure has not been observed on any TEM-image. Possible gold depositions on the seed particles are studied in elemental composition measurements in the next section.
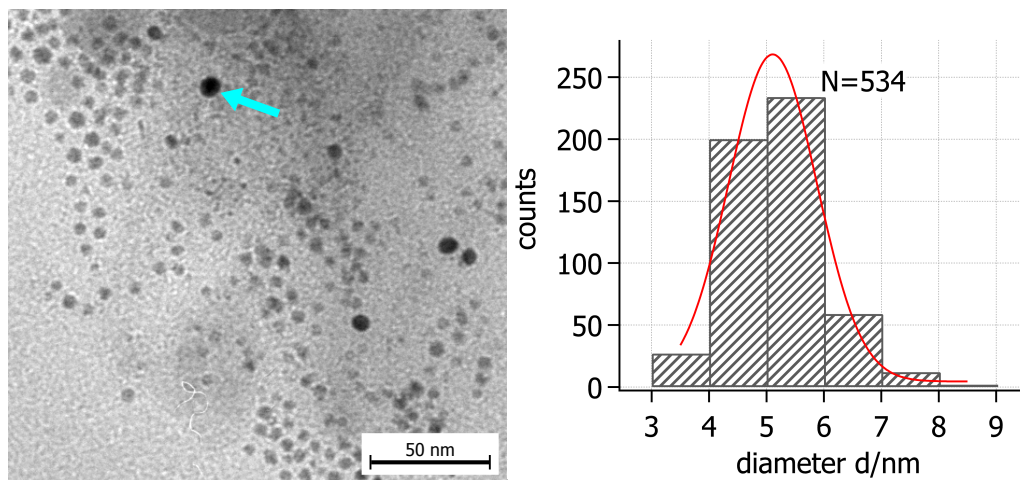
Fig. 7.18: TEM-image of *Bao2007dir* $5\,\mathrm{min}$ after the gold precursor is injected. The mean diameter of the low contrast-particle is $\langle d \rangle = 5.1\,\mathrm{nm} \pm 0.8\,\mathrm{nm}$, while the arithmetically estimated mean diameter of the high-contrast particles (see arrow) is $\langle d \rangle = 6.3\,\mathrm{nm} \pm 1.1\,\mathrm{nm}$. The red curve represents the gaussian fit of the histogram.
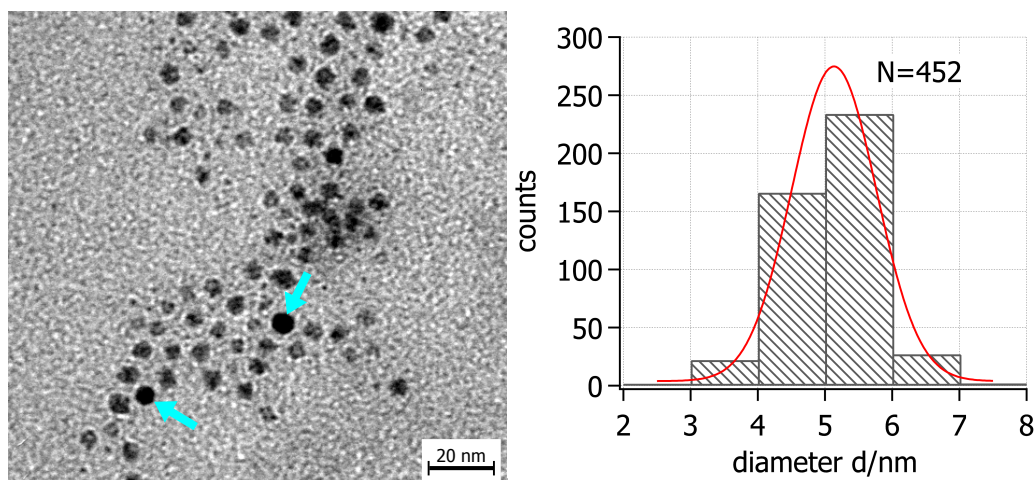
Fig. 7.19: TEM-image of *Bao2007dir* $20\,\mathrm{min}$ after the precursor injection. The sample looks unchanged and the mean diameters of low- and high-contrast particles are $\langle d \rangle = 5.1\,\mathrm{nm} \pm 0.6\,\mathrm{nm}$ and $\langle d \rangle = 5.8\,\mathrm{nm} \pm 0.5\,\mathrm{nm}$, repsecively. The red curve represents the gaussian fit of the histogram.
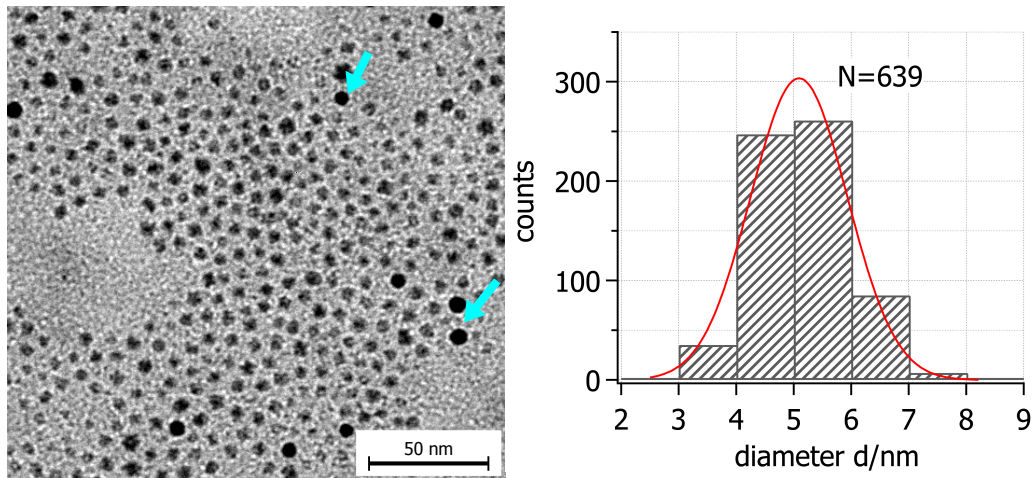
Fig. 7.20: TEM-image of *Bao2007dir* $45\,\mathrm{min}$ after the gold precursor is injected. The mean diameter of the low-contrast particles is $\langle d \rangle = 5.1\,\mathrm{nm} \pm 0.8\,\mathrm{nm}$ and the high-contrast particles have a mean diameter of $\langle d \rangle = 5.9\,\mathrm{nm} \pm 1.5\,\mathrm{nm}$. The red curve represents the gaussian fit of the histogram.
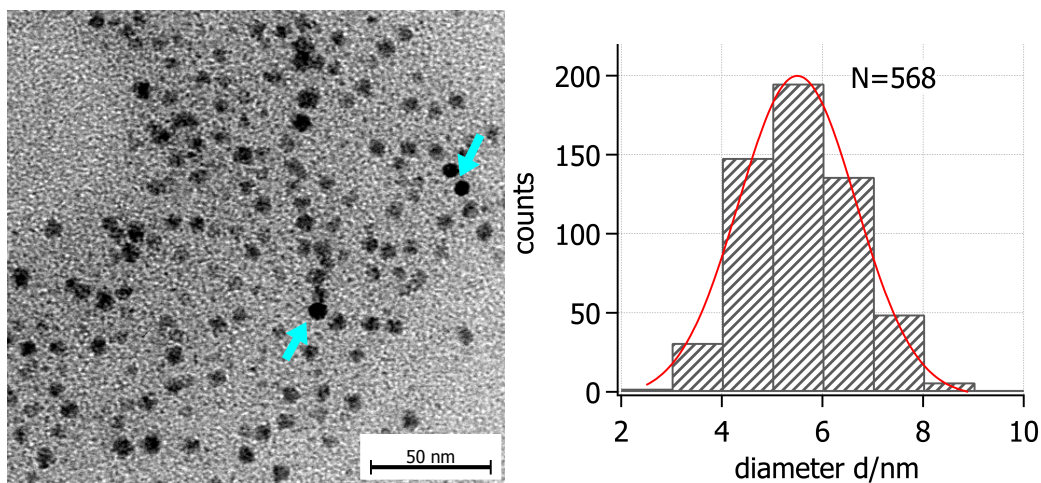
Fig. 7.21: TEM-image of *Bao2007dir* $60\,\mathrm{min}$ after the gold precursor is injected. The mean diameter of the low-contrast particles is $\langle d \rangle = 5.5\,\mathrm{nm} \pm 0.8\,\mathrm{nm}$ and the mean diameter of the high-contrast particles is $\langle d \rangle = 6.7\,\mathrm{nm} \pm 1\,\mathrm{nm}$. The red curve represents the gaussian fit of the histogram.
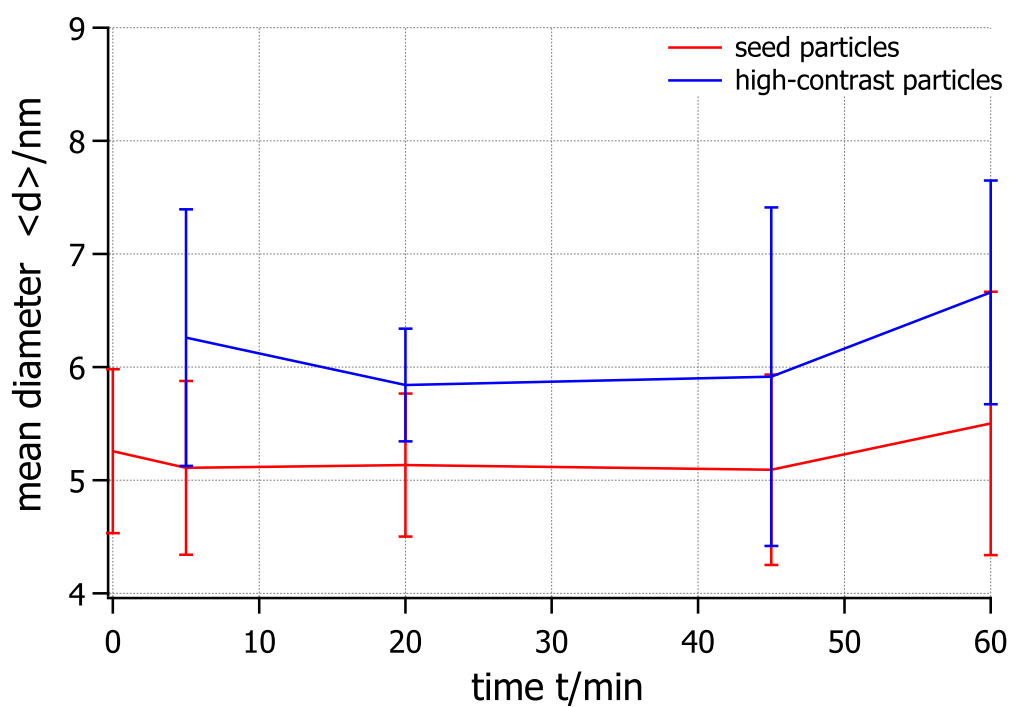
Fig. 7.22: Change in the mean diameter of the seed particles (red curve) and the high-contrast particles (blue curve) during the shell synthesis step. The standard deviation is noted as error bar for each value and the line connecting the points only serves as a guide to the eye.
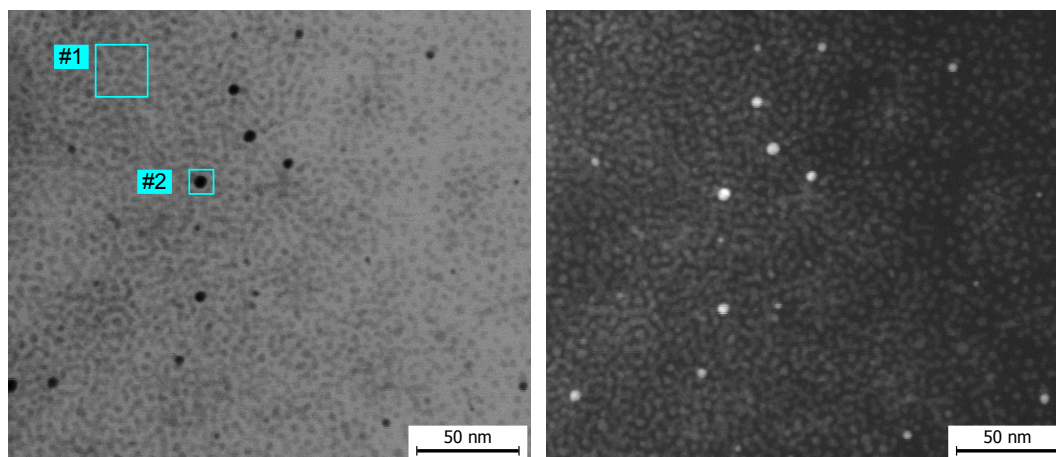
Fig. 7.23: BF- (left) and HAADF-image (right) of nanoparticles from *Bao2007red*, showing a multilayered arrangement of seed particles with single incorporated high-contrast particles. The frames show the locations of the EDX-analyses.

7.4.2. STEM-imaging and EDX-analysis

STEM-images (BF and HAADF) of the sample taken at the end of the synthesis *Bao2007red* are shown in Fig. 7.23. Isolated high-contrast particles are present in a multilayered arrangement of low-contrast seed particles. Areas, in which EDX-analyses are preformed are highlighted by blue frames and labeled. Only seed particles are located at position #1 in the STEM-images and the respective EDX-spectrum shown in Fig. 7.24 shows only peaks corresponding to cobalt, besides environmental elements[3]. This shows, that gold is not deposited at the seed particles, or at least not in detectable amounts. The second EDX-analysis is of a high-contrast particle, which is surrounded by cobalt seed particles at position #2 in Fig. 7.23. Small peaks for both gold and cobalt are found in the EDX-spectrum shown in Fig. 7.25. Only a single high-contrast particle is analyzed, explaining the weak signal of the gold peaks. The gold particle is surrounded by several cobalt seeds. It is possible that the high-contrast particle is of pristine gold, but this cannot be confirmed by EDX-measurements, because cobalt seed particles are always present in the background and therefore show up in the resulting EDX-spectrum.
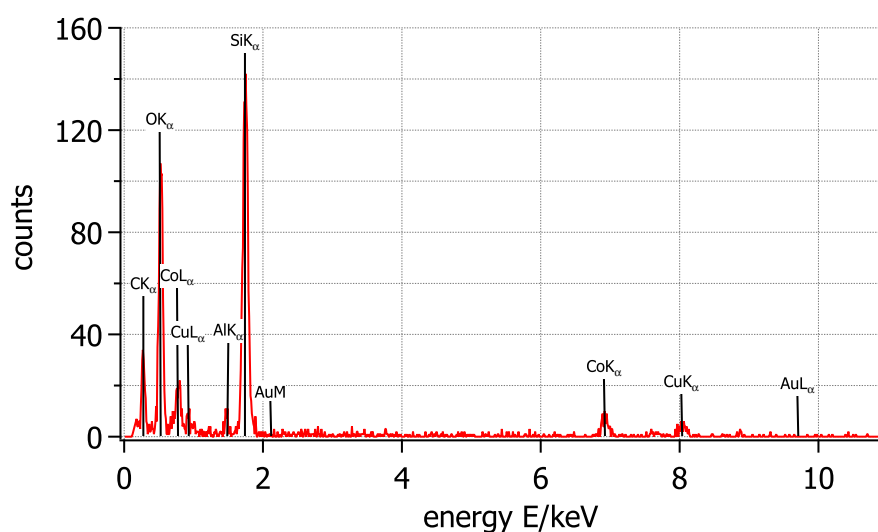
Fig. 7.24: EDX-analysis from position #1 in Fig. 7.23. Only low-contrast particles, presumably from pure cobalt are located in the selection frame. The EDX-spectrum only shows peaks corresponding to cobalt besides environmental elements, like carbon, oxygen, silicon, aluminum and copper.

---

[3]These are carbon, oxygen, copper, silicon and aluminum from air residues, the nanoparticles' surfactant coating, the TEM-grid and the aluminum chamber of the instrument.
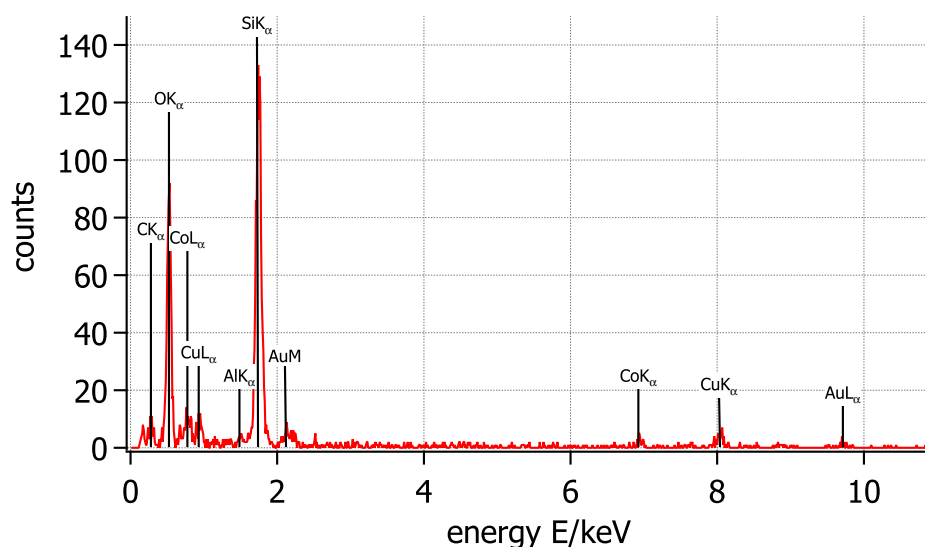
Fig. 7.25: An isolated high-contrast particle with several neighboring cobalt seeds is analyzed. The spectrum shows peaks corresponding to gold, totally absent in the analysis of the first selection frame. The cobalt seeds near by account for a weak cobalt signal, too. It is not possible to decide, whether or not the high-contrast particle consists of pure gold, based on this measurement.

STEM-images of the synthesis *Bao2007dir* are displayed in Fig. 7.26. An area thickly covered with low-contrast particles can be seen, which incorporates isolated high-contrast particles. The selection frames are shown in the STEM-image and the inset (Fig. 7.26, right image) shows the areas after the EDX-spectra are recorded. All nanoparticles in the area #1 melted away under the influence of the incident electron beam, while the EDX-spectrum is recorded, which has also been observed in Fig. 6.26. The spectrum, shown in Fig. 7.27 shows only peaks corresponding to cobalt or the environment. Gold is not deposited on the seed particles. The EDX-spectrum recorded at position #2, shown in Fig. 7.28, shows gold peaks, which are very weak and barely rise above the background. The comparably strong cobalt signal can be explained considering that the gold particle is incorporated in a cluster of cobalt seed particles. The cobalt particles in area #2 melt during the measurement, while the high-contrast particle stays intact during the measurement.

The seed particles of the syntheses *Bao2007red* and *Bao2007dir* are not altered by the shell synthesis step and no measurable amounts of gold are found at the seed particles. Heterogeneous nucleation has therefore not taken place. Gold is only found at isolated high-contrast particles in case of both synthe-
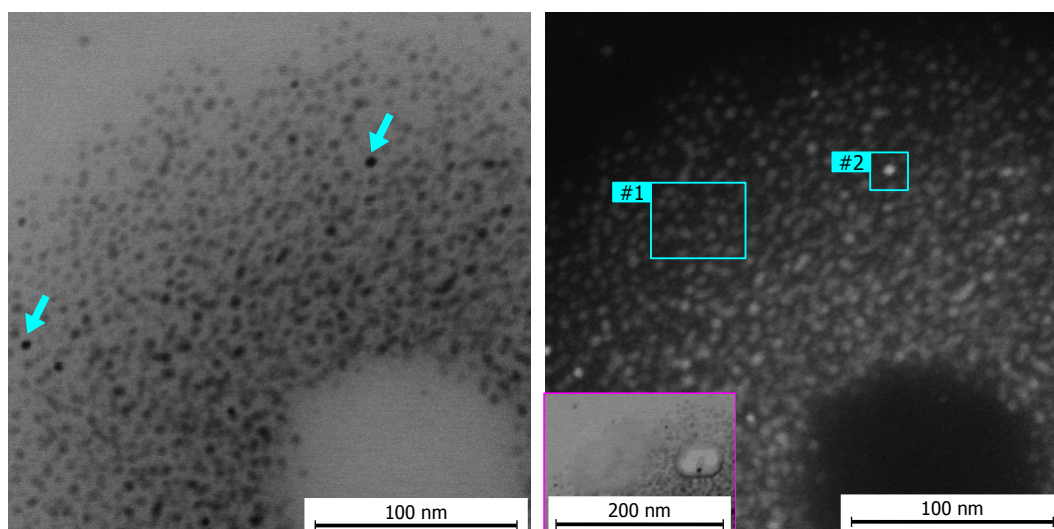
Fig. 7.26: BF- (left) and HAADF-image (right) of the sample *Bao2007dir* taken after the synthesis has been concluded. Position of the performed EDX-analyses are noted by the selection frames. It is not as easy as before to distinguish between high- and low-contrast particles. The arrows point to identified high-contrast particles. After the measurement the seed particles melted away, while the isolated high-contrast particle stayed intact, as can be seen in the inset.

ses *Bao2007red* and *Bao2007dir*. The results of the shell synthesis step of *Bao2007red* and *Bao2007dir* are different compared to the bimetallic particles obtained through the syntheses *Bao2005red* and *Bao2005dir*. Instead of interconnected gold and cobalt particles clearly indicating a heterogeneous nucleation event, the syntheses *Bao2007red* and *Bao2007dir* produced individual gold particles, which seem to have formed independently from the seed particles. This suggests, that the gold particles nucleated homogeneously. In this case, the results should be equal to those of the control experiment *Bao2007-gold* (see section 7.3). The control experiment has yielded homogeneously nucleated, almost monodisperse, gold particles with a mean diameter of $\langle d \rangle = 10.7\,\mathrm{nm} \pm 1.15\,\mathrm{nm}$, but the isolated gold particles found in both syntheses have only diameters around $6\,\mathrm{nm}$. The difference in mean diameter exceeds the standard deviation, which cannot be explained by experimental fluctuations. Hence, the seed particles must have an influence on the gold particle formation during the syntheses.
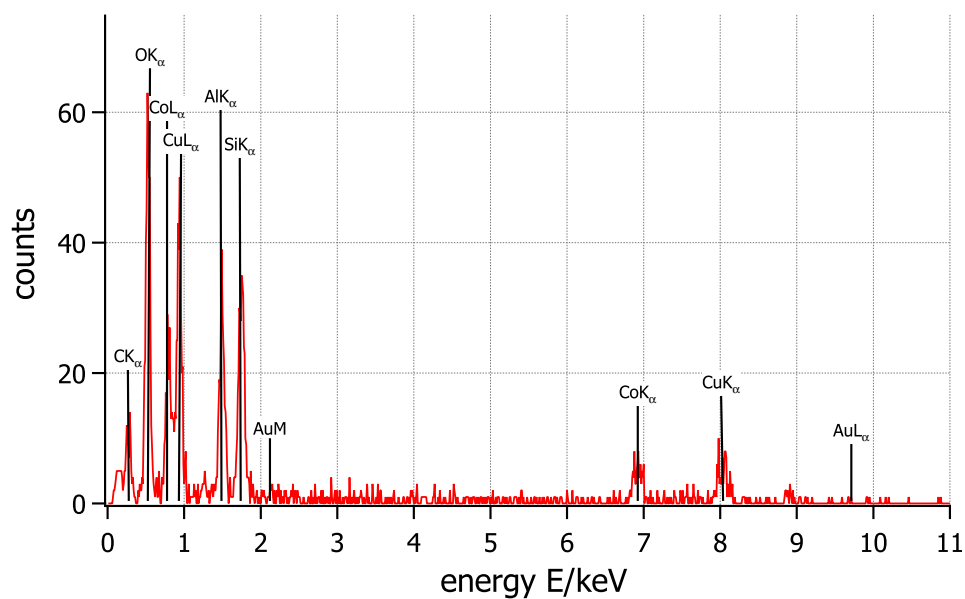
Fig. 7.27: EDX-spectrum of sample *Bao2007dir* taken at position #1 in Fig. 7.26. Only cobalt is found besides environmental elements.
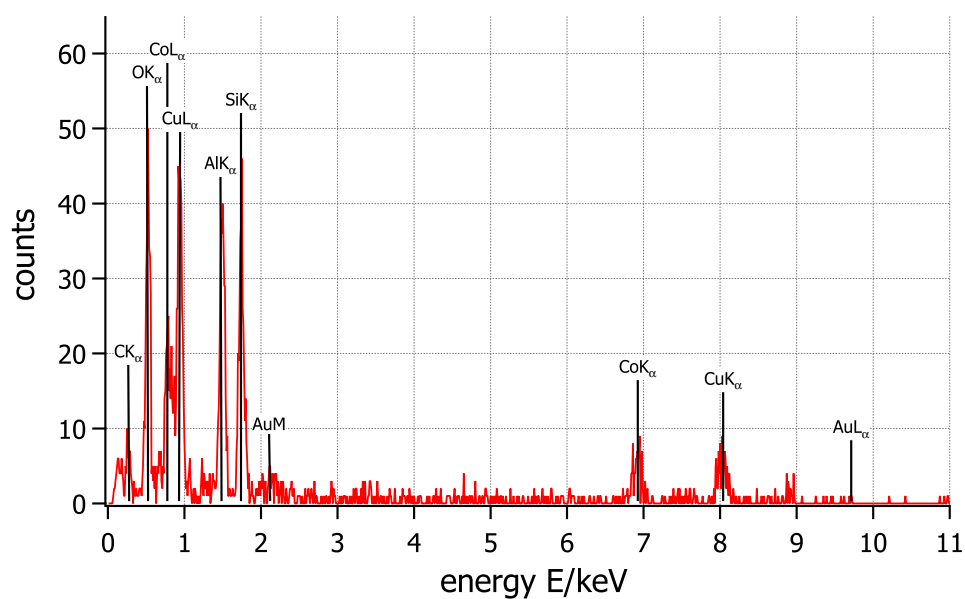
Fig. 7.28: EDX-spectrum of sample *Bao2007dir* taken at position #2 in Fig. 7.26. Besides environmental elements both cobalt and gold are found. The peaks corresponding to gold are very weak, because only a single particle has been analyzed, while several cobalt seeds are scanned (compare with inset of the STEM-image).

7.5. Conclusion

The nanoparticles synthesized in a reproduction of the synthesis route reported by Bao et al. [32] are not core-shell type particles. The cobalt nanoparticles produced by the syntheses *Bao2007red* and *Bao2007dir* do not serve as heterogeneous nucleation centers. The second reaction step conducted to cover the pre-formed cobalt seed particles with a gold shell produced only isolated gold particles. This result is achieved for both syntheses and therefore independent on the amount of used seed particles. The elemental distribution in the sample is determined by EDX-analyses. EDX-spectra recorded at areas where only cobalt seed particles are present show that gold is not deposited at the seed particles. Only EDX-spectra recorded at areas where high-contrast particles are present show peaks corresponding to gold. These results also differ from bimetallic nanoparticles reported in Bao et al. [32] in 2007. Both synthesis approaches, *Bao2007red* and *Bao2007dir*, conducted with different amounts of solvent produce cobalt seed particles with mean diameters of 6.5 nm and 5.3 nm, respectively, which corresponds to the sizes given in the report. Oleic acid, which is used as a surfactant during the syntheses is present on the nanoparticles' surface, as it dominates the interparticle distance. The role of the second surfactant, trioctylamine, in the synthesis is not yet determined, however it is unlikely that the amine is present on the particles' surface, because of the weaker binding affinity of the amine group compared to the carboxyl-group of oleic acid [21]. The cobalt nanoparticles behave superparamagnetically at room temperature and the shape of their magnetization curves is mostly determined by the particles' sizes. The nanoparticles crystallized during the syntheses in an fcc configuration and have not nucleated in the ϵ-cobalt phase, as is reported by the original publication by Bao et al. [32]. The reactants of the cobalt seed particle synthesis do not influence the crystal structure, as an alternative crystal configuration has been achieved with the same synthesis recipe.

Because core-shell type particles have not been obtained by any of the syntheses, literature is researched for successful reproductions of the recipe by Bao et al. [32]. The original article Bao et al. [32] 2007 is cited 63 times and the majority of these articles refers to it as an example for hybrid-structures in nanoparticles, the method of thermal decomposition for nanoparticle synthesis and mention the benefits of core-shell particles for bio-medical applications and their enhanced magnetic and optical properties [105, 117, 122, 129, 132, 134–152, 152–164]. All publications concerned with the production of cobalt-gold core-shell particles report syntheses, which are not similar to the article by Bao et al. [32]. Lu et al. [165] reports the production of large (100 nm) cobalt-gold core-shell

nanoparticles by a replacement reaction and analyzed the element distribution within the particles with convincing results. Peréz et al. [166] followed a completely different approach and prepared cobalt-core gold-shell nanoparticles by sputtering a target of cobalt and gold in a Nanocluster Deposition Source (Oxford Applied Research, Model NC200U-B) and rapidly cooling the formed clusters. TEM-images do not display a core-shell structure, but it is established by STEM-imaging and EDX-analysis. Song et. al. reported the synthesis [167] and investigated the particles [168] for fine-structure transitions in the core-region. TEM-images show particles with a mean diameter of 5 nm and a visible core-shell structure. The gold shells are depicted with less contrast than the cores in the TEM-images, which are blurry and details are barely visible. These results leave doubt, that core-shell type particles have actually been produced, because a shell around a cobalt particle with less contrast seen in a TEM-image is usually caused by an oxide shell. Gold, as has been thoroughly shown during TEM- and STEM-imaging in this thesis, causes high-contrast features and therefore does not cause this shell. Calderon et al. [169] further investigated particles[4] produced in the synthesis reported by Bao et al. [32] in 2007 using a combination of STEM-imaging and EDX-analysis in an element mapping. STEM- and HRTEM-images show multi-grain particles with a contrast-rich, multi grained shell, similar to the results in [32]. Fig. 7.29 shows an overview STEM-HAADF-image (taken from [169]), where two regions of interest are selected. The STEM-image and elemental maps of the left selected area are enlarged and shown in Fig. 7.29, too. The signals from the Au-L and Au-M maps recreate the STEM image. The elemental map of cobalt is expected to show the same features as the STEM-image, because the core-material is located within the gold-shell (see section 3.4 for comparison). Unfortunately the cobalt map does not resemble any structures from the STEM-image. A possible explanation can be the presence of residual cobalt-compounds formed during the synthesis in the background, which can cover up any distinct patterns. Possibly, the Co-K elemental map is recorded from the second selected area shown in the overview STEM-image, because features in both images show a slight resemblance. The core-shell structure is neither proven by the elemental mapping nor visible in the corresponding STEM-image.

Considering these publications there are no reports of a successful reproduction of the recipe published by Bao et al. [32], other than follow up investigations by the same group [169]. Furthermore, the core-shell structure is not clearly resolved in Z-contrast-images shown in Bao et al. [32] 2007 (see Fig. 4.3, (d)).

---

[4]H. Calderon is co-author of Bao et al. [32] and it can be assumed that the same particles are used for these analyses.
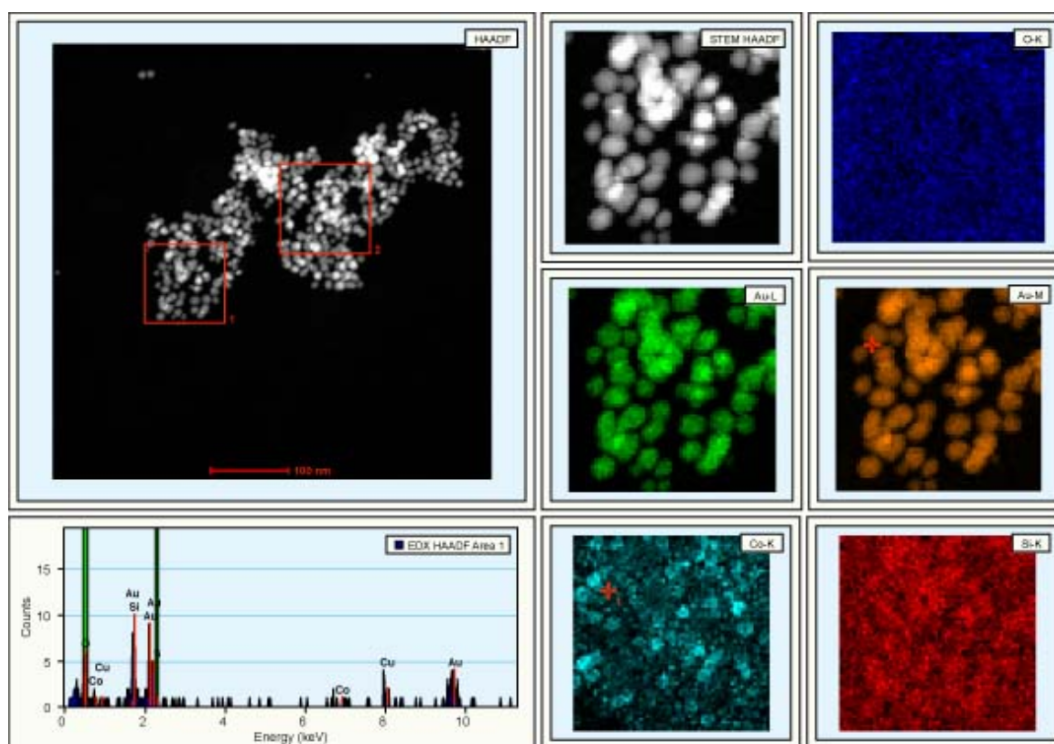
Fig. 7.29: EDX-mapping of cobalt-gold nanoparticle synthesized after Bao et al. [32]. Reprinted with permission from [169], Copyright ©2011, Cambridge University Press.

A definite production of cobalt gold core-shell type particles can neither be found in literature nor in the reproduced syntheses.

8. Summary

This thesis is concerned with the reproduction of two nanoparticle synthesis routes reported to yield cobalt-gold core-shell type nanoparticles. The goal of investigating these syntheses is to find out whether they can be used to produce core-shell type particles or to identify problems preventing a successful synthesis. The investigated syntheses are both conducted in a two step process first producing cobalt seed particles, which are afterwards used as heterogeneous nucleation centers in the second step used to synthesize the gold shell. Key parameters of all syntheses are summarized in Tab. 8.1.

The results of the syntheses *Bao2005red* and *Bao2005dir* based on Bao et al. [31] 2005 show, that the cobalt seed particles serve as heterogeneous nucleation centers. However, core-shell type particles have not been produced, because the gold is deposited only on limited areas on the seed particles. The gold is located in isolated nanoparticles attached to the surface and does not form a closed shell. The elemental distribution in the different nanoparticles has been determined by EDX-analyses. How many gold particles are attached to one seed particle is dependent on the seed concentration during the shell synthesis step. The seed particles used in the synthesis *Bao2005red* are interconnected with single gold particles. In contrast, the fewer seed particles used during the synthesis *Bao2005dir* are heavily covered and additional gold particles have been found, which are not in contact with any seed particles. The isolated gold particles are formed through a homogeneous nucleation event, which is happening simultaneously to the heterogeneous nucleation. The reaction mixture used for the shell synthesis step is able to homogeneously nucleate gold particles, as has been shown by the control experiment *Bao2005-gold*. This indicates, that the heterogeneous nucleation sites are saturated and only slowly reduce the gold monomer concentration. The remaining oversaturation in the solution still exceeds the homogeneous nucleation limit and nucleates the isolated gold particles. Hence, adding more monomers to the solution will result in the nucleation of more isolated gold particles and will not complete the shell growth. The reason for this behavior is found considering the interfacial energies between the participating materials. A low energy interface between

the core and the shell material is required to successfully form a core-shell type particle. The interface between the fcc-cobalt seed and the deposited fcc-gold particles is characterized as semi-coherent with a mismatch of 15 %, therefore interfaces of lowest energy cannot be formed. The interfacial energies only allow the formation of deposits with contact angles $\theta > 0°$, which decreases the interfacial energy $\gamma_{2,\ell}$ and makes the gold deposition possible. If ϵ-cobalt is considered, which is reported by Bao et al. [31] 2005 to compose the cobalt seed particles, it has been determined, that core-shell type particles between ϵ-cobalt and fcc-gold cannot be formed, either. The mismatch between both phases is 50 % and only incoherent interfaces can be formed, which have even higher interfacial energies than semi-coherent interfaces.

The syntheses *Bao2007red* and *Bao2007dir* based on Bao et al. [32] 2007 show different results, however a heterogeneous nucleation event has not been observed, either. Gold has not been detected at the seed particles during EDX-analyses. It is only found at isolated high-contrast particles, which are not in contact with any seeds, which at first indicates a homogeneous nucleation event. However, the mean diameter of these gold particles greatly differs from the mean diameter of particles produced by the control experiment *Bao2007-gold*. Therefore it is certain, that the seed particles influence the formation of the gold particles, but how they affect the gold particle synthesis cannot be determined from the data.

Core-shell type particles have not been produced from any synthesis approach discussed in this thesis. The semi-compatible crystal structures of fcc-cobalt and fcc-gold are found to prevent the formation of large interface areas, as needed for the successful production of core-shell type particles. ϵ-cobalt and fcc-gold only form incoherent interfaces, which likewise indicates that the formation of core-shell type particles is unlikely. The particle analyses of both published syntheses do not show the assumed core-shell nature of the nanoparticles, either. These results and the lack of literature reports on successful reproductions of any of the syntheses suggest, that the syntheses routes are at least unstable and cannot be used to produce core-shell type particles.

Tab. 8.1: Overview over parameters, particle diameters, crystal structures and magnetic properties of all syntheses in comparison to the original publications Bao et al. [31] 2005 and Bao et al. [32] 2007. The following abbreviations are used in the table: ODCB = ortho-dichlorbenzene, DOA = dioctylamine, TOA = trioctylamine, OA = oleic acid, OLA = oleylamine. The values marked with * give the Co-core diameter and Au-shell thickness reported in the publications for the assumed core-shell type particles.

	Bao et. al. [31] 2005	Bao2005red	Bao2005dir	Bao et. al. [32] 2007	Bao2007red	Bao2007dir
ODCB V/mL	-	5	12	-	5	12
surfactants		DOA & OA			TOA & OA	
$\langle d \rangle_{Co\text{-}seeds}$/nm	10	8.3 ± 1.2	9.8 ± 1	$5-6$	6.5 ± 0.9	5.3 ± 0.75
$\langle \delta \rangle_{Co\text{-}seeds}$/nm	-	4.6 ± 1	4.2 ± 1	-	4.7 ± 0.8	3.8 ± 0.8
crystal structure	ϵ-Co	Co-fcc		ϵ-Co	Co-fcc	
m_S/μemu	-	448.0	1273.4	-	398.3	239.5
m_R/μemu	-	1.2	8.1	-	0.54	1.39
H_c/Oe	-	1.5	0.8	-	2.76	27.6
gold source		HAuCl$_4$			$[(C_6H_5)_3P][AuCl]_4$	
OLA V/ml		0.25			0.5	
$\langle d \rangle_{Au\text{-}control}$/nm	-	3.5 ± 0.9		-	10.7 ± 1.15	
$\langle d \rangle_{Co\text{-}seeds\ 5\,min}$/nm	-	9 ± 1	7.6 ± 1	-	4.9 ± 0.7	$5.1 \pm 0,8$
$\langle d \rangle_{Au\text{-}NP\ 5\,min}$/nm	-	4.1 ± 1.8	5.2 ± 1.5	-	5.1 ± 1	6.3 ± 1.1
$\langle d \rangle_{Co\text{-}seeds\ 20\,min}$/nm	-	8.3 ± 1	7.3 ± 1.1	-	5.6 ± 0.9	5.1 ± 0.6
$\langle d \rangle_{Au\text{-}NP\ 20\,min}$/nm	-	3.8 ± 1.4	5.7 ± 1.6	-	5.1 ± 1	5.8 ± 0.5
$\langle d \rangle_{Co\text{-}seeds\ 45\,min}$/nm	-	8.8 ± 1	7.3 ± 1	-	5.3 ± 0.75	5.1 ± 0.8
$\langle d \rangle_{Au\text{-}NP\ 45\,min}$/nm	-	4.2 ± 1.8	5.9 ± 1.4	-	-	5.9 ± 1.5
$\langle d \rangle_{Co\text{-}seeds\ 60\,min}$/nm	6*	8.6 ± 1.1	7.3 ± 1.1	5-6*	-	5.5 ± 0.8
$\langle d \rangle_{Au\text{-}NP\ 60\,min}$/nm	1.5*	4.4 ± 1.7	5.6 ± 1.2	1.5-2*	5.2 ± 1	6.7 ± 1

9. Outlook

Although several problems preventing the synthesis of core-shell type particles for cobalt and gold have been identified, there are further topics, which could not be addressed in the course of this thesis. First of all, it is not determined yet, what defines the crystal structure of a cobalt nanoparticle. This thesis shows, that the used reactants do not determine the seed particles crystal structure. Hence, identifying the environmental factors influencing the synthesis may lead to stable synthesis routes for different modifications of cobalt. Furthermore, the amines used as a second surfactant besides oleic acid in the seed particle synthesis have a decisive influence on the particles' size. The difference between the amines is, that TOA with its third alkyl chain is much bulkier than DOA, which only has two non-polar tails. TOA possibly limits the monomer mobility in the solution, which would favor the formation of smaller nanoparticles. If the physical structure of the amine has an influence on the monomer mobility, than this can be tested, for example, by repeating the cobalt seed particle synthesis with octylamine instead of TOA or DOA. Octylamine has only a single alkyl chain and is therefore more compact than TOA or DOA. The resulting cobalt seed particles are expected to have a larger mean diameter, than the cobalt particles produced with DOA during the syntheses *Bao2005red* and *Bao2005dir*.

Binding affinities of different surfactants have not been systematically investigated, yet. Superseding experiments[1], investigating which surfactant can replace another with lower binding affinity, can be used to classify how strong different surfactants are attached to the surface of cobalt nanoparticles.

Considerations regarding the gold cobalt interfaces completely neglect surfactant and solvent effects, but surfactants and solvents can change the interfacial or surface energy of a surface they are attached to. This way, it may be possible to change the interfacial energies of participating crystal materials by using different solvents and surfactants for the synthesis step producing the cobalt seed particles and during the shell synthesis step, which probably allows the gold deposits to cover more of the seed particles.

---

[1]This was already done by Vogel [21] for TOPO with several stronger surfactants.

A. Appendix

A.1. Standardprocedures

A.1.1. Preparation of laboratory glass ware

All laboratory glassware used during the syntheses is prepared before to ensure a water-free environment. All used reaction flasks are connected to the Schlenk line and evacuated. Afterwards they are heated with a heat gun evaporating residual water, which is removed by the Schlenk line. When all residues are gone the containers are filled with inert gas, in this case argon. They are only open when connected to argon flow or inside a glove box, filled with inert gas.

A.1.2. Precipitation of nanoparticles

The nanoparticle suspensions need cleaning from reaction residues to be used for electron microscopy samples. Therefore the reaction solution is mixed with the double amount of dried acetonitrile. It is a non-solvent and disables steric stabilization through surfactant molecules. The nanoparticle suspension becomes unstable and the particles precipitate, especially after centrifugation. The supernatant containing the reaction residues is removed and the particle pellet is redispersed in the original volume of fresh solvent. This is repeated three times.

It is possible that particles hardly precipitate. In this case the amount of added acetonitrile needs to be increased. The maximum dimension of containers fitting in the centrifuge usually limits the added amounts. It is also possible to dilute the particle suspension with extra solvent before acetonitrile is added, if the particles cannot be precipitated otherwise.

A.2. Siegbahn- and IUPAC-notations of X-ray photons

IUPAC-notation	Siegbahn-notation
$K\text{-}L_3$	$K_{\alpha 1}$
$K\text{-}L_2$	$K_{\alpha 2}$
$K\text{-}M_3$	$K_{\beta 1}$
$K\text{-}M_2$	$K_{\beta 3}$
$L_3\text{-}M_5$	$L_{\alpha 1}$
$L_3\text{-}M_4$	$L_{\alpha 2}$
$M_5\text{-}N_7$	$M_{\alpha 1}$
$M_5\text{-}N_6$	$M_{\alpha 2}$

Tab. 1.1: List of selected transitions between two electron states noted in Siegbahn- and IUPAC-notation [170]. In case two transitions in one element occurre at approximately the same energy the notations are reduced. For example the transitions $K\text{-}L_2$ and $K\text{-}L_3$ are noted as $K\text{-}L_{2,3}$ following the IUPAC recommendation and as K_α following the Siegbahn-notation.

A.3. Additional measurement techniques

A.3.1. ZFC-measurements

ZFC-measurements to determine the blocking temperature of a nanoparticle sample were conducted by Bao et al. [32] 2007 and therefore a short introduction to the measurement technique is given, but this method is not used to investigate the nanoparticles synthesized for this thesis.

A nanoparticle sample is cooled down to 5 K and an external magnetic field is applied during unfreezing of the sample and its magnetic moment is recorded against its temperature. The magnetic moment shows a maximum value at the blocking temperature. The width of the peak is dependent on the width of the size-distribution. A narrow blocking peak indicates, that all particles switch from ferromagnetic to superparamagnetic behavior at the same temperature, which means, according to (**eq.** 2.28), that all particles have the same volume

and therefore the same diameter. Further details on ZFC-measurements are found for example in the thesis of Ennen [16].

A.3.2. UV-VIS spectroscopy

This technique has not been used during the nanoparticle characterization in this work. However it has been employed by several groups and was used to confirm the core-shell structure by Bao et al. [32]. Therefore a short introduction is given.
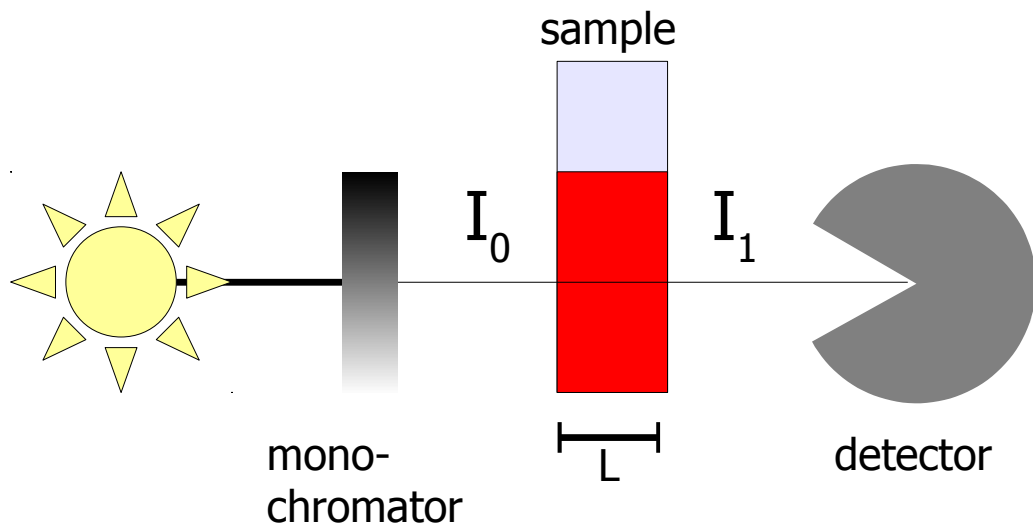
Fig. 1.1: Schematic of a UV-VIS spectrometer setup.

A monochromator selects single wavelengths from a light source emitting in the range between 200 nm and 1100 nm. The light is passed through a sample with thickness l[1]. The intensity I_1 measured behind the sample is compared to the initial intensity I_0. First a background spectrum from pure solvent is recorded, which is afterwards subtracted from the sample's spectrum. This ensures, that absorption effects from the solvent do not influence the results.

The Lambert-Beer-law

$$A_\lambda = \log_{10}\left(\frac{I_0}{I_1}\right) = \epsilon_\lambda \cdot c \cdot l \qquad \textbf{(eq. } 1.1)$$

---

[1]The sample thickness is usually also denoted as d. Since this letter is used for the nanoparticle diameter, l was chosen for the sample thickness in this case.

gives an expression for absorbance at a certain wavelength A_λ depending on the sample thickness l, the concentration c of the absorbing species and extinction coefficient ϵ_λ, which is a material constant. It is used for evaluation of UV-VIS spectroscopy measurements.

The method employed by Bao et al. [32] to confirm the formation of a closed gold shell is based on the work of Oldenburg et al. [93]. The group found, that the plasmon frequency of a metallic shell covering a dielectric core shifts through the spectrum, depending on the thickness ratios between core radius and shell thickness. This effect is based on the general Mie scattering theory for a particle consisting of concentric shells and the special solution for a particle with dielectric core and metallic shell predicts a particle with a variable optical resonance [171]. This was realized with 120 nm silica beads, which were gradually covered by growing gold clusters, which eventually resulted in a closed gold shell. The resonance peak in the spectrum shifted from initial 550 nm to over 800 nm during cluster growth and underwent a blue-shift back to 700 nm, once the shell was completed and only its thickness increased. The peak-shift is even more pronounced if bigger silica beads are used.

Bibliography

[1] Fraunhofer Allianz Nanotechnologie, 2014. URL `http://www.nano.fraunhofer.de/index.html`.

[2] European Comission. Introduction to Nanotechnology, 2013. URL `http://ec.europa.eu/nanotechnology/index_en.html`.

[3] Dr. Abbass A. Hashim (Ed.), editor. *The Delivery of Nanoparticles*, chapter 25 Nanoparticles in Ancient Materials: The Metallic Lustre Decorations of Medieval Ceramics, pages 525–540. InTech, 2012. URL `http://dx.doi.org/10.5772/34080`.

[4] Andreas Cassius. De Extremo Illo Et Perfectissimo Naturae Opificio Ac Principe Terraenorum Sidere Auro. *Hamburgis*, 1685. URL `https://download.digitale-sammlungen.de/pdf/1394958544bsb10310328.pdf`.

[5] Ludovico Cademartiri and Geoffrey A. Ozin. *Concepts of Nanochemistry*. Wiley-VCH, Weinheim, 2009.

[6] E. Ruska. Über Fortschritte im Bau und in der Leistung des magnetischen Elektronenmikroskops. *Zeitschrift für Physik*, 87(9-10):580–602, 1934. URL `http://dx.doi.org/10.1007/BF01333326`.

[7] G. Binnig, H. Rohrer, Ch. Gerber, and E. Weibel. Surface Studies by Scanning Tunneling Microscopy. In H. Neddermeyer, editor, *Scanning Tunneling Microscopy*, volume 6 of *Perspectives in Condensed Matter Physics*, pages 31–35. Springer Netherlands, 1993. URL `http://dx.doi.org/10.1007/978-94-011-1812-5_1`.

[8] G. Binnig, C. F. Quate, and Ch. Gerber. Atomic Force Microscope. *Phys. Rev. Lett.*, 56:930–933, Mar 1986. URL `http://dx.doi.org/10.1103/PhysRevLett.56.930`.

[9] Daniel L. Feldheim and Colby A. Foss Jr., editors. *Metal Nanoparticles : Synthesis, Characterization, and Applications.* Dekker, New York [u.a.], 2002. ISBN 0-8247-0604-8.

[10] Daniela Sudfeld. *Hochauflösende Mikrostrukturanalyse von magnetischen $(Fe_{1-x}Co_x)_{1-y}Pt_y$-Nanopartikeln.* Dissertation, Universität Bielefeld, 2005. URL `http://nbn-resolving.de/urn/resolver.pl?urn=urn:nbn:de:hbz:361-7145`.

[11] Ajay Kumar Gupta and Mona Gupta. Synthesis and Surface Engineering of Iron Oxide Nanoparticles for Biomedical Applications. *Biomaterials*, 26(18):3995 – 4021, 2005. URL `http://dx.doi.org/10.1016/j.biomaterials.2004.10.012`.

[12] Young-wook Jun, Jin-sil Choi, and Jinwoo Cheon. Formkontrolle von Halbleiter- und Metalloxid-Nanokristallen durch Nichthydrolytische Kolloidverfahren. *Angewandte Chemie*, 118(21):3492–3517, 2006. URL `http://dx.doi.org/10.1002/ange.200503821`.

[13] Edson Roberto Leite and Caue Ribeiro. *Crystallization and Growth of Colloidal Nanocrystals.* Springer briefs in materials. Springer, New York [u.a.], 2012. ISBN 978-1-4614-1307-3, 1-4614-1307-9.

[14] Harald F. Krug and Torsten Fleischer. Nanotechnologie - eine Bestandsaufnahme. *umwelt-medizin-gesellschaft*, 20:44–50, 2007. URL `http://www.itas.kit.edu/pub/v/2007/krfl07a.pdf`.

[15] Sergej P. Gubin, editor. *Magnetic Nanoparticles.* Wiley-VCH, Weinheim, 2009. ISBN 978-3-527-40790-3.

[16] Inga Ennen. *Magnetische Nanopartikel als Bausteine für granulare Systeme: Mikrostruktur, Magnetismus und Transporteigenschaften.* Dissertation, Universität Bielefeld, 2008. URL `http://nbn-resolving.de/urn/resolver.pl?urn=urn:nbn:de:hbz:361-14127`.

[17] A. E. Berkowitz, J. R. Mitchell, M. J. Carey, A. P. Young, S. Zhang, F. E. Spada, F. T. Parker, A. Hutten, and G. Thomas. Giant Magnetoresistance in Heterogeneous Cu-Co Alloys. *Phys. Rev. Lett.*, 68:3745–3748, 1992. URL `http://dx.doi.org/10.1103/PhysRevLett.68.3745`.

[18] A. Jordan, P. Wust, H. Fählin, W. John, A. Hinz, and R. Felix. Inductive Heating of Ferrimagnetic Particles and Magnetic Fluids: Physical Evaluation of their Potential for Hyperthermia. *International Journal*

of Hyperthermia, 9(1):51–68, 1993. URL http://dx.doi.org/10.3109/02656739309061478.

[19] Magforce The Nanomedicine Company, 2013. URL http://www.magforce.de/.

[20] B. D. Cullity and C. D. Graham. *Antiferromagnetism*, chapter 5, pages 151–173. John Wiley & Sons, Inc., 2008. ISBN 9780470386323.

[21] Britta Vogel. *Oxidation of Surfactant Stabilized Magnetic Cobalt Nanoparticles*. PhD thesis, Universität Bielefeld, 2011. URL http://nbn-resolving.de/urn:nbn:de:hbz:361-23747838.

[22] Jin Woo Cheon and Jong Park. Method for Synthesis of Core-Shell Type and Solid Solution Alloy Type Metallic Nanoparticles via Transmetalation Reactions and Applications of Same. US patent No. US20030039860 A1, 2004. URL https://www.google.com/patents/US6783569. filed in 2001.

[23] Woo-ram Lee, Min Gyu Kim, Joon-rak Choi, Jong-Il Park, Seung Jin Ko, Sang Jun Oh, and Jinwoo Cheon. Redox-Transmetalation Process as a Generalized Synthetic Strategy for Core-Shell Magnetic Nanoparticles. *Journal of the American Chemical Society*, 127(46):16090–16097, 2005. URL http://dx.doi.org/10.1021/ja053659j.

[24] J. Christopher Love, Lara A. Estroff, Jennah K. Kriebel, Ralph G. Nuzzo, and George M. Whitesides. Self-Assembled Monolayers of Thiolates on Metals as a Form of Nanotechnology. *Chemical Reviews*, 105(4): 1103–1170, 2005. URL http://dx.doi.org/10.1021/cr0300789.

[25] W.L. Zhou, E.E. Carpenter, J. Lin, A. Kumbhar, J. Sims, and C.J. O'Connor. Nanostructures of Gold Coated Iron Core-Shell Nanoparticles and the Nanobands Assembled Under Magnetic Field. *The European Physical Journal D - Atomic, Molecular, Optical and Plasma Physics*, 16 (1):289–292, 2001. URL http://dx.doi.org/10.1007/s100530170112.

[26] Lingyan Wang, Jin Luo, Mathew M. Maye, Quan Fan, Qiang Rendeng, Mark H. Engelhard, Chongmin Wang, Yuehe Lin, and Chuan-Jian Zhong. Iron Oxide-Gold Core-Shell Nanoparticles and Thin Film Assembly. *J. Mater. Chem.*, 15:1821–1832, 2005. URL http://dx.doi.org/10.1039/B501375E.

134

[27] Jennifer L. Lyon, David A. Fleming, Matthew B. Stone, Peter Schiffer, and Mary Elizabeth Williams. Synthesis of Fe-Oxide-Core/Au-Shell Nanoparticles by Iterative Hydroxylamine Seeding. *Nano Letters*, 4(4): 719–723, 2004. URL `http://dx.doi.org/10.1021/nl035253f`.

[28] S. Sao-Joao, S. Giorgio, J. M. Penisson, C. Chapon, S. Bourgeois, and C. Henry. Structure and Deformations of Pd-Ni Core-Shell Nanoparticles. *The Journal of Physical Chemistry B*, 109(1):342–347, 2005. URL `http://dx.doi.org/10.1021/jp040473i`.

[29] J. Yang, Jim Yang Lee, and Heng-Phon Too. Core-Shell Ag-Au Nanoparticles from Replacement Reaction in Organic Medium. *The Journal of Physical Chemistry B*, 109(41):19208–19212, 2005. URL `http://dx.doi.org/10.1021/jp052242x`.

[30] Hye-Young Park, Mark J. Schadt, Wang, I-Im Stephanie Lim, Peter N. Njoki, Soo Hong Kim, Min-Young Jang, Jin Luo, and Chuan-Jian Zhong. Fabrication of Magnetic Core@Shell Fe Oxide@Au Nanoparticles for Interfacial Bioactivity and Bio-separation. *Langmuir*, 23(17):9050–9056, 2007. URL `http://dx.doi.org/10.1021/la701305f`.

[31] Y. Bao, A. B. Pakhomov, and K. M. Krishnan. A General Approach to Synthesis of Nanoparticles with Controlled Morphologies and Magnetic Properties. *Journal of Applied Physics*, 97(10):10J317 –10J317–3, 2005. URL `http://dx.doi.org/10.1063/1.1853991`.

[32] Yuping Bao, Hector Calderon, and Kannan M. Krishnan. Synthesis and Characterization of Magnetic-Optical Co-Au Core-Shell Nanoparticles. *The Journal of Physical Chemistry C*, 111(5):1941–1944, 2007. URL `http://dx.doi.org/10.1021/jp066871y`.

[33] Victor K. LaMer and Robert H. Dinegar. Theory, Production and Mechanism of Formation of Monodispersed Hydrosols. *Journal of the American Chemical Society*, 72(11):4847–4854, 1950. URL `http://dx.doi.org/10.1021/ja01167a001`.

[34] Víctor Antonio de la Peña O'Shea, Iberio de P. R. Moreira, Alberto Roldán, and Francesc Illas. Electronic and Magnetic Structure of Bulk Cobalt: The α-, β, and ϵ-Phases from Density Functional Theory Calculations. *The Journal of Chemical Physics*, 133(2):024701, 2010. URL `http://dx.doi.org/10.1063/1.3458691`.

[35] Sergei P Gubin, Yurii A Koksharov, G B Khomutov, and Gleb Y. Yurkov. Magnetic Nanoparticles: Preparation, Structure and Properties. *Russian Chemical Reviews*, 74(6):489, 2005. URL `http://dx.doi.org/10.1070/RC2005v074n06ABEH000897`.

[36] Karl Winnacker and Roland Dittmeyer, editors. *Chemische Technik : Prozesse und Produkte, Band 2 - Neue Technologien*, chapter 9. Nanomaterialien und Nanotechnologie, pages 821 – 906. Wiley-VCH, Weinheim, 2004.

[37] John W. Mullin. *Crystallization*. Butterworth-Heinemann, Oxford [u.a.], 2004. ISBN 0-7506-4833-3.

[38] Jongnam Park, Jin Joo, Soo Gu Kwon, Youngjin Jang, and Taeghwan Hyeon. Synthesis of Monodisperse Spherical Nanocrystals. *Angewandte Chemie International Edition*, 46(25):4630–4660, 2007. URL `http://dx.doi.org/10.1002/anie.200603148`.

[39] Andreas Hütten, Daniela Sudfeld, Inga Ennen, Günter Reiss, Wiebke Hachmann, Ulrich Heinzmann, Klaus Wojczykowski, Peter Jutzi, Wahib Saikaly, and Gareth Thomas. New Magnetic Nanoparticles for Biotechnology. *Journal of Biotechnology*, 112(1-2):47 – 63, 2004. URL `http://dx.doi.org/110.1016/j.jbiotec.2004.04.019`.

[40] David A. Porter, Kenneth E. Easterling, and Mohamed Y. Sherif. *Phase Transformations in Metals and Alloys*. CRC Press, Boca Raton, FL [u.a.], 2009. ISBN 978-1-4200-6210-6.

[41] Dove PM, De Yoreo JJ, Weiner S., editor. *Biomineralization*, volume 54 of *Reviews in Mineralogy & Geochemistry*, chapter 3. Principles of Crystal Nucleation & Growth, pages 57 – 93. Mineralogical Society of America and Geochemical Society, 1st edition, 2003. ISBN 0-939950-66-9; 13 978-0-939950-66-9.

[42] Jess Patrick Wilcoxon and Paula P. Provencio. Heterogeneous Growth of Metal Clusters from Solutions of Seed Nanoparticles. *Journal of the American Chemical Society*, 126(20):6402–6408, 2004. URL `http://dx.doi.org/10.1021/ja031622y`.

[43] Howard Reiss. The Growth of Uniform Colloidal Dispersions. *The Journal of Chemical Physics*, 19(4):482–487, 1951. URL `http://dx.doi.org/10.1063/1.1748251`.

[44] M.P. Pileni. Self-Assemblies of Nanocrystals: Fabrication and Collective Properties. *Applied Surface Science*, 171(1-2):1 – 14, 2001. URL `http://dx.doi.org/10.1016/S0169-4332(00)00553-5`.

[45] Natalie Palina. *Novel Magnetic Nanoparticles: Size and Surfactant Effects on Geometric and Electronic Structure, probed using X-ray Absorption Spectroscopy*. PhD thesis, Universität Bonn, Physikalisches Institut, 2005. URL `http://hss.ulb.uni-bonn.de/2005/0627/0627.htm`.

[46] *Manual IGOR Pro Version 6.3*. WaveMetrics Inc., 2013.

[47] Eric W. Weisstein. "normal distribution.". From MathWorld–A Wolfram Web Resource., 2013. URL `http://mathworld.wolfram.com/LogNormalDistribution.html`.

[48] Andrey L. Rogach, Dmitri V. Talapin, Elena V. Shevchenko, Andreas Kornowski, Markus Haase, and Horst Weller. Organization of Matter on Different Size Scales: Monodisperse Nanocrystals and Their Superstructures. *Advanced Functional Materials*, 12(10):653–664, 2002. URL `http://dx.doi.org/10.1002/1616-3028(20021016)12:10<653::AID-ADFM653>3.0.CO;2-V`.

[49] Carl Wagner. Theorie der Alterung von Niederschlägen durch Umlösen (Ostwald-Reifung). *Zeitschrift für Elektrochemie, Berichte der Bunsengesellschaft für physikalische Chemie*, 65(7-8):581–591, 1961. URL `http://dx.doi.org/10.1002/bbpc.19610650704`.

[50] V. M. Burlakov and L. Kantorovich. Ostwald Ripening of Binary Alloy Particles. *The Journal of Chemical Physics*, 134(2):024521, 2011. URL `http://dx.doi.org/10.1063/1.3530287`.

[51] D. Sudfeld, K. Wojczykowski, W. Hachmann, S. Heitmann, K. Rott, T. Hempel, S. Kammerer, P. Jutzi, A. Hütten, and G. Reiss. Magnetic Cobalt Nanocrystals Organized in Patches and Chains. *Magnetics, IEEE Transactions on*, 38(5):2601–2603, 2002. URL `http://dx.doi.org/10.1109/TMAG.2002.803211`.

[52] Robert Finsy. On the Critical Radius in Ostwald Ripening. *Langmuir*, 20(7):2975–2976, 2004. URL `http://dx.doi.org/10.1021/la035966d`.

[53] Eckhard Limpert, Werner A. Stahel, and Markus Abbt. Log-Normal Distributions Across the Sciences: Keys and Clues. *BioScience*, 51(5):pp.

341–352, 2001. URL `http://dx.doi.org/10.1641/0006-3568(2001)051[0341:LNDATS]2.0.CO;2`.

[54] Eric W. Weisstein. "log normal distribution.". From MathWorld–A Wolfram Web Resource., 2013. URL `http://mathworld.wolfram.com/LogNormalDistribution.html`.

[55] Michael Peter. *Funktionalisierung und Kontrolle der Morphologie von Cobalt- und Siliciumdioxidnanopartikel*. Dissertation, Universität Bielefeld, Fakultät für Chemie, 2012.

[56] Dieter Horn and Jens Rieger. Organische Nanopartikel in wässriger Phase - Theorie, Experiment und Anwendung. *Angewandte Chemie*, 113(23):4460–4492, 2001. URL `http://dx.doi.org/10.1002/1521-3757(20011203)113:23<4460::AID-ANGE4460>3.0.CO;2-1`.

[57] Joachim Stöhr and Hans Christoph Siegmann. *Magnetism*. Springer-Verlag Berlin Heidelberg, 2006. ISBN 3-540-30282-4, 978-3-540-30282-7.

[58] Paul Allen Tipler and Gene Mosca. *Physik für Wissenschaftler und Ingenieure*. Elsevier, Spektrum Akad. Verl., München, 2004. ISBN 3-8274-1164-5.

[59] Wolfgang Nolting and Anupuru Ramakanth. *Quantum Theory of Magnetism*. Springer-Verlag Berlin Heidelberg, Berlin, Heidelberg, 2009. ISBN 978-3-540-85416-6.

[60] Horst Kuchling. *Taschenbuch der Physik*. Fachbuchverl. Leipzig im Carl-Hanser-Verl., München [u.a.], 2004. ISBN 3-446-22883-7.

[61] J. K. Watson. *Applications of Magnetism*. John, 1980. ISBN 0-471-03540-8.

[62] Ellen Ivers-Tiffée and Waldemar von Münch. *Werkstoffe der Elektrotechnik*, chapter 6. Magnetische Werkstoffe, pages 183–208. Teubner, 2007. URL `http://dx.doi.org/10.1007/978-3-8351-9088-7_6`.

[63] William D. Callister and David G. Rethwisch. *Materialwissenschaften und Werkstofftechnik. Eine Einführung*. Wiley-VCH-Verl., Weinheim, 2013. ISBN 978-3-527-33007-2, 3-527-33007-0.

[64] B. D. Cullity and C. D. Graham. *Fine Particles and Thin Films*, chapter 11, pages 359–408. John Wiley & Sons, Inc., 2008. ISBN 9780470386323.

[65] C.B. Murray, Shouheng Sun, Hugh Doyle, and T. Betley. Monodisperse 3d Transition-Metal (Co,Ni,Fe) Nanoparticles and Their Assembly into-Nanoparticle Superlattices. *MRS Bulletin*, 26:985–991, 11 2001. ISSN 1938-1425. URL `http://dx.doi.org/10.1557/mrs2001.254`.

[66] B. D. Cullity and C. D. Graham. *Magnetic Anisotropy*, chapter 7, pages 197–240. John Wiley & Sons, Inc., 2008. ISBN 9780470386323.

[67] Victor F. Puntes, Kannan M. Krishnan, and Paul Alivisatos. Synthesis, Self-Assembly and Magnetic Behavior of a Two-Dimensional Superlattice of Single-Crystal ϵ-Co Nanoparticles. *Applied Physics Letters*, 78(15): 2187–2189, 2001. URL `http://dx.doi.org/10.1063/1.1362333`.

[68] H. T. Yang, C. M. Shen, Y. K. Su, T. Z. Yang, H. J. Gao, and Y. G. Wang. Self-Assembly and Magnetic Properties of Cobalt Nanoparticles. *Applied Physics Letters*, 82(26):4729–4731, 2003. URL `http://dx.doi.org/10.1063/1.1586481`.

[69] Wolfgang Demtröder. *Experimentalphysik 1. Mechanik und Wärme.* Springer-Verlag Berlin Heidelberg, Berlin, Heidelberg, 2006. ISBN 978-3-540-29934-9.

[70] Ludwig Reimer. *Elektronenmikroskopische Untersuchungs- und Präparationsmethoden.* Springer, Berlin [u.a.], 1967.

[71] Ludwig Reimer and Gerhard Pfefferkorn. *Raster-Elektronenmikroskopie.* Springer, Berlin [u.a.], 1973. ISBN 3-540-06102-9, 0-387-06102-9.

[72] F. Krumeich. The Electron Microscopy Site - TEM, 2012. URL `http://www.microscopy.ethz.ch/elmi-home.htm`.

[73] Brent Fultz and James M. Howe. *Transmission Electron Microscopy and Diffractometry of Materials.* Springer-Verlag Berlin Heidelberg, Berlin, Heidelberg, 2008. ISBN 978-3-540-73886-2.

[74] David J. Smith. *Handbook of Microscopy for Nanotechnology*, chapter Chapter 14: High Resolution Transmission Electron Microscopy, pages 427–453. Kluwer Academic Publishers, Boston, MA, 2005. ISBN 978-1-4020-8006-7.

[75] Brent Fultz, James Howe. *Transmission Electron Microscopy and Diffractometry of Materials*, chapter 6. Electron Diffraction and Crystallography, pages 273 – 336. Springer Berlin Heidelberg New York, 2008. ISBN 978-3-540-73886-2.

[76] Dr. Aicha Hessler-Wyser. Intensive SEM/TEM Training Course. Slides from the Annual Course, 2011. URL `http://cime.epfl.ch/MSE-603`.

[77] F. Krumeich. Electron Microscopy Site - STEM, 2012. URL `http://www.microscopy.ethz.ch/elmi-home.htm`.

[78] J. M. Cowley. *Handbook of Microscopy for Nanotechnology,*, chapter 15: Scanning Transmission Electron Microscopy, pages 455 – 491. Kluwer Academic Publishers, Boston, MA, 2005. ISBN 978-1-4020-8006-7.

[79] D.B. Williams and C.B. Carter. *Transmission Electron Microscopy: A Textbook for Materials Science.* Number Bd. 1 in Cambridge library collection. Springer London, Limited, 2009. ISBN 9780387765006.

[80] S J Pennycook. Z-Contrast Transmission Electron Microscopy: Direct Atomic Imaging of Materials. *Annual Review of Materials Science*, 22 (1):171–195, 1992. URL `http://dx.doi.org/10.1146/annurev.ms.22.080192.001131`.

[81] Joseph I. Goldstein. *Scanning Electron Microscopy and X-Ray Microanalysis.* Springer, New York, NY, 2007. ISBN 978-0-306-47292-3.

[82] Frank Krumeich. Properties of Electrons, Their Interactions with Matter and Applications in Electron Microscopy, 2012. URL `http://www.microscopy.ethz.ch/downloads/Interactions.pdf`.

[83] Sebastian Kiehlmann. Physik IV: Quantenphysik, Atom- und Molekülphysik - Röntgenstrahlung, 2011. URL `http://lp.uni-goettingen.de/get/text/6634#`.

[84] J. A. Bearden and A. F. Burr. Reevaluation of X-Ray Atomic Energy Levels. *Rev. Mod. Phys.*, 39:125–142, Jan 1967. URL `http://dx.doi.org/10.1103/RevModPhys.39.125`.

[85] NIST - National Institute of Standards and Technology. X-ray Transition Energes Database, 2013. URL `http://physics.nist.gov/PhysRefData/XrayTrans/Html/search.html`.

[86] *MicroMag 2900 Alternating Gradient Magnetometer (AGM) Instruction Manual.* Princeton Measurement Corporation (now part of LakeShore), 575 MCCORKLE BLVD, WESTERVILLE, OH 43082, 2001.

[87] Inga Ennen. Charakterisierung von Cobalt-Nanopartikeln und Untersuchungen zur Herstellung granularer Strukturen. Diplomarbeit, Universität Bielefeld, Fakultät für Physik, 2003.

[88] Harald Krischner and Brigitte Koppelhuber-Bitschnau. *Röntgenstrukturanalyse und Rietveldmethode. Eine Einführung.* Vieweg, Braunschweig [u.a.], 1994. ISBN 3-528-48324-5.

[89] R.T. Downs and M. Hall-Wallace. The American Mineralogist Crystal Structure Database. American Mineralogist 88, 247-250., 2003. URL `http://rruff.geo.arizona.edu/AMS/amcsd.php`.

[90] FIZ/NIST Inorganic Crystal Structure Database (ICSD), 2008. URL `http://www.nist.gov/srd/nist84.cfm,http://www.fiz-karlsruhe.de/icsd.html`.

[91] Markus Meinert. Personal correspondance. University of Bielefeld, 2013.

[92] R.F. Egerton. Electron Energy-Loss Spectroscopy in the TEM. *Reports on Progress in Physics*, 72(1):016502, 2009. URL `http://dx.doi.org/10.1088/0034-4885/72/1/016502`.

[93] S.J. Oldenburg, R.D. Averitt, S.L. Westcott, and N.J. Halas. Nano-engineering of Optical Resonances. *Chemical Physics Letters*, 288(2-4):243 – 247, 1998. URL `http://dx.doi.org/10.1016/S0009-2614(98)00277-2`.

[94] Dmitry P. Dinega and M. G. Bawendi. A Solution-Phase Chemical Approach to a New Crystal Structure of Cobalt. *Angewandte Chemie International Edition*, 38(12):1788–1791, 1999. URL `http://dx.doi.org/10.1002/(SICI)1521-3773(19990614)38:12<1788::AID-ANIE1788>3.0.CO;2-2`.

[95] C. B. Shoemaker, D. P. Shoemaker, T. E. Hopkins, and S. Yindepit. Refinement of the Structure of β-Manganese and of a Related Phase in the Mn–Ni–Si system. *Acta Crystallographica Section B*, 34(12):3573–3576, Dec 1978. URL `http://dx.doi.org/10.1107/S0567740878011620`.

[96] R.W.G. Wyckoff. *Crystal Structures*, volume 1. Interscience Publishers, New York, 2nd edition edition, 1963. URL `http://books.google.de/books?id=n4IvAQAAIAAJ&dq=ISBN:0898743885,ISBN:9780898743883&hl=&source=gbs_api`.

[97] Victor F. Puntes, Kannan M. Krishnan, and A. Paul Alivisatos. Colloidal Nanocrystal Shape and Size Control: The Case of Cobalt. *Science*, 291 (5511):2115–2117, 2001. URL `http://dx.doi.org/10.1126/science.1058495`.

[98] Dorothy Farrell, Sara A. Majetich, and Jess P. Wilcoxon. Preparation and Characterization of Monodisperse Fe Nanoparticles. *The Journal of Physical Chemistry B*, 107(40):11022–11030, 2003. URL `http://dx.doi.org/10.1021/jp0351831`.

[99] Yuping Bao, Michael Beerman, Alexandre B. Pakhomov, and Kannan M. Krishnan. Controlled Crystalline Structure and Surface Stability of Cobalt Nanocrystals. *The Journal of Physical Chemistry B*, 109(15):7220–7222, 2005. URL `http://dx.doi.org/10.1021/jp044363n`.

[100] Markus Meinert. *Ferrimagnetic Heusler Compounds : from First Principles to Thin Films*. PhD thesis, Bielefeld University, 2011. URL `http://nbn-resolving.de/urn:nbn:de:hbz:361-24545839`.

[101] Mark Green. Organometallic Based Strategies for Metal Nanocrystal Synthesis. *Chem. Commun.*, 24:3002–3011, 2005. URL `http://dx.doi.org/10.1039/B501835H`.

[102] Taeghwan Hyeon. Chemical Synthesis of Magnetic Nanoparticles. *Chem. Commun.*, 0:927–934, 2003. URL `http://dx.doi.org/10.1039/B207789B`.

[103] Jae-Woo Kim, Sang H. Choi, Peter T. Lillehei, Sang-Hyon Chu, Glen C. King, and Gerald D. Watt. Cobalt Oxide Hollow Nanoparticles Derived by Bio-Templating. *Chemical Communications*, 32:4101–4103, 2005. URL `http://dx.doi.org/10.1039/B505097A`.

[104] Yadong Yin, Robert M. Rioux, Can K. Erdonmez, Steven Hughes, Gabor A. Somorjai, and A. Paul Alivisatos. Formation of Hollow Nanocrystals Through the Nanoscale Kirkendall Effect. *Science*, 304(5671):711–714, 2004. URL `http://dx.doi.org/10.1126/science.1096566`.

[105] E. Girgis, W.K.B. Khalil, A.N. Emam, M.B. Mohamed, and K. Venkat Rao. Nanotoxicity of Gold and Gold–Cobalt Nanoalloy. *Chemical Research in Toxicology*, 25(5):1086–1098, 2012. URL `http://dx.doi.org/10.1021/tx300053h`.

[106] L. Vitos, A.V. Ruban, H.L. Skriver, and J. Kollár. The Surface Energy of Metals. *Surface Science*, 411(1-2):186 – 202, 1998. URL `http://dx.doi.org/10.1016/S0039-6028(98)00363-X`.

[107] W.R. Tyson and W.A. Miller. Surface Free Energies of Solid Metals: Estimation from Liquid Surface Tension Measurements. *Surface Science*, 62 (1):267 – 276, 1977. URL `http://dx.doi.org/10.1016/0039-6028(77)90442-3`.

[108] Bernard Vinet, Lena Magnusson, Hasse Fredriksson, and Pierre Jean Desre. Correlations Between Surface and Interface Energies with Respect to Crystal Nucleation. *Journal of Colloid and Interface Science*, 255(2): 363 – 374, 2002. ISSN 0021-9797. doi: http://dx.doi.org/10.1006/jcis.2002.8627. URL `http://www.sciencedirect.com/science/article/pii/S0021979702986273`.

[109] Richard C. Tolman. The Effect of Droplet Size on Surface Tension. *The Journal of Chemical Physics*, 17(3):333–337, 1949. URL `http://dx.doi.org/10.1063/1.1747247`.

[110] Don H. Rasmussen. Energetics of Homogeneous Nucleation - Approach to a Physical Spinodal. *Journal of Crystal Growth*, 56(1):45 – 55, 1982. URL `http://dx.doi.org/10.1016/0022-0248(82)90011-2`.

[111] D. Jayaraman, C. Subramanian, R. Dhanasekaran, and P. Ramasamy. Kinetic Process of Homogeneous Nucleation Incorporating the Effect of Curvature . *Journal of Crystal Growth*, 79(1, Part 2):997 – 1000, 1986. URL `http://dx.doi.org/10.1016/0022-0248(86)90585-3`.

[112] J.W. Gibbs. *Transactions of the Connecticut Academy of Arts and Sciences.*, volume v.3 (1874-1878), chapter Equilibrium of Heterogeneous Substances, page 343. New Haven: Published by the Academy, 1874-1878. URL `http://www.biodiversitylibrary.org/item/32295`.

[113] R. Mahnke and J. Schmelzer. A New and General Formula for the Curvature Dependence of Surface Tension of Droplets. *Z. phys. Chemie (Leipzig)*, 266:1028–1031, 1985.

[114] Z. Kožíšek. Influence of the Curvature Dependence of Interfacial Energy on Homogeneous Nucleation Kinetics. *Crystal Research and Technology*, 26 (1):3–10, 1991. URL `http://dx.doi.org/10.1002/crat.2170260102`.

[115] Yuping Bao, Wei An, C. Heath Turner, and Kannan M. Krishnan. The Critical Role of Surfactants in the Growth of Cobalt Nanoparticles. *Langmuir*, 26(1):478–483, 2010. URL `http://pubs.acs.org/doi/abs/10.1021/la902120e`.

[116] Paul Boyer, David Ménard, and Michel Meunier. Nanoclustered Co-Au Particles Fabricated by Femtosecond Laser Fragmentation in Liquids. *The Journal of Physical Chemistry C*, 114(32):13497–13500, 2010. URL `http://dx.doi.org/10.1021/jp1037552`.

[117] Tapan Chatterji, Yixi Su, Gail N. Iles, Yi-Cheng Lee, Amit P. Khandhar, and Kannan M. Krishnan. Antiferromagnetic Spin Correlations in MnO Nanoparticles. *Journal of Magnetism and Magnetic Materials*, 322(21):3333–3336, 2010. URL `http://dx.doi.org/10.1016/j.jmmm.2010.06.019`.

[118] Yongjun Feng, Ting He, and Nicolas Alonso-Vante. In Situ Free-Surfactant Synthesis and ORR-Electrochemistry of Carbon-Supported Co_3S_4 and $CoSe_2$ Nanoparticles. *Chemistry of Materials*, 20(1):26–28, 2007. URL `http://dx.doi.org/10.1021/cm7024763`.

[119] M. Sachan, N. D. Walrath, S. A. Majetich, K. Krycka, and Chi-Chang Kao. Interaction Effects within Langmuir Layers and Three-Dimensional Arrays of ϵ-Co Nanoparticles. *Journal of Applied Physics*, 99(8):08C302, 2006. URL `http://dx.doi.org/10.1063/1.2168438`.

[120] Youhui Gao, Daisuke Shindo, Yuping Bao, and Kannan Krishnan. Electron Holography of Core-Shell Co/CoO Spherical Nanocrystals. *Applied Physics Letters*, 90(23):233105, 2007. URL `http://dx.doi.org/10.1063/1.2747052`.

[121] K.M. Krishnan, A.B. Pakhomov, Y. Bao, P. Blomqvist, Y. Chun, M. Gonzales, K. Griffin, X. Ji, and B.K. Roberts. Nanomagnetism and Spin Electronics: Materials, Microstructure and Novel Properties. *Journal of Materials Science*, 41(3):793–815, 2006. URL `http://dx.doi.org/10.1007/s10853-006-6564-1`.

[122] K.M. Krishnan. Biomedical Nanomagnetics: A Spin Through Possibilities in Imaging, Diagnostics, and Therapy. *IEEE Transactions on Magnetics*, 46(7):2523 –2558, 2010. URL `http://dx.doi.org/10.1109/TMAG.2010.2046907`.

[123] V. Kumar and S.K. Yadav. Synthesis of Different-Sized Silver Nanoparticles by Simply Varying Reaction Conditions with Leaf Extracts of Bauhinia variegata L. *Nanobiotechnology, IET*, 6(1):1 –8, 2012. URL `http://dx.doi.org/10.1049/iet-nbt.2010.0015`.

[124] Andrew H Latham and Mary Elizabeth Williams. Transmission Electron Microscope-Induced Structural Evolution in Amorphous Fe, Co, and Ni Oxide Nanoparticles. *Langmuir*, 24(24):14195–14202, 2008. URL `http://dx.doi.org/10.1021/la7035423`.

[125] JitKang Lim, Alexander Eggeman, Frederick Lanni, Robert D. Tilton, and Sara A. Majetich. Synthesis and Single-Particle Optical Detection of Low-Polydispersity Plasmonic-Superparamagnetic Nanoparticles. *Advanced Materials*, 20(9):1721–1726, 2008. URL `http://dx.doi.org/10.1002/adma.200702196`.

[126] Alexandre B. Pakhomov, Yuping Bao, and Kannan M. Krishnan. Effects of Surfactant Friction on Brownian Magnetic Relaxation in Nanoparticle Ferrofluids. *Journal of Applied Physics*, 97(10):10Q305–10Q305, 2005. URL `http://dx.doi.org/10.1063/1.1855195`.

[127] Lirong Ren, Lin He, Chinping Chen, Michael Wark, Chunping Li, Ping Che, and Lin Guo. Microstructure and Magnetic Properties of Tubular Cobalt–Silica Nanocomposites. *Journal of Magnetism and Magnetic Materials*, 312(2):405–409, 2007. URL `http://dx.doi.org/10.1016/j.jmmm.2006.11.126`.

[128] Justus Schällibaum, Florian H. Dalla Torre, Walter R. Caseri, and Jorg F. Loffler. Large-Scale Synthesis of Defined Cobalt Nanoparticles and Magnetic Metal-Polymer Composites. *Nanoscale*, 1:374–381, 2009. URL `http://dx.doi.org/10.1039/B9NR00230H`.

[129] Tianlong Wen and Kannan M Krishnan. Thermal Stability and Morphological Transformations of Au_{core} - Co_{shell} Nanocrucibles. *The Journal of Physical Chemistry C*, 114(35):14838–14842, 2010. URL `http://dx.doi.org/10.1021/jp1053666`.

[130] Yoh Yamamoto and Kyungwha Park. Metastability for the Blume-Capel Model with Distribution of Magnetic Anisotropy using Different Dynamics. *Phys. Rev. E*, 88:012110, 2013. URL `http://dx.doi.org/10.1103/PhysRevE.88.012110`.

[131] Svetlana Zinoveva. *Investigation of Co Nanoparticle Formation Using Time Dependent and Spatially Resolved X-ray Absorption Spectroscopy.* PhD thesis, Rheinischen Friedrich-Wihelms-Universität Bonn, Mathematisch-Naturwissenschaftliche Fakultät, 2008. URL `http://hss.ulb.uni-bonn.de/2008/1371/1371.pdf`.

[132] Stephanie H. Johnson, Craig L. Johnson, Steven J. May, Samuel Hirsch, M. W. Cole, and Jonathan E. Spanier. Co@CoO@Au Core-Multi-Shell Nanocrystals. *J. Mater. Chem.*, 20:439–443, 2010. URL `http://dx.doi.org/10.1039/B919610B`.

[133] Saikat Mandal and Kannan M. Krishnan. $Co_{core} Au_{shell}$ Nanoparticles: Evolution of Magnetic Properties in the Displacement Reaction. *J. Mater. Chem.*, 17:372–376, 2007. URL `http://dx.doi.org/10.1039/B613371C`.

[134] Dingsheng Wang and Yadong Li. One-pot Protocol for Au-Based Hybrid Magnetic Nanostructures via a Noble-Metal-Induced Reduction Process. *Journal of the American Chemical Society*, 132(18):6280–6281, 2010. URL `http://dx.doi.org/10.1021/ja100845v`.

[135] Tianlong Wen and Kannan M Krishnan. Cobalt-Based Magnetic Nanocomposites: Fabrication, Fundamentals and Applications. *Journal of Physics D: Applied Physics*, 44(39):393001, 2011. URL `http://dx.doi.org/10.1088/0022-3727/44/39/393001`.

[136] Javier Jimenez, Roman Sheparovych, Marcos Pita, Arántzazu Narvaez García, Elena Dominguez, Sergiy Minko, and Evgeny Katz. Magneto-Induced Self-Assembling of Conductive Nanowires for Biosensor Applications. *The Journal of Physical Chemistry C*, 112(19):7337–7344, 2008. URL `http://dx.doi.org/10.1021/jp800013n`.

[137] Albert Figuerola, Angela Fiore, Riccardo Di Corato, Andrea Falqui, Cinzia Giannini, Edoardo Micotti, Alessandro Lascialfari, Maurizio Corti, Roberto Cingolani, Teresa Pellegrino, et al. One-Pot Synthesis and Characterization of Size-Controlled Bimagnetic FePt-Iron Oxide Heterodimer Nanocrystals. *Journal of the American Chemical Society*, 130 (4):1477–1487, 2008. URL `http://dx.doi.org/10.1021/ja078034v`.

[138] Dong Chen, Jiajun Li, Chunsheng Shi, Xiwen Du, Naiqin Zhao, Jing Sheng, and Shuo Liu. Properties of Core-Shell Ni-Au Nanoparticles Synthesized Through a Redox-Transmetalation Method in Reverse Microemulsion. *Chemistry of materials*, 19(14):3399–3405, 2007. URL `http://dx.doi.org/10.1021/cm070182x`.

[139] Houde She, Yuanzhi Chen, Xiaozhen Chen, Kun Zhang, Ziyuan Wang, and Dong-Liang Peng. Structure, Optical and Magnetic Properties of Ni@ Au and Au@ Ni Nanoparticles Synthesized via Non-Aqueous Approaches. *Journal of Materials Chemistry*, 22(6):2757–2765, 2012. URL http://dx.doi.org/10.1039/C1JM14479K.

[140] Mallikarjuna N Nadagouda and Rajender S Varma. A Greener Synthesis of Core (Fe, Cu)-Shell (Au, Pt, Pd, and Ag) Nanocrystals Using Aqueous Vitamin C. *Crystal Growth and Design*, 7(12):2582–2587, 2007. URL http://dx.doi.org/10.1021/cg070554e.

[141] Sougata Sarkar, Arun Kumar Sinha, Mukul Pradhan, Mrinmoyee Basu, Yuichi Negishi, and Tarasankar Pal. Redox Transmetalation of Prickly Nickel Nanowires for Morphology Controlled Hierarchical Synthesis of Nickel/Gold Nanostructures for Enhanced Catalytic Activity and SERS Responsive Functional Material. *The Journal of Physical Chemistry C*, 115(5):1659–1673, 2010. URL http://dx.doi.org/10.1021/jp109572c.

[142] Youyi Sun, Binghua Yang, Ye Tian, Guizhen Guo, Wei Cai, Minghong He, and Yaqing Liu. Facile Synthesis of Ag-Fe_2O_3 Core-Shell Composite Nanoparticles by an In-Situ Method. *Micro & Nano Letters*, 6(2):82–85, 2011. URL http://dx.doi.org/10.1049/mnl.2010.0149.

[143] X Wei, D Le Roy, R Skomski, XZ Li, Z Sun, JE Shield, MJ Kramer, and DJ Sellmyer. Structure and Magnetism of MnAu Nanoclusters. *Journal of Applied Physics*, 109:07B523, 2011. URL http://dx.doi.org/10.1063/1.3559502.

[144] Xuegang Yu, Jiaqi Wan, Yan Shan, Kezheng Chen, and Xiaodong Han. A Facile Approach to Fabrication of Bifunctional Magnetic-Optical Fe_3O_4@ ZnS Microspheres. *Chemistry of Materials*, 21(20):4892–4898, 2009. URL http://dx.doi.org/10.1021/cm902667b.

[145] Jun Yang, Jim Yang Lee, and Jackie Y Ying. Phase Transfer and its Applications in Nanotechnology. *Chemical Society Reviews*, 40(3):1672–1696, 2011. URL http://dx.doi.org/10.1039/B916790K.

[146] Catherine Amiens, Bruno Chaudret, Diana Ciuculescu-Pradines, Vincent Collière, Katia Fajerwerg, Pierre Fau, Myrtil Kahn, André Maisonnat, Katerina Soulantica, and Karine Philippot. Organometallic Approach for the Synthesis of Nanostructures. *New Journal of Chemistry*, 37(11): 3374–3401, 2013. URL http://dx.doi.org/10.1039/C3NJ00650F.

147

[147] Neha Arora and Balaji R Jagirdar. Carbonization of Solvent and Capping Agent Based Enhancement in the Stabilization of Cobalt Nanoparticles and Their Magnetic Study. *Journal of Materials Chemistry*, 22(38): 20671–20679, 2012. URL `http://dx.doi.org/10.1039/C2JM33712F`.

[148] Davide Bochicchio and Riccardo Ferrando. Morphological Instability of Core-Shell Metallic Nanoparticles. *Physical Review B*, 87(16):165435, 2013. URL `http://dx.doi.org/10.1103/PhysRevB.87.165435`.

[149] Jennifer N Duggan, Michael J Bozack, and Christopher B Roberts. The Synthesis and Arrested Oxidation of Amorphous Cobalt Nanoparticles Using DMSO as a Functional Solvent. *Journal of Nanoparticle Research*, 15(11):1–16, 2013. URL `http://dx.doi.org/10.1007/s11051-013-2089-0`.

[150] E Folcke, JM Le Breton, W Lefebvre, J Bran, R Lardé, F Golkar, and JE Shield. Investigation of the Magnetic Properties of FeAu Nanoclusters in a W-Matrix: Evidence for Exchange-Bias Phenomenon. *Journal of Applied Physics*, 113(18):183903–183903, 2013. URL `http://dx.doi.org/10.1063/1.4803129`.

[151] Xue Han, Win-Jing Qin, Jing Sun, Jing Yang, Kai-Yang Niu, Hong-Li Wang, and Xi-Wen Du. Surfactant-Assisted Synthesis of ZnO–Au Nanostructure with Good Dispersibility. *Journal of Alloys and Compounds*, 477(1):661–664, 2009. URL `http://dx.doi.org/10.1016/j.jallcom.2008.10.083`.

[152] Yibo Hu, Kai Tao, Chunzheng Wu, Chen Zhou, Hongfeng Yin, and Shenghu Zhou. Size-Controlled Synthesis of Highly Stable and Active Pd@ SiO_2 Core–Shell Nanocatalysts for Hydrogenation of Nitrobenzene. *The Journal of Physical Chemistry C*, 117(17):8974–8982, 2013. URL `http://dx.doi.org/10.1021/jp3110375`.

[153] Amit P. Khandhar, R. Matthew Ferguson, Julian A. Simon, and Kannan M. Krishnan. Enhancing Cancer Therapeutics Using Size-Optimized Magnetic Fluid Hyperthermia. *Journal of Applied Physics*, 111(7):07B306–07B306, 2012. URL `http://dx.doi.org/10.1063/1.3671427`.

[154] Peter J. Krommenhoek, Junwei Wang, Nathaniel Hentz, Aaron C. Johnston-Peck, Krystian A. Kozek, Gregory Kalyuzhny, and Joseph B. Tracy. Bulky Adamantanethiolate and Cyclohexanethiolate Ligands Favor

Smaller Gold Nanoparticles with Altered Discrete Sizes. *ACS nano*, 6(6): 4903–4911, 2012. URL http://dx.doi.org/10.1021/nn3003778.

[155] J.G. Mattei, F. Pelletier, D. Ciuculescu, P. Lecante, J.C. Dupin, N. Yaacoub, J. Allouche, J.M. Greneche, D. Gonbeau, C. Amiens, et al. Formation of Bimetallic FeBi Nanostructured Particles: Investigation of a Complex Growth Mechanism. *The Journal of Physical Chemistry C*, 117 (3):1477–1484, 2013. URL http://dx.doi.org/10.1021/jp309408j.

[156] A. Rapallo, J.A. Olmos-Asar, O.A. Oviedo, M. Luduena, R. Ferrando, and M.M. Mariscal. Thermal Properties of Co/Au Nanoalloys and Comparison of Different Computer Simulation Techniques. *The Journal of Physical Chemistry C*, 116(32):17210–17218, 2012. URL http://dx.doi.org/10.1021/jp302001c.

[157] M. Stefan, C. Leostean, O. Pana, M.-L. Soran, R.C. Suciu, E. Gautron, and O. Chauvet. Synthesis and Characterization of Fe_3O_4@ ZnS and Fe_3O@ Au@ ZnS Core–Shell Nanoparticles. *Applied Surface Science*, 288: 180–192, 2013. URL http://dx.doi.org/10.1016/j.apsusc.2013.10.005.

[158] Duc Quy Vo, Eui-Jung Kim, and Sunwook Kim. Surface Modification of Hydrophobic Nanocrystals Using Short-Chain Carboxylic Acids. *Journal of Colloid and Interface Science*, 337(1):75–80, 2009. URL http://dx.doi.org/10.1016/j.jcis.2009.04.078.

[159] Yaolin Xu, Soubantika Palchoudhury, Ying Qin, Thomas Macher, and Yuping Bao. Make Conjugation Simple: A Facile Approach to Integrated Nanostructures. *Langmuir*, 28(23):8767–8772, 2012. URL http://dx.doi.org/10.1021/la301200g.

[160] Jiahua Zhu, Qingliang He, Zhiping Luo, Airat Khasanov, Yutong Li, Luyi Sun, Qiang Wang, Suying Wei, and Zhanhu Guo. Property Manipulated Polypropylene–Iron Nanocomposites with Maleic Anhydride Polypropylene. *Journal of Materials Chemistry*, 22(31):15928–15938, 2012. URL http://dx.doi.org/10.1039/C2JM32371K.

[161] Yujun Song, Shaoxia Ji, Yuan-Jun Song, Runsheng Li, Jie Ding, Xiaomiao Shen, Rongming Wang, Riwei Xu, and Xiaoyu Gu. In Situ Redox Microfluidic Synthesis of Core–Shell Nanoparticles and Their Long-Term Stability. *The Journal of Physical Chemistry C*, 117(33):17274–17284, 2013. URL http://dx.doi.org/10.1021/jp404402g.

[162] Haining Liu, Yaolin Xu, Ying Qin, Wesley Sanderson, Dorothy Crowley, C Heath Turner, and Yuping Bao. Ligand-Directed Formation of Gold Tetrapod Nanostructures. *The Journal of Physical Chemistry C*, 117(33): 17143–17150, 2013. URL `http://dx.doi.org/10.1021/jp405859x`.

[163] Kathryn L. Krycka, Julie A. Borchers, German Salazar-Alvarez, Alberto López-Ortega, Marta Estrader, Sonia Estrade, Elin Winkler, Roberto Daniel Zysler, Jordi Sort, Francesca Peiró, et al. Resolving Material-Specific Structures within $Fe_3O_4|$ γ-Mn_2O_3 Core| Shell Nanoparticles Using Anomalous Small-Angle X-Ray Scattering. *ACS Nano*, 7(2): 921–931, 2013. URL `http://dx.doi.org/10.1021/nn303600e`.

[164] Nabraj Bhattarai, Gilberto Casillas, Subarna Khanal, Daniel Bahena, J. Jesus Velazquez-Salazar, Sergio Mejia, Arturo Ponce, Vinayak P. Dravid, Robert L. Whetten, Marcelo M. Mariscal, et al. Structure and Composition of Au/Co Magneto-Plasmonic Nanoparticles. *MRS Communications*, 3(03):177–183, 2013. URL `http://dx.doi.org/10.1557/mrc.2013.30`.

[165] Yang Lu, Yang Zhao, Le Yu, Liang Dong, Ce Shi, Ming-Jun Hu, Yun-Jun Xu, Long-Ping Wen, and Shu-Hong Yu. Hydrophilic Co@Au Yolk/Shell Nanospheres: Synthesis, Assembly, and Application to Gene Delivery. *Advanced Materials*, 22(12):1407–1411, 2010. URL `http://dx.doi.org/10.1002/adma.200903298`.

[166] D. Llamosa Peréz, A. Espinosa, L. Martínez, E. Román, C. Ballesteros, A. Mayoral, M. García-Hernández, Ma-Hernandez, and Y. Huttel. Thermal Diffusion at Nanoscale: From CoAu Alloy Nanoparticles to Co@Au Core/Shell Structures. *The Journal of Physical Chemistry C*, 117:3101–3108, 2013. URL `http://dx.doi.org/10.1021/jp310971f`.

[167] Yujun Song, Jie Ding, and Yinghui Wang. Shell-Dependent Evolution of Optical and Magnetic Properties of Co@Au Core–Shell Nanoparticles. *The Journal of Physical Chemistry C*, 116(20):11343–11350, 2012. URL `http://dx.doi.org/10.1021/jp300118z`.

[168] Yujun Song, Yinghui Wang, Shaoxia Ji, and Jie Ding. Shell-Driven Fine Structure Transition of Core Materials in Co@Au Core-shell Nanoparticles. *Nano-Micro Letters*, 4(4):235–242, 2012. URL `http://dx.doi.org/10.3786/nml.v4i4.p235-242`.

150

[169] H. Calderon, Y. Bao, T. Wen, and K. Krishnan. Characterization of Core Shell Cu-Au Nanoparticles by Microscopy Techniques. *Microscopy and Microanalysis*, 17:1836–1837, 2011. URL `http://dx.doi.org/10.1017/S1431927611010051`.

[170] R. Jenkins, R. Manne, R. Robin, and C. Senemaud. Nomenclature, Symbols, Units and Their Usage in Spectrochemical Analysis - VIII. Nomenclature System for X-Ray Spectroscopy (Recommendations 1991). *Pure Appl. Chem.*, 63 (5):735 – 746, 1991. URL `http://dx.doi.org/10.1351/pac199163050735`.

[171] A. E. Neeves and M. H. Birnboim. Composite Structures for the Enhancement of Nonlinear-Optical Susceptibility. *J. Opt. Soc. Am. B*, 6(4):787–796, Apr 1989. URL `http://dx.doi.org/10.1364/JOSAB.6.000787`.

Danksagung

Nach etwas mehr als drei Jahren und gefühlten 10 kg Gummibärchen möchte ich an dieser Stelle diejenigen erwähnen, die mich während meiner Doktorarbeit unterstützt und entscheidend zum Gelingen beigetragen haben.

Prof. Dr. Andreas Hütten möchte ich für die Möglichkeit kurzfristig meine Doktorarbeit in seiner Arbeitsgruppe verfassen zu können und für viele Diskussionen danken. Prof. Dr. Thomas Huser danke ich für das Verfassen meines Zweitgutachtens.

Besonders möchte ich Nadine Mill danken, die alle Nanopartikel-Synthesen durchgeführt hat. Ihre Erfahrung hat zu schönen und reproduzierbaren Ergebnissen geführt. Dr. Karsten Rott danke ich für die technische Unterstützung in allen Bereichen meiner Arbeit.

Für die Einarbeitung am TEM danke ich Dr. Wiebke Hachmann. Ich konnte sehr von ihrem Sachverstand profitieren, was nach anfänglichen Schwierigkeiten zu sehr schönen TEM-Bildern geführt hat. Weiterhin danke ich ihr für die eher komplexe Einrichtung des HRTEMs, was mir kurzfristig die Möglichkeit gegeben hat, die Kristallstruktur meiner Partikel genauer zu Untersuchen.

Christian Sterwerf danke ich für die Durchführung der XRD-Messungen und Dr. Markus Meinert danke ich für seine Hilfe bei der Interpretation der XRD-Spektren und für die hilfreichen Diskussionen über verschiedene Kristallstrukturen und das Kobalt-Gold-Interface.

Dr. Annalena Wolff danke ich dafür, dass sie die FIB bedient und mir damit die detaillierten EDX-Analysen und STEM-Bilder meiner Nanopartikel ermöglicht hat. Die vielen hilfreichen Diskussionen, das Korrekturlesen meiner Arbeit und ihre moralische Unterstützung haben mir sehr geholfen und entscheidend zum Gelingen beigetragen.

Walid Hetaba von der TU Wien danke ich für zusätzliche EDX-Analysen und -Linescans, die leider nicht mehr in diese Arbeit gepasst haben. Dr. Julia Bader danke ich für die Möglichkeit meine Partikel mit IR-Spektroskopie

153